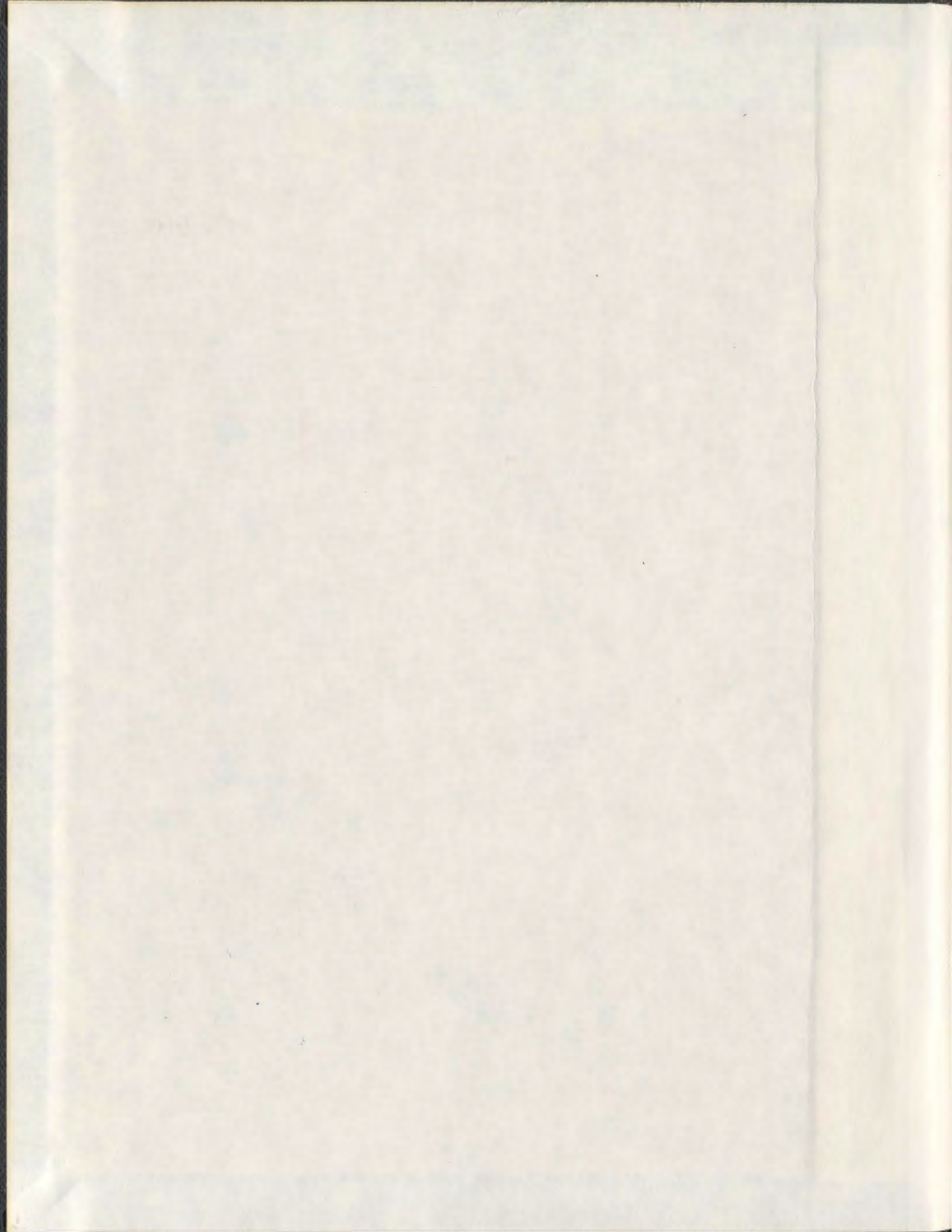
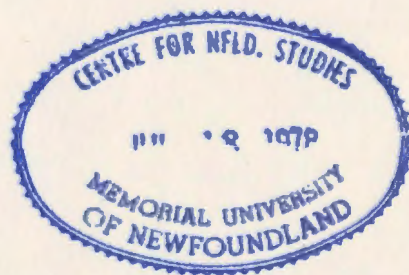


SEISMIC LIQUEFACTION OF HETEROGENEOUS SOIL:
MECHANISM AND EFFECTS ON STRUCTURAL RESPONSE

PRADIPTA CHAKRABORTTY



001311



**Seismic Liquefaction of Heterogeneous Soil:
Mechanism and Effects on Structural Response**

by

© Pradipta Chakraborty, B.E., M.Tech.

A thesis submitted to the
School of Graduate Studies
in partial fulfilment of the
requirements for the degree of

Doctor of Philosophy

Faculty of Engineering and Applied Science
Memorial University of Newfoundland

December 2008

St. John's

Newfoundland

Canada

To Silva.....

ABSTRACT

In the current practice of liquefaction prediction analysis, horizontally layered soil (with uniform properties within distinct soil layers) is usually assumed to estimate the liquefaction susceptibility of a soil deposit. However most of the soil properties of a natural deposit not only vary in the vertical direction but they could also vary in the horizontal direction, even within the so-called 'uniform' soil layers. This soil variability can be broadly classified into two main groups. They are the lithological heterogeneity (variability due to geological layers) and the small scale spatial variability. The first source of variability (variability due to layers) is considered properly in the current practice. But the second source of soil variability (small scale spatial variability), which is the subject of this research, is not properly addressed in general.

From recent numerical research it was observed in the case of seismically induced excess pore water pressure (EPWP) generation that more EPWP is generated during an earthquake in a heterogeneous soil deposit than in a homogeneous soil with equivalent average soil relative density. EPWP is generated in the loose sand pockets first and then the water migrates into the neighbouring dense soil, and softens the dense soil by reducing the effective stress. However, to date, a limited amount of experimental verifications are available to the practicing engineering community to help in recognizing, quantifying and accepting the above-mentioned behaviour of heterogeneous soils. Therefore the first major objective of the present study is to investigate, quantify, and explain the effects of small scale soil heterogeneity on seismically induced liquefaction using both numerical modelling and centrifuge experiments. The second

major objective of this research is to provide recommendations for seismic design of structures on heterogeneous soil.

A series of three centrifuge tests were performed in this study: one on homogeneous soil and two on heterogeneous soil. The test on uniform soil was performed on a soil deposit with the soil relative density lower than the average soil relative density of heterogeneous soil. The results, such as EPWP, accelerations, and settlements were monitored and measured throughout the test duration. However, it is very difficult and expensive to monitor all these responses everywhere in the model. Therefore, a numerical model was calibrated and validated from the centrifuge test results on uniform soil first. Then, the liquefaction mechanism in heterogeneous soil was studied in more details using the numerical simulations. Experimental results support the conclusion of previous research that more EPWP is generated in a heterogeneous soil than in the corresponding homogeneous soil. From this study it is concluded that although the average soil relative density of heterogeneous soil deposit (test2 and test3) was larger than that of the uniform soil (test1), the liquefaction resistance of the heterogeneous soil was lower than that of the uniform soil due to water migration from loose to dense soil pockets in heterogeneous soil deposit.

In the last part of this research, a parametric study was performed for finding the effects of soil heterogeneity on the structural response. The numerical model validated based on the results from the centrifuge experiments with heterogeneous soil was used in this study. Dynamic analyses were performed for various types of structures situated on heterogeneous soil. Based on the type of structure, this segment of the research is divided into two parts. The performance of a tower structure (where total settlements and base

rotations were of primary interest) was studied in the first part. In the second part, the performance of a frame structure (where total and differential settlements were of primary interest) was studied. Quantitative and qualitative recommendations for geotechnical design practice are provided for structures on liquefiable heterogeneous soil deposits for a wide range of soil relative densities. The results of reliability analysis for the structure situated on heterogeneous soil are presented in the form of fragility curves and combined damage curves.

Current design guidelines for spectral amplification of seismic motion were also verified for a range of soil properties, and updated guidelines were also provided after considering the effect of soil heterogeneity. The effect of soil variability was found to be not very significant in the studied ranges for calculating the values of spectral amplification factors. There is a less than 10% change in the values of F_a and F_v for heterogeneous soil compared to that in equivalent homogeneous soil.

ACKNOWLEDGEMENTS

I would like to express my sincere appreciation to all those who have supported me during pursuing the degree of Doctor of Philosophy. First of all, I would like to thank my supervisor, Dr. Radu Popescu, for his academic guidance, valuable technical comments and offering me the financial support and chance for doing this research.

I am also grateful to my co-supervisor and a member of my thesis review committee, Dr. Ryan Phillips for his guidance during centrifuge tests. I would also like to thank the other member of my thesis review committee, Dr. Leonard Lye, for his guidance, providing partial funding and for introducing me to design of experiment. Their recommendations have certainly improved the quality of the thesis. Special thanks are due to Dr. Bipul Hawladar for his suggestions during early phase of this research.

The financial support provided by the School of graduate studies at Memorial University of Newfoundland and the National Science and Engineering Research Council Research Assistantship are acknowledged with deep appreciation.

I would like to thank the members in CCORE centrifuge lab (Dr. Hesham Dief, Gerry, Don, Derry and Karl) for their help during testing program and my friends living in various parts of the world including those in St. John's. Special thank goes to Prem Kumar and Talukder for their help in submitting this thesis.

Finally I would like to thank my mother (ma), Aunt (chotomasimoni), Uncle (chotokaku), father (bapi), elder brother (dadabhai), and boudi for their support and encouragement throughout various stages of this study and my life. Their love, blessings, support, encouragement and sacrifices have been instrumental in guiding me to carry out my doctoral studies.

TABLE OF CONTENTS

ABSTRACT.....	II
ACKNOWLEDGEMENTS	V
TABLE OF CONTENTS	VI
LIST OF TABLES	IX
LIST OF FIGURES	XI
LIST OF PICTURES.....	XXII
LIST OF SYMBOLS AND ABBREVIATIONS	XXIII
CHAPTER 1	1
1.1. Introduction	1
1.2. Research Objectives	3
1.3. Original Contributions.....	4
1.4. Thesis Outline.....	6
CHAPTER 2	8
Literature review	8
2.1. Introduction	8
2.2. Soil Liquefaction	9
2.2.1 Assessment of Soil Liquefaction Potential	10
2.2.1.1 Empirical Methods Based on Field Test Data	10
2.2.1.2 Methods Based on Laboratory Tests	16
2.2.2 Prediction of Soil Liquefaction	19
2.3 Centrifuge Testing in Geotechnical Earthquake Engineering	20
2.3.1 Background of Geotechnical Centrifuge Modelling	21
2.3.2 Advantages of Centrifuge Tests	21
2.3.3 Disadvantages of Centrifuge Tests.....	22
2.3.4 Geotechnical Centrifuge Modelling of Soil Liquefaction.....	23
2.3.5 Assessment of Soil Relative Density during Centrifuge Tests	25
2.3.5.1 General.....	25
2.3.5.2 Needle Probe: Simplified Measurement Procedure.....	25
2.3.5.3 In-flight cone penetration test.....	27
2.3.5.4 Stress-densification.....	27
2.4 Numerical Modelling of Soil Liquefaction	29
2.4.1 Uncoupled Analysis	29
2.4.2 Partially-Coupled Analysis	30
2.4.3 Coupled Analysis	31
2.5 Influence of Soil Heterogeneity.....	32
2.5.1 General.....	32
2.5.2 Effect of Soil Heterogeneity on Various Geotechnical Problems.....	35
2.5.3 Effect of Soil Heterogeneity on Soil Liquefaction.....	36
2.5.3.1 Effect of Less Permeable Soil Layers on Soil Liquefaction	37

2.5.3.2	Effect of Small Scale Variability of Soil Properties on Liquefaction.....	37
2.6	Reliability in Geotechnical Engineering	44
2.6.1	Fundamentals of Reliability-Based Design.....	44
2.6.2	Application of Reliability in Assessment of Soil Liquefaction Potential	47
2.6.3	Reliability Studies for Heterogeneous Soil	48
2.6.4	Effect of Frequency Content on Structural Response	49
2.6.5	Fragility Curves in Geotechnical Earthquake Engineering.....	53
2.6.6	Design of Experiments (DOE).....	57
2.6.6.1	Overview	57
2.6.6.2	Two-Level Factorial Design.....	58
2.6.6.3	Central Composite Response Surface Design	60
CHAPTER 3	62
The Numerical Model and its Parameters	62
3.1.	Introduction	62
3.2.	Mathematical Model.....	63
3.3.	Estimation of Constitutive Parameters	66
3.4.	Liquefaction Strength Analysis	70
CHAPTER 4	77
Experimental Program	77
4.1.	Characteristics of Equipment and Centrifuge Facility at C-CORE.....	77
4.2.	Soil Characteristics and Centrifuge Test Setup	80
4.3.	Sample Preparation.....	84
4.4.	Saturation of Models for Centrifuge Tests	86
4.4.1	Pore Fluid.....	87
4.4.2	Saturation Procedure.....	88
4.5.	Instrumentation and Measurements.....	93
4.6.	Centrifuge Test Procedure and Results	96
4.6.1.	Measurement of Soil Relative Density	97
4.6.2.	Earthquake Simulation Test.....	98
4.6.3.	Discussion of Centrifuge Test Results	99
4.7.	Difficulties and Sources of Error during the Centrifuge Tests.....	110
4.8.	Summary and Conclusions	114
CHAPTER 5	121
Liquefaction Mechanisms for Heterogeneous Soil	121
5.1.	Introduction	121
5.2.	Liquefaction in Heterogeneous Soil: Preliminary Studies	122
5.3.	Numerical Modelling of Centrifuge Tests.....	127
5.3.1.	Calibration of the Numerical Model.....	128
5.3.2.	Finite Element Model.....	134
5.3.3.	Numerical Simulation of Centrifuge Tests: Model Validation	136
5.4.	Liquefaction Mechanism in Heterogeneous Soil: Results and Discussion	143
5.5.	Summary and Conclusions.....	151

CHAPTER 6	157
Reliability Analysis of Structures on Heterogeneous Soil	157
6.1. Introduction	157
6.2. Monte Carlo Simulation	158
6.2.1. Methodology of Monte Carlo Simulation	158
6.2.2. Stochastic Soil Properties.....	160
6.3. Tower Structure on Heterogeneous Soil.....	161
6.3.1. General	161
6.3.2. Seismic Motions.....	163
6.3.3. Finite Element Model.....	164
6.3.4. Results and Discussions	166
6.3.4.1. Pore Water Pressures, Deformations and Accelerations.....	166
6.3.4.2. Maximum Structural Displacements	172
6.3.4.3. Fragility Curves for the Response Variable.....	174
6.3.4.4. Combined Damage Curve.....	174
6.3.4.5. Design Recommendations	178
6.4. Frame Structure on Heterogeneous Soil.....	181
6.4.1. General	181
6.4.2. Seismic Input Acceleration Time Histories	182
6.4.3. Finite Element Model.....	184
6.4.4. Replacement Models for Settlements.....	186
6.4.4.1. Response Surface Method	186
6.4.4.2. Statistical Analysis of Results and Discussions.....	187
6.4.4.3. Validation of Response Surface Model (RSM)	190
6.4.5. Site Amplification Study.....	194
6.4.5.1. Base Case- Uniform Soil	194
6.4.5.2. Effect of the Presence of Structure:	196
6.4.5.3. Effect of Water Table Depth:	197
6.4.5.4. Effect of Soil Relative Density:	197
6.4.5.5. Effect of Fundamental Period of the Structure:	199
6.4.5.6. Effect of Soil Variability:	199
6.4.5.7. Design Recommendations on Amplification of Seismic Ground Motion	200
6.4.6. Results and Discussion.....	218
6.4.6.1. Maximum Structural Deformation Responses.....	218
6.4.6.2. Fragility Curves	226
6.4.6.3. Design Recommendations for Selecting an Equivalent Uniform Soil Strength	231
6.5. Summary and Conclusions	236
CHAPTER 7	255
Concluding Remarks	255
7.1. Summary and Conclusions	255
7.2. Scope of future study.....	260
REFERENCES	263
APPENDIX A	281
APPENDIX B	324

LIST OF TABLES

Table 2.1: Scaling relations in centrifuge modelling (N= Centrifuge scaling factor).....	61
Table 3.1: The parameters of the multi-yield plasticity model.....	72
Table 3.2: Correlations for the multi-yield plasticity model parameters.....	73
Table 4.1: Structural Properties of different components of frame structure in model scale	116
Table 4.2: Location of the transducers at prototype scale	117
Table 4.3: Specifications of the instruments used in centrifuge tests (after C-CORE, 2005).....	118
Table 4.4: Location of the pore pressure transducers, LVDT, and accelerometers in test 1	119
Table 4.5: Location of the pore pressure transducers, LVDT, and accelerometers in test 2	119
Table 4.6: Location of the pore pressure transducers, LVDT, and accelerometers in test 3	120
Table 5.1: Experimental and numerical results of cyclic undrained triaxial tests on uniform and layered soil samples (for cyclic stress ratio CSR=0.166)	154
Table 5.2: Parameters of the multi-yield plasticity model used for the saturated soil.....	155
Table 5.3: Poisson's ratio for different types of sand	156
Table 5.4: Constitutive parameters for linear-elastic materials used in the numerical simulation	156
Table 6.1: The correlations used for estimating parameters and the values of the multi-yield plasticity model parameters used in the analysis.....	239
Table 6.2: The parameters of the multi-yield plasticity model, and the values used for the saturated soil in the deterministic analysis.....	241
Table 6.3: The damage levels used in the study for generating combined damage curves	241
Table 6.4: Minimum Arias Intensities corresponding to several probabilities of exceeding three threshold levels of total settlements for a tower structure constructed on liquefiable uniform or variable soil.....	242
Table 6.5: Minimum Arias Intensities corresponding to several probabilities of exceeding three threshold levels of base rotation for a tower structure constructed on liquefiable uniform or variable soil.....	243
Table 6.6: Different factors used in Face-Centred Central Composite Design and their high and low levels.....	244

Table 6.7: Design layout for Response Surface Model-I using Face-Centred Central Composite Design and calculated (from FE analysis) responses.....	245
Table 6.8: Equations for Response Surface Models	246
Table 6.9: Validation of Response Surface Model-IV.....	249
Table 6.10: Comparison of the short (0.2s) and long period (1.0s) amplification factors, F_a and F_v results for different types of soil	250
Table 6.11: Arias Intensities (in m/s) corresponding to various exceedance probabilities for various threshold levels of structural settlements and various soil conditions	252
Table 6.12: Arias Intensities (in m/s) corresponding to various exceedance probabilities for various threshold levels of structural settlements and various soil conditions	253
Table 6.13: Practical recommendations on equivalent uniform soil relative density (D_r^e)	254
Table A.1: Earthquake data base used in the analyses with frame structure	281
Table A.2: Properties of various selected seismograms used in the finite element analysis	290
Table A.3: Design layout for Response Surface Model-II using Face-Centred Central Composite Design and calculated (from FE analysis) responses.....	294
Table A.4: Design layout for Response Surface Model-III (without replication) using Face-Centred Central Composite Design and calculated (from FE analysis) responses	295
Table A.5: Design layout for Response Surface Model-III (with 5-replication) using Face-Centred Central Composite Design and calculated (from FE analysis) responses.....	296
Table A.6: Design layout for Response Surface Model-IV using Face-Centred Central Composite Design and calculated (from FE analysis) responses.....	300
Table A.7: Design layout for Response Surface Model-IIIB (with 10-replication) using Face-Centred Central Composite Design and calculated (from FE analysis) responses	301
Table A.8: Validation of Response Surface Model-I.....	305
Table A.9: Validation of Response Surface Model-II	306
Table A.10: Validation of Response Surface Model-III	307

LIST OF FIGURES

Figure 2.1: Empirical methods based on field test data.....	11
Figure 2.2: Graph used to determine the CRR for clean and silty sands for magnitude 7.5 earthquakes (after Youd et al., 2001).....	12
Figure 2.3: Recommended CRR and CPT data along with empirical liquefaction data (after Robertson and Wride, 1998)	14
Figure 2.4: Recommended CRR and V_{s1} data along with empirical liquefaction data (after Andrus and Stokoe, 2000).....	16
Figure 2.5: Simplified measurement circuit (SG: signal generator, V_s : voltage at signal generator, ΔV_N : voltage drop at needle probe; after Cho et al., 2004).....	26
Figure 2.6: Inherent soil variability (after Phoon and Kulhawy, 1999a).....	34
Figure 2.7: Classification of soil Variability, uncertainty in soil properties and their effects.....	35
Figure 2.8: Flowchart for simulation of mV-nD non Gaussian stochastic fields (after Popescu et al., 1998b).....	43
Figure 2.9: Fundamentals of Reliability Analysis (after Haldar and Mahadevan, 2000)..	46
Figure 2.10: Base input accelerations and predicted accelerations at the base of the structure: comparison of Arias intensities (after Chakraborty et al., 2004b).....	53
Figure 2.11: Example of a typical Fragility curve (after Deodatis et al., 2000).....	55
Figure 2.12: Illustration of experiment design layouts for a two level full factorial design with three factors. Circles are showing the design points.....	59
Figure 2.13: Illustration of experiment design layouts for a Central-Composite Response Surface design (face centred) with three factors. Circles are showing the design points; squares are showing the centre points.....	60
Figure 3.1: Main features of the multi-yield plasticity soil constitutive model (after Popescu 1995).....	65
Figure 3.2: Liquefaction strength analysis using laboratory tests (Prevost and Popescu, 1996).....	71

Figure 4.1: Particle size distribution curve for Fraser river sand used in the centrifuge tests (after C-CORE, 2005).....81

Figure 4.2: Schematic diagram of centrifuge tests a. plan: test 1; b. plan: test 3; c. elevation: test 1; d. elevation: test 3.....83

Figure 4.3: Sand falling height vs. relative density relation.....85

Figure 4.4: Schematic diagram for preparing loose pockets in heterogeneous soil using two lightweight movable blocks (block1 and block2).....85

Figure 4.5: Schematic Diagram for Saturation Setup.....90

Figure 4.6: Average soil height (at model scale) during test 3 (heterogeneous soil). These values are average of 5 measurements at 50mm interval in z-direction starting at 43mm from side wall. There are Duxseal layers between 0-54mm and 683-737mm in x-direction. Plan is shown in the inset with dotted points for measurement location.....93

Figure 4.7: Cone penetration test results during test3 (tested up to 250mm soil depth). Desired locations of loose pockets are also shown in the figure. Test location is shown in Figure 4.2.....98

Figure 4.8: Recorded excess pore water pressure (EPWP) ratio with respect to the initial effective vertical stress at 6 locations in homogeneous soil (test1).....100

Figure 4.9: Recorded excess pore water pressure (EPWP) ratio with respect to the initial effective vertical stress at 2 locations in test2 and 4 locations below structure in test3 (heterogeneous soil) a. P1: dense soil; b. P2: loose soil; c. P3: dense soil; d. P4: loose soil.....101

Figure 4.10: Recorded excess pore water pressure (EPWP) ratio with respect to the initial effective vertical stress at 4 locations in the free field in test2 and in test3 (heterogeneous soil) a. P5 & P9: dense soil; b. P6 & P10: loose soil; c. P7 & P11: dense soil; d. P8 & P12: loose soil.....102

Figure 4.11: Comparison of EPWP ratio time histories in the free field between medium dense homogeneous soil (test1) and loose soil pockets in heterogeneous soil (test 2 and 3): a. P6 or P10; b. P8 or P12.....103

Figure 4.12: Comparison of EPWP ratio between homogeneous and heterogeneous soil (dense sand zone) in the free field a. P6: Medium dense vs. P5: Dense; b. P8: Medium dense vs. P7: Dense.....	103
Figure 4.13: Comparison of EPWP ratio time histories below structure: a. between medium dense homogeneous soil (test1) and loose soil pockets in heterogeneous soil (test 2 and 3); b. between medium dense homogeneous soil (test1) and dense soil pockets in heterogeneous soil (test 3).....	104
Figure 4.14: Recorded settlement of building in test homogeneous soil (PC1).....	105
Figure 4.15: Recorded settlement of building in heterogeneous soil (test2 and 3). Downward settlement is positive and upward is negative. No LVDT were placed at L3 and L4 in test2.....	105
Figure 4.16: Recorded accelerations in homogeneous soil (test1). Transducer locations are shown in Figure 4.2. There was no accelerometer at A6 in test1. A2 does not record anything due to connection problem.....	107
Figure 4.17: Recorded accelerations in heterogeneous soil (test3). No acceleration time histories were recorded during test2 due to a problem in data acquisition system. Transducer locations are shown in figure 4.2.....	108
Figure 4.18: Comparison of Arias Intensity evolution with time in the free field between homogeneous and heterogeneous soil: a. Mid depth: A5; b. Near surface: A7.....	109
Figure 4.19: Comparison of Arias Intensity variation (with depth) in the free field between homogeneous and heterogeneous soil. Depths are at prototype scale. Arias Intensities are calculated until 45s.....	109
Figure 5.1: Predicted relative vertical displacement (water-solid) at the interface of silt and sand in the layered sample. Upward (vertical) relative displacements are positive.....	123
Figure 5.2: Effect of loose pocket/layer inside dense soil deposit: a. Comparison of computed excess pore water pressure (EPWP) ratios in the free field (dense sand) for tests BG4 and BG5; b. Computed relative movement of water with respect to the solid phase at the interface between loose and dense sand in test BG5. Positive displacements are upward (vertical) and left to right	

(horizontal); c. Finite element mesh with transducer locations (after Popescu et al., 2006).....	124
Figure 5.3: a. EPWP ratio time histories for the chess-board type heterogeneous soil computed at two adjacent locations in the free field (one in the loose soil: element 1, and the other in the dense soil: element 2); b. EPWP ratio in the free field in element 2; c. Finite element mesh (after Popescu et al., 2006).....	126
Figure 5.4: a. Finite element mesh: chess-board-like alternating loose and dense sands; b. Finite element mesh: isolated loose sand pockets in dense sand; Evolution of excess pore water pressure (EPWP) ratio with respect to the initial effective vertical stress at 2 locations in heterogeneous and uniform soil: c. Element A; d. Element B (after Popescu and Chakraborty, 2006).	127
Figure 5.5: Liquefaction strength analysis: a. relation between soil relative density and cyclic stress ratio (CSR) which causes liquefaction in $N_L=10$ cycle (obtained from Vaid et al., 2001); b. illustrative example for calculating X_{pp} from element test. An example for calculating X_{pp} for 40% soil relative density is shown by arrows.....	133
Figure 5.6: Finite element meshes used in the numerical simulation of centrifuge tests on homogeneous and heterogeneous soil.....	135
Figure 5.7: Recorded and computed excess pore water pressure (EPWP) ratio with respect to the initial effective vertical stress at 4 locations in test1 (medium dense homogeneous soil): a. Below structure at shallow depth: P2; b. Below structure at larger depth: P3; c. Free field at shallow depth: P6; d. Free field at larger depth: P8.....	138
Figure 5.8: Recorded and computed excess pore water pressure (EPWP) ratio with respect to the initial effective vertical stress at 4 locations in the free field in test3 (heterogeneous soil): a. P5: Dense sand; b. P10: Loose sand; c. P7: Dense sand; d. P8: Loose sand.....	139
Figure 5.9: Recorded and computed excess pore water pressure (EPWP) ratio with respect to the initial effective vertical stress at 4 locations below structure in	

test3 (heterogeneous soil): a. P1: Dense sand; b. P2: Loose sand; c. P3: Dense sand; d. P4: Loose sand.....	140
Figure 5.10: Comparison of excess pore water pressure (EPWP) ratio between homogeneous and heterogeneous soil at time $t=30s$ (depths at prototype scale).....	141
Figure 5.11: Recorded and computed settlement of building in test1 (homogeneous soil): a. L1; b. L2.....	141
Figure 5.12: Recorded and computed settlement of building in test3 (heterogeneous soil): a. L1; b. L2.....	142
Figure 5.13: Recorded and computed accelerations in test1 (homogeneous soil).....	142
Figure 5.14: Recorded and computed accelerations in test3 (heterogeneous soil).....	143
Figure 5.15: Computed EPWP ratio time histories in test3 (heterogeneous soil) in the middle of two adjacent dense and loose soil pockets in the free field: a. Element <i>A</i> : Dense soil vs. Element <i>B</i> : Loose soil; b. Element <i>B</i> : Loose soil vs. Element <i>C</i> : Dense soil; c. Element <i>B</i> : Loose soil vs. Element <i>D</i> : Dense soil; d. Finite element mesh with element locations.....	144
Figure 5.16: Computed EPWP ratio time histories in test3 (heterogeneous soil) computed at two adjacent locations: a. Free field (one in the loose soil: element E, and the other in the dense soil: element F); b. below structure (one in the loose soil: element G, and the other in the dense soil: element H); elements are shown in Figure 5.15(d).....	146
Figure 5.17: Computed relative movement of water in the free field (lower depth) with respect to the solid phase at the interface location between loose and dense sand in test on heterogeneous soil: a. vertical movement at two different nodes; b. horizontal (x) and vertical (y) movement at same node in homogeneous soil; c. horizontal (x) and vertical (y) movement at same node in heterogeneous soil. Positive relative displacements are upward (vertical) and left to right (horizontal); d. Finite element mesh with locations of nodes.....	146
Figure 5.18: Computed relative movement of water in the free field (higher depth) with respect to the solid phase at the interface location between loose and dense	

sand in test on heterogeneous soil: a. vertical movement at two different nodes in homogeneous and heterogeneous soil; b. horizontal (x) and vertical (y) movement at same node in homogeneous and heterogeneous soil. Positive relative displacements are upward (vertical) and left to right (horizontal); nodes are shown in Figure 5.17(d).....	147
Figure 5.19: Computed relative movement of water below structure with respect to the solid phase at the interface location between loose and dense sand in test on heterogeneous soil: a. vertical movement at two different nodes in homogeneous and heterogeneous soil; b. horizontal (x) and vertical (y) movement at same node in homogeneous and heterogeneous soil. Positive relative displacements are upward (vertical) and left to right (horizontal); nodes are shown in Figure 5.17(d).....	147
Figure 5.20: Evolution of predicted contours of excess pore water pressure ratios during tests on homogeneous and heterogeneous soil: a-f. in test1; g-l. in test3; The end of earthquake shaking is at time=20.5s.....	149
Figure 5.21: Evolution of predicted contours of volumetric strain: a-e. in test1; f-j. in test3 at the end of analysis (time=89s); The end of earthquake shaking is at time=20.5s; The end of analysis is at time=89s.....	150
Figure 5.22: Predicted contours of maximum shear strain at the end of analysis (time=89s): a. Test1; b. Test3 (locations of loose pockets are shown by red lines).....	151
Figure 5.23: Flowchart showing liquefaction mechanism in heterogeneous soil.....	152
Figure 6.1: Comparison of the response spectra for the acceleration time histories used in the analysis.....	164
Figure 6.2: Finite element mesh of soil-structure model.....	166
Figure 6.3: Excess pore water pressure contours for variable soil, seismic motion type 1, sample #51 (IA=1.15m/s, PGA=0.28g).....	167
Figure 6.4: Maximum shear strain contours and deformed mesh for variable soil, seismic motion type 1, sample #51. Deformation magnification factor = 3.....	168

Figure 6.5: Maximum shear strain contours and deformed mesh at time $T=10$ sec. for variable soil, seismic motion type 1, and various soil samples and seismic motion intensities. Deformation magnification factor = 3.....	169
Figure 6.6: Excess pore water pressure contours for sample #51 at time $T=10$ sec: a. uniform soil, seismic motion type 1; b. variable soil, seismic motion type 1; c. uniform soil, seismic motion type 3; d. variable soil, seismic motion type 3.....	170
Figure 6.7: Maximum shear strain contours and deformed mesh for sample #51 at time $T=10$ sec: a. uniform soil, seismic motion type 1; b. variable soil, seismic motion type 1; c. uniform soil, seismic motion type 3; d. variable soil, seismic motion type 3. Deformation magnification factor = 3.....	171
Figure 6.8: Comparison between Arias Intensities of base input accelerations and that of the computed accelerations at the base of the structure.....	172
Figure 6.9: Predicted maximum values of structural responses: a. maximum settlement and b. base rotation, for all cases analyzed.....	173
Figure 6.10: Comparison between analysis results for various cases in terms of fragility curves: a. settlements; b. rotations.....	175
Figure 6.11: Fragility curves for structure on randomly variable soil deposit subjected to type 3 seismic motion: a. settlements; b. rotations.....	176
Figure 6.12: Venn diagram of damages.....	177
Figure 6.13: Type-I damage curve: probability of damage due to exceeding a. level-2 maximum settlement and/or level-2 maximum base rotation; b. level-3 maximum settlement and/or level-2 maximum base rotation.....	179
Figure 6.14: Type-II damage curve: probability of damage due to exceeding a. both level-2 maximum settlement and level-2 maximum base rotation; b. both level-2 maximum settlement and level-1 maximum base rotation.....	180
Figure 6.15: Response spectra at 5% damping of the selected records: a. for uniform soil; b. for variable soil. The arrows at 1Hz frequency in figure a shows how $S_a(1.0)$ values in Figure 6.24 are obtained.....	183
Figure 6.16: Finite element mesh of soil-structure model.....	184
Figure 6.17: Scatter plot for the validation of Replacement Model-I.....	190

Figure 6.18: Scatter plot for the validation of Replacement Model-II.....191

Figure 6.19: Scatter plot for the validation of Replacement Model-III, IIIA and IIIB...192

Figure 6.20: Scatter plot for the validation of Replacement Model-IV.....193

Figure 6.21: Amplification functions for loose saturated soil ($D_r=45\%$) site: a. Free field- Node4; b. Below structure- Node5; c. Partial finite element mesh showing output node locations.....195

Figure 6.22: Comparison of Arias Intensity for different soil conditions- input vs. response at the foundation level: a. loose soil: free field vs. below structure; b. loose soil: saturated vs. unsaturated; c. loose vs. dense soil; d. structure I vs. structure II; e. loose saturated soil: uniform vs. variable; f. loose saturated variable soil vs. dense saturated uniform soil vs. dense saturated variable soil.....198

Figure 6.23: Comparison of peak acceleration for different soil conditions- input vs. response at the foundation level: a. loose soil: free field vs. below structure; b. loose soil: saturated vs. unsaturated; c. loose vs. dense soil; d. structure I vs. structure II; e. loose saturated soil: uniform vs. variable; f. loose saturated variable soil vs. dense saturated uniform soil vs. dense saturated variable soil.....201

Figure 6.24: Regression equations of spectral amplification vs. input spectral acceleration for loose saturated, cohesionless soil: a. AF(0.2) or F_a vs input S_a at $T=0.2s$; b. AF(0.5) vs input S_a at $T=0.5s$. The star markers in the figure are showing the values obtained from 90 analyses performed on loose saturated soil.....202

Figure 6.25: Regression equations of spectral amplification vs. input spectral acceleration for loose unsaturated cohesionless soil: a. AF(0.2) or F_a vs input S_a at $T=0.2s$; b. AF(0.5) vs input S_a at $T=0.5s$205

Figure 6.26: Regression equations of spectral amplification vs. input spectral acceleration for dense saturated cohesionless soil: a. AF(0.2) or F_a vs input S_a at $T=0.2s$; b. AF(0.5) vs input S_a at $T=0.5s$207

Figure 6.27: Regression equations of spectral amplification vs. input spectral acceleration for dense unsaturated cohesionless soil: a. AF(0.2) or Fa vs input Sa at T=0.2s; b. AF(0.5) vs input Sa at T=0.5s.....209

Figure 6.28: Regression equations of spectral amplification vs. input spectral acceleration for loose saturated heterogeneous soil (CV=0.2): a. AF(0.2) or Fa vs input Sa at T=0.2s; b. AF(0.5) vs input Sa at T=0.5s.....211

Figure 6.29: Regression equations of spectral amplification vs. input spectral acceleration for loose saturated heterogeneous soil (CV=0.5): a. AF(0.2) or Fa vs input Sa at T=0.2s; b. AF(0.5) vs input Sa at T=0.5s.....213

Figure 6.30: Comparison of spectral amplification vs. spectral acceleration for loose soil: a. AF(0.2) or Fa vs input Sa at T=0.2s; b. AF(1.0) or Fv vs input Sa at T=0.5s.....215

Figure 6.31: Comparison of spectral amplification vs. spectral acceleration for dense soil: a. AF(0.2) or Fa vs input Sa at T=0.2s; b. AF(1.0) or Fv vs input Sa at T=0.5s.....216

Figure 6.32: Maximum Bending Moment ratio (with respect to the structure on loose saturated soil) for different soil conditions. Where, bending moment ratio= maximum bending moment in the structure resting on other type of soil/maximum bending moment in the structure resting on loose saturated soil.....219

Figure 6.33: Maximum story drift ratio (with respect to the structure on loose saturated soil) for different soil conditions. Where, drift ratio= (maximum story drift at floor level in the structure resting on other type of soil/maximum story drift at floor level in the structure on loose saturated soil.....220

Figure 6.34: Maximum base shear ratio (with respect to the structure on loose saturated soil) for different soil conditions. Where, base shear ratio=(maximum base shear in the structure resting on other type of soil/maximum base shear at floor level in the structure on loose saturated soil.....221

Figure 6.35: Scatter plot of maximum total settlement at left footing for different soil conditions below structure.....222

Figure 6.36: Scatter plot of maximum differential settlement for different soil conditions below structure.....	223
Figure 6.37: Fragility curves for maximum total settlement.....	225
Figure 6.38: Fragility curves for maximum differential settlement.....	227
Figure 6.39: Fragility curves for structure on randomly variable loose saturated soil (COV=0.5) deposit subjected to 18 selected seismic motions: a. total settlement of left footing; b. differential settlement.....	228
Figure 6.40: Type-I damage curve: probability of damage due to exceeding a. 10cm maximum total settlement and/or 3cm maximum differential settlement; b. 10cm maximum total settlement and/or 0.4cm maximum differential settlement.....	229
Figure 6.41: Type-II damage curve: probability of damage due to exceeding a. 5cm maximum total settlement and 3cm maximum differential settlement; b. 5cm maximum total settlement and 0.4cm maximum differential settlement.....	230
Figure 6.42: Comparison for maximum total settlements for the structure on loose heterogeneous soil and equivalent uniform soil.....	233
Figure 6.43: Comparison for maximum differential settlements for the structure on loose heterogeneous soil and equivalent uniform soil.....	234
Figure 6.44: Comparison for maximum settlements for the structure on dense heterogeneous soil and equivalent uniform soil.....	235
Figure A.1: Fragility curve for maximum total settlements.....	308
Figure A.2: Fragility curve for maximum base rotation.....	309
Figure A.3: Type-I damage curve: probability of damage due to exceeding a. level-1 maximum settlement and/or level-1 maximum base rotation; b. level-2 maximum settlement and/or level-1 maximum base rotation; c. level-3 maximum settlement and/or level-1 maximum base rotation.....	310
Figure A.4: Type-I damage curve: probability of damage due to exceeding a. level-1 maximum settlement and/or level-2 maximum base rotation.....	311
Figure A.5: Type-I damage curve: probability of damage due to exceeding a. level-1 maximum settlement and/or level-3 maximum base rotation; b. level-2	

maximum settlement and/or level-3 maximum base rotation; c. level-3 maximum settlement and/or level-3 maximum base rotation.....	312
Figure A.6: Type-II damage curve: probability of damage due to exceeding a. both level- 1 maximum settlement and level-1 maximum base rotation; b. both level-3 maximum settlement and level-1 maximum base rotation.....	313
Figure A.7: Type-II damage curve: probability of damage due to exceeding a. both level- 1 maximum settlement and level-2 maximum base rotation; b. both level-3 maximum settlement and level-2 maximum base rotation.....	314
Figure A.8: Type-II damage curve: probability of damage due to exceeding a. both level- 1 maximum settlement and level-3 maximum base rotation; b. both level-2 maximum settlement and level-3 maximum base rotation; c. both level-3 maximum settlement and level-3 maximum base rotation.....	315
Figure A.9: Fragility curve for maximum total settlements exceeds 5cm.....	316
Figure A.10: Fragility curve for maximum total settlements exceeds 10cm.....	317
Figure A.11: Fragility curve for maximum total settlements exceeds 15cm.....	318
Figure A.12: Fragility curve for maximum total settlements exceeds 20cm.....	319
Figure A.13: Fragility curve for maximum differential settlements exceeds 0.5cm.....	320
Figure A.14: Fragility curve for maximum differential settlements exceeds 1.5cm.....	321
Figure A.15: Fragility curve for maximum differential settlements exceeds 3cm.....	322
Figure A.16: Fragility curve for maximum differential settlements exceeds 5cm.....	323
Figure B.1: Mean Amplification functions for loose saturated soil ($D_r=45\%$) site sorted by Arias intensity (m/s).....	324
Figure B.2: Mean amplification functions for loose unsaturated soil ($D_r=45\%$) site: a. Free field- Node4; b. Below structure- Node5. Locations of nodes are shown in Figure 6.21.....	325
Figure B.3: Mean amplification functions for dense saturated soil ($D_r=85\%$) site: a. Free field- Node4; b. Below structure- Node5.....	326
Figure B.4: Mean amplification functions for dense saturated soil ($D_r=85\%$) site for structure II: Below structure- Node5.....	327
Figure B.5: Amplification function for variable soil in the free field (Node 4).....	327

LIST OF PICTURES

Picture 1: Centrifuge at C-CORE.....	79
Picture 2: Earthquake simulator (after C-CORE, 2005).....	79
Picture 3: Frame structure on two strip footings.....	82
Picture 4: Setup for sand raining during test 2.....	84
Picture 5: Top view of the model with placed instruments in test1 at two different depths; (a) at 5m depth; (b) at 1m depth; PP* is a PPT used for pile testing (not related with this thesis).....	86
Picture 6: Model during saturation under vacuum.....	91
Picture 7: Elevation of heterogeneous soil model during saturation in test2.....	92
Picture 8: Elevation of heterogeneous soil model after saturation in test3.....	92
Picture 9: Placing the box on centrifuge arm using forklift truck during test3.....	95
Picture 10: Top view of partially excavated model after test3.....	95
Picture 11: Centrifuge model ready to fly for first flight during test1.....	96
Picture 12: Top view of the model failed during saturation.....	110

LIST OF SYMBOLS AND ABBREVIATIONS

1D	One-dimensional
2D	Two-dimensional
3D	Three-dimensional
a_{\max}	Peak ground acceleration
$a(t)$	Ground acceleration at time instant t
α^s	Solid acceleration
ANOVA	Analysis of Variance method
b	Body force per unit mass
B_0	Bulk modulus
BPT	Becker penetration test
C	A sand stiffness number that is independent of void ratio
C_B	Correction factor for SPT borehole diameter
C_E	Correction factor for SPT hammer energy ratio
C_N	A factor to correct measured SPT penetration resistance for overburden pressure
C_Q	Normalizing factor for cone penetration resistance
C_S	Correction for SPT sampler with or without liners
C_R	Correction factor for SPT rod length
C_u	Uniformity coefficient
CCD	Central Composite Design
CDF	Cumulative density function
CV, COV	Coefficient of variation (= standard deviation/mean)

CPT	Cone penetration test
CRR	Cyclic resistance ratio
CSR	Cyclic stress ratio
D_r	Soil relative density
D_{r0}	Initial relative density at 0 kPa
e	Measurement error
e_{max}	Maximum void ratio
e_{min}	Minimum void ratio
ESB	Equivalent shear beam
EPWP	Excess pore water pressure
F	Formation factor
F_a	Short period (0.2s) amplification factor
F_v	Long period (1.0s) amplification factor
$F_G(x)$	Gaussian distribution function
$F_{nG}(x)$	Non-Gaussian distribution function
f	Form factor
$f_G(x)$	Gaussian stochastic field
$f_{nG}(x)$	Non-Gaussian stochastic field
G_0	Low strain elastic shear modulus
G_{max}	Elastic shear modulus at very low strain
i	Current
I_A	Arias intensity
k	Hydraulic conductivity

k_0	Coefficient of lateral stress
MSF	Magnitude-scaling factor
N	Centrifuge scaling factor
N_l	Measured standard penetration resistance at certain depth
$(N_l)_{60}$	Corrected SPT (N-value) value
n	Power exponent
n^w	Porosity
NCEER	National Centre for Earthquake Engineering Research
P_a	Atmospheric pressure
P^w	Pore fluid pressure
PDF	Probability distribution function
q_c	Measured cone tip resistance
q_{cIN}	Corrected cone tip resistance
R	Resistance
R_{soil}	Resistance of the soil at the tip of the needle probe
R_w	Resistance of the free pore fluid measured by the needle probe
r_d	A factor that depends upon depth and stiffness of soil column
$S^0(k)$	Target cross spectral density matrix
$S_G(k)$	Cross-spectral density matrix of Gaussian mV-nD field
$S_{nG}(k)$	Cross-spectral density matrix of non-Gaussian mV-nD field
S_F	Nominal safety factor
SPT	Standard penetration test
t	Deterministic trend component

V	Voltage
V_s	Voltage at signal generator
V_S	Shear wave velocity
V_{SI}	Overburden stress-corrected shear wave velocity
v^s (v^w)	solid (fluid) velocity
VELACS	Verification of Liquefaction Analysis by Centrifuge Studies
w	Random component
X_{pp}	Dilation parameter
z	Depth
α	Stress strain curve coefficient
ΔV_N	Voltage drop at needle probe
ξ	<i>In-situ</i> soil property
ε_{dev}^{max}	Maximum deviatoric strain
λ^w	Fluid bulk modulus
μ_S, σ_S	Mean and standard deviation of load
μ_R, σ_R	Mean and standard deviation of resistance
ν	Poisson's ratio
ρ_s	Solid mass density
ρ_w	Fluid mass density
σ'_0	Effective overburden pressure
σ_0	Total overburden pressure
σ'_{vo}	Vertical effective stress

$\sigma^{1,S}$ Solid (effective) stress

ϕ Friction angle at failure

ψ Dilation angle

CHAPTER 1

1.1. Introduction

Liquefaction induced settlement of foundations during an earthquake is a major cause of damage to all types of structures, including buildings. Extensive damage to buildings due to soil liquefaction related settlements was observed during most of the major earthquakes; e.g. Niigata earthquake (1964), Kobe earthquake (1995), and Turkey earthquake (1999). In the current practice of liquefaction prediction analysis, the concept of equivalent uniform soil is usually considered for assessing the liquefaction susceptibility of the soil. Most soil properties of a natural deposit not only vary in the vertical direction but they can also vary in the horizontal direction, even within the so-called 'uniform' soil layer. This soil variability can be broadly classified into two main groups. They are the lithological heterogeneity (e.g. variability due to geological layers) and the small scale spatial variability (e.g. variability due to presence of loose pockets). The first source of variability (variability due to layers) has been properly considered in current practice. But the second source of soil variability (small scale spatial variability), which is the subject of this research, is not properly addressed in general. From past numerical research it was observed that in the case of seismically induced excess pore water pressure (EPWP) generation, more EPWP is generated in a heterogeneous soil deposit than in a homogeneous soil with equivalent average geo-mechanical properties. This will also result in larger liquefaction induced structural settlements in heterogeneous

soil. Therefore, small scale soil heterogeneity must be taken into consideration in design to accurately determine liquefaction induced structural damage.

In addition to inducing uncertainty in the computed response, small scale spatial variability of soil properties within geologically distinct layers affects the mechanical behaviour of geotechnical systems. For example, in phenomena involving the presence of a failure surface (such as in case of slope failure or bearing capacity failure) the actual failure surface can deviate from its theoretical position to pass selectively through weaker soil zones. The average mobilized strength is also reduced when compared to that of a corresponding uniform soil. It is therefore desirable that the effects of spatial variability of liquefiable soil on structural response be accounted for in geotechnical earthquake engineering design.

Recent numerical studies identified that heterogeneous soils subjected to seismic loads that is likely to have significant influence on design practices in geotechnical earthquake engineering. It was observed in heterogeneous cohesionless soil that EPWP was generated in the loose sand pockets first. Then, the water migrated into the neighbouring dense soil and softened it by reducing the effective stress. However, to date, a limited amount of experimental verifications are available to the practicing engineering community to help in recognizing, quantifying and accepting the above-mentioned behaviour of heterogeneous soils. Therefore, further studies are required for explaining the liquefaction phenomena in heterogeneous soil.

1.2. Research Objectives

The liquefaction mechanism in heterogeneous soil will be studied in this research. There is very limited amount of experimental verification available to the practicing engineering community to help in properly understanding this mechanism in heterogeneous soil. Therefore, the present research has two major objectives. The first objective is to investigate, understand, and quantify the effects of small scale soil heterogeneity on seismically induced liquefaction. This will be done by means of a physical (geotechnical centrifuge test) as well as a numerical (using finite element methods) modelling. In the early stages of this research, numerical modelling will be used to simulate small scale laboratory tests (undrained cyclic triaxial test performed by Konrad and Dubeau, 2002) and centrifuge tests (Ghosh and Madabhushi, 2003) on non-homogeneous soil, performed by the other researchers. An important part of this study consisted of a series of dynamic centrifuge tests on heterogeneous soil and, later on, numerical modelling will be used to back analyse the centrifuge tests performed by the author. The numerical model used in the study is the multi-yield surface plasticity constitutive model implemented in the finite element computer code Dynaflo (Prevost, 2002)

The second main objective of this research is to provide recommendations for seismic design of structures on heterogeneous soil. This will be done by means of parametric studies using the numerical model validated based on centrifuge experiments with heterogeneous soil. Two different types of structures (tower and frame buildings) will be considered in this research. Design recommendations for the spectral amplification of seismic ground motion will also be provided.

To achieve these two main objectives, the present research will:

1. Study the mechanism by which soil heterogeneity affects liquefaction potential, by reproducing and analysing in detail the results of undrained cyclic laboratory soil tests on non-homogeneous soil samples, by means of finite element simulations.
2. Include a series of centrifuge tests (on homogeneous and heterogeneous soil models) as an important part of the research in geotechnical earthquake engineering.
3. Calibrate and validate a state of the art numerical model based on the results of a series of centrifuge tests.
4. Study the liquefaction mechanism in heterogeneous soil using both centrifuge experiments and numerical modelling.
5. Provide geotechnical design recommendations for structures on liquefiable heterogeneous soil deposits, based on the results of a reliability analysis.
6. Update design guidelines for spectral amplification of seismic ground motion.

1.3. Original Contributions

This research has the following original contributions:

1. Designing and performing a series of original geotechnical centrifuge experiments for heterogeneous soil deposits subjected to earthquake loading.
2. Investigating and explaining the mechanism by which soil heterogeneity affects liquefaction potential, by reproducing and analysing in detail the results of

undrained cyclic triaxial tests on non-homogeneous (layered) soil samples, by means of finite element simulations.

3. Calibrating and validating the multi-yield surface plasticity model parameters based on the results of centrifuge tests performed by the author on heterogeneous Fraser River sand deposits. This calibrated numerical model can then be used for further analysis.
4. Explaining the liquefaction mechanism in heterogeneous soil by a detailed analysis of centrifuge test results (performed by the Author) using both a) actual experimental records and b) numerical results. The calibrated numerical model allowed a considerably more detailed analysis of liquefaction process than possible with current centrifuge instrumentation. This idea of a detailed analysis of experimental results by means of numerical modelling was also applied in this research for studying relevant experiments performed by other researchers.
5. Geotechnical design recommendations for structures on liquefiable soil deposits, by directly including the effects of soil-structure interaction while assessing structural damage produced by earthquakes. The model used here not only accounts for the effects of soil nonlinearity and heterogeneity, but also allows effects of differential settlements of structure footings to be accounted for as an element of structural distress. On the other hand, the state-of-the-art so far is to apply the ground motion at the base of the structure without including the effect of differential settlements in loss estimations.
6. Update the current design guidelines for spectral amplification of seismic ground motion travelling through uniform and heterogeneous soil. Guidelines are

provided for calculating the short (0.2s) and long period (1.0s) amplification factors, F_a and F_v for different site conditions.

1.4. Thesis Outline

This research addresses two major aspects. Therefore, the thesis can be divided into two parts besides the literature review. The first part (Chapters 3, 4 and 5) contains geotechnical centrifuge experiments, numerical model calibration and validation, and an explanation of liquefaction mechanism in heterogeneous soil. The second part (Chapter 6) focuses on reliability of structures on heterogeneous soil. It is based on the conclusions and the analysis methods developed and validated in the first part. The second part includes parametric studies, which result in design recommendations.

This thesis is divided into seven chapters.

Chapter 1 is an introduction about the research. It also contains the objectives of this research, original contributions from this research and the outline of this thesis.

Chapter 2 is a literature review, which is divided into three major parts. In part one, soil liquefaction and conventional procedures used for determining the effect of soil liquefaction are explained briefly (in subsection 2.1, 2.2, 2.3 and 2.4). In the second part (subsection 2.5), the available studies related to the influence of soil heterogeneity on different geotechnical phenomenon (focusing mainly on soil liquefaction) are discussed. In the last part, literature related to reliability analysis in geotechnical engineering is discussed (subsection 2.6).

Chapter 3 contains a brief description of the finite element computer code Dynaflo, the numerical model used in this research, and the procedure for estimating different constitutive parameters of the model.

In this research, three earthquake simulation geotechnical centrifuge tests were performed using the centrifuge facilities at C-CORE and Memorial University of Newfoundland in St. John's. The different aspects of centrifuge tests and test results are discussed in detail in **Chapter 4**.

The numerical model calibration and validation using the results of the centrifuge tests performed by the author are presented in **Chapter 5**. The liquefaction mechanism in heterogeneous soil is also described in this chapter, from the detailed analysis of i) actual experimental results and ii) numerical simulation results.

Chapter 6 deals with the parametric studies using a numerical model, validated by centrifuge experiments with heterogeneous soil. In the first part of this parametric study (subsection 6.3), tower structures are considered where total settlements and base rotations are of primary interest. In the second part (subsection 6.4) of the parametric study, a frame structure on heterogeneous soil is considered where total and differential settlements are of primary interest. Summary and conclusions are presented in subsection 6.5.

Concluding remarks and recommendations for further study are presented in **Chapter 7**.

CHAPTER 2

Literature review

2.1. Introduction

The major objective of the present study is to explain the mechanism of soil liquefaction on heterogeneous soil and to investigate the seismic performance of a structure that is situated on heterogeneous liquefiable soil. Hence, available literature related to these topics are addressed in a systematic way in this chapter.

Natural soil properties randomly vary from one point to another, even within so called 'uniform' soil layers. In addition to inducing uncertainty in the computed response, natural spatial variability of soil properties within geologically distinct layers affects the mechanical behaviour of geotechnical systems. For example, in the event of landslides or bearing capacity failures, the actual failure surface can deviate from its theoretical position to pass selectively through weaker soil zones and thus the average mobilized strength is reduced when compared to that of a corresponding uniform soil (Focht and Focht 2001, Popescu et al. 2005a). In seismically induced soil liquefaction, it has been seen (Popescu et al. 1997, 2005b, 2005c, 2006) that a larger amount of excess pore water pressure (EPWP) is generated in a heterogeneous soil than in the corresponding uniform soil having geotechnical properties equal to the average properties of the variable soil.

The seismically induced soil liquefaction is a major problem in geotechnical earthquake engineering. After the devastating earthquake at Alaska and Niigata in 1964, this phenomenon has received a lot of attention in the last four decades. Different

methodologies have been proposed to estimate and understand the consequences of seismically-induced liquefaction on the performance of geotechnical systems. This soil liquefaction phenomenon and its different estimation procedures are discussed in following sections.

2.2 Soil Liquefaction

The appropriate definition for soil liquefaction has been the subject of a continuing debate within the geotechnical profession. Soil liquefaction (as defined by Castro and Poulos, 1977) is a phenomenon wherein a mass of saturated soil, when subjected to monotonic or cyclic loading, loses its partial or full shear resistance due to the generation of EPWP. Marcuson (1978) defined soil liquefaction as the transformation of a granular material from a solid to a liquefied state as a consequence of increased pore water pressure.

The large ground deformation, induced by liquefaction, is a leading cause of disaster during earthquakes. This phenomenon occurs most commonly in loose to medium dense granular soils, which have a tendency to compact when sheared. In saturated soils, the dissipation of EPWP may be prevented by the presence of silty or clayey seam inclusions, or may not have enough time to dissipate due to rapid loading; as in the case of seismic loads. In this situation, the tendency for compaction results in an increase in pore water pressure. This leads to a reduction in effective stress, and a corresponding decrease in the frictional shear strength. If the EPWP generated at certain location in a purely frictional soil (e.g., sand) reaches the initial value of the effective vertical stress, then, theoretically, all shear strength is lost at that location and the soil

liquefies and behaves like a viscous fluid. EPWP's are also induced in moderate to dense granular materials subjected to cyclic loads, but due to their tendency to dilate during shear, the softening is only temporary, leading to increased cyclic shear strains, but not to major strength loss and large ground deformations. This phenomenon is known as cyclic mobility (Youd et al., 2001; Popescu et al., 2006).

Liquefaction is associated with the tendency for soil grains to rearrange when sheared. Therefore, anything (such as particle cementation, soil fabric etc.) that prevents the rearrangement of soil grains will increase the liquefaction resistance. Natural soil deposits prior to the Holocene age (more than 10,000 years old) are usually not prone to liquefaction (Youd and Perkins, 1978). Various methods have been developed in the last four decades for assessing and predicting the soil liquefaction. Different methods for assessing soil liquefaction are discussed in the next section.

2.2.1 Assessment of Soil Liquefaction Potential

The currently available methods of liquefaction potential assessment can be divided into two groups:

- a) Empirical methods based on field test data
- b) Methods based on laboratory tests

2.2.1.1 Empirical Methods Based on Field Test Data

After the earthquakes in Alaska (1964) and Niigata (1964), Seed and Idriss (1970) developed a methodology known as the 'simplified procedure' for evaluating liquefaction resistance of soil deposits. Since then, the procedure has been modified and updated by the authors as well as by the other researchers. Seed et al. (1983) included the magnitude-scaling factor in the calculation for cyclic stress ratio (CSR) induced by an earthquake at

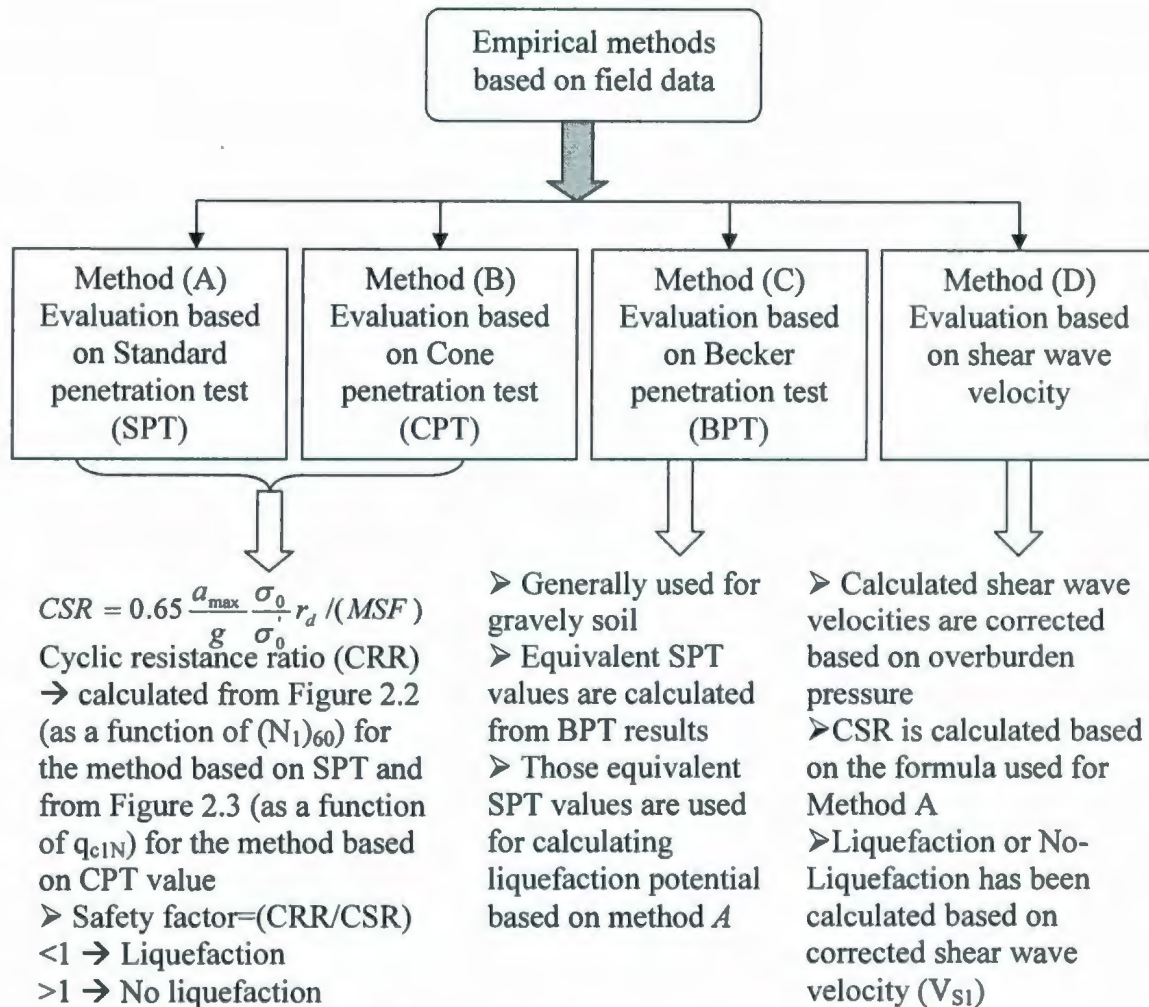


Figure 2.1: Empirical methods based on field test data.

a given depth in horizontal soil deposit. Later several researchers proposed various empirical methods based on different types of field test (SPT, CPT, BPT, shear wave velocity) results. Some of such commonly used methods have been shown in Figure 2.1. In all these methods, CSR has been calculated for a given earthquake amplitude at a certain depth in the soil deposit using the following relation:

$$CSR = 0.65 \frac{a_{max}}{g} \frac{\sigma_0}{\sigma'_0} r_d / (MSF) \quad (2.1)$$

where MSF is a magnitude-scaling factor, σ'_0 is the effective overburden pressure, σ_0 is the total overburden pressure, and a_{max} is the peak ground acceleration.

The r_d is a factor that depends upon depth and stiffness of soil column, which can be calculated from r_d vs. effective overburden pressure graph or from the following relations (Youd et al., 2001):

$$r_d = 1.0 - 0.00765z \quad \text{for } z \leq 9.15 \text{ m} \quad (2.2)$$

$$r_d = 1.174 - 0.0267z \quad \text{for } 9.15\text{m} < z \leq 23 \text{ m} \quad (2.3)$$

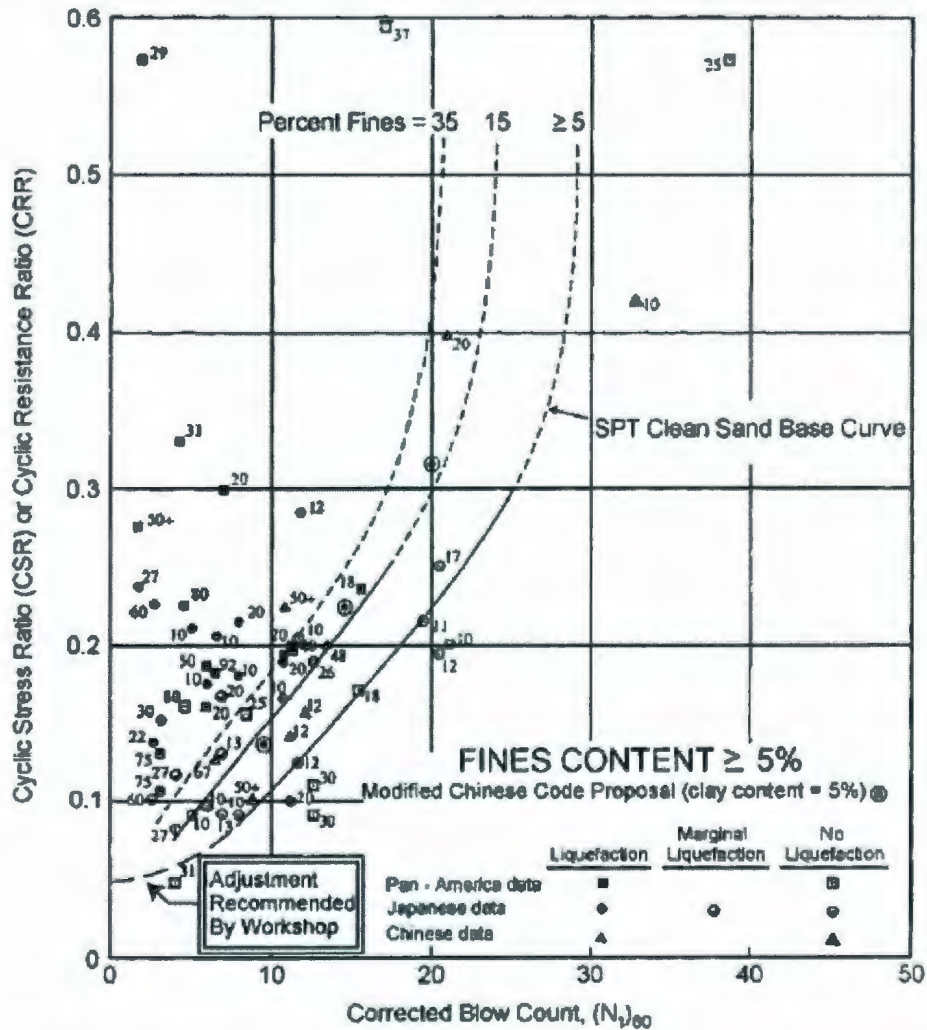


Figure 2.2: Graph used to determine the CRR for clean and silty sands for magnitude 7.5 earthquakes (after Youd et al., 2001).

In the 'simplified procedure' (after calculating CSR) the corrected SPT (N-value) value can be calculated using the following equation:

$$(N_1)_{60} = N_1 C_N C_E C_B C_R C_S \quad (2.4)$$

where N_1 is the measured standard penetration resistance at certain depth, C_N is a factor to correct measured penetration resistance for overburden pressure, C_E is the correction factor for hammer energy ratio, C_B is the correction factor for borehole diameter, C_R is the correction factor for rod length, and C_S is the correction for sampler with or without liners. A more detailed discussion about these factors can be found in Youd et al. (2001). After determination of $(N_1)_{60}$, the cyclic resistance ratio (CRR) can be calculated from Figure 2.2 (first presented by Seed et al. (1983) and later modified by various researchers [see NCEER-96 (National Centre for Earthquake Engineering Research) workshop (Youd et al., 2001)]). By comparing this value with CSR (From Eq. 2.1), a factor of safety for liquefaction potential can be inferred. If the safety factor at a particular depth is less than 1, liquefaction is expected at that location.

Another commonly used empirical method is based on cone penetration resistance value. Robertson and Campanella (1985) and Seed and De-Alba (1986) proposed this method, which is essentially similar to the previous one, but uses *in-situ* recorded cone tip resistance and friction ratio. The method was extensively documented by Robertson and Wride (1998). In recent years this method has become more popular because CPT gives more reliable results than SPT. The use of this method is increasing, as more and more CPT data are available from sites affected by earthquakes. The curve recommended by Robertson and Wride (1998) for calculating CRR from normalised cone tip resistance is shown in Figure 2.3. The corrected cone tip resistance (q_{c1N}) can be calculated from the following equation:

$$q_{c1N} = C_Q \frac{q_c}{P_a} \quad (2.5)$$

where q_c is the measured cone tip resistance and P_a is 100kPa or approximately one atmosphere of pressure in the same units used for σ'_{vo} , σ'_{vo} is the vertical effective stress, C_Q is the normalizing factor for cone penetration resistance; $C_Q = \left(\frac{P_a}{\sigma'_{vo}}\right)^n$, and n is an exponent that varies with soil type (0.5 to 1.0).

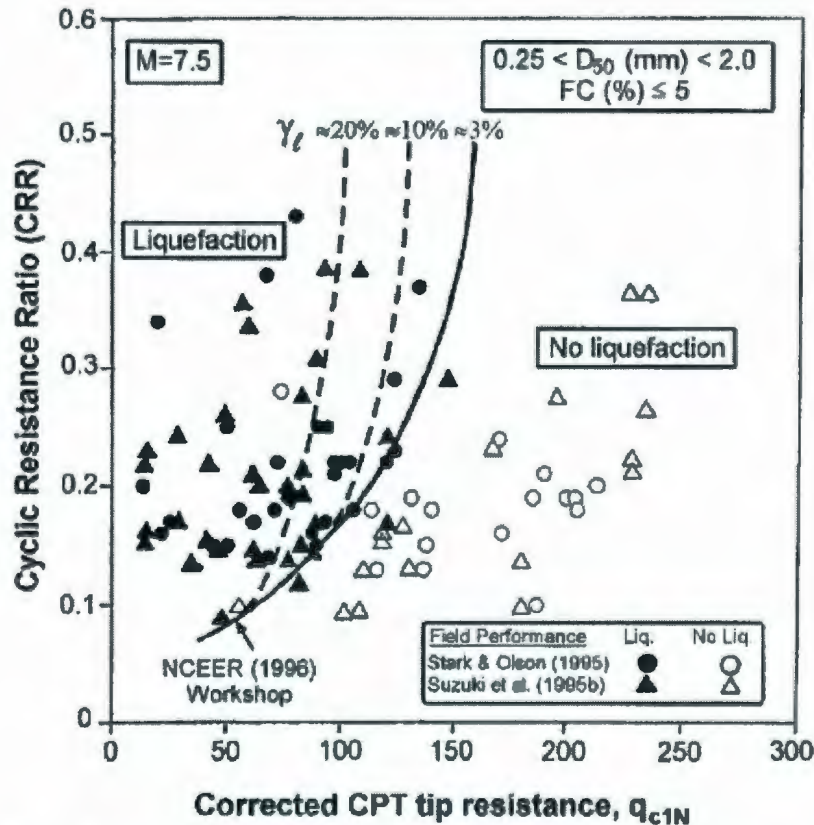


Figure 2.3: Recommended CRR and CPT data along with empirical liquefaction data (after Robertson and Wride, 1998).

However, soils with significant gravel contents cannot be reliably evaluated using CPT or SPT because the gravel particles are larger in relation to the effective size of the penetrometers. So for these types of soils, Becker penetration test (BPT) results are used for finding equivalent SPT values. Those equivalent SPT values are used for finding the liquefaction resistance of the soil (Harder and Seed, 1986).

Another empirical method commonly used is the soil liquefaction evaluation method based on shear wave velocity. Andrus and Stokoe (1997, 2000) proposed this method for calculating liquefaction potential in granular soil based on shear wave velocity (V_s). The use of V_s for evaluation of liquefaction resistance is effective because both V_s and the liquefaction resistance are similarly influenced by the same factors (e.g., void ratio, soil type etc.). Youd et al. (2001) have mentioned numerous advantages (e.g., measurements are possible in soils that are difficult to penetrate with CPT or SPT) and disadvantages (e.g., V_s directly related to small-strain shear modulus whereas liquefaction is a large strain phenomenon) of this method. Andrus and Stokoe (1997, 2000) and NCEER recommended criteria for measuring the liquefaction resistance using V_{s1} is shown in Figure 2.4. In Figure 2.4, overburden stress-corrected shear wave velocity (V_{s1}) can be calculated using the following equation:

$$V_{s1} = V_s \left(\frac{P_a}{\sigma'_{v0}} \right)^{0.25} \quad (2.6)$$

where $P_a = 100\text{kPa}$ or approximately one atmosphere of pressure and σ'_{v0} is the initial effective vertical stress in the same unit as P_a .

Popescu et al. (1997) compared the liquefaction susceptibility of a soil deposit estimated by the simplified methods that uses empirical correlations between normalized penetration resistance and cyclic resistance ratio for level ground conditions, with the numerical analysis results for a stochastically variable soil. The analyses were performed for four different types of input motion (generated based on four different response spectra). It was found that stochastic model predictions were in good agreement with the results of the liquefaction assessment based on those empirical correlations. It was

concluded by Popescu et al. (1997) that the simplified method, which is based on field measurement results, implicitly accounts for natural soil variability. The simplified method is designed for horizontal soil deposits and gives a good estimation of the liquefaction susceptibility at the site, but cannot account for a series of factors, such as: seismic effects on structures (e.g. total and differential settlements), effects of seismic loading rate, etc.

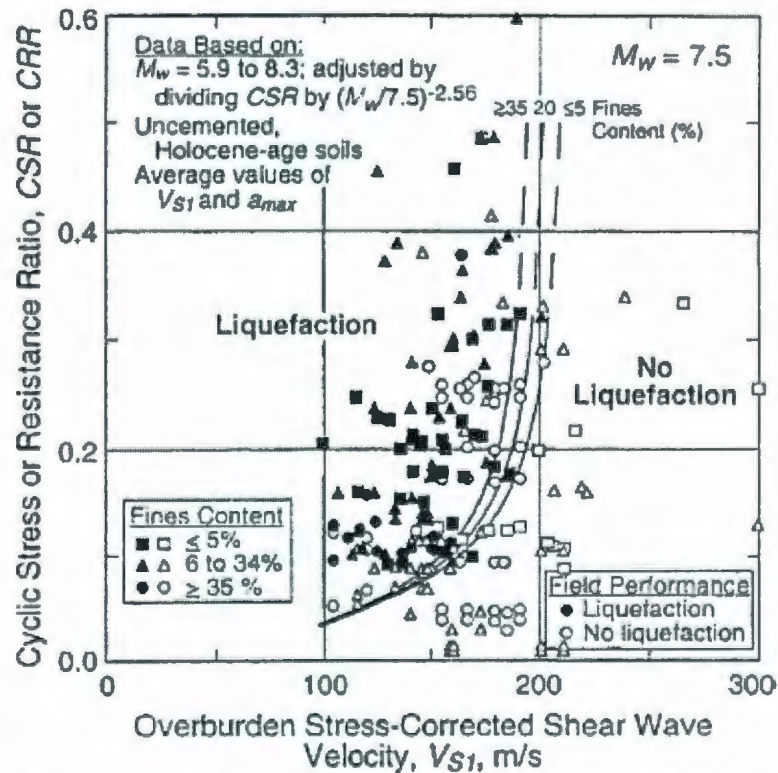


Figure 2.4: Recommended CRR and V_{s1} data along with empirical liquefaction data (after Andrus and Stokoe, 2000).

2.2.1.2 Methods Based on Laboratory Tests

Laboratory tests are one of the effective means of evaluating soil liquefaction. Most commonly used laboratory tests for the evaluation of soil liquefaction are the undrained cyclic triaxial test and the undrained cyclic simple shear test.

a) Evaluation Based on Undrained Cyclic Triaxial Test

During an earthquake, the soil is subjected to a series of cyclic shear strains that reverse directions many times. Such deformation conditions can best be reproduced in the laboratory by a simple shear test conducted under cyclic conditions (Prakash, 1981). However, they may also be approximately reproduced by the cyclic triaxial compression tests. In the 1960s, comprehensive laboratory investigation programs on liquefaction of sands were initiated at the University of California, Berkeley. Seed and Lee (1966) reported the first set of comprehensive triaxial test data on sand. After that, undrained cyclic triaxial tests have been widely used for evaluating the liquefaction phenomena in sandy soil. In cyclic triaxial tests, the 45° -inclined plane in the specimen represents the shear plane (typically the horizontal plane) in the ground and the cyclic shear stress (i.e., the half of the deviator stress) on that plane simulates the cyclic loading during an earthquake.

At a given initial void ratio and stress state, the sample preparation method has a significant effect on the strength of the sample (Vaid and Sivathayalan, 2000). Vaid and Sivathayalan (2000) documented a comprehensive study on Fraser River sand using different sample preparation methods. It was concluded that moist-tamping samples resulted in a very strain softening response; the strength ultimately reached the steady state. The air-pluviated specimen was also strain softened but to a lesser extent, demonstrating a quasi steady state type response. However, water-pluviated sample did not strain soften but behaved in a strain-hardening (dilative) manner for the range of relative densities and soil types investigated. The sample preparation method has quite significant influence on the cyclic resistance of soils. Wijewickreme et al. (2005) documented for Fraser River sand that, specimens reconstituted by the water-pluviation

exhibit higher cyclic strengths compared to those prepared by air-pluviation. For more details about the effect of sample preparation method on liquefaction strength, the reader is referred to Jafari-Mehrabadi (2006).

b) Evaluation Based on Cyclic Simple Shear Test

Peacock and Seed (1968) documented the first comprehensive study using cyclic shear apparatus on liquefaction (Prakash, 1981). The authors performed liquefaction analyses of clean uniform Monterey, California, sand using cyclic simple shear apparatus. It was observed that the cyclic stress required to cause initial liquefaction under simple shear conditions was considerably less than the cyclic stress required to cause initial liquefaction under triaxial conditions. Vaid and Sivathayalan (1996) and Riemer and Seed (1997) documented some relationship between the liquefaction resistance of sands evaluated from triaxial tests and simple shear tests. Vaid and Sivathayalan (1996) reported that the ratio (C_r) between cyclic resistance in simple shear and that in triaxial test depends on the soil relative density and the level of confining stress. At a given confining stress and relative density, the cyclic stress ratio required to induce liquefaction was reported smaller under simple shear than that under triaxial condition. It was found that at a relative density of 40%, C_r was about 0.78 irrespective of the confining stress level. However, at the dense soil ($D_r=72\%$) it varies between 0.62 and 0.7 when the confining stress increases from 50 to 400 kPa.

Yoshimine et al., (1999) studied the undrained shear strengths measured in the laboratory for clean Toyoura (Japan) sand (Yoshimine et al., 1998). Later, those laboratory test results were compared with field performance data. The correlation given by Tatsouka et al. (1990) was used for converting the soil relative density to equivalent

cone resistance (q_{c1N}). It was reported that the behaviour of clean Toyoura sand in simple shear was consistent with the field performance observations. Triaxial compression tests overestimate the undrained shear strength and triaxial extension tests underestimate the undrained strength.

Other commonly used laboratory tests for studying the undrained behaviour of sand is the hollow cylinder torsional shear test. However, it is now well known that laboratory soil test results exhibit a large scatter due to errors related to sample disturbance (during sample collection, transportation and preparation), spatial variability of soil properties in natural deposits, testing errors, which affect their reliability (Prevost and Popescu, 1996). In spite of all this, laboratory tests are still very useful tools for assessing soil liquefaction potential.

2.2.2 Prediction of Soil Liquefaction

All the previous methods described in this chapter, such as 'simplified procedure' are useful for assessing the soil liquefaction. However, neither these methods (based on field test data) are able to consider the effect of EPWP redistribution due to dissipation, nor are they able to calculate the amount of deformation for a soil deposit. Calculating deformation usually requires performing some type of dynamic analysis. There are several methods available for predicting soil liquefaction and deformation, considering EPWP redistribution. The available methods for predicting liquefaction can be broadly divided into two groups:

- a) Methods based on physical modelling
- b) Methods based on numerical techniques (finite element methods)

Methods Based on Physical Modelling

The most basic and simple physical modelling method for predicting soil liquefaction is the shake table test. Another commonly used physical modelling technique for predicting soil liquefaction is centrifuge test. This method will be discussed in more details in section 2.3.

Shake Table Test

This method also known as 1-g shake table test. Soil is placed in a tank resting upon a shake table. Seismic motion is applied to the base of the table. Liquefaction susceptibility of the soil is observed for certain level of acceleration using this method. For more details about the method, refer to Finn et al. (1971), and Arya et al. (1978).

2.3 Centrifuge Testing in Geotechnical Earthquake Engineering

The more advanced and effective physical modelling method for predicting soil liquefaction is the centrifuge test. Centrifuge model testing represents one of the major physical modelling tools available to geotechnical researchers. This method is quite popular in recent times. The *in-situ* soil condition can be simulated in the laboratory by artificially increasing the gravitational force. For example, if a 10cm deep model container is filled with soil, placed at the end of the centrifuge arm and subjected to a centrifugal acceleration of 100g, the pressure and stress are increased by a factor of 100. So, the vertical stress at the base of the model container is equivalent to the vertical stress at a depth of $0.1\text{m} \times 100 = 10\text{m}$ real *in-situ* conditions. For interpreting the centrifuge results scaling relations are very important (see Taylor, 1995 for scaling law in centrifuge). Scaling relations for some of the important parameters are tabulated in Table 2.1. There is a difference in the scaling factor for dynamic and diffusion time. Usually

this difference is resolved by using a pore fluid with viscosity N -times (N = centrifuge scaling factor) larger than the viscosity of water.

2.3.1 Background of Geotechnical Centrifuge Modelling

In 1869, E. Phillips in France initiated the idea of the small scale modelling in the centrifuge to study self weight stresses in beams. Geotechnical engineers started using centrifuge as a research tool in Russia (former USSR) as early as 1936. Various techniques have been used by different researchers in earlier days for simulating earthquake motions. Zelikson et al. (1981) used the detonation of explosives to generate ground motion. Schofield (1981) described the bumpy road concept which was implemented and used in the Cambridge University centrifuge by Kutter (1983). Arulanandan et al. (1982) used a system which uses the piezoelectric effects to produce ground motion. Prevost and Scanlon (1983) implemented a method using a hydraulic hammer to strike a plate buried at the bottom of the soil model. Aboim (1986) used the more advanced electro-hydraulic method which can theoretically deliver various types of desired motion to the model (Yang, 1996). The world's most powerful centrifuge to date has been installed by the US Army Corps of Engineers and is capable of spinning a payload of up to 8000kg and providing inertial accelerations of up to 350g (Dief, 2000). With the implementation of various advanced earthquake shakers, centrifuge tests have become a useful tool for the research in geotechnical earthquake engineering. It has been widely used in different dynamic problems, such as the performance of deep and shallow foundations during earthquake, embankments, retaining walls, slope stability, and soil liquefaction.

2.3.2 Advantages of Centrifuge Tests

There are numerous advantages of using centrifuge as a tool in geotechnical earthquake engineering. Some of which, as documented by Hausler (2002), are as follows:

- Easy to monitor a small scale model which actually represents a large soil deposit in a prototype scale. It might be difficult to monitor such a large soil deposit during an earthquake. Using a centrifuge test will make it much easier.
- Efficient, cost effective and less laborious as compared to full scale testing.
- Repeated testing on similar models for experimental validation is much easier.
- Direct observation is possible for modes of failure and deformation. It is also much easier to identify new failure modes and mechanisms using centrifuge tests.
- It is a very useful tool for validating various numerical modelling techniques.

2.3.3 Disadvantages of Centrifuge Tests

There are a few disadvantages of using centrifuge as a tool in geotechnical earthquake engineering. Some of which, as documented by Hausler (2002), are as follows:

- **Boundary effects:** The side walls of a rigid model container limit the lateral deformation of the soil and provide a high coefficient of lateral earth pressure at rest. For a flexible container, the side walls may expand outward during flight, reducing the lateral resistance and allowing more space for expansion. The side walls are not frictionless and might affect the vertical deformation of the soil.

Mechanical and inertial interaction of the container wall and soil are also present in a rigid wall container. This effect might be eliminated by using flexible equivalent shear beam (ESB) containers, ideally matching the stiffness of a soil

column. Use of a rigid box in earthquake simulation centrifuge experiments induces a series of unwanted seismic waves that are generated by the reflection of seismic waves at each end wall of the box and are subsequently reflected back by the opposite wall. This phenomenon, which may induce a behaviour in the model different from the real field, is partly attenuated by placing Duxseal (a relatively soft material) at each end wall of the box to create absorbing boundaries. Duxseal has been used in the centrifuge experiments to prevent this seismic wave reflection from the lateral boundaries of the rigid centrifuge box, thus helping the soil deposit to behave like a semi-infinite medium.

The container bottom, where input motion is applied, represents a rather unnatural geological transition. The bottom of the model container provides a no fluid flow boundary condition. Dissipation of EPWP in deep soil might be prolonged because of this impermeable bottom boundary.

- Nonlinear stress distribution: the stress distribution within the model is slightly nonlinear due to an increasing radius of rotation with the depth of the model, which results in a variation in the g -level inside the model.
- Scaling and measurement error: Measurement and other instrumental errors might be amplified through adherence to the scaling relationship.

2.3.4 Geotechnical Centrifuge Modelling of Soil Liquefaction

In the last twenty five years, centrifuge modelling has been widely used in soil liquefaction studies. The Verification of Liquefaction Analysis by Centrifuge Studies (VELACS) project, sponsored by the National Science Foundation (NSF), was one of the largest research projects in this area. Researchers from various universities and industries

were actively involved on that project. The VELACS project showed the effectiveness of centrifuge tests for studying the effects of earthquake loading in cohesionless soil (Arulanandan and Scott, 1993, 1994). A study on mitigation of seismic liquefaction effects, based on centrifuge and numerical modelling, was documented by Jafari-Meharabadi (2006). Eight centrifuge tests were performed at C-CORE and the numerical study was performed at Memorial University (<http://geosim.engr.mun.ca/>) and University of British Columbia (<http://www.civil.ubc.ca/liquefaction/>).

Several centrifugal studies of seismic behaviour of tower structures on soil foundation were reported: Morris (1979) and Weissman and Prevost (1989) on tower structures on dry soil, and Madabhushi and Schofield (1993) on tower structures on saturated soil. Several tests with different input seismic accelerations have been performed to study the effect of characteristic frequency. Madabhushi and Schofield (1993) concluded that when the predominant frequency of input seismic motion was lower than the characteristic frequency of the system, the initial characteristic frequency of the system decreased during shaking to a value close to the predominant input seismic frequency due to build up of excess pore pressure and subsequent degradation of soil stiffness. Ghosh and Madabhushi (2003) performed a series of centrifuge experiments to analyze the effects of a localized loose patch in a dense sand deposit subjected to seismic loads. Most of the available literature on the simulation of soil liquefaction using centrifuge tests were either with uniform soil or layered soil deposits. However, until now, there is no other centrifuge study available with spatially variable (variability in both the horizontal as well as vertical direction) soil.

2.3.5 Assessment of Soil Relative Density during Centrifuge Tests

2.3.5.1 General

The micro-scale spatial variability of soil properties affects the soil responses in small scale laboratory tests as well as model scale centrifuge tests. Therefore it is very important to accurately determine the small scale variability of soil properties. For a cohesionless soil, most of the soil properties depend on soil relative density. Various direct and indirect methods have been developed to measure the soil relative density in the centrifuge tests. One of the most commonly used method is the in-flight cone penetration test. Cho et al. (2004), Lee (2003) presented a new method for determining soil profile during centrifuge tests using a needle probe. The method involved a needle probe pushed into the soil which measured the porosity of the soil medium along its path. Sodium chloride salt is added with the pore fluid to make the pore fluid electrically conductive.

2.3.5.2 Needle Probe: Simplified Measurement Procedure

Soil porosity is calculated from the measured resistivity of the soil-fluid medium. The electrical needle probe is a two lead coaxial conductor. It is manufactured by inserting an insulated wire inside a thin hypodermic needle, and filling the space between the wire and the inside wall of the needle with epoxy resin. The outside diameter of the needle is about 2.1mm. Since the needle probe needs to be mechanically strong to be pushed into the soil, a stainless steel tube is preferred for the outer conductor. Lee (2003) showed that soil impedance at low frequencies is resistive in nature. Therefore a simplified measurement procedure has been documented based on resistance only, $V=i*R$. This method requires the determination of current (i), and drop in voltage (V) to

measure the resistance (R) of the soil-fluid medium. The simplified measurement circuit is shown in Figure 2.5. It consists of a signal generator, a known resistor ($10\text{k}\Omega$), and a two-channel oscilloscope or an analog/digital (A/D) board. The current through the system, $i = (V_s - \Delta V_N) / R_{fix}$ is determined by measuring the voltage at the source V_s and the

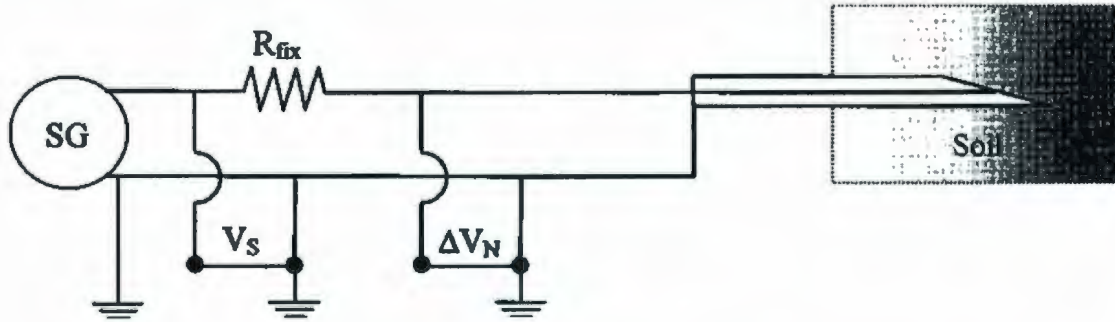


Figure 2.5: Simplified measurement circuit (SG: signal generator, V_s : voltage at signal generator, ΔV_N : voltage drop at needle probe; after Cho et al., 2004).

drop in voltage across the needle ΔV_N ; therefore, the voltage drops across the known resistor (R_{fix}) is $V_s - \Delta V_N$. Then, soil-pore fluid medium resistance R_{soil} at the tip of the needle probe is:

$$R_{soil} = \frac{\Delta V_N}{i} = \frac{\Delta V_N}{V_s - \Delta V_N} R_{fix} \quad (2.7)$$

If there is free pore water above the soil surface during a centrifuge test, and if it is assumed that pore fluid conductivity is uniform, then the formation factor can be directly calculated from the measured resistance (R_{soil}).

$$\text{Formation factor } (F) = R_{soil} / R_w \quad (2.8)$$

where R_w is the resistance of the free pore fluid measured by the needle probe and R_{soil} is the resistance of the soil-fluid medium measured at different depths using the same needle probe. Soil porosity (n) can be directly calculated from this formation factor using following relation:

$$n = F\left(\frac{1}{f}\right) \quad (2.9)$$

The average form factor (f), is a function of the particle shape and grain size distribution, and has been shown empirically and theoretically (Li et al., 2005) to be independent on the porosity. Therefore, f can be measured from disturbed or reconstituted samples of the soil-fluid medium during calibration.

2.3.5.3 In-flight cone penetration test

Another commonly used method for estimating soil relative density during centrifuge test is cone penetration test. The use of CPTs in geotechnical centrifuges is described for instance by Bolton et al. (1999) and is related more to the behaviour of a driven pile. Soil relative density is determined from the penetration resistance offer by the cohesionless soil. A pore pressure transducer, located directly behind the cone tip, is sometimes used (same as *in-situ* CPT) for measuring the pore pressures developing during penetration process. A centrifuge test with the 9.5mm diameter cone at a g-level of 70 represents a prototype cone of 66.5cm. The results of these CPT during centrifuge tests can be used for evaluating the soil in terms of relative density or strength or location of boundaries between different materials (Laue, 2002). The efficiency of CPT in centrifuge tests has been studied in a European research program between 5 different geotechnical centrifuge facilities (Renzi et al., 1994; Bolton et al., 1998).

2.3.5.4 Stress-densification

Stress densification occurs during a physical model test (e.g. centrifuge test), due to consolidation settlements in cohesionless soil. Park and Byrne (2004) developed a relation for calculating the amount of stress densification during a centrifuge test. In geotechnical centrifuge model testing, the model is usually prepared by air pluviation of

dry cohesionless soil into the model container at very low stress (in 1g). It is then subjected to a higher acceleration field (e.g. 70g). The stress increased accordingly causing high stresses at the base and low stress at the bottom of the model (non-uniform stress densification). This ultimately increases the density of the soil deposit (larger increase in higher depth and vice-versa) during a centrifuge test.

The amount of stress densification depends on the level of vertical effective stress at that location, soil type, and initial relative density of the soil. The steps for calculating stress densification are as follows:

1. Calculate the vertical effective stress (σ'_v) at a location where stress densification has to be calculated.
2. Calculate α using following relation:

$$\alpha = \left(\frac{1 + e_{\max}}{e_{\max} - e_{\min}} - D_{r0} \right) \frac{2(1.5 - D_{r0})}{C} \quad (2.10)$$

where e_{\max} and e_{\min} are the maximum and minimum void ratio, D_{r0} is the initial relative density at 0 kPa, C is a sand stiffness number that is independent of void ratio and the value for eight different type of sands are presented by Park and Byrne (2004).

3. Calculate new relative density (D_r) after stress densification based on the following relation:

$$D_r = D_{r0} + \alpha \sqrt{\frac{\sigma'_v}{P_a}} \quad (2.11)$$

where P_a is the atmospheric pressure (100 kPa).

2.4 Numerical Modelling of Soil Liquefaction

Both methods described in the preceding sections for liquefaction predictions are time-consuming and expensive. Therefore, different numerical codes have been developed to simulate and predict soil liquefaction utilising the advanced computation facility available nowadays. For a highly nonlinear behaviour, like in the case of saturated soil under earthquake loading, these numerical simulations are very useful and cost-effective. Based on the type of mathematical formulation and the techniques of solving, they are broadly classified as coupled, partially-coupled and uncoupled analyses. To calculate the responses more accurately, these numerical models should be calibrated and validated first, based on centrifuge tests. One of the largest studies for finding the effectiveness of these numerical models was the VELACS, sponsored by the NSF between 1991 and 1993. Some of the numerical models used in the VELACS project were: Dynaflo [multi yield plasticity model], DIANA-SWAN, SWANDYNE [generalised plasticity model], DYSAC2, LINOS, SUMDES [bounding surface model], LIQCA [classical plasticity], and QUAD4 [total stress] (Arulanandan and Scott, 1993). Results from the VELACS project indicated that the partially-coupled or uncoupled solution schemes used in that study did not perform particularly well. Different types of available finite element analysis techniques are briefly discussed here.

2.4.1 Uncoupled Analysis

Numerical simulation using uncoupled analysis involves evaluating different key aspects of behaviour separately, and shearing the results between different groups of separate analysis results. The effectiveness of this type of analysis depends on whether

there is any strong interdependence between phenomena, such that they significantly affect each other during dynamic loading. If there is not a strong interdependence between them, an uncoupled analysis may provide reasonable predictions of behaviour and performance.

One of the common uncoupled analysis techniques is the use of Newmark's method. In this approach, a dynamic ground response analysis is performed using the equivalent linear method with programs such as SHAKE (for one-dimensional case) or QUAD4 (for two-dimensional case). Limit equilibrium analyses are then performed, using degraded soil properties in the soil profile, to calculate the yield acceleration producing a factor of safety of one for each potential sliding surface. The lateral displacement is then typically estimated for the surface with the lowest yield acceleration by double-integrating the portion of the average acceleration record that exceeds the yield value (Cooke, 2000).

2.4.2 Partially-Coupled Analysis

In a partially-coupled or loosely-coupled analysis, the solution generally does not directly account for all of the interactions between the solid and fluid media, but uses some simplifications. For instance, in some partially-coupled analytical solutions the mechanical equilibrium equations may be solved first, and then the plastic volumetric strain estimated on the basis of the shear strain that occurs. The plastic volumetric strain is then applied to the system to get the increments in pore water pressure that occurs at that time. This cycle of calculations is then repeated for subsequent times. The partially-coupled analyses tend to use more readily obtainable soil properties and less complex soil

models. However, these simplifications can result in inaccuracies in predicted behaviour (Cooke, 2000).

2.4.3 Coupled Analysis

In coupled numerical analysis the analysis domain, such as a liquefiable soil deposit, is expressed by coupled field equations. These equations are solved by considering coupling between solid and fluid phase under dynamic loading (inertial coupling is an added advantage). A fully-coupled effective stress analysis is the one where solution scheme directly accounts for the dynamic interaction between the solid and fluid media, and the mechanical equilibrium and flow equations are solved simultaneously. The advantage of fully-coupled analyses is that the solution directly accounts for the solid-fluid interaction and, from that standpoint, is more complete. However, some parameters required in fully-coupled analyses to describe the interaction between the fluid and solid, as well as the overall soil mass behaviour, might be difficult to determine (Cooke, 2000).

Various researchers have studied the effectiveness of different fully coupled finite element codes for predicting the behaviour of saturated soil under dynamic loading. Jafari-Meharabadi (2006) reported the successful prediction of eight centrifuge tests for finding the seismic liquefaction countermeasures for waterfront slopes using Dynaflow. Li et al. (1998) reported the successful prediction of a site response for the 1986 Lotung earthquake in Taiwan using the finite element code SUMDES (Li et al., 1992). Arulanandan et al. (1997) reported successful use of DYSAC2 for predicting the behaviour of liquefiable soil deposits in the Marina District of San Francisco during the

1989 Loma Prieta earthquake. Madabhushi and Zeng (1998) successfully predicted the seismic response of a gravity quay wall on liquefiable sand modeled in the centrifuge using the code SWANDYNE.

Success is also reported in the literature with using solutions that are partially coupled in varying degrees for predicting the behaviour of liquefiable soil. Puebla et al. (1997) reported on the successful use of an elasto-plastic soil constitutive model, UBCSAND, implemented in the computer program FLAC (Cundall, 1995) to predict the pore pressure development and deformations in liquefiable sand beneath an embankment built in the field. Finn (1988, 1991) reported the successful validation of TARA-3 using centrifuge studies.

Based on the available literature it has been observed that partially or fully-coupled finite element computer codes have been able to predict the measured behaviour of liquefiable soils successfully. The degree of success appears dependent on the type of problem analyzed in some cases. Therefore, a critical part of selecting and using a numerical code is verifying its ability to predict the behaviour for the range of conditions of interest.

2.5 Influence of Soil Heterogeneity

2.5.1 General

In the case of seismically induced soil liquefaction, it was proven both experimentally (Budiman et al. 1995, Konrad and Dubeau 2002), and by numerical analyses (Popescu et al. 1997, Chakraborty et al. 2004a) that a larger amount of EPWP is generated in a heterogeneous soil than in the corresponding uniform soil, having geo-

mechanical properties equal to the average properties of the variable soil. Most of the soil properties of a natural deposit are variable in nature. Therefore, soil heterogeneity must be taken into consideration in soil liquefaction analysis.

In-situ soil properties may vary for a variety of reasons, such as depositional environment, degree of weathering, and physical environment (Jones et al., 2002). Phoon and Kulhawy (1999a) represented the spatial variation of soil properties using a simple model:

$$\xi(z) = t(z) + w(z) + e(z) \quad (2.12)$$

where ξ = *in-situ* soil property, t =deterministic trend component, w =random component, e =measurement error and z = depth. The trend and random components are explained graphically in Figure 2.6. The scale of fluctuation provides a measure of the estimated distance over which a soil property of interest shows strong correlation. A soil parameter with a small scale of fluctuation changes rapidly with position, and one with a long scale of fluctuation changes over greater distance. Another important term in quantifying soil variability is the coefficient of variation (COV = standard deviation/mean) of a soil parameter. It represents a relative measure of dispersion of the parameter. The COV has been commonly used to describe the variation of most of the geotechnical soil properties and *in-situ* test parameters.

The source of soil heterogeneity can be broadly classified into two (shown in Figure 2.7) main categories (Elkateb et al., 2003a). The first source of variability is lithological heterogeneity which is due to the presence of different geological layers. The second source of heterogeneity is small scale spatial soil variability, which is due to the thin layers embedded in a soil medium or the presence of loose soil pockets within a

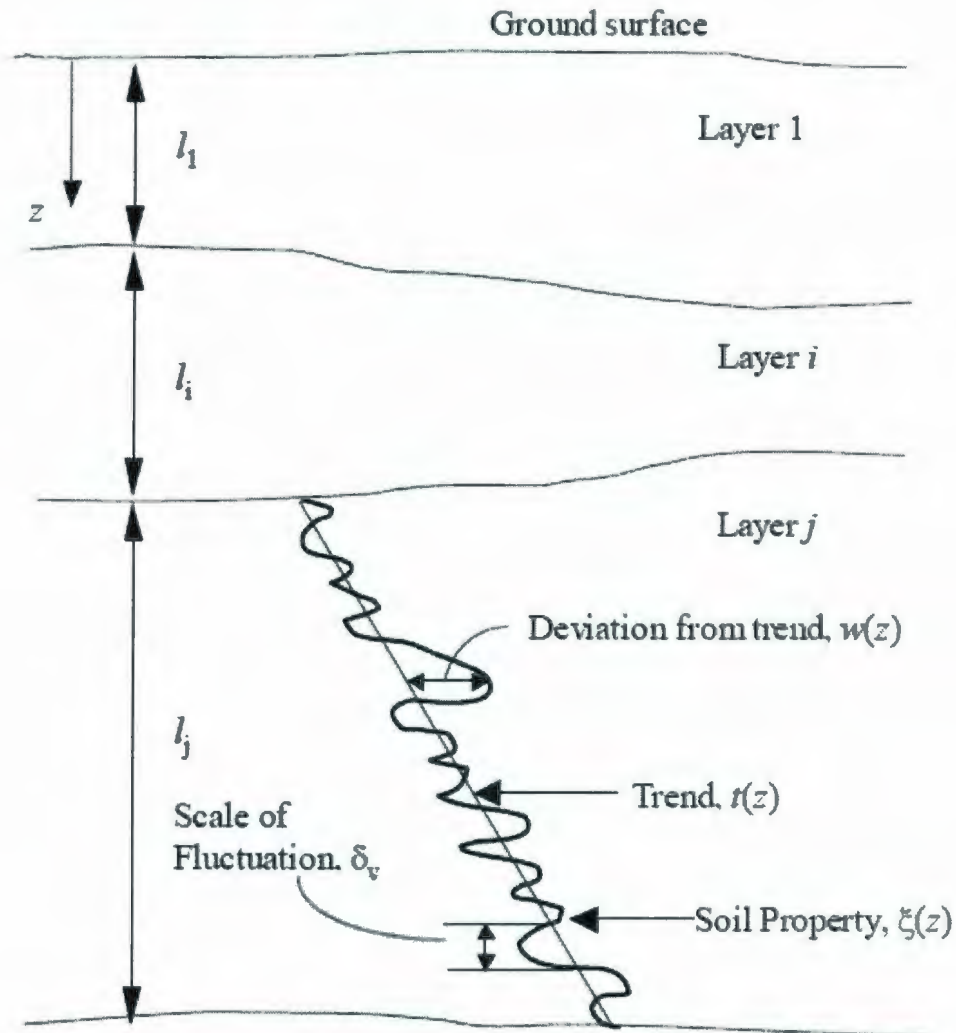


Figure 2.6: Inherent soil variability (after Phoon and Kulhawy, 1999a).

more uniform soil mass. These two types of soil heterogeneity combine with uncertainties in the soil properties (shown in Figure 2.7). The uncertainties in soil properties can occur due to different types of errors: measurement, transformation (modelling), and statistical (due to small sample size). Phoon and Kulhawy (1999a & b) quantified the small scale variability, the measurement errors, and the transformation errors as the primary source of geotechnical uncertainty. To evaluate geotechnical variability on a general basis for reliability based design procedure, it is necessary to assess different uncertainties (e.g., measurement error, transformation uncertainty, and

statistical uncertainty) separately (Phoon and Kulhawy, 1999a & b). Some useful guidelines on the values of coefficient of variation (*COV*) of measurement error, transformation error and overall properties were also presented in the paper.

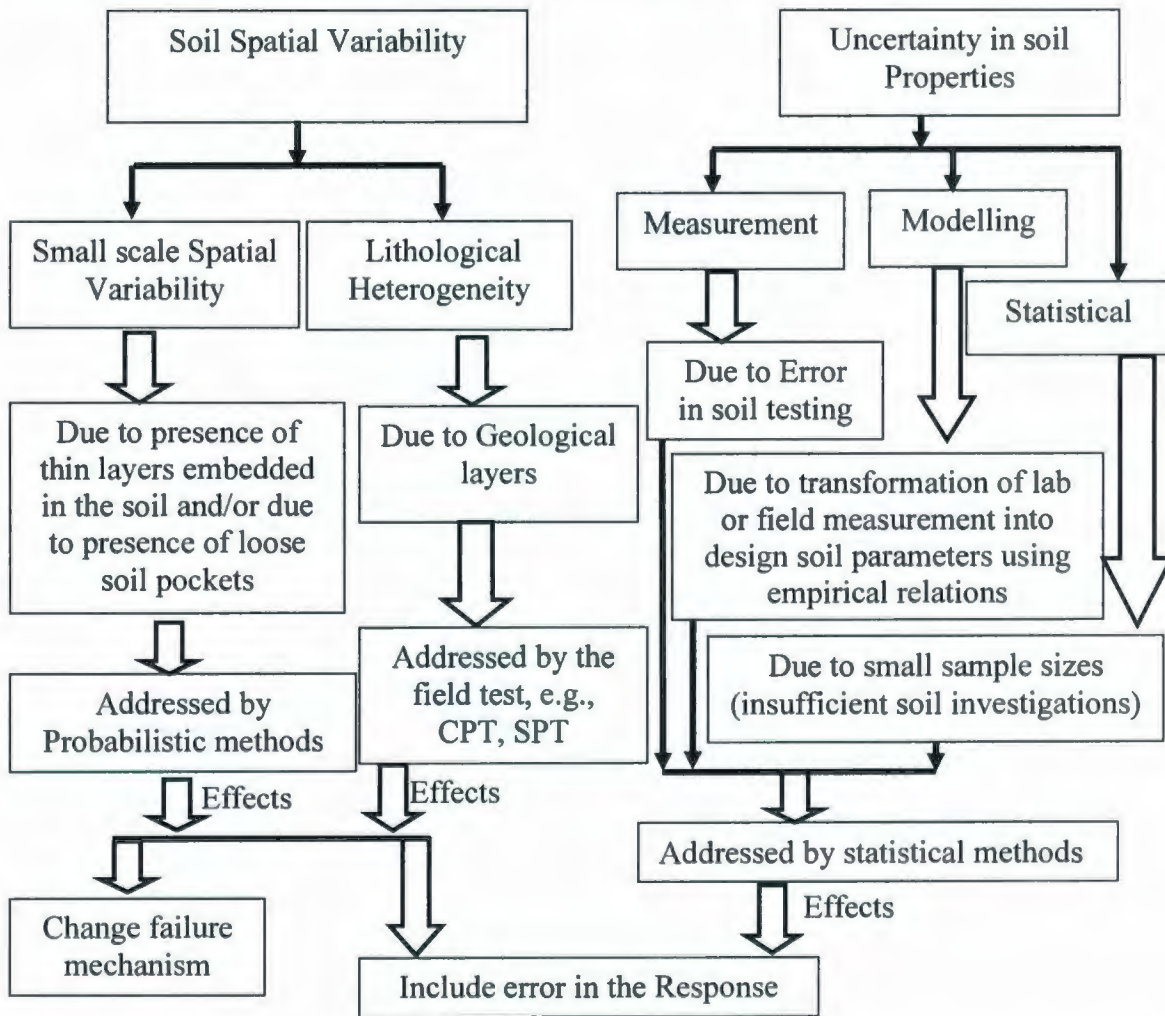


Figure 2.7: Classification of soil Variability, uncertainty in soil properties and their effects.

2.5.2 Effect of Soil Heterogeneity on Various Geotechnical Problems

The influence of soil heterogeneity on different geotechnical problems are discussed in this section. Paice et al. (1996) documented a study on elastic settlement of a uniformly loaded flexible strip footing resting on spatially variable soil. A parametric

study was performed for a range of coefficients of variation (*COV*) and scale of fluctuation of Young's modulus to find out the effects on elastic settlement. It was found that with a *COV* of Young's modulus = 42% (recommended value) the settlement was measured to be 12% higher than deterministic (based on average Young's modulus) value. It was concluded that in the event of higher variances the expected settlements can considerably exceed the deterministic value.

Popescu et al. (2005a), Nobahar (2003) studied the effects of spatial variability of soil properties on the static bearing capacity failure. It was found that spatial variability not only affects the response of the system but also changes the mechanism of bearing capacity failure. The failure surface tends to deviate from its theoretical (deterministic) position and passes through weaker zones in soil. It was concluded that there are two types of effects of inherent spatial variability of soil properties on the response of soil system. One is mechanical (reduction in average strength due to deviations of the failure surface from its theoretical deterministic position to pass through weaker soil zones) and the other is statistical (variability in the response). It was also concluded that these mechanical effects are generally enhanced by nonlinear behaviour.

2.5.3 Effect of Soil Heterogeneity on Soil Liquefaction

Like other geotechnical problems, soil heterogeneity also adversely affects soil liquefaction. Effects of heterogeneity of soil on its liquefaction resistance were analysed and presented for the first time by Ohtomo and Shinozuka (1990). Later on, Popescu (1995) and Popescu et al. (1997, 1998a, 2005c) presented a systematic study on the pattern and amount of EPWP build up in heterogeneous soil. Budiman et al. (1995)

performed a series of undrained cyclic triaxial tests on sand samples with up to 25% gravel inclusions. It was found that the liquefaction resistance of sand with gravel inclusions was lower than that of uniform sand. Moreover, the reduction in liquefaction resistance was more pronounced for samples with a higher content of gravel. Fenton and Vanmarcke (1998), Konrad and Dubeau (2002) and Chakraborty et al. (2004a) have presented some studies on liquefaction resistance of heterogeneous soil. Koutsourelakis et al. (2001, 2002) presented a stochastic approach for the design of a simple structure founded on liquefiable soil.

2.5.3.1 Effect of Less Permeable Soil Layers on Soil Liquefaction

Soil deposits are often composed of many sub-layers because of sedimentation processes. Sometimes it may happen that a less permeable soil layer is sandwiched between two sand layers. If these layers are subjected to cyclic loading, a water film might form beneath the less permeable soil layer due to the migration of pore water. Fiegel and Kutter (1994) reported this phenomenon during a centrifuge experiment with layered soil. Kokusho (1999, 2000a, 2000b) observed the formation of water film during a shake table test. Kokusho and Kojima (2002) concluded from their experiment that liquefaction of layered sand is associated with the presence of a water film beneath a less pervious layer due to the local migration of pore water.

2.5.3.2 Effect of Small Scale Variability of Soil Properties on Liquefaction

Konrad and Dubeau (2002) performed a series of undrained cyclic triaxial tests on uniform sand, uniform silt and layered soil (sand and silt layers). From the results, they concluded that the cyclic strength of the stratified sand-silt samples was decreased considerably when compared to that of 100% sand or 100% silt sample at the same void

ratio and subjected to identical undrained cyclic loads. Chakraborty et al. (2004a) numerically simulated the undrained triaxial tests performed by Konrad and Dubeau (2002). It was concluded that the EPWP in the sand with highly compressible material inclusions increases more rapidly than in clean sand, due to water migration from the soft layer, which causes an early reduction of strength in the sand and resulting failure due to liquefaction. This aspect will be discussed in more details in chapter 5. Popescu (1995), and Popescu et al. (1996, 1997, 1998a, 2005b) conducted a systematic study of the effect of soil heterogeneity on liquefaction by performing stochastic analyses using Monte Carlo simulations. It was concluded that spatial variability of soil properties affects both the pattern and the amount of dynamically induced EPWP. It was also concluded that, for the same average values of soil parameters, more pore water pressure build up was predicted by the stochastic model than by a deterministic analysis using the same soil strength as the average soil strength used in the Monte Carlo simulations. More EPWP was predicted for the same CV of spatial variation when the soil strength fluctuations followed a symmetrical probability distribution function (PDF) – e.g. truncated Gaussian – than for a positively skewed PDF – e.g. Lognormal (Popescu et al., 1996). A parametric study to estimate the characteristic percentile of soil strength to be used in deterministic analysis was also performed by Popescu et al. (1997). The characteristic percentile is the percentile of soil strength of uniform soil, which will predict an amount of EPWP build-up equivalent to that predicted by the Monte Carlo simulation of heterogeneous soil. From the result of the parametric study it was concluded that, for the type of soil deposit analysed (loose to medium dense hydraulically placed sand) and the range of input motions considered, 80-percentile of soil strength is found to be a good characteristic

value to be used in deterministic dynamic analysis. In that study, 80-percentile was defined by the selected value of cone resistance (q_c) which was selected in such a way that 80% of the measured cone resistance values are larger than that value.

Koutsourelakis et al. (2001, 2002) analysed the effects of spatial variability of soil properties on liquefaction for a wide range of earthquake intensities, and presented fragility curves for a simple structure on liquefiable soil.

All these numerical studies were two-dimensional analyses of liquefaction, considering plane strain behaviour. Fenton and Vanmarcke (1998) made an attempt to address the three-dimensional (3D) aspect of soil liquefaction based on records at the Wildlife Site, Imperial Valley, California. The soil properties were modelled as a 3D random field, but due to limited computational resources the liquefaction analysis was carried out in one dimension without considering any coupling in horizontal direction. This study can only deal with the initiation of liquefaction for that particular point, but it did not include the effects of pore water pressure redistribution before and after the initial liquefaction.

Elkateb et al. (2003b) presented another stochastic analysis of the same site. A 3D stochastic analysis was performed using limited number of available CPT data. The empirical method suggested by Robertson and Wride (1998) was used for the liquefaction analysis using CPT values. Although this approach did not capture any interaction between zones of soil with different liquefaction strength, this study provided some interesting conclusions on the effects of loose zones on probability of liquefaction failure. The study concluded that depending solely on safety factors might not be accurate measure of liquefaction susceptibility. In addition, an empirical technique also has been

developed to compare ground variability of potentially liquefiable sites on a qualitative basis.

Popescu et al. (2005c) studied the 3D effects in seismic liquefaction of stochastically variable soil. A Monte Carlo simulation technique using a non-Gaussian stochastic field for soil properties and a fully coupled nonlinear dynamic finite element analysis has been used for 2D and 3D analysis. The result confirmed earlier findings, such as more EPWP build up predicted by stochastic analyses accounting for soil variability than by corresponding deterministic analyses considering uniform soil with the same properties as the average properties of the variable soil. The results also concluded that when differential settlements are not important, a 2D plane strain stochastic analysis or even deterministic analyses (using a proper characteristic percentile of soil strength) could provide sufficiently accurate information. When liquefaction of limited soil volumes and corresponding differential settlements are important, only 3D analyses can correctly capture the structural behaviour.

- **Simulation of Stochastic Fields**

- a) **General**

Several methods are available to solve a large number of engineering problems involving uncertain quantities described by stochastic process or fields. However, Monte Carlo simulation appears to be the only universal method that can provide accurate solutions for certain problems in stochastic geotechnical engineering involving non-linearity, large variations of uncertain parameters and non-Gaussian probability distribution. One of the most important parts of Monte Carlo simulation is the generation of sample functions of the stochastic field. In the last three or four decades, several

methods have been developed for digitally simulating sample functions of a random field. These random fields (Vanmarcke, 1983) may be homogeneous or non-homogeneous, one-dimensional or multi-dimensional, uni-variate or multi-variate, Gaussian or non-Gaussian. However, because of mathematical difficulties and the lack of observed data, most of the earlier generation techniques, as well as analytical approaches, are limited to dealing with Gaussian fields. There are several methods to generate a sample function of a Gaussian field (e.g., Spectral representation method, covariance decomposition, autoregressive moving average (ARMA) model etc.). Rice (1954) first described the concept of spectral representation method. Shinozuka (Shinozuka and Jan, 1972; Shinozuka, 1972) applied it for simulation purposes including multidimensional, multivariate and non-stationary cases. Yang (1972, 1973) showed that the Fast Fourier Transform (FFT) technique can be used to improve the computational efficiency of the spectral representation algorithm. Shinozuka (1974) extended the application of the FFT technique to multi-dimensional cases. Yamazaki and Shinozuka (1988) developed an iterative procedure to simulate uni-variate, non-Gaussian stochastic fields using spectral representation method. Popescu et al. (1998b) combined the work done on the spectral representation method by Yamazaki and Shinozuka (1988), Shinozuka and Deodatis (1996) and Deodatis (1996b), and extended it to multi-variate, multi-dimensional and non-Gaussian stochastic fields. First, a multivariate, multidimensional (mV-nD) Gaussian stochastic field is generated using the advantage of FFT. Then, this Gaussian field is transformed into a non-Gaussian vector field, compatible with a prescribed cross-spectral density matrix and with prescribed marginal probability distribution function, through a memoryless non-linear transformation. Grigoriu (1998) also developed a simulation

algorithm for generating realizations of non-Gaussian stationary, memoryless, and non-linear translation processes with a specified marginal distribution and covariance function.

b) Generation of Sample Functions of a Random Field

The soil material properties do not follow Gaussian PDF's since they do not take negative values. Therefore, there is a need to simulate sample functions of non-Gaussian fields representing the spatial distribution of various material properties over the analysis domain. According to the methodology described by Popescu (1995), an mV-nD Gaussian random field is first generated taking advantage of the FFT techniques. Then, the Gaussian vector field is transformed into a non-Gaussian random field, compatible with a prescribed cross-spectral density matrix and with prescribed non-Gaussian marginal probability distribution functions, through a non-linear transformation in conjunction with an iterative scheme. The flowchart for simulation of mV-nD non-Gaussian stochastic vector field is shown in Figure 2.8 (Popescu et al., 1998b). The sample functions are generated next from that non-Gaussian stochastic field for use in finite element analyses.

c) Finite Element Analysis with Stochastic Input

The last step of Monte Carlo simulation (all steps are discussed in detail in Chapter 6) consists of deterministic nonlinear dynamic finite element analysis with stochastic input for each of the stochastic samples. The analyses are performed using a finite element code. When the spectral representation method is used for stochastic field generation, there is a chance of having two different meshes: one for the random field discretization, and another for the finite element analysis. A data transfer is therefore

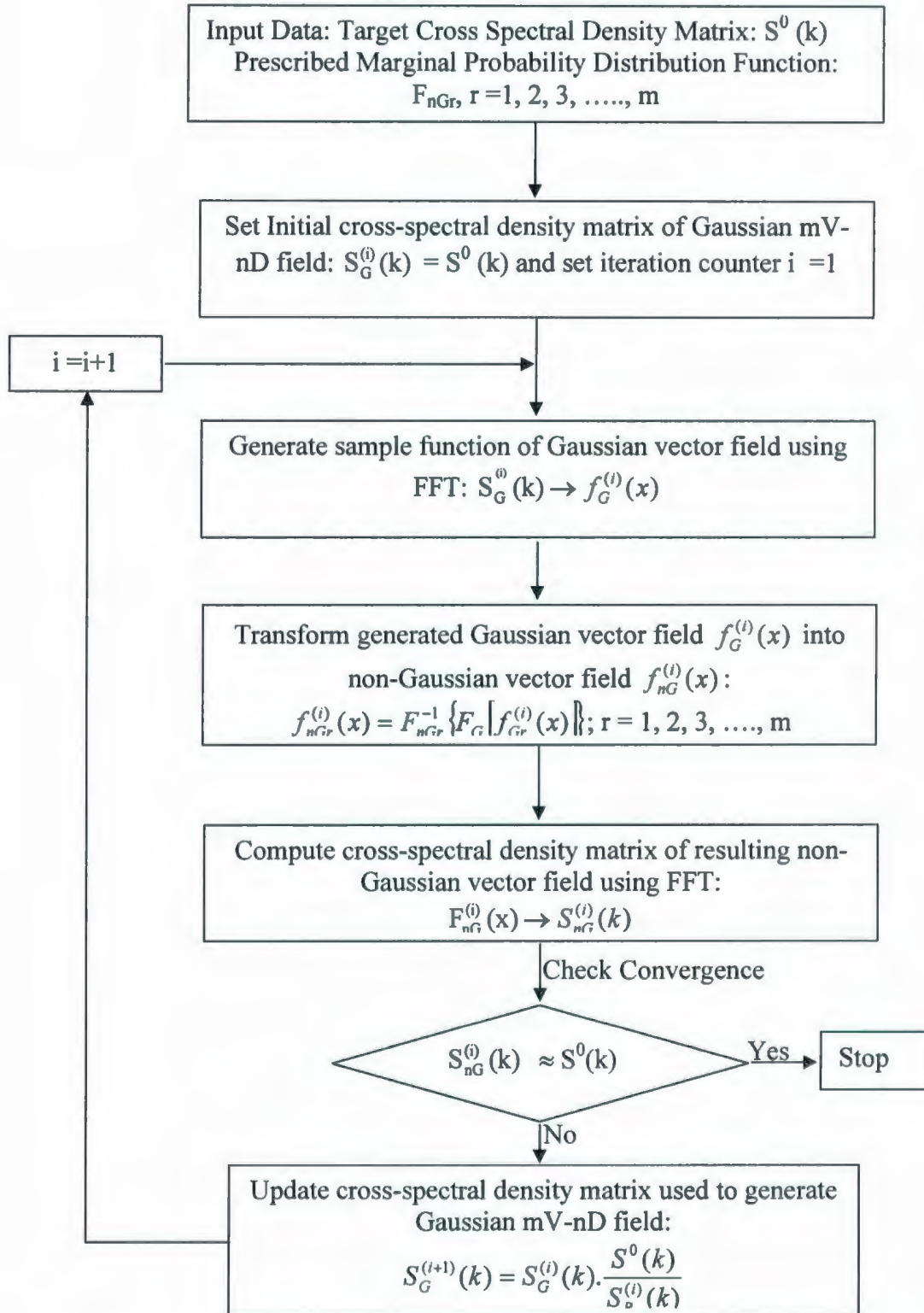


Figure 2.8: Flowchart for simulation of mV-nD non Gaussian stochastic fields (after Popescu et al., 1998b).

required from one mesh to the other. Several methods, proposed by various authors, are

available. The following two methods are most widely used:

- a) The midpoint method (Shinozuka and Dasgupta, 1986): It is a point discretization type method. The random field is represented by its values at the centroids of the finite elements.
- b) The local averaging method (Vanmarcke, 1977): Each finite element is assigned an average of stochastic field values over the element domain.

For Gaussian fields, the spatial averaging method seems to be a more logical approach to random field discretization and will provide better accuracy than the midpoint method for coarse meshes (Der Kiureghian and Ke, 1988). However, for the case of non-Gaussian fields the midpoint method is most appropriate since it preserves the original probability distribution. This method is used in this research. For more details about this method the reader is referred to Popescu (1995).

2.6 Reliability in Geotechnical Engineering

Probabilistic analysis is now a useful tool in Geotechnical engineering and related fields. It has been widely used in different fields of Geotechnical earthquake engineering such as, soil liquefaction studies, studies of safety of dams, seismic hazard analysis, etc.

2.6.1 Fundamentals of Reliability-Based Design

Most observable phenomena in the world have some degree of uncertainty. Therefore, satisfactory performance of a system cannot be absolutely ensured. The only assurance that can be given is the probability of success in satisfying some performance criteria. In engineering terminology, this probabilistic assurance of performance is

referred to as reliability (Haldar and Mahadevan, 2000). In reliability-based design, the measure of safety is expressed by the reliability index and the probability of failure. The probability of failure is related to the shaded area representing the overlap between load (S) and resistance (R) of the probability density function (PDF) curve, as shown in Figure 2.9. The performance function (Z) can be described as:

$$Z = R - S \quad (2.13)$$

and the probability of failure is defined as: $P_f = P(Z < 0)$.

If one assumes that both the loads and the resistance are normally distributed (which is in general not accurate), the probability of failure can be expressed as:

$$P_f = 1 - \phi \left[\frac{\mu_R - \mu_S}{\sqrt{\sigma_R^2 + \sigma_S^2}} \right] \quad (2.14)$$

where ϕ is the cumulative density function (CDF) of the standard normal variate, μ_S and σ_S are the mean and standard deviation of load, μ_R and σ_R are the mean and standard deviation of resistance. The probability of failure depends on the ratio of the mean and standard deviation of Z. This ratio is commonly known as the 'safety index' or 'reliability index (β)' and is expressed as:

$$\beta = \frac{\mu_Z}{\sigma_Z} = \frac{\mu_R - \mu_S}{\sqrt{\sigma_R^2 + \sigma_S^2}} \quad (2.15)$$

where μ_Z and σ_Z are the mean and standard deviation of Z.

Reliability based design methods can be further explained using the following simple case where two variables are considered, one relating to the demand of the system or load (S) and the other is the capacity of the system or resistance (R). Assuming they are normally distributed, both the load and the resistance can be characterised by their

means (μ_S , μ_R) and standard deviations (σ_S , σ_R). The corresponding probability density functions (PDF) are shown in Figure 2.9. The deterministic (nominal) values (S_N , R_N) of load and resistance, used in conventional safety factor-based approach, are also shown in Figure 2.9.

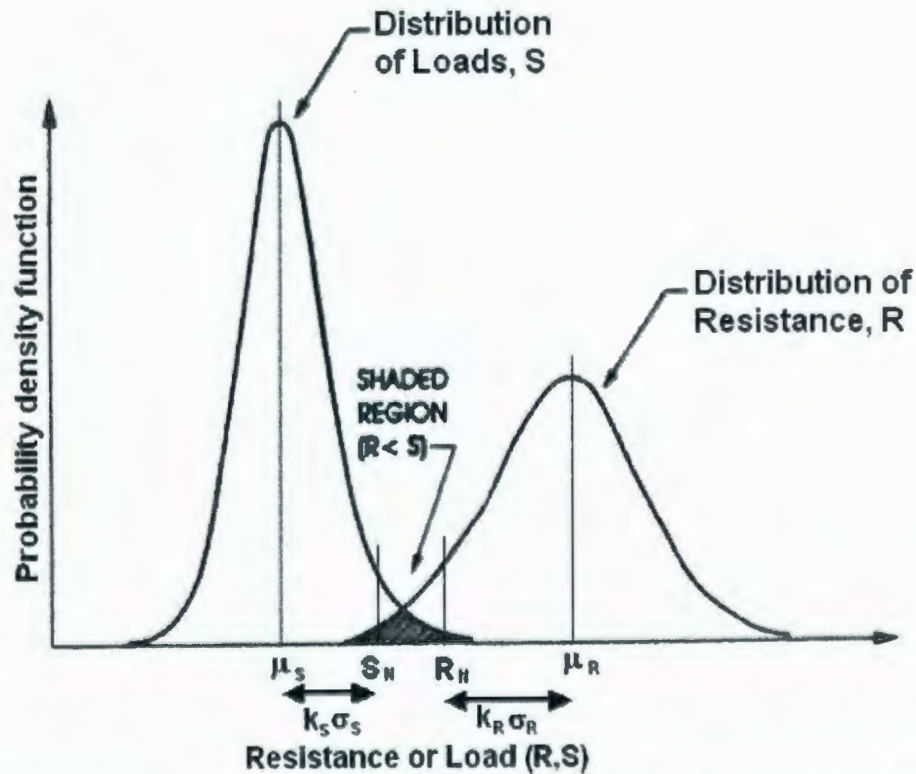


Figure 2.9: Fundamentals of Reliability Analysis (after Haldar and Mahadevan, 2000).

$$\text{Nominal safety factor, } S_F = \frac{R_N}{S_N}. \quad (2.16)$$

The nominal resistance, R_N is usually a conservative value (perhaps one, two or more standard deviations below the mean value). The nominal load, S_N is also a conservative value (one or more standard deviations above the mean value; Haldar and Mahadevan, 2000).

The tools available to the engineer for reliability analysis are divided into three broad categories (Christian, 2004). First are the methods of direct reliability analysis. Here, the uncertainties in properties, loads, water level etc. are expressed by analytical models to obtain probabilistic descriptions of the behaviour of a system. The second category includes event trees, fault trees and influence diagrams, which describe the interaction among events and conditions in a system. The third category includes other statistical techniques. In general, some problems are so poorly defined that it is not feasible to formulate mechanical models, and the engineer must rely on sample statistics (e.g., determination of landslides in broad areas).

Duncan (2000) presented a research on the importance of factor of safety and probability of failure. In the research the author concluded that probability of failure should not be viewed as a replacement for factor of safety, but as a supplement. Computing both the factor of safety and the probability of failure is better than computing either one alone. With a relatively small additional effort to perform reliability analyses, the importance of analyses can be increased considerably. Reliability concepts can be applied to settlement analyses as well. This can provide a measure of the accuracy of settlement computations and can be used to estimate the magnitude of settlement that has a very small probability of being exceeded.

2.6.2 Application of Reliability in Assessment of Soil Liquefaction Potential

Various authors applied reliability analysis in assessing soil liquefaction potential. Among whom, Juang et al. (2002) presented a probability-based method for evaluating the liquefaction potential. Two different approaches (logistic regression and Bayesian

mapping) for calculating the probabilities of liquefaction were used in the study. The probability-based methods were also compared with empirical methods such as Seed and Idriss (1970) (based on SPT), Robertson and Wride (1998) (based on CPT), and Andrus and Stokoe (2000) (based on shear wave velocity). It was shown that the Bayesian mapping approach is preferred over the logistic regression approach for estimating the site-specific probability of liquefaction. From the comparison with three empirical methods it was concluded that probabilistic methods can be used for calculating liquefaction potential with a reasonable accuracy.

2.6.3 Reliability Studies for Heterogeneous Soil

In the last decade, a series of papers appeared in the literature where the effects of inherent soil heterogeneity on the mechanical behavior of various problems in geomechanics were assessed quantitatively. The methodology used in essentially all these studies were Monte Carlo Simulation (MCS). Paice et al. (1996) studied settlements of foundations on elastic soil, Griffiths and Fenton (2000) and Tantalla et al. (2001) studied slope stability, Popescu (1995), Popescu et al. (1997 and 1998a) and Koutsourelakis et al. (2002) studied seismically induced soil liquefaction, and Nobahar and Popescu (2000 and 2001), Griffiths et al. (2002), Fenton and Griffiths (2003) and Nobahar (2003) studied the bearing capacity of shallow foundations. A common conclusion of most of these studies was that nonlinear phenomena are more strongly affected by inherent soil heterogeneity. For example, Paice et al. (1996) predicted up to 12% increase in average settlements for an elastic heterogeneous soil with coefficient of variation $COV = 42\%$, compared to corresponding settlements of a uniform soil deposit with the same mean properties.

Nobahar and Popescu (2001) and Griffiths et al. (2002) found a 20 to 30% reduction in the mean bearing capacity for heterogeneous soils with $COV = 50\%$, compared to the corresponding bearing capacity of a uniform soil with the same mean properties. Popescu et al. (1998a) predicted an increase of about 20% in the amount of pore water pressure build-up for a heterogeneous soil deposit with $COV = 40\%$, compared to the corresponding results of uniform soil with the same mean properties (Popescu et al. 2005a). It is worth to mention here that, as is the fact the soil heterogeneity modifies the assumed failure mechanisms and therefore, may invalidate the use of first-order reliability methods and perturbation techniques that postulate the existence of an average response.

Though expensive computationally, it appears that MCS is the only approach that can accurately capture the effects of inherent soil spatial variability in the soil liquefaction problem where the mechanism can change from one realization (sample function) of the random soil properties to another (Popescu et al. 2005b). Moreover, MCS is the only currently available, universal methodology for accurately solving problems in stochastic mechanics involving strong nonlinearities and large variations of non-Gaussian uncertain system parameters, as is the case of the soil liquefaction problem considered in the present study.

2.6.4 Effect of Frequency Content on Structural Response

Apart from soil liquefaction and soil heterogeneity, the frequency content of seismic ground motion also has a significant influence on the dynamic response of a soil-structure system. The seismic ground motion characteristics mainly depend on three

factors; distance from the seismic source, local soil conditions and the intensity of the earthquake. The characteristics of seismic ground motion also change from one place to another, due to the wave propagation effects and filtering of seismic waves in the soil layers.

Dynamic response of a soil-structure system depends on its characteristic frequency. Every soil-structure system has its own characteristic frequency depending upon its dynamic properties. This characteristic frequency may decrease during dynamic excitation as a result of degradation of effective shear modulus, due to pore water pressure build up in saturated soil. Madabhushi and Schofield (1993) showed this phenomenon by conducting a series of centrifuge tests on tower-soil systems. From the result it was concluded that the onset of partial liquefaction alters the dynamic characteristics of the tower-soil system. It was also concluded that when the natural frequency of the tower-soil system was higher than the driving frequency of the earthquake, the excess pore pressure led to degradation of soil stiffness causing a sudden lowering of the natural frequency to a discrete frequency at which the energy of the earthquake was concentrated. However, it was also reported, when the initial natural frequency was less than or equal to the driving frequency of the earthquake, the generation of excess pore pressure did not cause significant changes in the natural frequency of the tower-soil system.

Popescu et al. (1997) presented a study on the effects of characteristic frequency on liquefaction of a stochastically variable soil. From the predicted result it was observed that larger pore pressures were developed in the soil layer when using input motions with lower frequency content. It was also observed that the peak values of predicted EPWP

ratio were situated at lower elevations as the loading rate decreased. In the study, larger pore pressure and horizontal displacement for input motions with lower frequency content were also predicted.

Popescu (2002) presented a study on the effects of seismic loading rate on soil liquefaction. The effect of frequency content of seismic ground motion was illustrated using two examples. First, a numerical analysis for a soil deposit was performed to find the effect of loading rate. After that, an analysis for an embankment dam was performed. In the first example, the author predicted significantly larger pore pressures and horizontal displacements at the ground level for an input motion with lower frequency content, compared to the case with higher frequency content. For the embankment dam, the author also found that the structural response was strongly affected by the frequency content of the seismic ground motion. The embankment dam was analysed for three seismic acceleration time histories; all with different frequency contents but the same intensity. In one case, moderate structural damage and deformation was found, which stabilized after the end of shaking. In the other two cases of seismic motion with lower frequency content, the numerical model predicted progressive slope failures after the end of the shaking and post earthquake failure of the dam. Build-up of EPWP leads to changes in the vibration characteristics (reduction in characteristic frequency) of saturated soil deposits during earthquakes. Ground motions having the maximum spectral amplitudes in the range of the new characteristic periods deliver more energy to the system and may produce more damage. Therefore, special attention should be placed upon low frequency seismic inputs.

Ghosh and Madabhushi (2003) presented a numerical analysis on the effect of input motion with different types of frequency content on the dynamic response of the system. From the result it was concluded that the interaction between the frequency content of the seismic motion and generation of EPWP could change the dynamic response of the soil-structure system. The results showed significantly large pore pressure for input motions with lower frequencies because more energy was delivered to the system for low frequency seismic inputs.

Chakraborty et al. (2004b) presented a 2D analysis of a simple tower structure resting upon a homogeneous liquefiable soil. Two types of earthquake input motions recommended by the Uniform Building Code (1994); type 1, for rocks and stiff soils, and type 3, for soft soils were used. The maximum spectral amplitudes for type 3 accelerations are in a lower frequency range than for type 1. It was concluded that the characteristic frequency of the soil-structure system goes down to a value close to the dominant frequency of the type 3 input accelerations due to soil softening. Therefore, considerably more structural damage was predicted for structures excited by type 3 accelerations than for those excited by type 1 input. The reduction in specific seismic energy was due to filtering of seismic ground motion in the soil. Liquefaction and consequent soil softening was also discussed in the paper. This is shown in Figure 2.10 in terms of Arias Intensity. Arias Intensity is a measure of seismic energy (intensity) and the formula for calculating it will be discussed in Chapter 6. From the figure it is observed that for input acceleration with lower Arias Intensity, reduction in specific seismic energy due to filtering of seismic ground motion is not significant. However, for seismic input with higher Arias Intensity, the reduction in specific seismic energy is very high

(approximately 75%). This reduction in seismic energy will also affect the spectral amplification factor (the short (0.2s) and long period (1.0s) amplification factors, F_a and F_v) provided in seismic design building codes. In the building code, F_a and F_v are determined based on equivalent linear or nonlinear analyses where the effect of EPWP build-up was not considered. As shown in the above mentioned studies, for saturated soil the effect of EPWP build-up is important for calculating F_a and F_v . Therefore, there is a scope of further research in this area.

2.6.5 Fragility Curves in Geotechnical Earthquake Engineering

For expressing the results, obtained from Monte Carlo simulation, fragility curves are sometime used. The likelihood of structural damage, due to different levels of

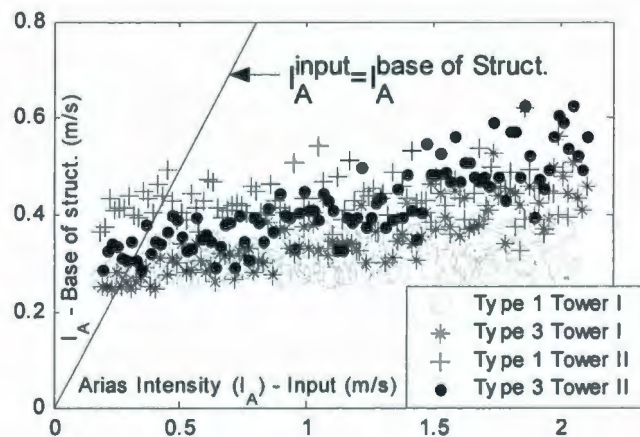


Figure 2.10: Base input accelerations and predicted accelerations at the base of the structure: comparison of Arias intensities (after Chakraborty et al., 2004b).

earthquake ground motion intensity, can be expressed by fragility curves. Fragility curves express the probability of exceeding various threshold values in the response as a function of load intensity. Fragility curves have been used extensively in earthquake engineering to describe the seismic vulnerability of structures as a function of the severity

of earthquake ground motion (Shinozuka et al., 2000; Shinozuka, 1998, 2000; Yamaguchi and Yamazaki, 2000; Deodatis et al., 2000; Popescu et al., 2005b etc).

The fragility curves can be expressed in the form of two-parameter lognormal distribution functions. The estimation of these two parameters is done by maximum likelihood method treating each event of exceeding or not exceeding a certain threshold, as a realization from a Bernoulli experiment. Shinozuka (1998) proposed this method for generating fragility curves. The likelihood function is expressed as (Shinozuka, 1998):

$$M = \prod_{k=1}^N [F(a_k)]^{y_k} [1 - F(a_k)]^{1-y_k} \quad (2.17)$$

where $F(.)$ represents the fragility curve for a specific state of damage, a_k is the peak ground acceleration (i.e., load intensity) value of the K^{th} set of acceleration time histories, y_k represent the realizations of the Bernoulli random variable Y_k with $y_k=0$ when damage is not exceeded or $y_k=1$ when damage is exceeded under peak ground acceleration (PGA) equal to a_k , and N is the total number of sets of time histories for which the structure is analysed. Under the lognormal assumption, $F(.)$ takes the following analytical form:

$$F(a) = \phi \left[\frac{\ln \left(\frac{a}{\mu} \right)}{\sigma} \right] \quad (2.18)$$

where a represents the PGA, and $\phi[.]$ is the standardized normal distribution function. The two parameters μ and σ (median and lognormal standard deviation) are estimated satisfying the following equations:

$$\frac{\delta \ln M}{\delta \mu} = \frac{\delta \ln M}{\delta \sigma} = 0 \quad (2.19)$$

The calculation is performed numerically by implementing a straightforward optimisation algorithm. Figure 2.11 shows a typical example of the lognormal fragility curve based on Bernoulli's experiment.

Shinozuka et al. (2000), Shinozuka (1998, 2000), Yamaguchi and Yamazaki (2000) and Deodatis et al. (2000) applied this fragility analysis using the maximum likelihood method for bridges and presented the fragility curves for different damage states of the bridge for different PGA. Tantalla et al. (2001) used fragility analysis for slope stability analysis. Koutsourelakis et al. (2001) used fragility analysis for a simple structure resting upon a liquefiable soil and presented fragility curves for different damage states of the structure against Arias Intensity.

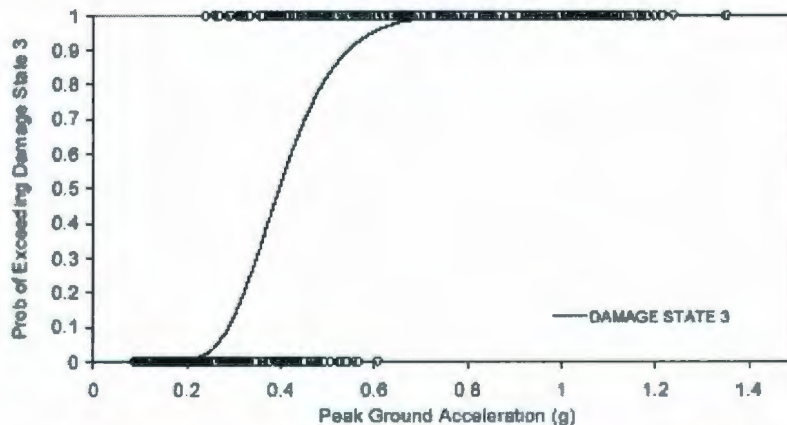


Figure 2.11: Example of a typical Fragility curve (after Deodatis et al., 2000).

Shinozuka and Kishimoto (1989) performed a fragility analysis based on liquefaction susceptibility of a site in New Madrid, USA. The authors used the method suggested by Seed and Idriss (1970) and Iwasaki et al. (1978), for calculating liquefaction potential and liquefaction resistance factor without considering spatial variation of soil

properties and pore pressure redistribution before and after initial liquefaction. The results were presented for the seismic reliability analysis of oil pipelines at the New Madrid site. The fragility curves were used for presenting the results of the liquefaction hazard on the basis of liquefaction resistance factor and liquefaction potential index.

Most of the current research on fragility analysis use PGA, pseudo spectral acceleration, velocity or displacement to characterize seismic intensity. However, they cannot capture the essential properties of the ground motion. Because, the probability law of a stochastic process cannot be specified by its maximum value over a time interval. Kafali and Grigoriu (2004) presented a new method for expressing the earthquake load intensity as a fragility surface. In that method, system fragility was calculated as a function of moment magnitude and source to site distance. From the result it was concluded that, fragility is the probability of a system reaching a limit state as a function of some measures of seismic intensity and it needs to be plotted against parameters of the probability laws of ground acceleration rather than properties of its sample (e.g., PGA).

Popescu et al. (2005c) performed a 3D seismic liquefaction analysis of stochastically variable soil (discussed earlier in the section 2.3.3.2). The method proposed by Shinozuka for constructing fragility curves was used in the study. The comparison results of the stochastic analyses (2D and 3D) and the deterministic analyses were presented in terms of fragility curves. Arias Intensity was used for expressing load intensity in the fragility curves. Arias Intensity was found to provide a better measure of earthquake severity than PGA (Koutsourelakis et al., 2001) or root mean square acceleration. Arias Intensity is calculated after considering the total duration and

amplitudes of earthquake motion. Therefore, the Arias Intensity is used for constructing fragility curves in this thesis.

2.6.6 Design of Experiments (DOE)

2.6.6.1 Overview

In the last part of this research (parametric study), a statistical methodology called Design of Experiments (DOE) is used for finding the significant factors, which control the seismic response of structures on liquefiable soil. Generally, an experiment is a test in which purposeful changes are made to the input variable of a system so that we may observe and identify the reasons for changes in the output responses (Montgomery, 1997). A detailed review of the basic procedures of the DOE and its advantages are documented by Lye (2002, 2003). The advantages of using DOE in this study are:

- Reduction in the number of required experiments (FE runs in this case) for finding the effects of different factors on the response. A two-level full factorial design method is used for this purpose.
- Validation of the results from the one-factor at a time method using more advanced statistical methods. The effects of different factors on the response are obtained from full Monte Carlo simulation, combined with the one-factor at a time method. Therefore, to validate the results obtained from this method, DOE is used in the preliminary stage of this study.
- This method easily and automatically captures any interaction effect between two or more factors on the responses.

Two of the most commonly used methods in DOE are the two-level factorial design and Central Composite Response Surface design. Design-Expert® software version 7.1.3 was used in this study. The methods used in this study (i.e., two-level full factorial design, and Central Composite Response Surface design) are described briefly in the following sections.

2.6.6.2 Two-Level Factorial Design

This is a very efficient method commonly used in DOE. Factorial designs are used primarily for screening significant factors, but can also be used sequentially to develop and refine a model. Various researchers used this method as an efficient tool for identifying the most significant parameters and for modelling (e.g., Zangeneh et al., 2002). For example, Nobahar (2003) used factorial design method with centre points for modelling soil-structure interaction problem. There are various types of factorial design such as general factorial, two-level full factorial, three-level full factorial and fractional factorial design methods (Montgomery, 1997). In a two-level full factorial design, the effects of k factors are studied at only two levels for each factor. In this method, 2^k experiments are required and also called 2^k factorial design. The design points for a two-level factorial design for a three factor problem are shown in Figure 2.12.

The first step of this method is the selection of possible important factors and their ranges. In the two-level factorial design, two different levels of all the factors are considered (maximum and minimum). Some special notations are usually used in two-level factorial design methods. Upper case letters denote the effect of the factor, and lower case letters denote their treatments. For example, A is the effect of factor A , AB is

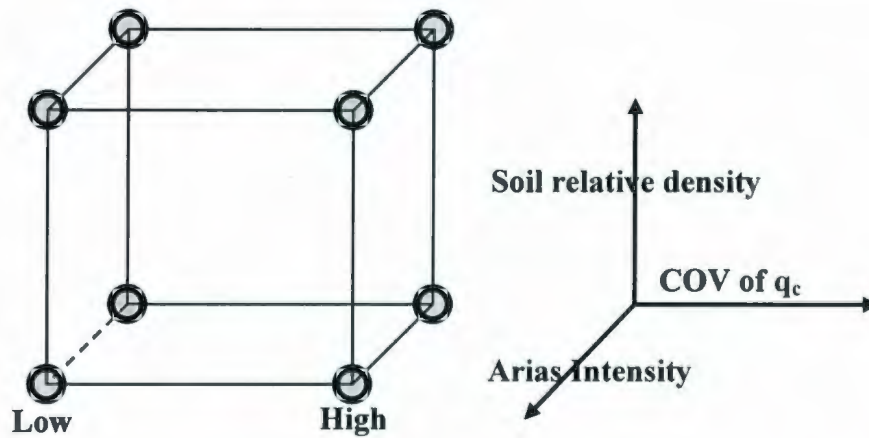


Figure 2.12: Illustration of experiment design layouts for a two level full factorial design with three factors. Circles are showing the design points.

the interaction effect of factor A and B , and abc denotes an experiment in which high-level (maximum) values of factor A , B and C and low-level (minimum) values of the other factors are used. In an analysis with k number of factors, the two-level factorial design requires 2^k experiments. To reduce the number of experiments, fractional factorial method can be used. The models are then formulated using the significant factors. Analysis of variance (ANOVA) method is usually used for determining whether the formulated model is significant or not. Normal probability plot or half normal plot may also used as a visual tool for this purpose. On these plots, all the significant effects (main or interaction) fall outside a straight line formed by all non-significant effects. A regression model is developed next using those significant effects. Apart from ANOVA, various methods are used to diagnose whether or not the model is appropriate such as normality of residuals and homogeneity of variance. If the residuals of the model do not have constant variance, the response should be transformed. For example, if the residual distribution is funnel shaped, a log transformation may give a more uniform distribution. If the predicted R^2 value is greater than 0.9, it gives a satisfactory regression model.

Some extra runs may be performed next, using the factor values inside the range of the study to verify the validity of the developed regression model.

2.6.6.3 Central Composite Response Surface Design

A more advanced method in design of experiments is the Central Composite Response Surface design. A response surface with curvature can be modelled more efficiently using this method. In an analysis with three factors, a Central-Composite Response Surface design requires fifteen experiments. The design points for Central-Composite Response Surface design for a three factor problem are shown in Figure 2.13.

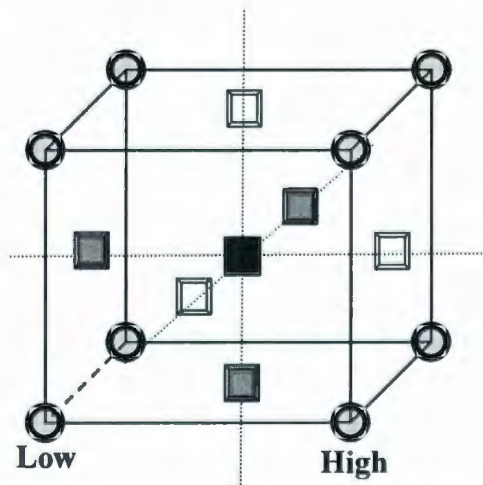


Figure 2.13: Illustration of experiment design layouts for a Central-Composite Response Surface design (face centred) with three factors. Circles are showing the design points; squares are showing the centre points.

This method has three groups of design points: two-level factorial design points ($2^3 = 8$ for three factors), axial points ($2 \times 3 = 6$ for three factors) and centre points (1 in the Figure 2.13). The location of the axial point depends upon alpha value. For a face centred Central Composite Response Surface design the alpha value is 1. The various steps for analysing results are same as that for the case of two-level factorial design (already discussed in Section 2.6.6.2).

Table 2.1: Scaling relations in centrifuge modelling (N= Centrifuge scaling factor)

Parameter	Model	Prototype
Length	1	N
Area	1	N^2
Volume	1	N^3
Acceleration	1	1/N
Mass	1	N^3
Force	1	N^2
Energy	1	N^3
Time (dynamic)	1	N
Time (diffusion)	1	N^2
Stress	1	1
Strain	1	1
Density	1	1
Frequency	1	1/N

CHAPTER 3

The Numerical Model and its Parameters

3.1. Introduction

The numerical analyses were performed in this research using the finite element computer code Dynaflow (Prevost, 2002). In seismic analysis of saturated soils involving EPWP build-up, two important aspects need to be addressed: (a) solid and fluid coupled field equations have to be used in a step by step dynamic analysis to correctly capture the inertial and dissipative terms and (b) accurate simulation of dynamically induced EPWP build-up and continuous softening of the material requires soil models able to reproduce the experimentally observed nonlinear hysteretic behaviour and shear stress induced anisotropic effects and to reflect the strong dependency of plastic dilatancy on effective stress ratio. The first aspect is addressed in the Dynaflow code by the extension of Biot's theory into the nonlinear regime, discussed in more detail by Popescu et al., 2006. The second aspect can be addressed by using an advanced plasticity model, such as multi-yield or bounding surface plasticity, in combination with kinematic hardening rules. These advanced plasticity soil constitutive models usually require a relatively large number of parameters and a well-defined methodology for calibrating those parameters based on results of standard in-situ and/or laboratory soil tests. The mathematical model used in Dynaflow for this study and the calibration of different parameters in that model are discussed in this chapter.

3.2. Mathematical Model

The finite element calculations were conducted in terms of effective stresses, using fully coupled solid-fluid equations and a multi-yield plasticity soil constitutive model for the treatment of saturated porous media. The coupled field equations for multiphase media are solved based on an extension of the Biot formulation (Biot, 1955, 1962) into the nonlinear regime (Prevost, 1989). During deformation, the solid particles in porous media which form the soil skeleton undergo irreversible motions such as slips at grain boundaries, creations of voids by particles coming out of a packed configuration, and combinations of such irreversible motions. When the particulate nature and the microscopic origin of the phenomena involved are not explicitly sought phenomenological equations then provide an adequate description of the behaviour of the various phases which form the soil medium. In multiphase theories, the conceptual model is thus one in which each phase (or constituent) enters through its averaged properties, obtained as if the particles were smeared out in space. In other words, the particulate nature of the constituents is described in terms of phenomenological laws as the particulates behave collectively as a continuum. Soil is thus viewed herein as consisting of a solid skeleton interacting with the pore fluids (Popescu et al., 2006). The dynamic response is obtained from the following coupled equations (Prevost, 2002):

$$\rho^S \mathbf{a}^S = \nabla \cdot \boldsymbol{\sigma}^{*S} - (1 - n^w) \cdot \nabla p^w - \xi \cdot (\mathbf{v}^S - \mathbf{v}^w) + \rho^S \mathbf{b} \quad (3.1)$$

$$\rho^w \frac{d\mathbf{v}^w}{dt} = \rho^w (\mathbf{v}^S - \mathbf{v}^w) \cdot \nabla \mathbf{v}^w - n^w \nabla p^w + \xi \cdot (\mathbf{v}^S - \mathbf{v}^w) + \rho^w \mathbf{b} \quad (3.2)$$

where the motion of the solid phase is used as the reference motion. In equations (3.1) and (3.2), $\boldsymbol{\sigma}^{*S}$ = solid (effective) stress, \mathbf{a}^S = solid acceleration, \mathbf{v}^S (\mathbf{v}^w) is the solid

(fluid) velocity, \mathbf{b} = body force per unit mass, p^w = pore fluid pressure, $\rho^s = (1 - n^w)\rho_s$ and $\rho^w = n^w\rho_w$ with ρ_s = solid mass density, ρ_w = fluid mass density and n^w = porosity; $\xi = n^{w^2}\gamma_w \mathbf{k}^{-1}$, with \mathbf{k} = hydraulic conductivity, $\gamma_w = \rho_w g$ = fluid unit weight, and $g = (\|\mathbf{b}\|)$ = acceleration of gravity.

In the case of a *compressible* pore fluid, the pore fluid pressure is determined from the computed velocities through time integration of the following equation:

$$\frac{dp^w}{dt} = -(\lambda^w / n^w) [\nabla \cdot (1 - n^w) \mathbf{v}^s + \nabla \cdot (n^w \mathbf{v}^w)] \quad (3.3)$$

where λ^w = fluid bulk modulus. In the case of an *incompressible* pore fluid, the pore fluid pressure is determined from the computed velocities through the following equation:

$$p^w = -(\lambda^w / n^w) [\nabla \cdot (1 - n^w) \mathbf{v}^s + \nabla \cdot (n^w \mathbf{v}^w)] \quad (3.4)$$

where λ^w = a penalty parameter used to enforce the incompressibility constraint (Prevost, 1982, 1985).

The multi-yield plasticity constitutive model has been validated in the past for analysis of liquefaction phenomenon (Popescu and Prevost 1993, 1995). The model is a kinematic hardening model based on a relatively simple plasticity theory (Prevost 1985), and is applicable to both cohesive and cohesionless soils. The main features of the multi-yield plasticity soil constitutive model are shown in Figure 3.1. Fundamental theory behind the model has originated from the concept of a 'field of work-hardening moduli' (Mroz 1967) by approximating the nonlinear elastic plastic stress-strain curve into a number of linear segments with constant shear moduli. This results in defining a series of

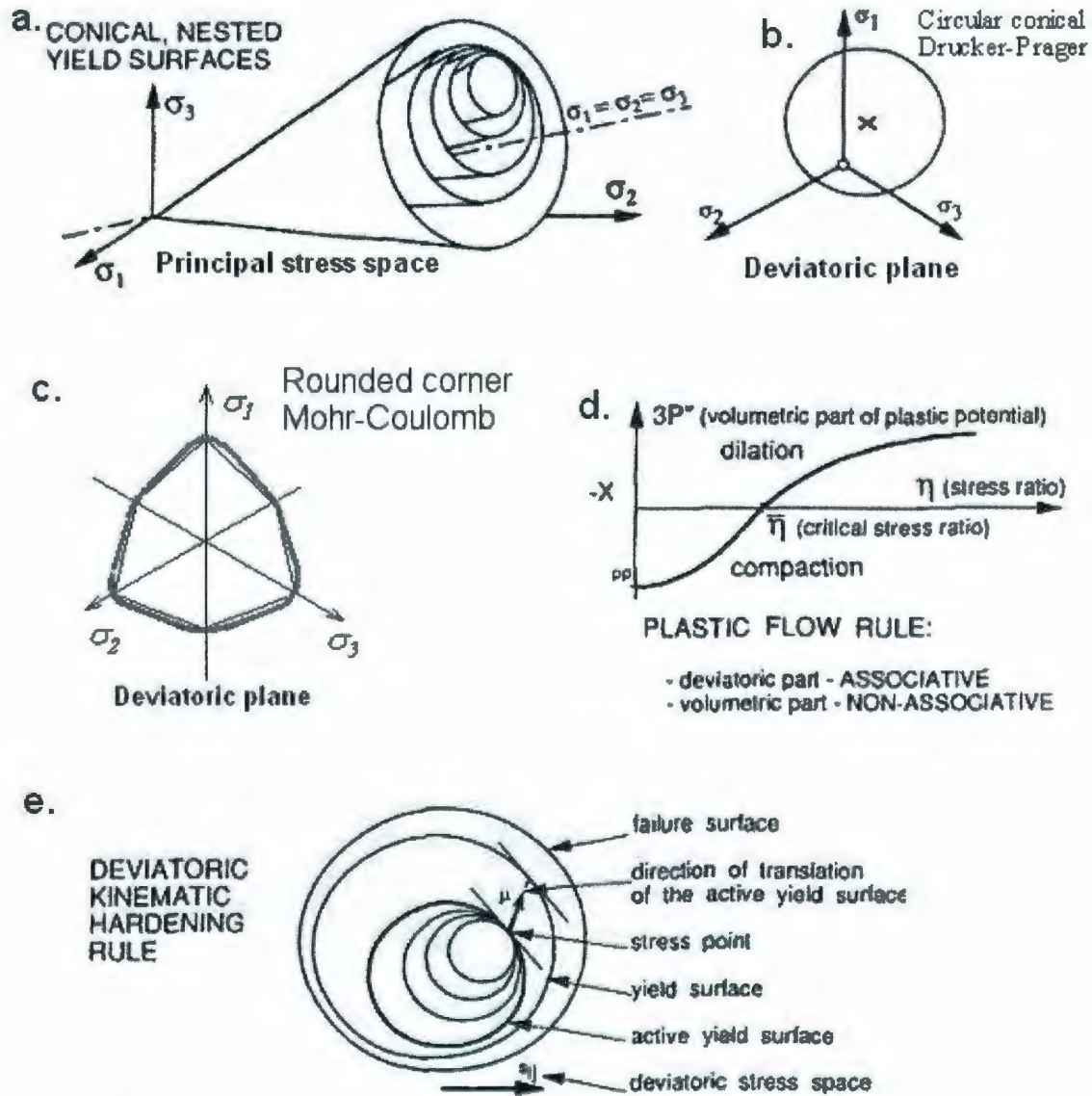


Figure 3.1: Main features of the multi-yield plasticity soil constitutive model (after Popescu 1995).

nested yield surfaces in the stress space. Each yield surface corresponds to a region of a constant shear modulus. The outermost surface is related to zero shear modulus, and is called failure surface. Both Drucker-Prager and Mohr-Coulomb type surfaces can be used in the model for frictional materials (sands). However, rounded corner Mohr-Coulomb type yield surfaces were used in this study. The plastic potential is assumed to be associative for its deviatoric component and non-associative for its dilatational

(volumetric) component. The volumetric component is defined to account for dependence of soil dilatational behavior on the mobilized stress ratio. The soil hysteretic behavior and shear stress-induced anisotropic effects are simulated by a purely deviatoric kinematic hardening rule. Accurate simulation of shear induced plastic dilation and of hysteretic effects under cyclic loading together with full coupling between solid and fluid equations (discussed earlier) allows capturing the build up and dissipation of pore water pressures and gradual softening and hardening of soil materials (Prevost, 1989).

3.3. Estimation of Constitutive Parameters

As mentioned earlier, any efficient soil constitutive model usually requires a relatively large number of parameters and a well-defined methodology for calibrating those parameters. A well-defined methodology of parameter estimation for multi-yield surface plasticity model parameters from the results of conventional laboratory tests (e.g., triaxial, simple shear) is documented by Popescu and Prevost (1993) and from *in-situ* (e.g., standard penetration, cone penetration) soil tests by Popescu (1995). The multi-yield plasticity soil constitutive model, its implementation algorithm, and the methodology for estimating the constitutive model parameters have been repeatedly validated in the past for soil liquefaction computations, based on both centrifuge experimental results (e.g. Popescu and Prevost, 1993, 1995; Jafari-Mehrabadi, 2006) and full-scale measurements (e.g. Keanne and Prevost, 1989).

The multi-yield surface plasticity constitutive model parameters can be divided into state parameters (obtained from general laboratory soil tests), low-strain elastic parameters (describing elastic deformability), yield and failure parameters (used for

generating the nested yield surfaces), and dilation parameters (used to calculate the plastic volumetric strain). The commonly used constitutive parameters of the multi-yield plasticity model are listed in Table 3.1.

a) State Parameters:

Porosity (n^w): The porosity is usually calculated from the soil relative density and void ratios. The following relations are usually used for calculating porosity:

$$e = e_{max} - D_r(e_{max} - e_{min}) \quad (3.5)$$

$$n^w = e / (1 + e) \quad (3.6)$$

Hydraulic conductivity (k): The standard procedures for determining hydraulic conductivity are constant-head or falling-head permeability tests. When actual test results are not available, various correlations are used based on the soil type. In cases where experimental results are unavailable, hydraulic conductivity can be approximated using the well known equations proposed by the Hazen or Kozen-Carman equation. To include the effect of soil relative density of the sand, the equation proposed by Shahabi et al. (1984) can be used. Some of the commonly used correlations are listed in Table 3.2.

b) Low strain elastic parameters:

Low strain elastic shear (G_0) and bulk (B_0) moduli: The low strain shear modulus (strain level 0.05 to 0.1%) corresponds to the assumed elastic range of soil behaviour within the first yield surface. Low strain shear and bulk moduli are related through Poisson's ratio (ν) using the following equation:

$$B_0 = \frac{2G_0(1 + \nu)}{3(1 - 2\nu)} \quad (3.7)$$

Based on the results from resonant column tests or *in-situ* shear wave velocity measurements, different correlations are derived by several researchers for calculating

shear modulus at very low strains (G_{max} , strain level of 0.0001% to 0.01%). The low strain shear modulus is usually determined from G_{max} and modulus degradation curves (Ishibashi and Zhang, 1993). Some of the commonly used equations for calculating G_{max} are shown in Table 3.2. The commonly used value for power exponent (n) and Poisson's ratio are also shown in Table 3.2.

c) Yield and failure parameters:

The yield and failure parameters are used to describe the initial position, size and plastic modulus corresponding to each yield surface. The ϕ , ε_{dev}^{max} , and k_0 are included in a modified hyperbolic expression proposed by Prevost and Keane (1989) and a wide range of soil stress-strain relations described by Griffiths and Prevost (1990).

Friction angle at failure (ϕ): The friction angle at failure, in compression and extension, can be obtained from the results of monotonic triaxial compression and extension tests (Vaid et al., 2001). It can also be estimated from the correlation obtained from in-situ tests such as CPT (Robertson and Campanella, 1983; Kulhawy and Mayne, 1990) or SPT (Schmertman, 1975). Some of these correlations are tabulated in Table 3.2.

Maximum deviatoric strain (ε_{dev}^{max}): The maximum deviatoric strain, inferred based on results of drained triaxial or simple shear tests, is used in the multi-yield plasticity model to develop the backbone curve for building the nested yield surfaces. The best way for estimating maximum deviatoric strain is by performing a p-constant triaxial test (Azizian, 2004). In absence of that type of test, drained cyclic triaxial test results can be used for estimating maximum deviatoric strain, both in compression and extension.

Coefficient of lateral stress (k_0): The parameter coefficient of lateral stress in Dynaflo is used only for generating the deviatoric stress-strain backbone curves

(Griffiths and Prevost, 1990) and the initial locations of yield surfaces in the stress space (Prevost, 1989). Its value depends on the type of consolidation (e.g., anisotropic or isotropic) applied in the laboratory soil tests, which is used for calibrating the model parameters.

Stress strain curve coefficient (α): Hayashi et al. (1992) proposed an expression using a hyperbola whose shape depends on the characteristic of the grain size distribution through the stress-strain curve coefficient α . The major advantage of the model proposed by Hayashi et al. (1992) is that it is based on real experimental results. The equation for calculating α is shown in Table 3.2.

d) Dilation Parameters:

Dilation angle (ψ): The dilation parameters are used in the plastic flow rule for calculating the so-called plastic dilation (shear-induced plastic volumetric strain). **The dilation angle (ψ) in DYNAFLOW and in the thesis represents the phase transformation angle.** This definition for dilation angle is not the one which normally used in the literature. The value of ψ is a unique property for a specific type of sand. It is not affected by the mode of loading or soil relative density (Vaid and Chern, 1985; Vaid and Thomas, 1995; Vaid et al., 2001).

Dilation parameter: The dilation parameter, X_{pp} , is a scale coefficient for plastic dilation, basically depending on relative density and soil type (Popescu, 1995). The dilation parameter accounts for the ratio between rates of plastic volumetric strain and shear strain. All the multi-yield plasticity model parameters except the dilation parameter (X_{pp}) can be estimated from results of conventional field (e.g. CPT) or laboratory soil tests. After that, the dilation parameter (X_{pp}) is estimated by performing a liquefaction

strength analysis (which will be discussed in next subsection). A methodology for estimating X_{pp} from *in-situ* test results is documented by Popescu (1995). The provided equation for calculating X_{pp} (for Erksak sand) is shown in Table 3.2.

As discussed in the above sub-section, various correlations recommended by various authors are used (when actual test results are not available) for estimating multi-yield plasticity constitutive model parameters (except X_{pp}). However, uncertainty in estimated soil properties and spatial variability of the soil properties often cause engineers to use the available correlation formulae along with their judgement to reasonably estimate the required model parameters. More correlation charts and equations may be found in other references, such as Popescu (1995), Prevost and Popescu (1996) and Kulhawy and Mayne (1990).

3.4. Liquefaction Strength Analysis

After estimating all the other multi-yield model parameters from conventional laboratory or *in-situ* test results, the dilation parameter (X_{pp}) should be estimated next, by performing the liquefaction strength analysis as described by Popescu and Prevost (1993). Constitutive experiments (element tests) are used for this purpose. This analysis is based on fitting the experimental liquefaction strength curve using finite element simulations of either cyclic undrained triaxial (element tests) or cyclic simple shear tests. The liquefaction strength curve is a plot of the cyclic stress ratio as a function of the number of cycles necessary to induce initial liquefaction in an undrained cyclic soil test. The cyclic stress ratio is expressed either as $\sigma_d/2\sigma_0'$ (for triaxial test), where σ_d is the single amplitude cyclic axial stress and σ_0' is the initial effective confining stress; or as

τ_h / σ_{v0}' (for simple shear tests), where τ_h is the double amplitude cyclic shear stress and σ_{v0}' is the initial effective vertical stress. The constitutive experiment procedure consists of repeating a test on an element with changing the value of X_{pp} and keeping constant the rest of the multi-yield model parameters to obtain the same result as obtained in laboratory tests. The number of cycles to liquefaction (N_L) is evaluated from each element test by considering the occurrence of initial liquefaction. The occurrence of initial liquefaction is considered in this study as the occurrence of 5% double amplitude axial strain or EPWP ratio reaches unity - whichever comes first. Element tests are performed for different cyclic stress ratios and assumed dilation parameter values. The final dilation parameter value is determined by fitting the experimental liquefaction strength curve with the computed one. A sample of experimental (test points) and predicted (from Dynaflo) liquefaction strength curves are shown in Figure 3.2. For a detailed description of the procedure, refer to Popescu and Prevost (1993) and Popescu (1995).

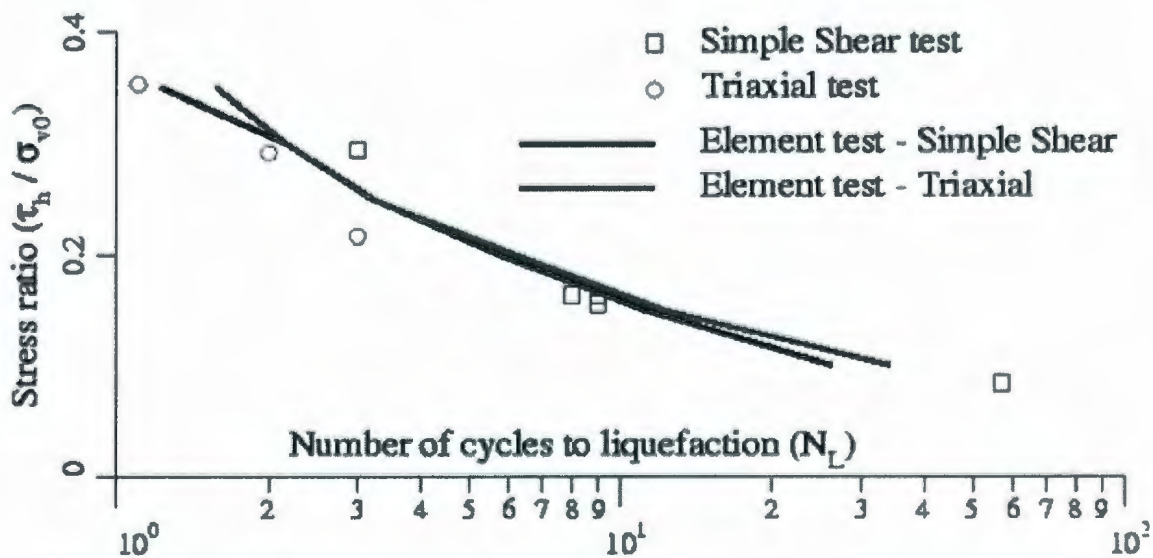


Figure 3.2: Liquefaction strength analysis using laboratory tests (Prevost and Popescu, 1996).

Table 3.1: The parameters of the multi-yield plasticity model

Constitutive parameter	Symbol	Type
Mass density – solid	ρ^s	State parameters
Porosity	n^w	
Hydraulic conductivity	k	
Low strain elastic shear and bulk moduli	G_0, B_0	Low strain elastic parameters
Poisson's ratio	ν	
Power exponent	n	
Friction angle at failure	ϕ	Yield and failure parameters
Maximum deviatoric strain (comp/ext)	ε_{dev}^{max}	
Coefficient of lateral stress	k_0	
Stress-strain curve coefficient	α	
Dilation angle	ψ	Dilation parameters
Dilation parameter	X_{pp}	

Table 3.2: Correlations for the multi-yield plasticity model parameters

Parameter	Correlations	Comments	Reference
Hydraulic Conductivity (k)	Chart: $k = f(\text{soil type})$	Typical values for all soils	Terzaghi and Peck (1967)
	$k = \frac{1}{k_s} \frac{\gamma}{S^2} \frac{e^3}{\mu(1+e)}$ <p>where γ= unit weight, μ= dynamic viscosity, e= void ratio, k_s= factor depending on pore shape and ratio of length of actual flow path to soil bed thickness, S= specific surface area</p>	Kozen-Carman equation	Lambe and Whitman (1969)
	$k = 1.2 C_u^{0.735} D_{10}^{0.89} \frac{e^3}{1+e}$	Medium and fine sand	Shahabi et al. (1984)
	$k = 2.4622 \left[D_{10}^2 \frac{e^3}{(1+e)} \right]^{0.7825}$ <p>where D_{10} is in mm</p>		Chapuis (2004)
	$k = 10^{-2} D_{10}^2$ where D_{10} in mm, and k in m/s	Sandy soil	Hazen (1930)
	Chart: $k = f(e, D_{10})$	Sand and gravel mixtures	USACE (1994)
	Table: $k = f(\text{soil type}, D_{20})$	All soils	Creager et al. (1945)

Table 3.2 (cont.): Correlations for the multi-yield plasticity model parameters

Shear modulus (G)	$G_{max} = 70 \frac{(2.17 - e)^2}{(1 + e)} \left(\frac{p_0}{p_a} \right)^{0.5}$ <p>where G_{max} is the shear modulus at very low strains, p_a is the atmospheric pressure (100 kPa) and p_0 is the effective mean confining stress in same unit as p_a</p>	Dry sand ($\gamma \leq 10^{-4}$)	Hardin and Richart (1963)
	$G_{max} = \frac{2630(2.17 - e)^2}{(1 + e)} p_0^{0.5}$	Rounded Ottawa sand	Richart et al. (1970)
	$G_{max} = \frac{1230(2.97 - e)^2}{(1 + e)} p_0^{0.5}$	Angular Ottawa sand	Richart et al. (1970)
	$G_{max} = 400 P_a e^{(1.39 D_r)} \left(\frac{p_0}{p_a} \right)^{0.43}$	Tricino sand	Belloti et al. (1986)
Poisson's ratio (ν)	$\nu = 0.1 + 0.3 \phi_{rel}$ <p>where $\phi_{rel} = \frac{(\phi - 25)}{(45 - 25)}$, ϕ is the friction angle at failure</p>	Sand	Kulhawy and Mayne (1990)
	$\nu = 0.2 \dots 0.4$	Loose sand	Das (2005)
	$\nu = 0.25 \dots 0.4$	Medium sand	
	$\nu = 0.3 \dots 0.45$	Dense sand	
	$\nu = 0.2 \dots 0.4$	Silty sand	
	$\nu = 0.1 \dots 0.3$	Loose sand	Kulhawy and
$\nu = 0.3 \dots 0.4$	Dense Sand	Mayne (1990)	

Table 3.2 (cont.): Correlations for the multi-yield plasticity model parameters

Power exponent (n)	n = 0.7	Nevada sand (fine)	Popescu and Prevost (1993)
	n = 0.4 0.6	Conventional value for cohesionless soils	Popescu (1995)
	n = 0.65 0.75	Ticino sand	Belloti et al. (1986)
Friction angle at failure (ϕ)	$\phi = 17.6 + 11.0 \log \frac{q_c}{p_a}$ <p>where q_c is the cone penetration resistance</p>	$R^2 = 0.64$ and $SD = 2.8^0$	Kulhawy and Mayne (1990)
	$\phi = \tan^{-1} \left[0.1 + 0.38 \log \frac{q_c}{\sigma_{v0}'} \right]$	-	Robertson and Campanella (1983)
	Chart: $\phi = f(D_r)$	Fine sand	NAVFAC (1982)
	$\phi = \tan^{-1} \left[\frac{N_{SPT}}{12.2 + 20.3 \frac{\sigma_{v0}'}{p_a}} \right]^{0.34}$ <p>where N_{SPT} is the standard penetration test resistance, σ_{v0}' is the initial effective vertical stress</p>	Cohesionless soil Depth >12m	Schmertmann (1975)

Table 3.2 (cont.): Correlations for the multi-yield plasticity model parameters

Stress-strain curve coefficient (α)	$\alpha = 0.037D_{\max} - 0.027C_u + 0.217$ <p>where D_{\max} is the maximum particle size, C_u is the uniformity coefficient</p>	Various types of sand	Hayashi et al. (1992)
Coefficient of lateral stress at rest (k_0^r)	$k_0^r = 1 - \sin \phi$	NC sands	Jaky (1948)
	$k_0^r = f(\phi)$	-	Ochiai (1977)
	$\frac{\sigma'_{h0}}{p_a} = \frac{(q_c/p_a)^{1.25}}{35e^{(Dr/20)}}$	Calibration chamber data	Kulhawy et al. (1989)
Dilation angle (ψ)	34°	Fraser River sand	Vaid et al. (2001)
	Chart: $\psi = f(q_c, p', \text{soil type})$	Various sand	Been et al. (1987)
Dilation parameter (X_{pp})	$\log X_{pp} = 7.07 - 11.4 \times \left(0.1 \frac{15 + q_c \sqrt{P_a / (\sigma'_{v0})^{0.39}}}{25 - q_c \sqrt{P_a (\sigma'_{v0})^{0.39}}} \right)^{0.13}$	Erksak sand	Popescu (1995)

CHAPTER 4

Experimental Program

The research related to physical centrifuge modelling of soil liquefaction on heterogeneous soil is discussed in this chapter. The centrifuge facility and the characteristics of equipments are discussed next in section 4.1. The centrifuge test setup is discussed in section 4.2. The sample preparation and saturation process are discussed in sections 4.3 and 4.4 respectively. Instrumentation and measurement procedure are discussed in section 4.5. The centrifuge test procedures and test results are discussed in section 4.6. The difficulties faced during centrifuge tests are briefly discussed in section 4.7. The summary and conclusion of the centrifuge tests are discussed in section 4.8.

4.1. Characteristics of Equipment and Centrifuge Facility at C-CORE

C-CORE's centrifuge facility is located in the Memorial University, St. John's campus. This facility is a two-story building, containing a main bay, a control room, a cold room, the model preparation and radiography laboratories, electrical and mechanical workshops, offices and a circular chamber containing an Acutronic 680-2 centrifuge (made in France). The facility, which is funded by the industry and government and maintained by C-CORE, is located adjacent to S J Carew building. The facility is in working condition since June, 1993.

The C-CORE centrifuge has the ability to test the model at 200g and has a radius of 5.5m to the surface of the swinging platform. The swinging platform is located at one end of the centrifuge arm and is used for carrying the test package. The test package is at

a working radius of 5m. The maximum rotational speed is 189 rpm. The centrifuge has a maximum payload capacity of 2200kg to an inertial acceleration equivalent to 100g at 5m radius. This capacity reduces to 650kg due to the increase in self weight of the platform at 200g. The maximum payload size is 1.4m long, 1.1m wide and 1.2 to 2m high. The other end of the arm holds a counter weight of 22000 kg. The activities inside the package and the centrifuge operation are visually monitored with the cameras; one mounted on the test package and four on the chamber wall. The centrifuge is equipped with six rotary joints which permit fluids to flow through the central axis of the machine to the platform. Electrical signals from the transducers are acquired and recorded by a data acquisition system located above the centrifuge and relayed to the computer in centrifuge control room in the main building. Picture 1 shows the C-CORE's centrifuge. The efficient and safe use of the centrifuge is ensured by adopting the routine checking procedures. The procedures are similar to those adopted at the Geotechnical Centrifuge Centre of Cambridge University Engineering Department as presented by Schofield (1980).

During testing, the input ground motion is applied at the base of the box using an electro-hydraulic (Phillips et al., 2004) earthquake shaker (shown in Picture 2). The earthquake simulator (developed by Actidyn Systems) is capable of generating 40g sine acceleration on a 400kg model at frequencies up to 200 Hz or more, and it may generate larger accelerations up to 60g on smaller payloads. The fully computerized multi-degree of freedom control system can generate several modes of excitation such as: sine, broadband noise, or arbitrary transient waveforms with both amplitude and frequency control (C-CORE, 2005).



Picture 1: Centrifuge at C-CORE.



Picture 2: Earthquake simulator (after C-CORE, 2005).

The data acquisition system collects data simultaneously with the operation of the earthquake shaker. The Matrix system includes 8 analogue data inputs low pass filtered at 1 kHz and sampled at 2.56 kHz per channel using VXI hardware. This hardware has a further 24 channels of analogue inputs controlled by Data Physics 620 data acquisition software. These 24 inputs are typically filtered at 2 kHz and sampled at 5.12 kHz per channel for a 16 second period before, during and after the earthquake event. These 24 channels are usually used for collecting data from the instrumentation in the model (C-CORE, 2005). Therefore, as per present data acquisition system, maximum twenty-four instruments (similar or of different types) can be monitored during an earthquake-simulation centrifuge test.

4.2. Soil Characteristics and Centrifuge Test Setup

The soil for centrifuge experiments was selected from the Fraser River Delta in British Columbia. Fraser River sand receives huge research attention because of an expected large number of seismic events and higher liquefaction susceptibility in a relatively important area. The Fraser River sand is grey coloured medium grained sand, and is comprised of 40% quartz, quartzite and chert, 11% feldspar, and 45% unstable rock fragments. The soil grains are angular to sub-rounded (Vaid and Sivathayalan, 1996). The batch of the sand used here had an average particle size D_{50} of 0.26mm with the fine content (passing #200-sieve) of 0.4%. The particle size distribution curve is shown in Figure 4.1 for the batch of Fraser River sand used in the centrifuge tests. The maximum and minimum dry densities are 1.67g/cm^3 and 1.4g/cm^3 . The maximum and

minimum void ratios are 0.94 and 0.62, respectively. The specific gravity of the batch of sand is 2.71 (C-CORE, 2005).

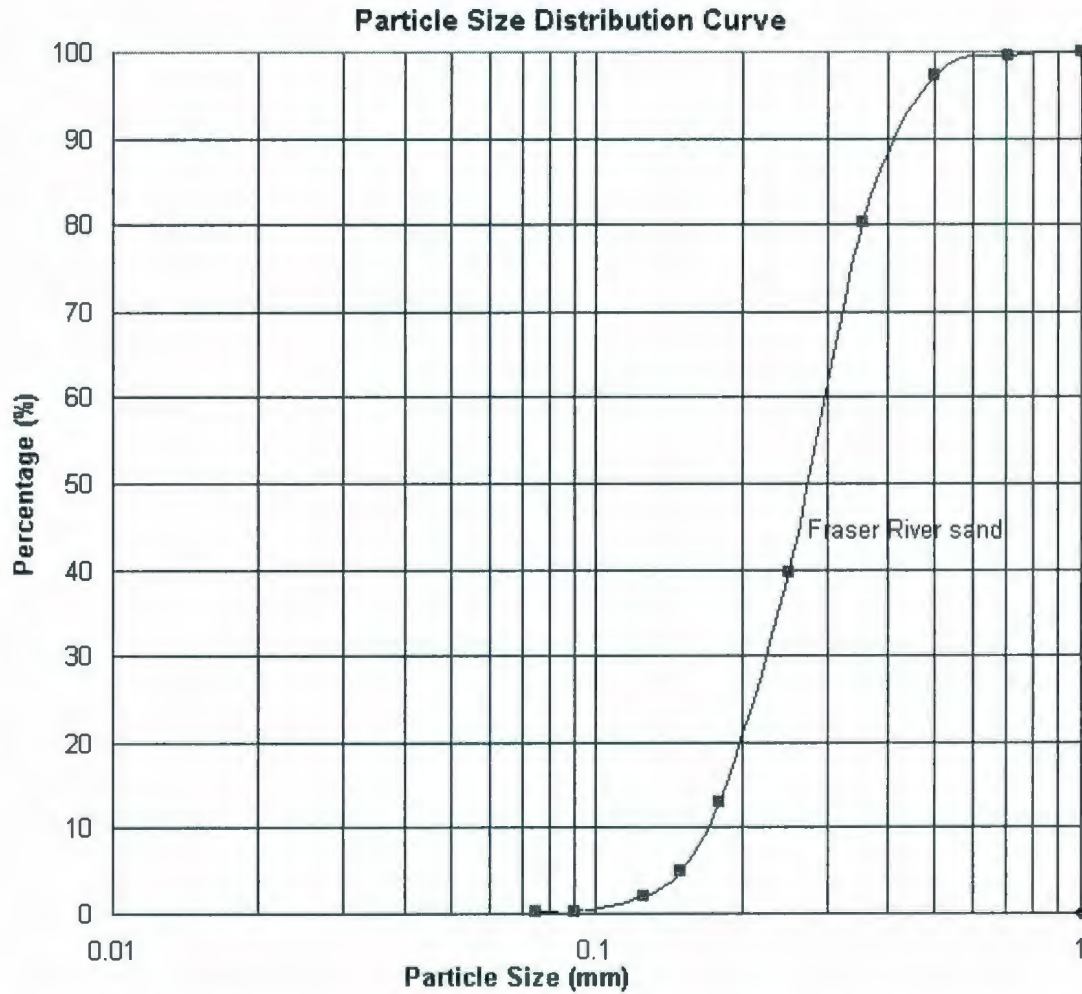
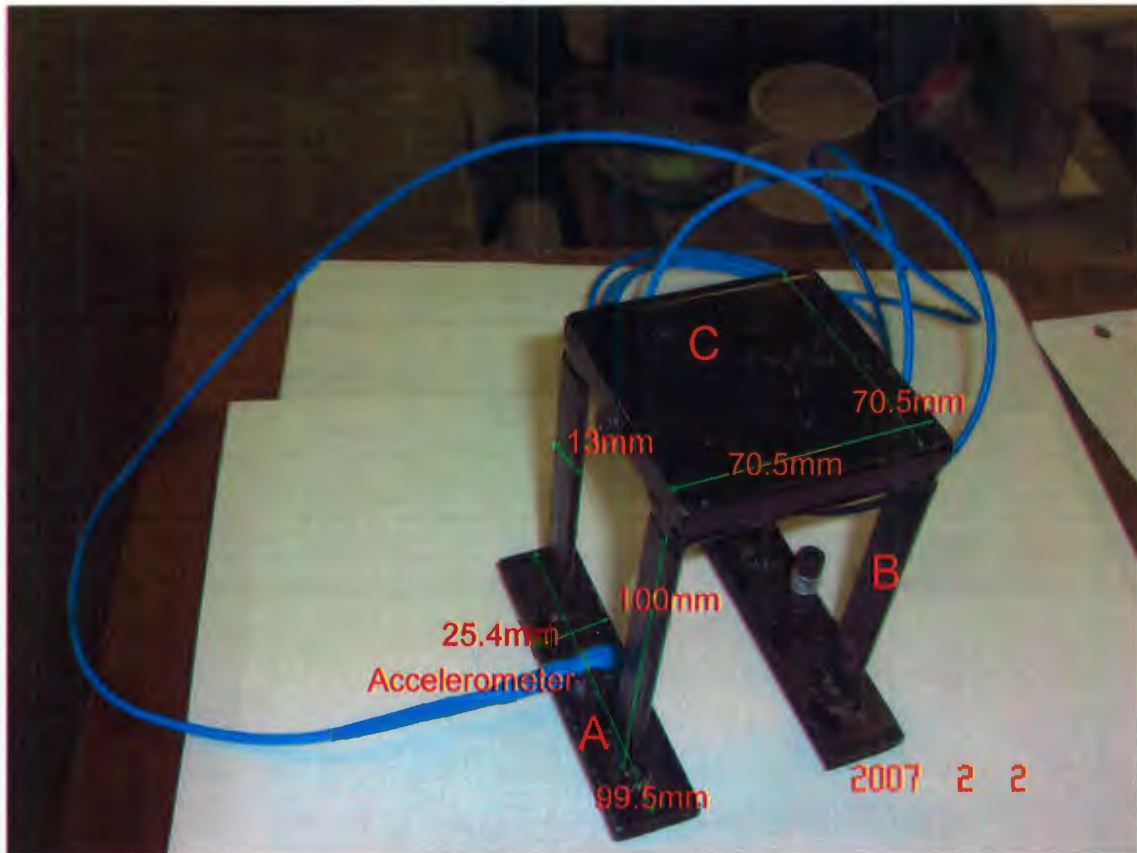


Figure 4.1: Particle size distribution curve for Fraser river sand used in the centrifuge tests (after C-CORE, 2005).

Three liquefaction tests were conducted on Fraser River sand at 70g's to determine the prototype behaviour of heterogeneous soil in a centrifuge model. The internal dimensions of the model container are 73.7cm (length) x 28.1cm (width) x 57cm (depth). The first test was performed on a medium dense homogeneous soil ($D_r = 55\%$). A 16m deep medium dense sand deposit was overlying on 4m deep dense ($D_r = 75\%$)

cohesionless soil layer. A frame structure (shown in Picture 3) placed on two strip footings was placed on that soil deposit. The structure was built of mild steel plates of different thickness. The dimensions of those plates are shown in Table 4.1. Performance of the frame structure under a synthetic earthquake was studied. The characteristic frequency of the structure is 2.1Hz (at prototype scale). The bearing pressure below footings is 110 kPa at 70g. A 5.4cm (at model scale) Duxseal layer has been placed at the two transversal walls of the rigid box to reduce boundary effects by partially preventing wave reflection.



Picture 3: Frame structure on two strip footings.

The second and the third tests were performed on heterogeneous soil. As there were several malfunctioning transducers in test 2, test 3 was a repeat of test 2 with more transducers duplicating key locations. Both test 2 and test 3 were performed using a new

model container. The internal dimensions of the new model container are 73.7cm (length) x 27.5cm (width) x 57cm (depth). One of the advantages of this box is that transverse side walls are made of with thick plexiglass. Therefore, it was possible to monitor the whole soil depth of the model during saturation and tests. In both models, 2-metre thick loose soil ($D_r=35\%$) pockets were placed within a 16m deep dense soil ($D_r=75\%$) deposit. This heterogeneous soil was overlying a 4m thick dense soil layer. The dimensions of loose pockets are shown in Figure 4.2d. The same structure was also placed on the heterogeneous soil to find the effect of soil heterogeneity on the responses. The model configurations with the transducer locations for uniform and variable soil are shown in Figure 4.2. Locations of all the transducers in x-y-z coordinates, at prototype scale, are shown in Table 4.2.

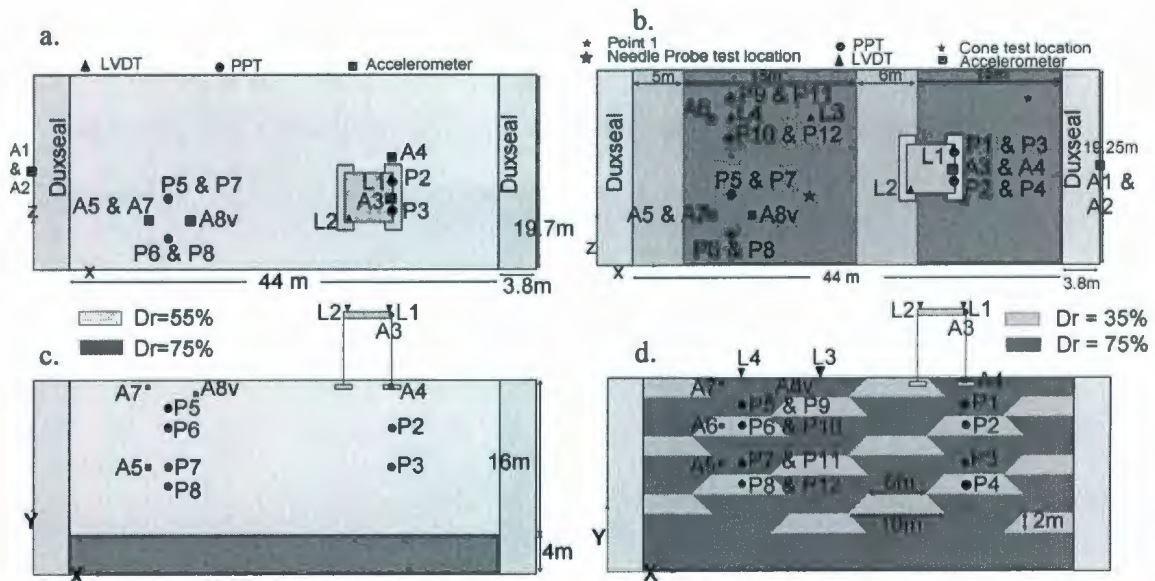
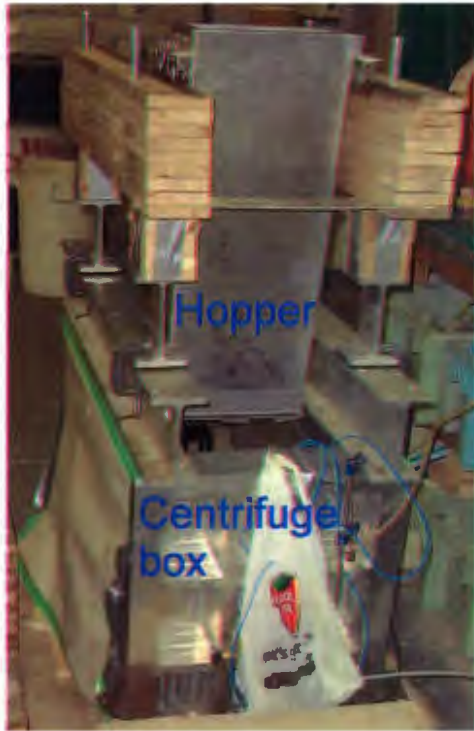


Figure 4.2: Schematic diagram of centrifuge tests a. plan: test 1; b. plan: test 3; c. elevation: test 1; d. elevation: test 3.

4.3. Sample Preparation



Picture 4: Setup for sand raining during test 2.

All centrifuge models were prepared by air-pluviation of dry Fraser River sand into the model container using a hopper (shown in Picture 4). First, a 22-25mm thick drainage layer was placed before raining the sand. In the drainage layer, coarse sands with particle size larger than 1mm and less than 2mm were used. This drainage layer was used to uniformly distribute the fluid throughout the sample during saturation.

A geo-textile membrane was used on the top of this drainage layer to prevent the sands from going inside more porous drainage layer. After placing this membrane, about 54mm thick Duxseal layer was placed at the sidewalls perpendicular to the direction of seismic acceleration. The Duxseal layer was used for partially reducing the boundary effects. Sand layers were deposited next using a hopper. The sand was raining from the hopper through two rows of holes of about 3mm in diameter and spaced 8mm apart. The width of the hopper equals the width of the box. The hopper was manually moved back and forth along the length of the box. The relative density of the soil was controlled by the falling height of sand. Numerous trials have been performed, before preparing the model, to obtain a relation for sand falling height and achieved relative density. During all these trials and model preparations, the

hopper speed was kept constant at about 10cm/sec. The relation between sand falling height and the achieved relative density is shown in Figure 4.3. When the sand deposit

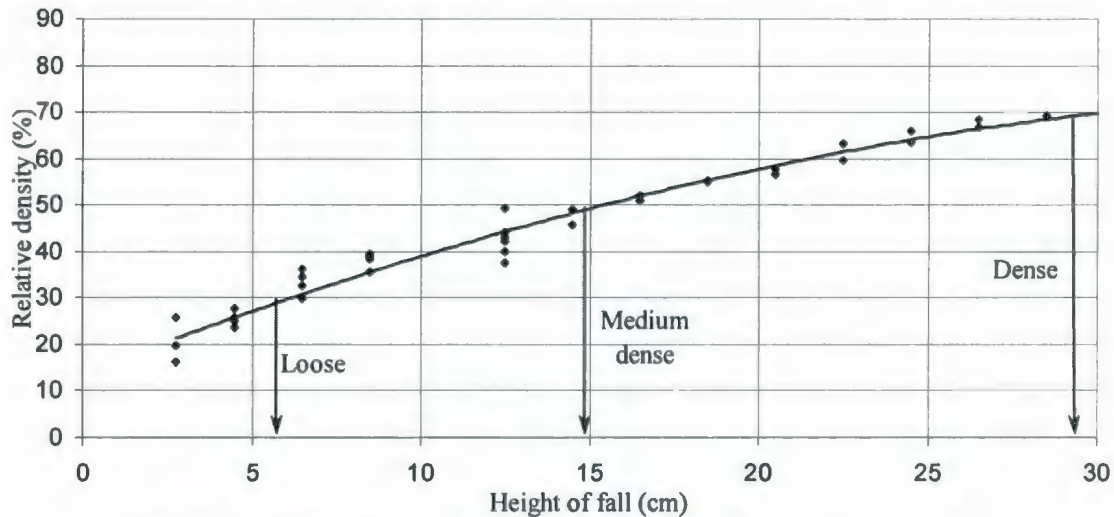


Figure 4.3: Sand falling height vs. relative density relation.

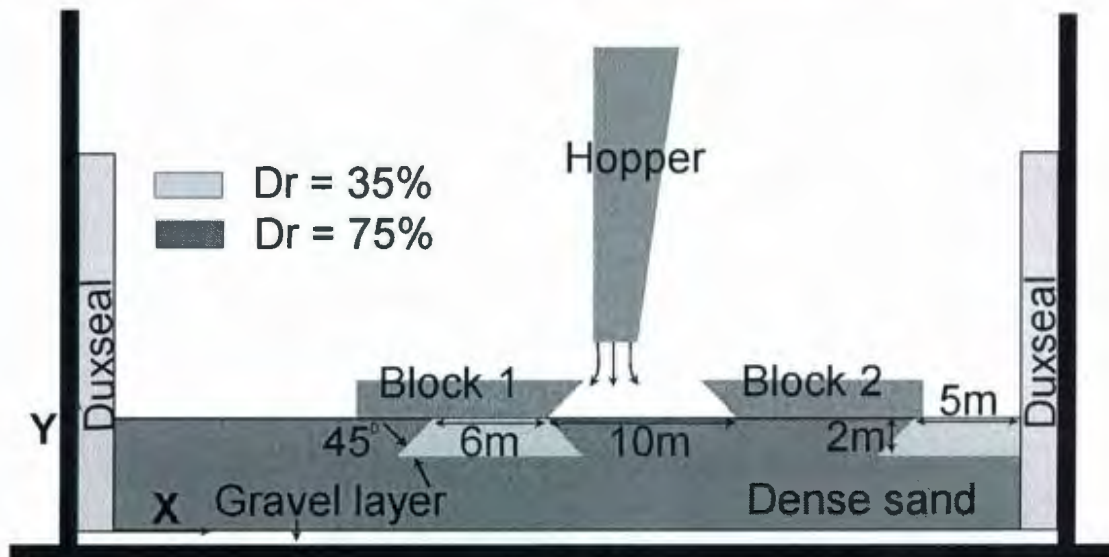
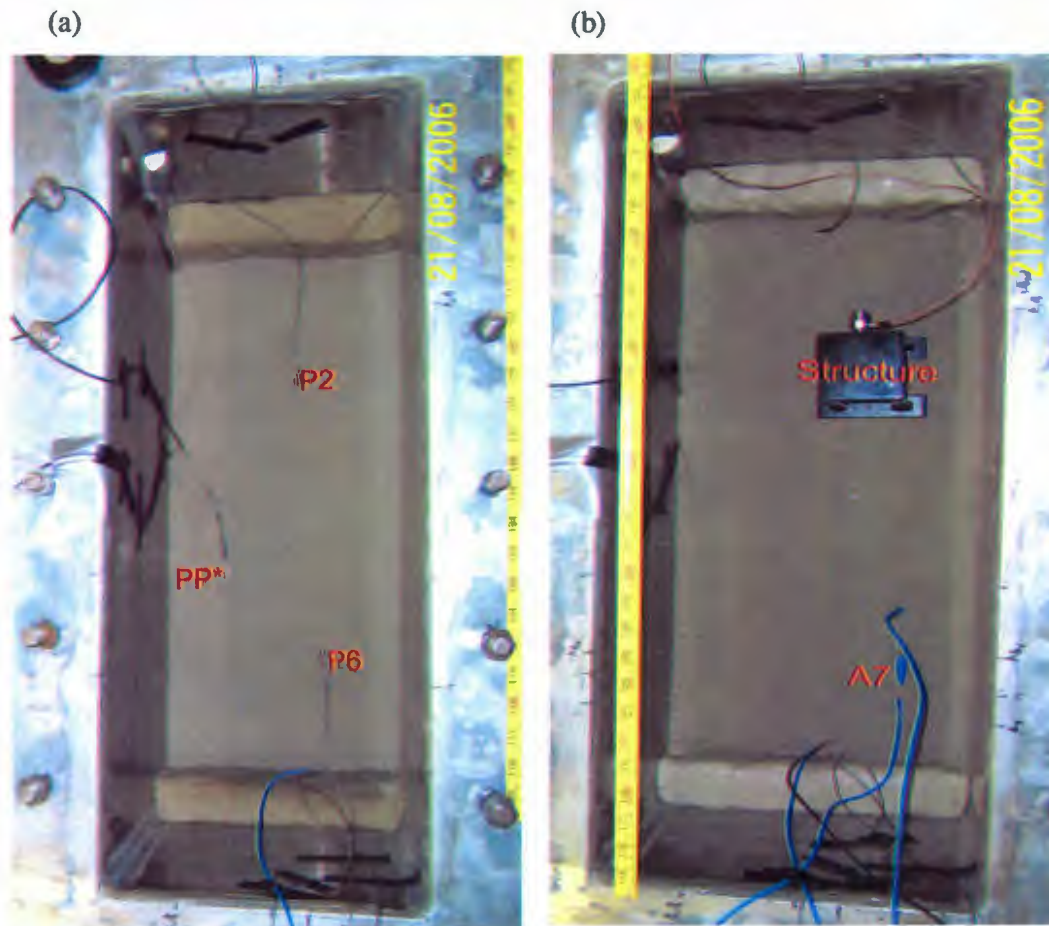


Figure 4.4: Schematic diagram for preparing loose pockets in heterogeneous soil using two lightweight movable blocks (block1 and block2).

reached the selected height of the transducer, sand raining was stopped to place the accelerometers and the pore pressure transducers. Top views of the model at two different elevations are shown in Picture 5. There are 16 loose pockets at 8 different depths inside the heterogeneous soil. In each horizontal layer, the loose pockets were deposited first.



Picture 5: Top view of the model with placed instruments in test1 at two different depths; (a) at 5m depth; (b) at 1m depth; PP* is a PPT used for pile testing (not related with this thesis).

Then, the remaining spaces were filled with dense sand. The preparation of a loose pocket in heterogeneous soil is shown in Figure 4.4. Two light weight trapezoidal blocks (block1 and block2 as shown in Figure 4.4) were used for constructing loose pockets during Sand raining.

4.4. Saturation of Models for Centrifuge Tests

After the sand raining was finished, the model was placed under vacuum for de-airing and saturation. The pore fluid characteristic, procedure and setup for sample saturation are explained in this section.

4.4.1 Pore Fluid

The hydroxypropyl methylcellulose (HPMC) solution has been selected as pore fluid in the centrifuge tests. The HPMC fluid used in these centrifuge tests was prepared by mixing Methocel F50 powder manufactured by DOW Chemical Company with water. This fluid was also used in the previous centrifuge tests at C-CORE during LRI and COSTA-Canada projects (C-CORE, 2005). Pore fluids, having viscosity greater than water are usually used in geotechnical centrifuge tests, to accurately satisfy the scaling laws related to the movement of pore fluid through the soil during dynamic loading events. To fulfil the scaling laws regarding pore pressure dissipation, the permeability of the soil could be reduced by a scaling factor of 70 (in this case), by increasing the fluid viscosity by 70 times (Hausler, 2002). However, a pore fluid with a kinematic viscosity of 70 times that of water would significantly increase the amount of time required for saturation of the model and also might affect the degree of saturation of the model. Therefore, a target pore fluid viscosity of approximately 35 times that of the water was used in these tests. For a 35cSt HPMC mixture at 25⁰C, a mass of HPMC powder of 1.92% of the entire solution volume is required. A mass of benzoic acid powder, equal to approximately 1% of the mass of the HPMC powder, was added to the cellulose powder to prevent any bacterial growth which might occur in the prepared fluid. The pore fluid is prepared by mixing required amount (as discussed earlier) of HPMC and benzoic acid powder mixture with the required amount of deionised water at room temperature. The mixture will foam a lot while agitating with an electric mixer. The powder must be added in increments of about 250gms. If too much powder is added at a time then the powder may clot and stick together in the solution. Therefore, the target viscosity will not be

achieved. After preparing the fluid it should be tested for viscosity and transferred into a reservoir where it is de-aired for at least 48 hours. The viscosity highly depends upon the temperature. Since the solution must be prepared a few days prior to the test, it is difficult to get the exact target viscosity during centrifuge tests.

4.4.2 Saturation Procedure

Vacuum saturation process was used here for the model saturation. The schematic diagram of the saturation process is shown in Figure 4.5. Different components of the saturation setup during test 1 are shown in Picture 6. Before starting the saturation process, the fluid must be de-aired for at least 48hrs by applying vacuum. The connection line from fluid container to the box was then filled with fluid by controlling the valve V6, and V4 (shown in Figure 4.5). The connection line between CO₂ container and the box (up to V5) was then filled with CO₂. After replacing all the air inside both the connection line (for fluid and CO₂), the model was placed under vacuum for at least 48 hours for de-airing. The suction inside the box was kept at about 80 kPa during de-aeration process. All the valves except V1 and V11 were kept closed during de-airing. It is possible to de-air the pore fluid container (by opening V10) in parallel with the model. However it was preferred to de-air the pore fluid container before starting preparation of the model. It has helped to finish de-airing the fluid container before closing the model container lid. After applying vacuum for about 48hours, most of the air inside the soil was removed. Rest of the air was replaced by more soluble CO₂. Carbon dioxide gas was introduced into the model at almost atmospheric pressure by controlling the valve V7, V5, V8, V12, V3_a and V3_b. A depressurization chamber (CO₂ container) was used for reducing the high

pressure of the gas which was coming from a compressed gas cylinder. While applying CO₂, valve V1 and V10 were closed. But V11 was not touched until the end of the saturation process. Gradually, over the period of approximately half an hour, the pressure inside sealed model container was brought back to the atmospheric pressure using CO₂. It took between 8-10 buckets of CO₂ to bring the box back to the atmospheric pressure. Following this process, the model container was again placed under vacuum (by opening the valve V1) to bring the vacuum level back to the 75kPa. After approximately 20 minutes, the CO₂ was applied again to remove the rest of the air. These processes have been repeated for 2-3 times. The major portions of the gas inside the soil voids were CO₂ which is more soluble in water than air. This CO₂ flushing was helped to increase the degree of saturation. Next, the valve V2 was opened to control the vacuum difference (if any) between model container and fluid container. After few minutes, valve V6, V4, V3_a and V3_b were opened to allow pore fluid inside the model. The flow rate of the fluid was kept very low to reduce the chances of sample disturbance. The fluid was entering into the model container under the gravity force (due to head difference) only. The average flow rate was about 0.4litre per hour. It has taken about 2-4days to complete the saturation process. During saturation of heterogeneous soil, it was observed that the dense soil in the same layer saturated before loose pockets (shown in picture 7), probably because of higher suction induced by smaller voids in the dense sand. When the fluid level reached about 12-15mm above the soil surface, the valves were closed.

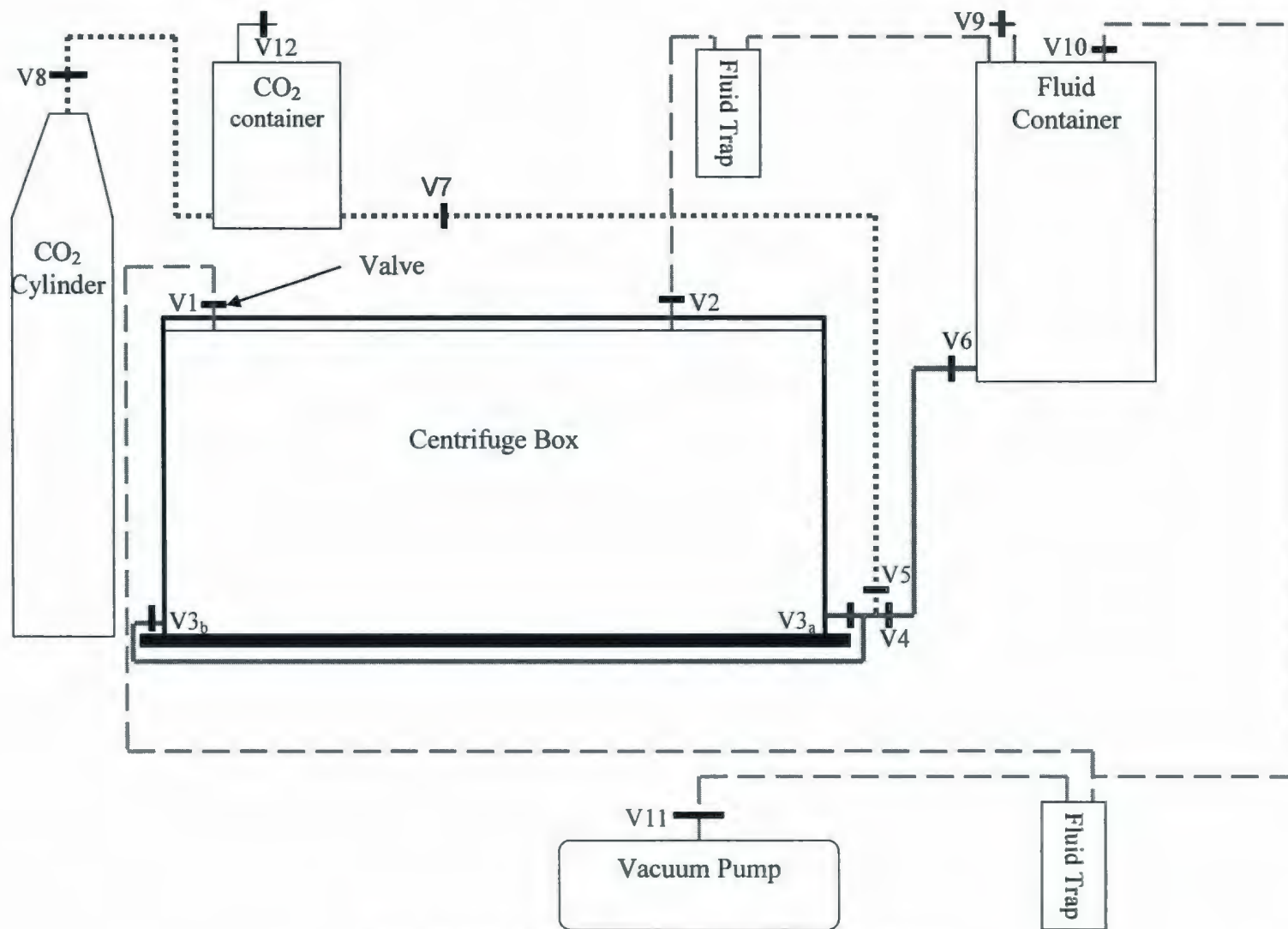
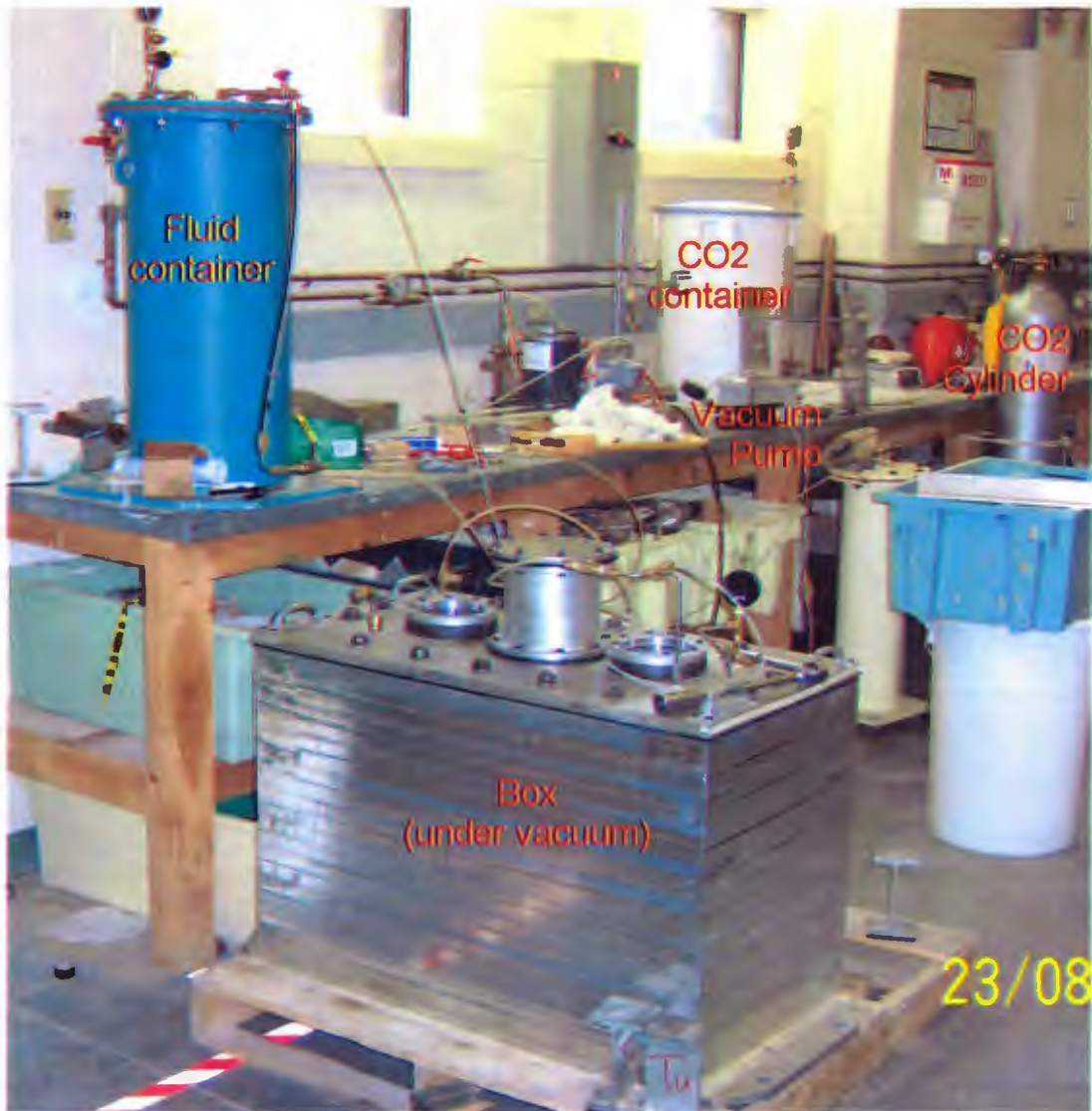
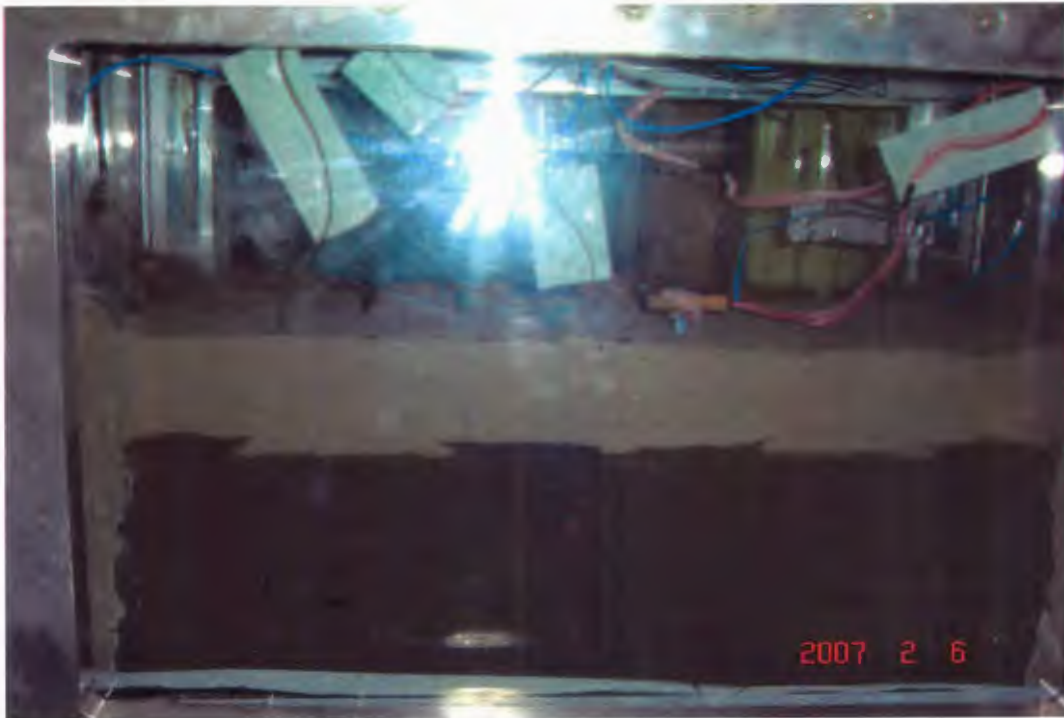


Figure 4.5: Schematic Diagram for Saturation Setup.

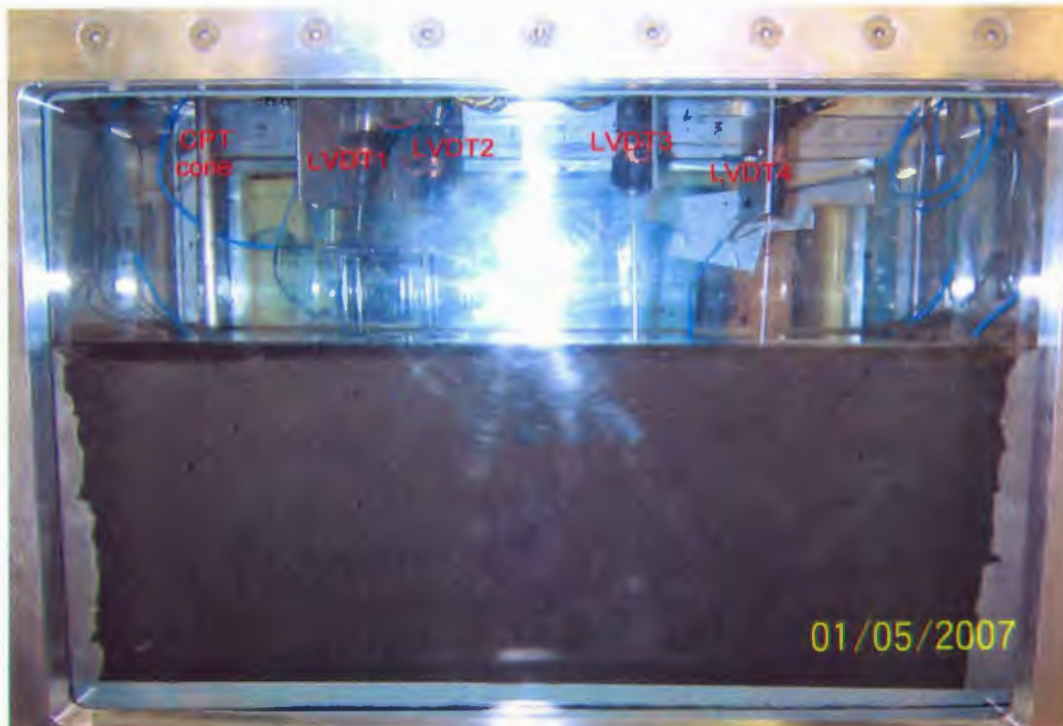


Picture 6: Model during saturation under vacuum.

Once the saturation process was complete the vacuum was released step by step with a rate of decrement of about 15kPa in 10mins. A surface profile (shown in Figure 4.6 for test 3) was then constructed by measuring the soil surface at different locations. The measurements were manually taken before and after the saturation at predefined, equally spaced locations using rulers. The linear variable differential transformers (LVDT) were then placed at the desired locations (shown in Picture 8) using LVDT holders. Next, the



Picture 7: Elevation of heterogeneous soil model during saturation in test2.



Picture 8: Elevation of heterogeneous soil model after saturation in test3.

model was carefully moved to the centrifuge arm for testing. A pallet jack was used to move the box from the laboratory to centrifuge chamber. Then, a forklift truck was used to place the box onto the centrifuge arm (shown in Picture 9). All the instruments were then connected with the signal conditioning box. Next, the model was tested at 70g inertial acceleration level.

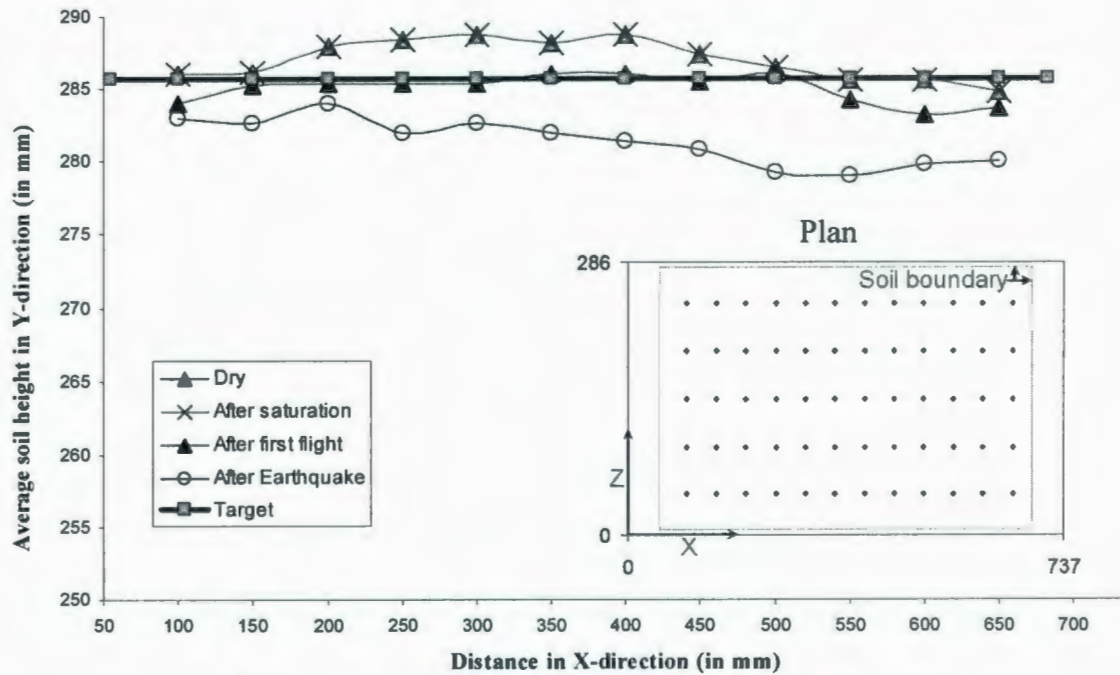


Figure 4.6: Average soil height (at model scale) during test 3 (heterogeneous soil). These values are average of 5 measurements at 50mm interval in z-direction starting at 43mm from side wall. There are Duxseal layers between 0-54mm and 683-737mm in x-direction. Plan is shown in the inset with dotted points for measurement location.

4.5. Instrumentation and Measurements

Experimental results, such as accelerations, pore water pressures and settlements were monitored throughout the tests. During first two tests, six PPTs, two LVDTs and seven accelerometers were used. In test 3 twelve PPTs, four LVDTs and eight accelerometers were used. The pore pressure transducers (PPT) were Druck miniature

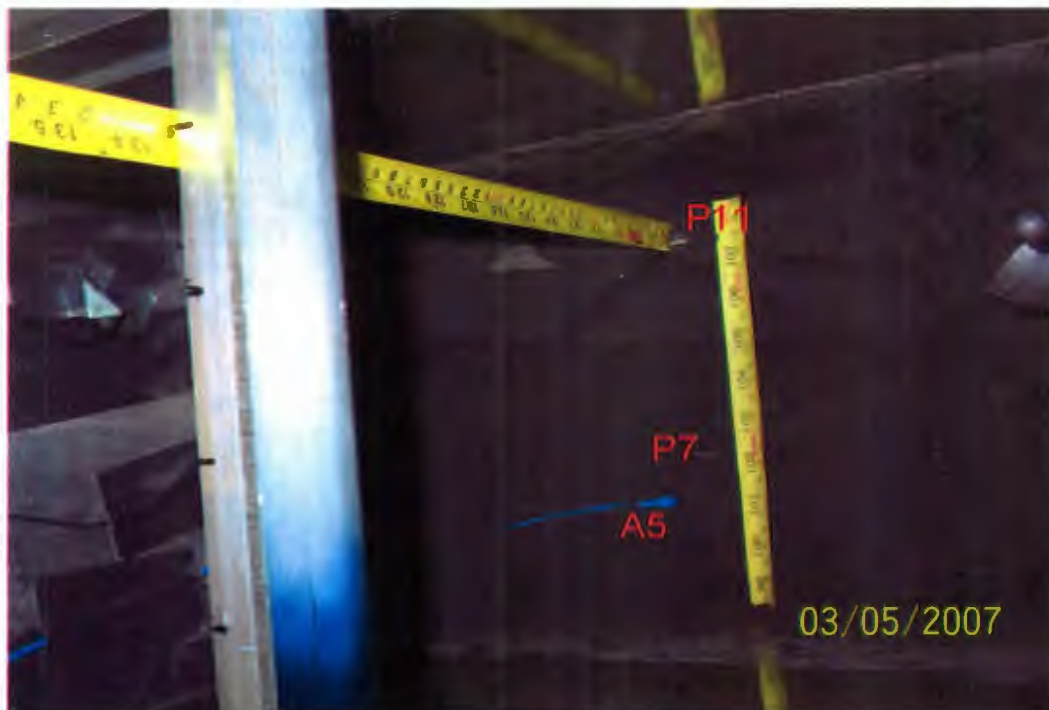
model PDCR81. The PPT consists of a single crystal silicon diaphragm with a fully active strain gage bridge diffused into the surface. The transducers were supplied with a porous stone, which was used to protect the diaphragm against the pressure applied by the soil. The transducers are available for various pressure ranges. The maximum pressure ranges for the transducer used in the tests were: 15psi, 100psi and 200psi. The specifications for PPT are presented in Table 4.3. The accelerometers used in the experiments were ICP (Integrated circuit piezoelectric) miniature model 353B18 manufactured by PCB Piezotronic Inc. The specifications for the accelerometers are listed in Table 4.3. The settlements were measured using general purpose Linear Variable Differential Transformers (LVDT) of the Trans-Tek series model 240. The specifications for LVDT are also presented in Table 4.3.

Calibration factors were used to convert the recorded voltage output of the instrument into engineering unit. For example, PPT recordings are converted to 'kPa', accelerometer readings to 'g' and LVDT readings to 'mm'. The calibration factors for PPT and LVDT were determined by manual calibration, performed before each test and also compared with old calibrated constants or the one provided by the manufacturer. Horizontal and vertical locations of the transducer were carefully measured using rulers. The position of each accelerometer was measured at the tip of the accelerometer along its centreline. Similarly, the position of each PPT was measured at the centre of the porous stone. Pore pressure transducers were placed within the soil deposit with the plane of their porous stones oriented vertically and the transducers parallel to the direction of shaking. The final locations of the transducers after each test were also measured to calculate the transducer movement during the testing. The partially excavated model with transducers

is shown in Picture 10. The locations of the instruments before and after the



Picture 9: Placing the box on centrifuge arm using forklift truck during test3.

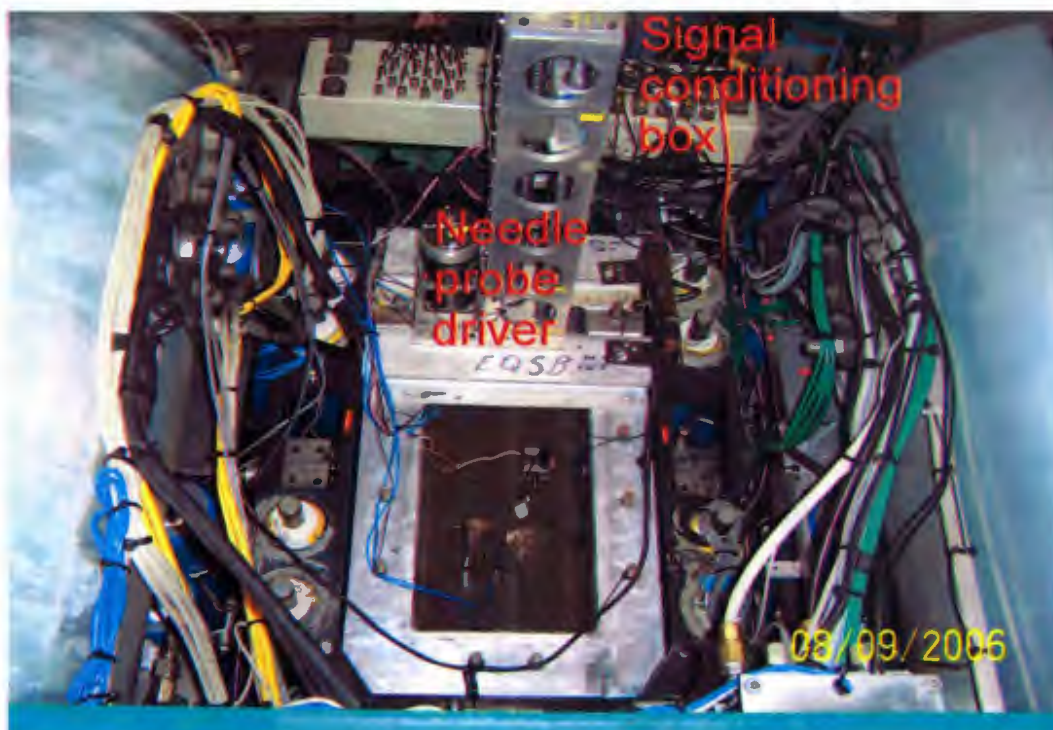


Picture 10: Top view of partially excavated model after test3.

test for tests 1, 2 and 3 are tabulated in Table 4.4, Table 4.5 and Table 4.6 respectively.

4.6. Centrifuge Test Procedure and Results

Each of the three centrifuge tests have been performed in two flights. During the first two tests, the needle probe measurements were performed in the first flight and then the centrifuge was stopped to remove the needle probe driving (shown in Picture 11) actuator. The centrifuge was spun up again and the earthquake simulation test was performed in the second flight. During the third test, in-flight cone penetration test was performed in the first flight and the earthquake simulation test was performed in the second flight. The rotational speed of the centrifuge was increased gradually from 0 to about 113rpm. The actual inertial acceleration calculated was about $70 \pm 0.5g$ during all three tests. The centrifuge speed was kept constant for about 15-20mins for soil consolidation before doing the cone penetration / needle probe test. This soil consolidation ultimately affects the relative density of the sand in the model.



Picture 11: Centrifuge model ready to fly for first flight during test1.

4.6.1. Measurement of Soil Relative Density

In test 3, an in-flight cone penetration test was performed using a 9.5mm diameter sand cone to check the presence of loose pockets after the model was consolidated under its self weight at 70g in the centrifuge. The penetration velocity was 3mm/s and total soil penetration depth was 250mm. The cone penetration resistance measured in test 3 is shown in Figure 4.7. The target locations of loose pockets are also shown in the figure. Since the thickness of the loose pocket (i.e., 29mm) was less than 6 times the cone diameter; this test results cannot be used to determine the exact location of loose pockets. However it gives a qualitative idea about the location of loose pockets and overall penetration resistance.

The soil surface was also measured carefully at 60 locations to calculate an average soil density. The measurements were done in a grid of 12x5 (shown in Figure 4.6) at four instants during each tests (i.e., before saturation, after saturation, before applying earthquake and after applying earthquake). All the average soil surface measurements in test 3 are shown in Figure 4.6. It was observed that the soil depth before and after saturation was the same. Therefore, it is concluded that there was no sample disturbance or change in soil relative density during saturation. The calculated overall average soil relative density was found to be 60.58% for dry and as well as saturated soils during test 3. Similarly, the average relative density of the model after the first centrifuge flight was found to be 64.48%, which is very close to the theoretical relative density of 64.42% for the heterogeneous soil model considered in the study.

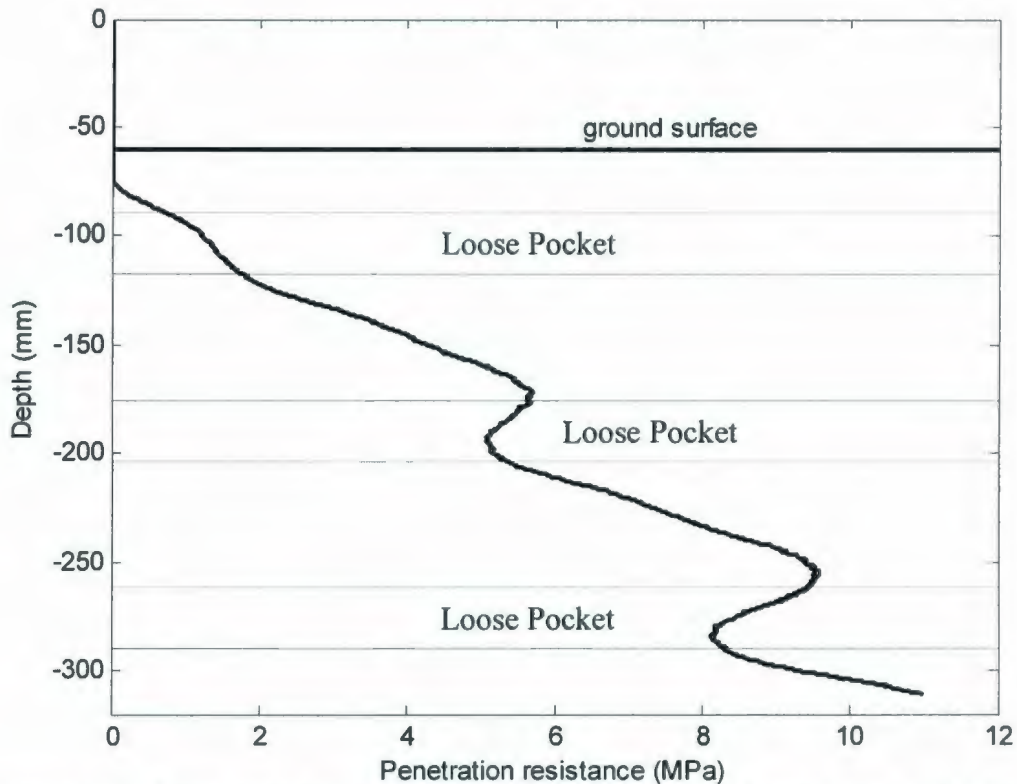


Figure 4.7: Cone penetration test results during test3 (tested up to 250mm soil depth). Desired locations of loose pockets are also shown in the figure. Test location is shown in Figure 4.2.

4.6.2. Earthquake Simulation Test

The earthquake simulation test was performed in second flight during all the three tests. The rotational speed of the centrifuge was increased gradually from 0 to about 113rpm for the second time. The centrifuge rotational speed was kept constant for about 10mins for stabilizing all the pore pressure transducers. Then the input ground motion was applied in the horizontal direction at the base of the box using an electro-hydraulic earthquake shaker (EQS). A synthetic acceleration time history, a 2% probability of exceedance in 50 years for Vancouver area based on the firm ground target spectrum in Canadian building code (NBCC 2005), was used in all three centrifuge tests. The synthetic acceleration time history was then amplified by 1.46 to obtain a PGA of 0.25g during centrifuge tests. Before each of the geotechnical model test, the earthquake

simulator (EQS) was tuned using a dummy payload at the desired centrifuge acceleration level for about two hours period. A dummy payload, similar in mass and centre of mass to the geotechnical model is mounted on the EQS and is subjected to a pre-test comprising about 8 random bursts of uncorrelated accelerations in the range 40 to 300Hz. The actuator's gain and phase transfer functions are assessed from the average system response to these bursts. The target earthquake motion is assessed from the prescribed earthquake motion defined in prototype terms (Phillips et al., 2004). The prescribed motion is scaled in amplitude and time according to the centrifuge scaling laws. Due to constraints of C-CORE's centrifuge shaker, the input motion had a frequency range between 40 to 200 Hz (0.57 to 2.86Hz at prototype scale). Next, the input motion is base line corrected by removing any residual displacement or velocity at the end of the record. Due to complexity in the EQS, the actual applied motion in each test may not always be the same as desired target motion. Therefore, to minimise this difference between target and applied motions, a very careful tuning is required before each test.

4.6.3. Discussion of Centrifuge Test Results

The recorded EPWP are presented in terms of their ratio (EPWP ratio = $EPWP/\sigma_v'$) with respect to the initial vertical effective stress (σ_v') at six different locations in test 1 (2 locations below structure and 4 locations in the free field in homogeneous soil) are shown in Figure 4.8. The EPWP ratios below the structure in heterogeneous soil are shown in Figure 4.9. Recorded EPWP ratios in the free field in heterogeneous soil are shown in Figure 4.10. Some of the pore pressure transducers did not work properly due to various reasons (mentioned in the figure). Recorded EPWP

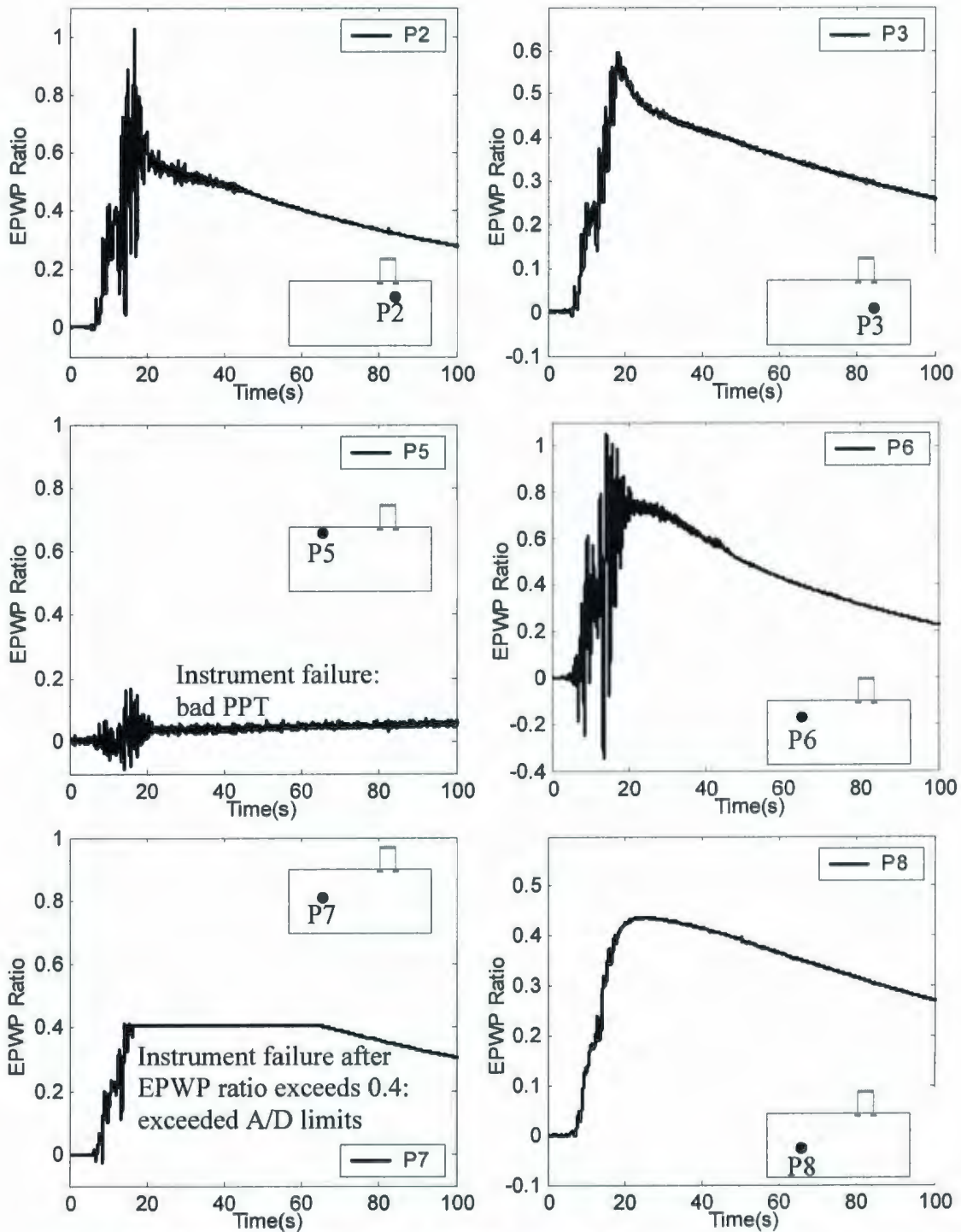


Figure 4.8: Recorded excess pore water pressure (EPWP) ratio with respect to the initial effective vertical stress at 6 locations in homogeneous soil (test1).

ratios of those transducers which worked properly are compared here between the results on homogeneous and heterogeneous soil model.

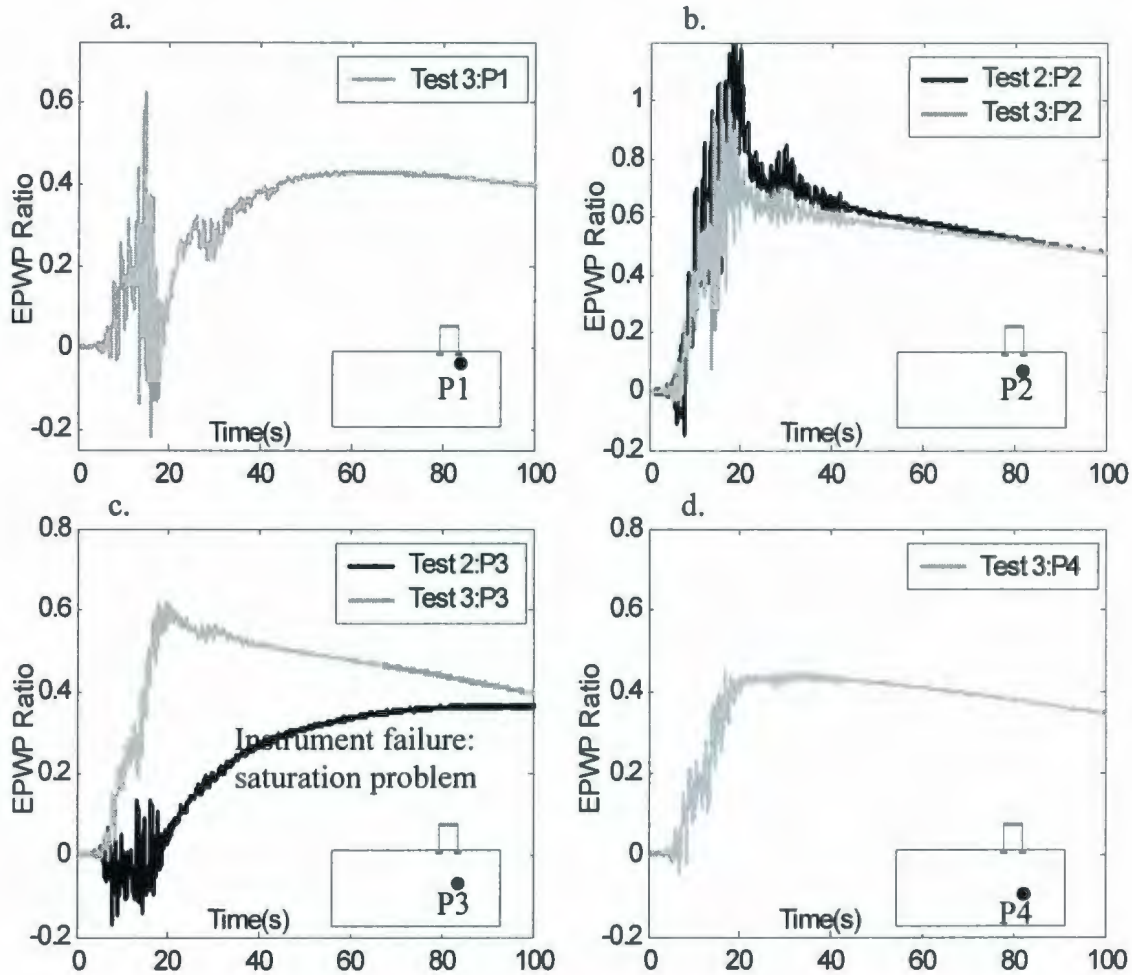


Figure 4.9: Recorded excess pore water pressure (EPWP) ratio with respect to the initial effective vertical stress at 2 locations in test2 and 4 locations below structure in test3 (heterogeneous soil) a. P1: dense soil; b. P2: loose soil; c. P3: dense soil; d. P4: loose soil.

From the EPWP ratio results it has also been observed that EPWP generation in the heterogeneous soil (test 2 and 3) are larger than those generated in homogeneous soil (test 1) at corresponding locations. This has been observed while comparing the EPWP ratio results, between medium dense uniform soil and loose soil pockets in the heterogeneous soil (shown in Figure 4.11 and 4.13a), as well as in the EPWP ratio results between medium dense uniform soil and dense soil in heterogeneous soil (shown in Figure 4.13b).

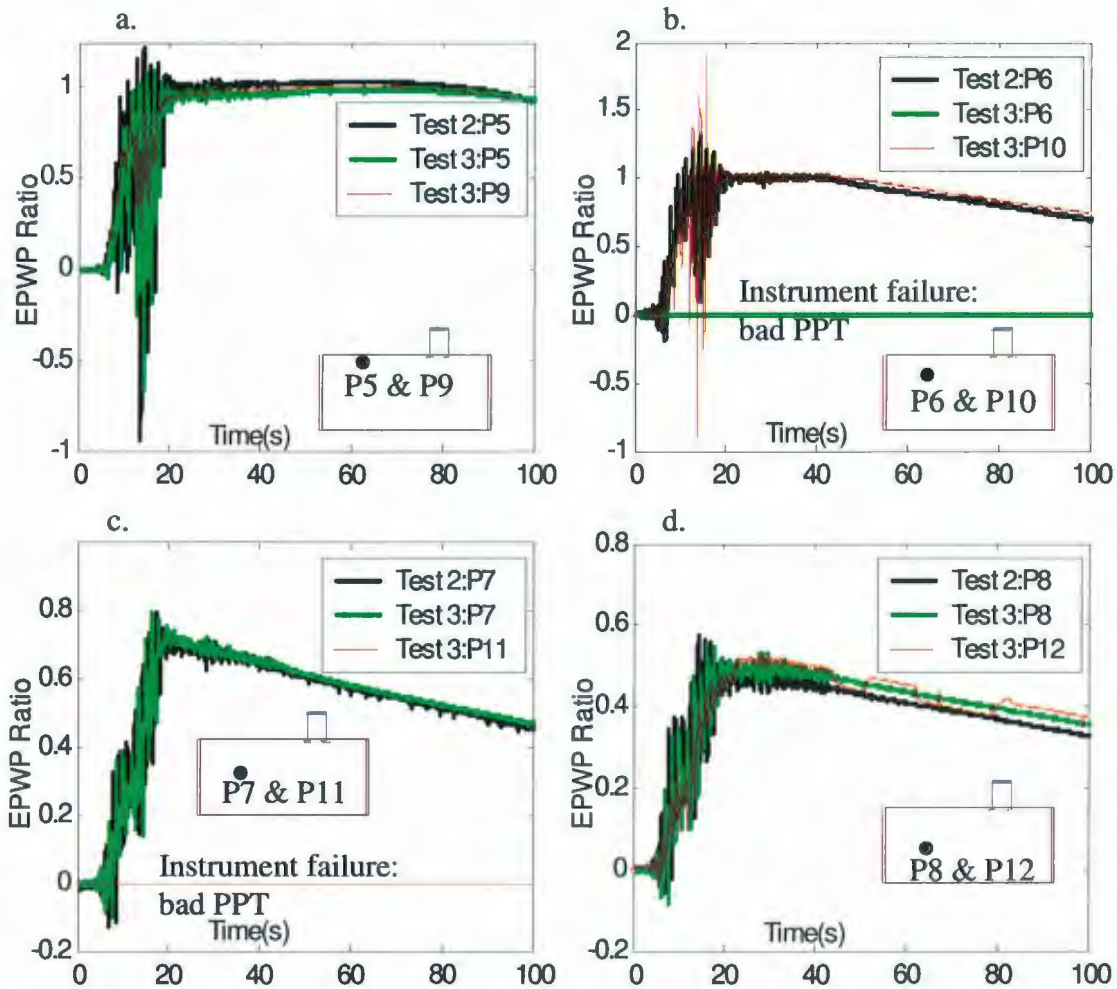


Figure 4.10: Recorded excess pore water pressure (EPWP) ratio with respect to the initial effective vertical stress at 4 locations in the free field in test2 and in test3 (heterogeneous soil) a. P5 & P9: dense soil; b. P6 & P10: loose soil; c. P7 & P11: dense soil; d. P8 & P12: loose soil.

For example, at 5m depth (*P6*) in the free field in a loose pocket in heterogeneous soil EPWP ratio reached 1 between 20s and 40s, indicating full liquefaction of the soil whereas in homogeneous soil EPWP ratio was less than 0.8. Transducers *P5* and *P7* did not work properly during test 1. Therefore, a direct comparison between medium dense uniform soil in test 1 and dense soil in tests 2 and 3 at the same elevations in the free field could not be obtained from the Figures 4.8 and 4.10. However, from similar comparison (shown in Figure 4.13b) below structure (*P3*), it is evident that EPWP ratio in dense sand

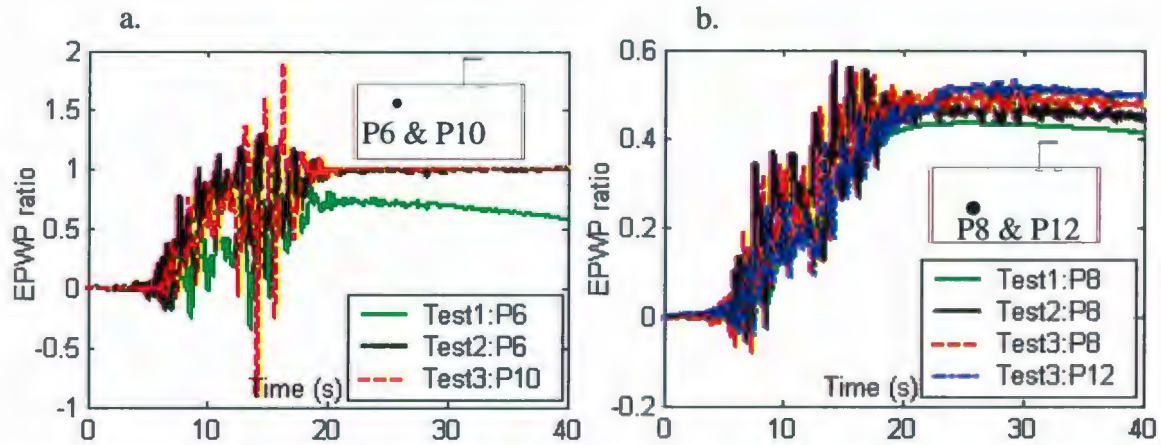


Figure 4.11: Comparison of EPWP ratio time histories in the free field between medium dense homogeneous soil (test1) and loose soil pockets in heterogeneous soil (test 2 and 3): a. P6 or P10; b. P8 or P12.

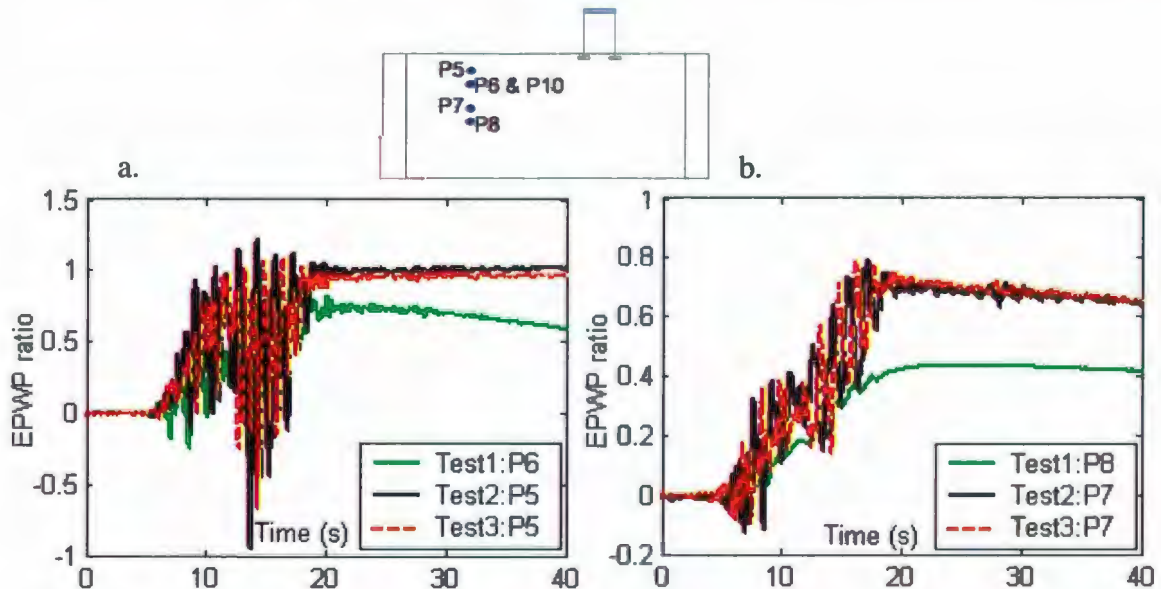


Figure 4.12: Comparison of EPWP ratio between homogeneous and heterogeneous soil (dense sand zone) in the free field a. P6: Medium dense vs. P5: Dense; b. P8: Medium dense vs. P7: Dense.

in heterogeneous soil is also larger than that in medium dense sand in homogeneous soil at corresponding locations. The comparison of recorded EPWP ratio between dense sand in heterogeneous soil in the free field and medium dense uniform sand at higher depth is shown in Figure 4.12. It has been observed that EPWP ratio near the ground surface (P6/P10 and higher) in heterogeneous soil has residual values of one, indicating full

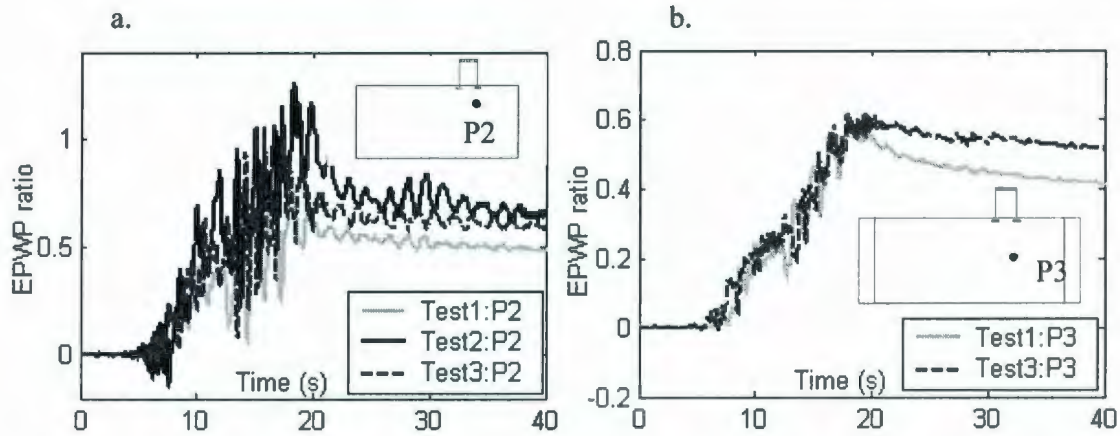


Figure 4.13: Comparison of EPWP ratio time histories below structure: a. between medium dense homogeneous soil (test1) and loose soil pockets in heterogeneous soil (test 2 and 3); b. between medium dense homogeneous soil (test1) and dense soil pockets in heterogeneous soil (test 3).

liquefaction of the soil in these areas (both loose soil – e.g. P10 and dense soil – e.g. P5). However, the homogeneous soil did not fully liquefy. These results confirm earlier numerical findings discussed in sub-section 2.5.3 that more EPWP is generated in heterogeneous soil (both loose and dense soil zones) than in the corresponding homogeneous soil.

From the comparison of the evolution of EPWP ratio below the structure (Figure 4.13a) and in the free-field (Figure 4.11a), it has been observed that the EPWP ratios below the structure (for both homogeneous and heterogeneous soil) are smaller than those recorded at similar depth in the free-field. This is believed to be due to higher initial effective stress below the structure.

Settlement of the structure footings were also monitored during the tests. Recorded settlements of the building top in test 1 are shown in Figure 4.14. In the figure, *L1* and *L2* are representing the settlements of two strip footings during earthquake. Similar results for building settlements in test 2 and 3 (on heterogeneous soil) are shown

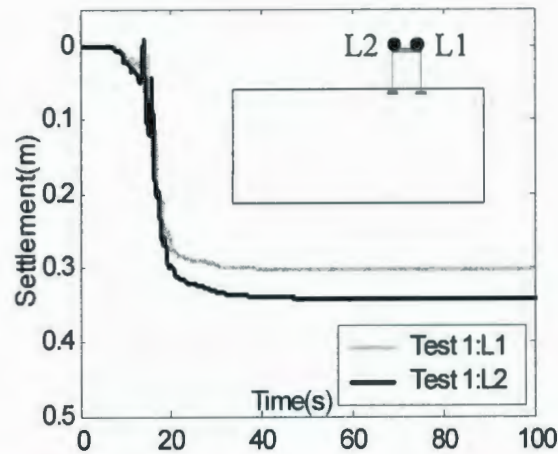


Figure 4.14: Recorded settlement of building in test homogeneous soil (PC1).

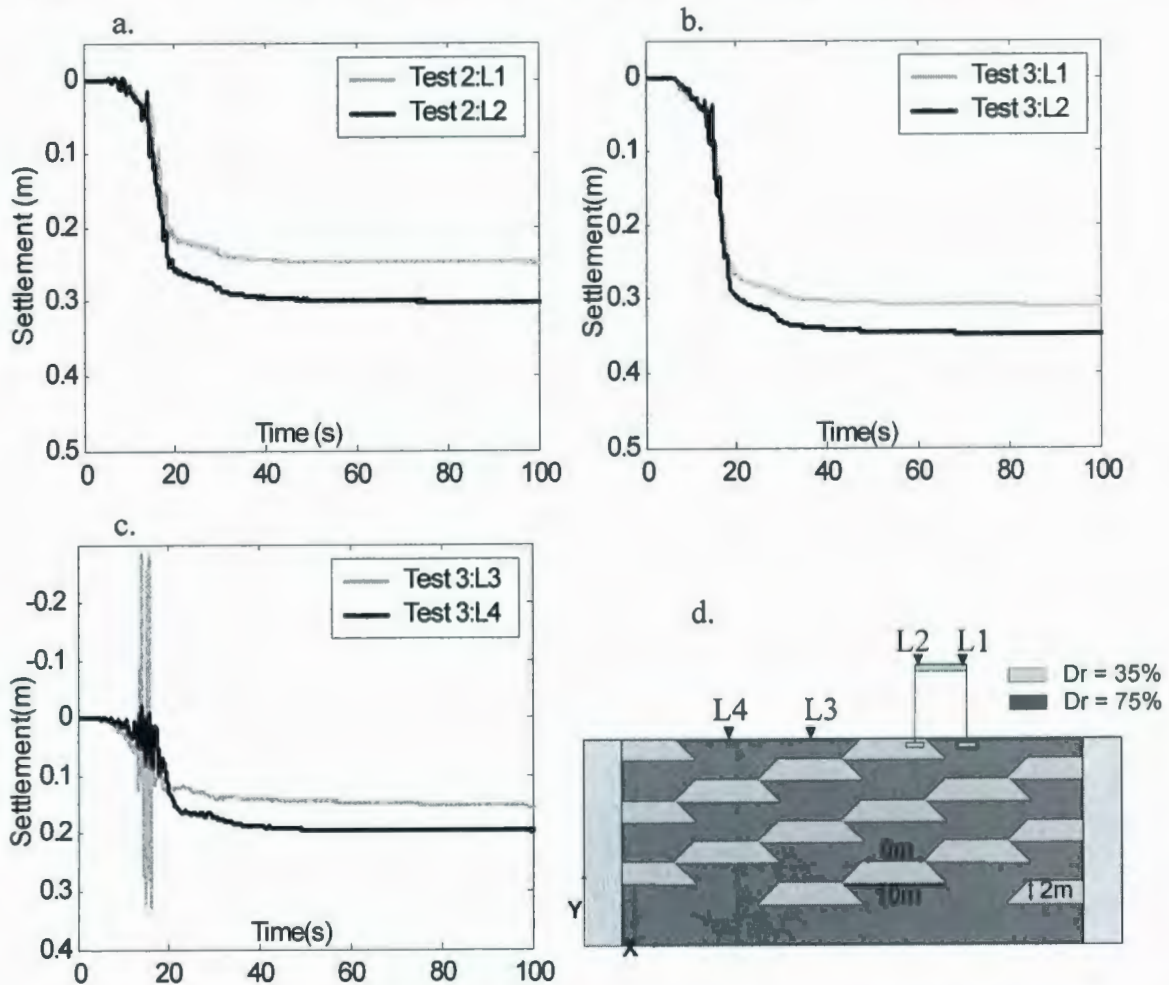


Figure 4.15: Recorded settlement of building in heterogeneous soil (test2 and 3). Downward settlement is positive and upward is negative. No LVDT were placed at L3 and L4 in test2.

in Figure 4.15. During test 3, 2LVDTs were placed in the free field area to measure the free field settlement/heave. Those recorded results are also shown in Figure 4.15c. However, after the test (during excavation of the model) it was observed that the glass plates attached at the end of those two LVDTs were sunk about 1-2mm. Therefore, those recorded settlements at *L3* and *L4* were affected due to sinking of those glass plates.

Vertical and horizontal components of the applied input motion were recorded using the accelerometers at the centrifuge shaker platform. One vertical accelerometer was installed on the centrifuge box platform to measure any acceleration in vertical direction generated during shaking. A second vertical accelerometer was placed at the foundation level in the free field to record the vertical acceleration at that level. The measured acceleration time histories in test 1 (on homogeneous soil) at different locations in the model are shown in Figure 4.16. Similar measurements in test 3 are shown in Figure 4.17. Unfortunately, no acceleration was recorded during test 2 because of a problem in the data acquisition card. The acceleration records at *A7* and *A8* (where soil is liquefied) showed large high-frequency acceleration spikes during the strong ground motion. These spikes are coincident with the negative pore pressure spikes during the strong ground motion, and have been termed as de-liquefaction shock waves by Kutter and Wilson (1999). Earlier, in centrifuge model tests, various researchers have reported this type of acceleration spikes associated with the onset of dilation (Dobry et al., 1995; Fiegel and Kutter, 1992; Kutter and Wilson, 1999) for uniform and layered soil deposit. However at larger depth (*A5*) these dilation spikes are not very significant. The results of the centrifuge tests also showed the amplification of the earthquake energy when seismic waves travel through soil. Figure 4.18 shows the comparison of the Arias Intensity (Arias,

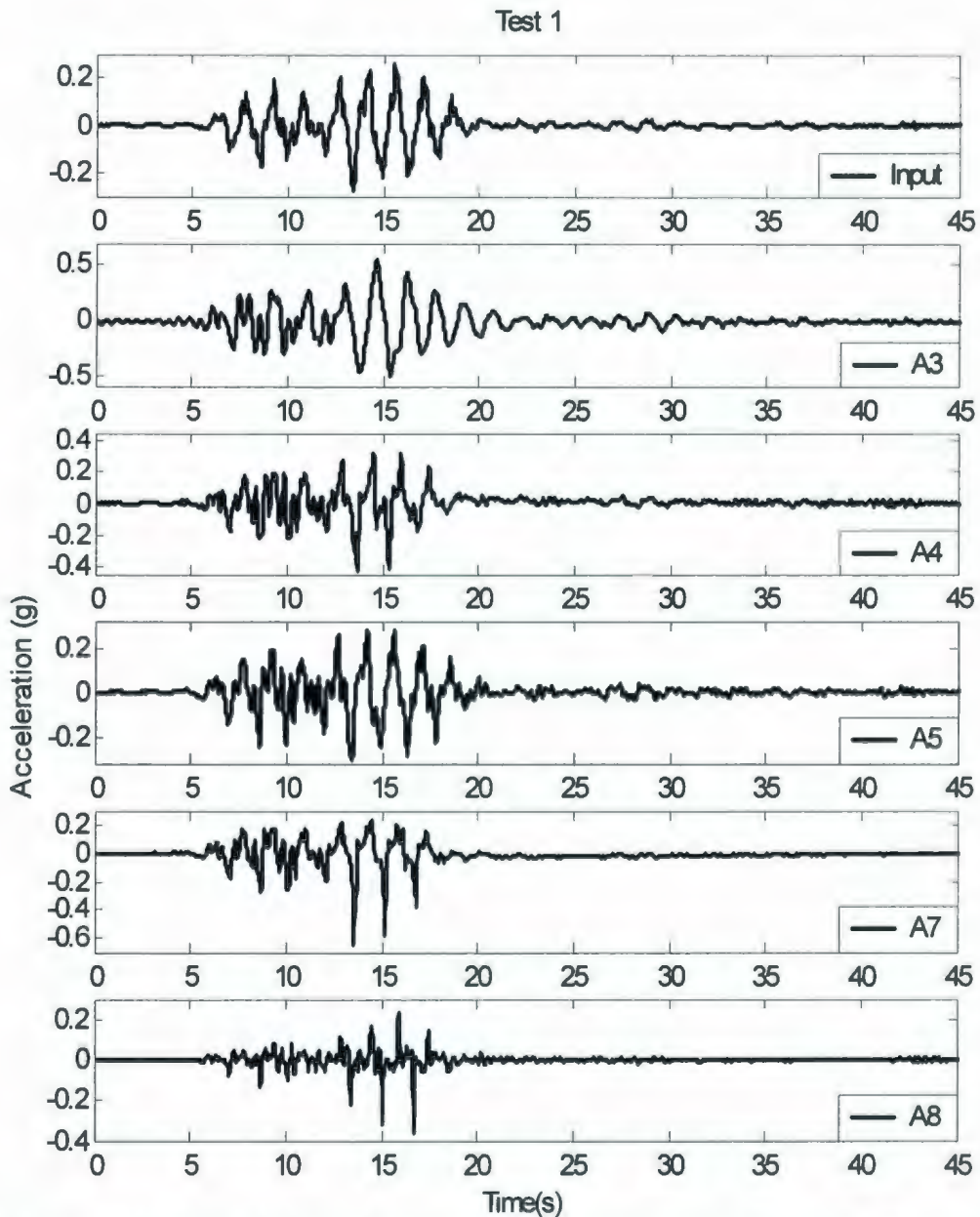


Figure 4.16: Recorded accelerations in homogeneous soil (test1). Transducer locations are shown in Figure 4.2. There was no accelerometer at A6 in test1. A2 does not record anything due to connection problem.

1970) evolution with time between homogeneous (test 1) and heterogeneous soil (test 3) in the free field. From the results shown in Figure 4.18a (input vs. A5) and 4.18b (input vs. A7) it is obvious that input motion is amplified more in homogeneous soil than in heterogeneous soil. The comparison of Arias Intensity evolution with depth during the

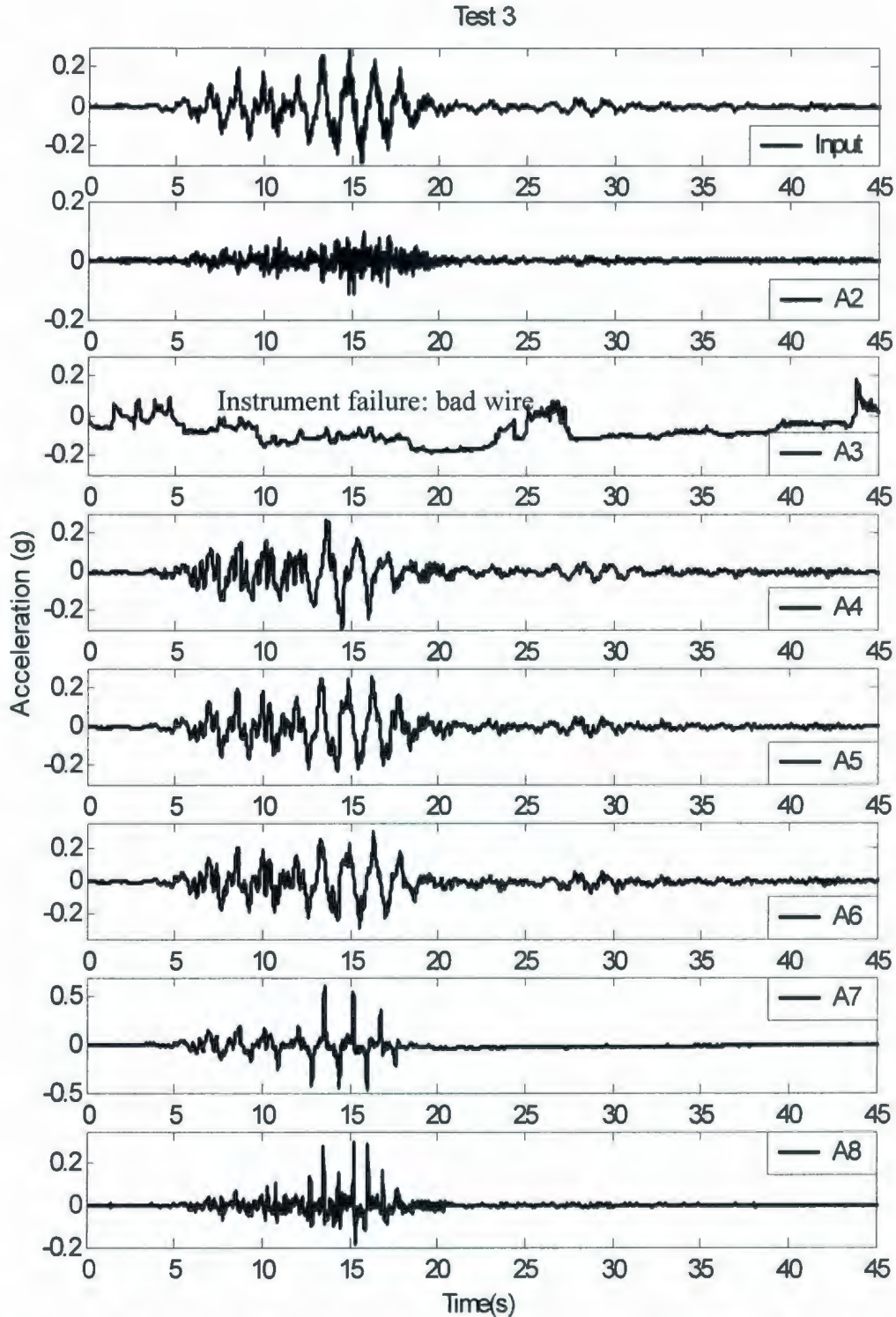


Figure 4.17: Recorded accelerations in heterogeneous soil (test3). No acceleration time histories were recorded during test2 due to a problem in data acquisition system. Transducer locations are shown in figure 4.2.

tests on uniform and variable soil deposits is shown in Figure 4.19. Although, the

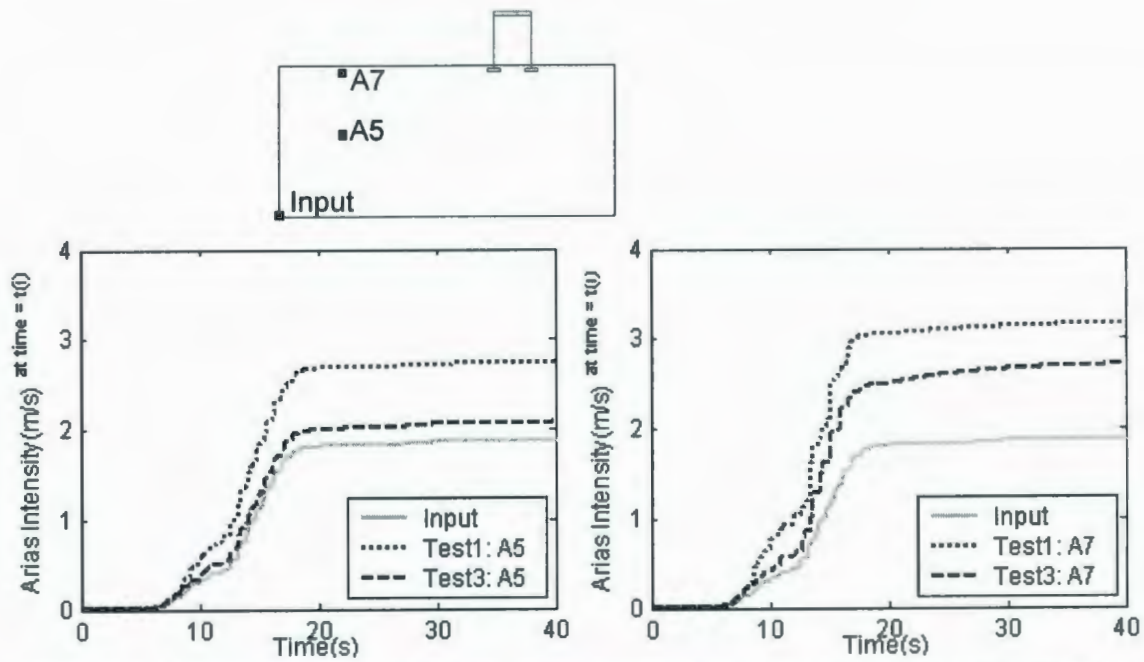


Figure 4.18: Comparison of Arias Intensity evolution with time in the free field between homogeneous and heterogeneous soil: a. Mid depth: A5; b. Near surface: A7.

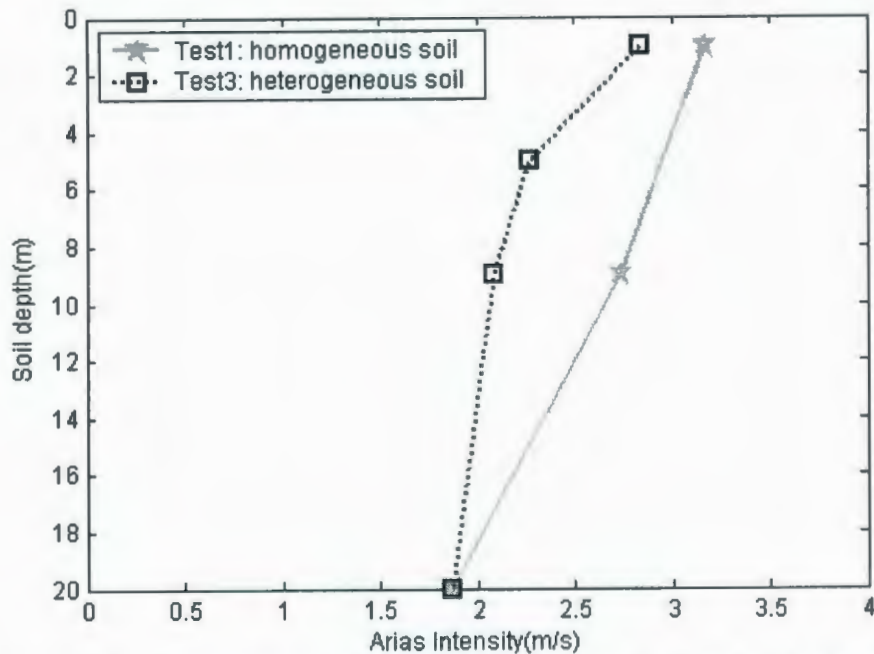


Figure 4.19: Comparison of Arias Intensity variation (with depth) in the free field between homogeneous and heterogeneous soil. Depths are at prototype scale. Arias Intensities are calculated until 45s.

heterogeneous soil deposit was on an average denser than the homogeneous soil, Arias Intensity amplification was lower than that of the uniform soil, due to higher EPWP build-up in the heterogeneous soil.



Picture 12: Top view of the model failed during saturation.

4.7. Difficulties and Sources of Error during the Centrifuge Tests

This is a difficulty faced during the series of centrifuge tests:

- **Model failure during saturation:** Two models failed during saturation due to air leak inside the model through an invisible opening on the side wall of the box. The top-view of one of the failed model is shown in Picture 12. After closely observing the reason for failure, it was noticed that there was a small crack in the bottom corners of side wall. Although, pore fluid was not coming out, air was entering through that small opening while the model was under vacuum during saturation. The evidence of soil disturbance

(cracks in the top surface) was found in those failed models. It was assumed that this air leak in the sidewall of the container caused this disturbance in the saturated soil model. This problem was solved by changing the centrifuge box before doing test 2 and 3.

Apart from this difficulty, there are various potential sources that might contribute errors in the measured responses. Some of them are discussed below:

- **Sample disturbance:** Although the tests were performed with care, there are a few sources which might cause disturbance in the sample. One major source is during transportation of the model from laboratory to the centrifuge arm. A pallet jack and a forklift were used for this purpose. Another source of error is during the saturation of model under vacuum. However, during these series of tests, average soil depths were measured before and after saturation. It showed that there were no sample disturbances during saturation (soil depth before and after saturation was the same). In heterogeneous soil, loose pockets were built first; and then the dense soil layer was prepared by filling remaining area in a horizontal layer with dense soil. This might cause slight densification in the loose pockets. Localised soil disturbances are also possible while placing instruments. A cone penetration test was performed to identify the position of loose pockets. However, as it was mentioned earlier in sub-section 4.6.1, this cone was not able to identify the exact location of loose pockets. Therefore, it was not possible from cone test to directly quantify the amount of densification in loose pockets. Some other instruments (e.g., needle probe, resistivity probe) should be use during centrifuge tests to quantify the amount of densification in loose pockets.

- **Use of two different centrifuge containers:** After the first centrifuge test, two models failed during saturation because of leak on the container walls. Therefore, second

and third tests were performed using a new container. The use of two different containers might induce some variability in the results. However, the inside dimension of both the containers were the same. Therefore, it was assumed that this source of error is not significant for these series of tests.

○ **Pore fluid viscosity:** The viscosity of pore fluid is dependent on the fluid temperature, which is also dependent on the ambient air temperature. Pore fluid viscosity was measured before model saturation during each test. The target viscosity was 35cSt for these tests. However, the measured viscosity was 35 ± 4 cSt at a temperature of 20° C. But, the tests were done after another 6-7 days. Therefore, the variation in air temperature might have caused changes in the viscosity of pore fluid. However, no temperature reading was taken inside the model during testing; only the ambient air temperature was taken. Therefore, the exact fluid viscosity during the test can not be estimated. From the ambient air temperature (26, 20, 22° C during test 1, 2, and 3 respectively) inside the room, it is assumed that there was no significant influence of this factor on these tests results.

○ **g-level variation:** During the all three centrifuge tests, rotational speed was 111.9rpm. But, due to slight variation (0.1rpm) in rotational speed, the inertial acceleration can be slightly lower or higher (0.1g) than 70g. Again for a constant angular velocity, the g-level increases with the increase in radius of rotation, which results in a variation in the g-level through the depth of the model. This variation was estimated for all the tests and it was not significant (less than ± 0.5 g) in these tests. This might have induced very small error in the responses (e.g. settlements), because these test results are presented considering inertial acceleration level as 70g. For example, maximum total

settlement at left footing (during test 1) was recorded as 0.3m (considering g-level as 70g). If it is assume that there was an error of $\pm 0.5g$ in the centrifuge g level, then there is a $\pm 0.002m$ error in the reported results. This error is less than 1% and therefore not significant.

- **Instrument position:** The measured instrument positions (placed and excavated) for accelerometer, pore water pressure transducers and other length measurements in the model are assumed to be accurate within $\pm 1mm$. The movement of some of the transducer were measured during excavation of the model. Although the final location of each instruments were measured after the test, it is very difficult to determine the exact location of the transducer during earthquake shaking. It is depends upon the amount of consolidation settlements, the amount of EPWP build up in the model during earthquake, the amount of softening in the surrounding soil and the resulting slight movement of the transducer. This might induced some error in the test results. The maximum recorded movement of PPTs (those worked properly) during all three tests at model scale are: 4mm in test 1, 6mm in test 2 and 7mm in test 3. The results are presented here considering the locations of transducers at just before applying earthquake. The transducer location was verified, based on the total pore water pressure measured just before applying the earthquake motion. It was found those transducer movements happened during consolidation settlements. Therefore, the presented test results are not affected due to this source of error.

- **Error in LVDT reading:** The LVDTs were connected using cantilever steel plate holders. However at 70g that LVDT holder can bend slightly which might have induced some error in the settlement records. During test 3, 2 LVDTs were placed in the free field

area to measure soil settlement / heave. There were glass plates attached with the end of each LVDT rod. After the test, it was found that those plates were sunk about 1-2mm at model scale, which include some error in the measured free field settlements (L3 and L4).

- **Difference between target and applied motion:** As mentioned earlier, the centrifuge shaker at C-CORE is tuned first using a dummy load. Next, the model is loaded in the centrifuge bay by replacing the dummy load. If the dummy load is not same as the weight of the model, the real applied motion in that test may not always be the same as the desired target motion. Sometimes, slight difference in the applied motion might be present which might cause slight difference in the results between two tests while comparing. However, during these three reported tests, the dummy load in each test was same as the corresponding weight of the model. The difference between target and applied input motion was minimised in all the three tests. Therefore, the presented test results are not affected due to this source of error.

4.8. Summary and Conclusions

A series of centrifuge liquefaction tests were conducted to find out the seismic behaviour and liquefaction mechanism for heterogeneous soil. Two tests were performed on heterogeneous soil deposit and one test was performed on homogeneous soil deposit. The test on uniform soil was performed on a soil deposit with the soil relative density which is lower than the average relative density of heterogeneous soil deposit. The results such as EPWPs, accelerations, settlements were monitored and measured throughout the test duration.

Based on the detailed analysis of centrifuge test results, this study provided an explanation of two important behaviours. (a) From the study it is concluded that, although the average relative density of heterogeneous soil deposit was higher than that in homogeneous soil, liquefaction resistance was lower in heterogeneous soil than that in homogeneous soil. (b) The higher EPWP ratio generated in the free field compared to that below the structure showed that the presence of structure is causing higher liquefaction resistance in the soil.

Table 4.1: Structural Properties of different components of frame structure in model scale

Part	No. of component	Length (mm)	Width (mm)	Thickness (mm)	Volume (mm ³)	Density kg/ m ³	Mass (kg)	Figure
Strip footing	2	99.5	25.4	6.35	16048.355	7831	0.1257	Label as A in Picture 3
Beam with two columns	2	270.5 (100X2+70.5)	13	3.175	11164.888	7831	0.0874	Label as B in Picture 3
Slab	1	70.5	70.5	9.5	47217.375	7831	0.3698	Label as C in Picture 3
<p>Total mass of the structure (including welding and connector) = 0.8kg; Natural frequency of the structure=2.11Hz (Prototype), and 147.9Hz (Model scale)</p> <p>Bearing pressure below each footing=1.56kPa @1g, and 109.25kPa @70g</p>								

Table 4.2: Location of the transducers at prototype scale

Instrument Type	Label	Test 1				Test 2				Test 3			
		X (m)	Y (m)	Z (m)	Location / Soil type	X (m)	Y (m)	Z (m)	Location / Soil type	X (m)	Y (m)	Z (m)	Location / Soil type
Pore pressure transducer	P1	-	-	-	-	-	-	-	-	36.5	17	12	Dense
	P2	36.8	15	9	Medium	36.5	15	12	Loose	36.5	15	8	Loose
	P3	36.8	11	6	Medium	36.5	11	8	Dense	36.5	11	12	Dense
	P4	-	-	-	-	-	-	-	-	36.5	9	8	Loose
	P5	13.8	17	7	Medium	13.6	17	7	Dense	13.6	17	7	Dense
	P6	13.8	15	3	Medium	13.6	15	3	Loose	13.6	15	3	Loose
	P7	13.8	11	7	Medium	13.6	11	7	Dense	13.6	11	7	Dense
	P8	13.8	9	3	Medium	13.6	9	3	Loose	13.6	9	3	Loose
	P9	-	-	-	-	-	-	-	-	13.6	17	17	Dense
	P10	-	-	-	-	-	-	-	-	13.6	15	13	Loose
	P11	-	-	-	-	-	-	-	-	13.6	11	17	Dense
	P12	-	-	-	-	-	-	-	-	13.6	9	13	Loose
LVDT	L1	36.3	26	9	Structure	36.1	26	12	Structure	36.1	26	12	Structure
	L2	32.3	26	5	Structure	32.1	26	8	Structure	32.1	26	8	Structure
	L3	-	-	-	-	-	-	-	-	21	20.2	15	Free field
	L4	-	-	-	-	-	-	-	-	13.6	20.2	15	Free field
Accelerometer	A1	Base of the box (Input)				Base of the box (Input)				Base of the box (Input)			
	A2	Base of the box (vertical)				Base of the box (vertical)				Base of the box (vertical)			
	A3	36.8	26	7	Str.(top)	36.5	26	10	Str.(top)	36.5	26	10	Str.(top)
	A4	36.8	19	12	Str. (Base)	36.5	19.3	10	Str. (Base)	36.5	19.3	10	Str. (Base)
	A5	11.8	11	5	Medium	22.8	13.7	5	Dense	11.6	11	5	Dense
	A6	-	-	-	-	-	-	-	-	11.6	15	15	Loose
	A7	11.8	19	5	Medium	11.6	19.1	5	Dense	11.6	19	5	Dense
	A8	15.6	17.6	5	Medium	15.5	17.8	5	Dense	11.6	17.6	5	Dense

Notes: Loose → Loose soil (Dr=35%), Medium → Medium dense soil (Dr=55%), Dense → Dense soil (Dr=75%); str.(top) → Top of the structure

Table 4.3: Specifications of the instruments used in centrifuge tests (after C-CORE, 2005)

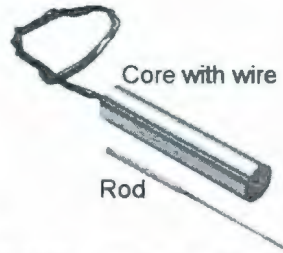
Pore pressure transducer	Specification	Accelerometer	Specification	Linear Variable Differential Transformers (LVDT)	Specification
Dimensions	6.5mm X 11.7mm	Dimensions	7.1mm X 18.8mm	Working range	± 25.4mm
Weight	29.8gms with 15ft cable	Weight	1.8gms	Maximum working range	± 38.1mm
Excitation voltage	5 V	Voltage sensitivity	10 mV/g ± 5%	Frequency response	DC to 100Hz
Output voltage	75 mV	Measurement range	±500g peak	Input	6 to 30 VDC
Output impedance	1000 ohms	Frequency range	1 to 10000 Hz ± 5%	Nominal output	4.6 to 24.8 VDC
Operating temperature	-5 ⁰ to 250 ⁰ F	Operating temperature	-65 ⁰ to 250 ⁰ F	Operating temperature	-54 ⁰ to 121 ⁰ C
Mechanical shock	1000g for 1ms in each axes will not affect calibration	Mounted resonance frequency	>70 kHz	Output impedance	5600 ohms
Resolution	Infinite	Sensing element	Quartz shear	Resolution	Infinite
Figure	Model: Druck PDCR 81 	Figure	Model: PCB Piezotronic 353B18 	Figure	Model: Trans-Tek series 240 

Table 4.4: Location of the pore pressure transducers, LVDT, and accelerometers in test 1

Type	Name	Before test (model scale)			After test (model scale)		
		X (mm)	Y (mm)	Z (mm)	X (mm)	Y (mm)	Z (mm)
Pore Pressure Transducer	P2	526	214	129	526	214	125
	P3	526	157	86	526	157	78
	P5	197	243	100	197	243	100
	P6	197	157	43	197	157	45
	P7	197	214	100	197	230	88
	P8	197	129	43	197	125	40
LVDT	L1	519	371	129	519	371	129
	L2	461	371	71	461	371	71
Accelerometer	A3	526	371	100	526	371	100
	A4	526	271	170	525	271	170
	A5	169	157	71	169	157	88
	A7	169	271	71	169	271	71
	A8v	226	251	71	226	251	71

Table 4.5: Location of the pore pressure transducers, LVDT, and accelerometers in test 2

Type	Name	Before test (model scale)			After test (model scale)		
		X (mm)	Y (mm)	Z (mm)	X (mm)	Y (mm)	Z (mm)
Pore Pressure Transducer	P2	522	213	172	527	207	172
	P3	522	157	115	522	155	115
	P5	194	242	100	200	237	100
	P6	194	214	43	196	210	43
	P7	194	157	100	190	163	95
	P8	194	130	43	194	129	43
LVDT	L1	515	371	172	515	371	172
	L2	458	371	115	458	371	115
Accelerometer	A3	522	371	144	522	367	144
	A4	522	275	144	522	271	144
	A5	325	195	71	325	196	81
	A7	165	273	71	166	266	71
	A8v	222	251	71	222	247	71

Table 4.6: Location of the pore pressure transducers, LVDT, and accelerometers in test 3

Type	Name	Before test (model scale)			After test (model scale)		
		X (mm)	Y (mm)	Z (mm)	X (mm)	Y (mm)	Z (mm)
Pore Pressure Transducer	P1	522	243	172	522	242	172
	P2	522	215	115	522	215	115
	P3	522	157	172	522	156	172
	P4	522	129	115	522	128	115
	P5	194	243	100	194	242	100
	P6	194	215	43	194	219	43
	P7	194	157	100	194	164	100
	P8	194	129	43	194	136	43
	P9	194	243	243	194	238	243
	P10	194	215	186	194	215	186
	P11	194	157	243	194	163	236
	P12	194	129	186	194	129	191
LVDT	L1	515	371	172	515	371	172
	L2	458	371	115	458	371	115
	L3	300	287	214	300	287	214
	L4	194	287	214	194	287	214
Accelerometer	A3	522	371	144	522	371	144
	A4	522	275	144	522	275	144
	A5	165	157	71	165	166	71
	A6	165	215	214	165	218	214
	A7	165	271	71	165	271	71
	A8v	222	251	71	222	248	71

CHAPTER 5

Liquefaction Mechanisms for Heterogeneous Soil

5.1. Introduction

In this part of the research, liquefaction mechanism in heterogeneous soil was studied and explained. Some preliminary numerical studies were performed using finite element computer code Dynaflow to identify the liquefaction mechanism. In recent years some numerical and experimental research, closely related to this study, has been reported. Brief discussions about those studies are presented in Section 5.2. Next, a series of three geotechnical centrifuge tests were performed in this research: one on homogeneous soil and two on heterogeneous soil. The centrifuge test results were already discussed in detail in Chapter 4. The test on uniform soil is performed on a soil deposit with the soil relative density which is lower than the average relative density of heterogeneous soil deposit. The results, such as EPWP, accelerations, and settlements are monitored and measured at some predetermined locations throughout the test duration. However, it is very difficult and expensive to monitor all these responses everywhere in the model. Therefore, the numerical model is calibrated and validated from the centrifuge test results on uniform and variable soil. The calibration and validation of the numerical model are discussed in Section 5.3. Next, the liquefaction mechanism in heterogeneous soil is studied in more detail using the numerical simulations. The explanation of liquefaction mechanism is presented in Section 5.4. Some qualitative and quantitative guidelines are provided in Section 5.5.

5.2. Liquefaction in Heterogeneous Soil: Preliminary Studies

As mentioned in Chapter 2, Konrad and Dubeau (2002) conducted undrained cyclic triaxial tests on fine uniform Ottawa sand, uniform silica silt and layered soil (sand and silt layers). Experimental results in terms of the number of cycles to liquefaction, corresponding to a cyclic stress ratio $CSR=0.166$ are shown in Table 5.1. Chakraborty et al. (2004a) performed a detailed numerical analysis of the behavior of non-homogeneous soil samples studied by Konrad and Dubeau (2002) using finite element code DYNFLOW. The multi-yield plasticity soil constitutive model (Prevost, 1985) implemented in DYNFLOW was calibrated first, based on the experimental results obtained by Konrad and Dubeau (2002) for uniform dense sand and uniform silt samples. The cyclic undrained triaxial test on samples made of one sandwiched silt layer in dense sand was simulated next. The number of cycles to liquefaction resulting from the numerical analyses for $CSR=0.166$ are presented in Table 5.1 for comparison. Although the number of cycle causing liquefaction was not exactly the same as the experimental values, the results of numerical simulations exhibit the same tendency observed in the experiments. Chakraborty et al. (2004a) analyzed the mechanism by which a sample made of two different soils liquefies faster than each of the soils tested separately in uniform samples. The explanation, resulting from a detailed analysis of the numerical results, was that water was squeezed out from the more deformable silt layer and injected into the neighbouring dense sand. Figure 5.1 illustrates the predicted relative movement at two interface nodes in the layered sample. Predicted relative movement (water-solid) at the sand-silt interface in layered triaxial sample indicates that water was squeezed out from the silt layer and injected into dense sand thus causing a reduction in liquefaction strength. This phenomenon is similar to injecting water into a sample during undrained triaxial

tests as reported by Atigh and Byrne (2004) and Vaid and Eliadorani (1998). It is important to note that, as concluded from the numerical simulations, the dense sand liquefied first in the sandwiched samples, while this material was found to be more resistant to liquefaction than the silt when tested in uniform samples.

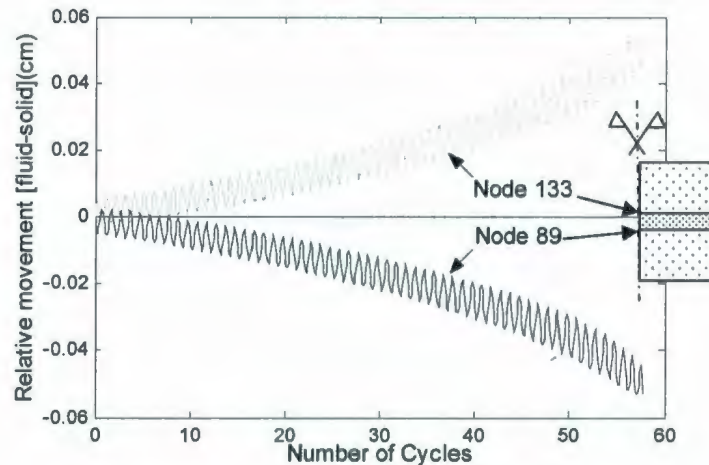


Figure 5.1: Predicted relative vertical displacement (water-solid) at the interface of silt and sand in the layered sample. Upward (vertical) relative displacements are positive.

Regarding liquefaction mechanisms of soil deposits involving one type of soil material but with spatially variable strength, Ghosh and Madabhushi (2003) performed a series of centrifuge experiments to analyze the effects of a localized loose pocket/layer in a dense sand deposit subjected to seismic loads. It was observed that EPWP is generated first in the loose sand patches, and then the water migrates into the neighbouring dense sand, reduces the effective stress and softens the dense soil. Based on these centrifuge experimental results, Popescu et al. (2006) calibrated a numerical model implemented in DYNAFLOW and reproduced numerically two of the centrifuge experiments (tests BG4 and BG5). A loose layer (shown by 2 thick black lines in Figure 5.2c) was present in the dense soil deposit in test BG4 and a single loose pocket (shown by dark patch below foundation in Figure 5.2c) was

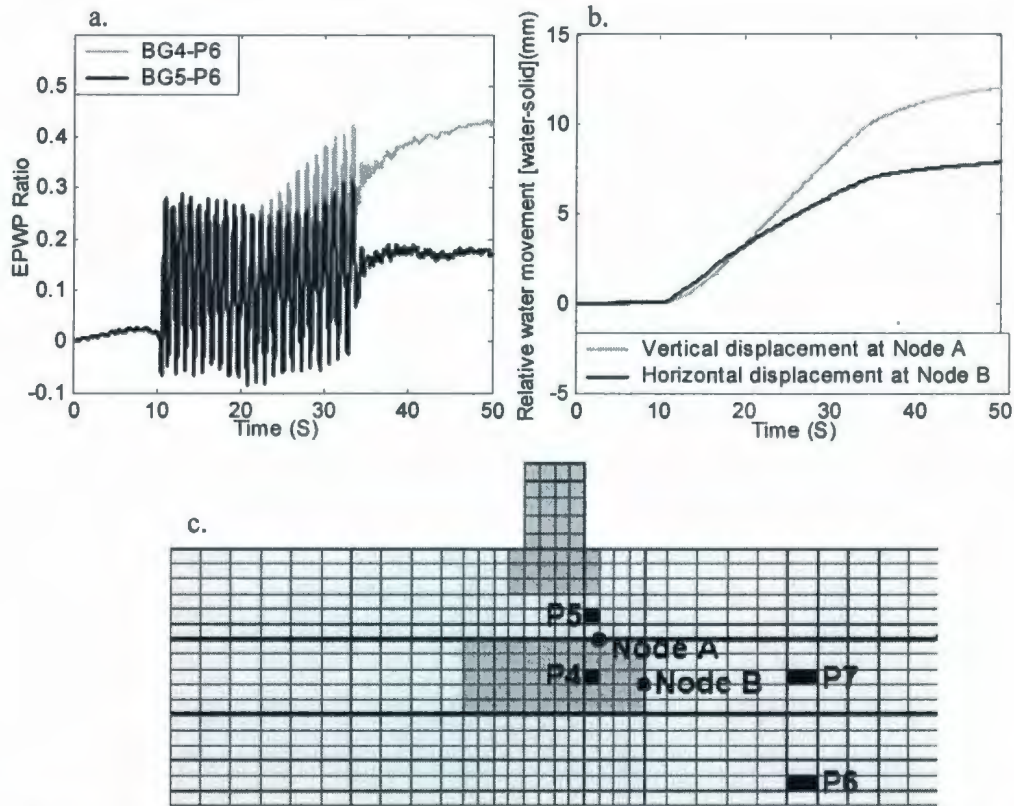


Figure 5.2: Effect of loose pocket/layer inside dense soil deposit: a. Comparison of computed excess pore water pressure (EPWP) ratios in the free field (dense sand) for tests BG4 and BG5; b. Computed relative movement of water with respect to the solid phase at the interface between loose and dense sand in test BG5. Positive displacements are upward (vertical) and left to right (horizontal); c. Finite element mesh with transducer locations (after Popescu et al., 2006).

present in test BG5. Computed EPWP ratios at the same location (transducer P6 in dense sand in the free field) for tests BG4 and BG5 are shown in Figure 5.2a. An increase in residual EPWP ratio from about 0.2 in test BG5 to about 0.4 in test BG4 is attributed to water migration from the loose sand layer, present in the free field close to location P6 in test BG4, but not present in the free field in test BG5. The effects of water migration with gradual increase in EPWP in test BG4 as compared to test BG5 can be observed starting at time $T=20$ sec. Simulation of water migration from loose to dense sand by the numerical model is illustrated in Figure 5.2b by computed time histories of relative water displacements (relative to the solid phase) at two locations

at the interface between loose and dense sand in test BG5. It has been concluded from the study that the finite element model was able to simulate the observed phenomena and the pore pressure gradient created from the initial liquefaction of loose sands leads to migration of water in the adjacent dense sands and makes the dense soil susceptible to liquefaction.

To quantify the effects of alternate loose and dense soil patches, as encountered in natural soil deposits, a hypothetical chess board-type soil-structure system (Figure 5.3c) was also analyzed by Popescu et al. (2006). The soil was made of a chess board-like pattern of alternating loose (relative density, $D_r=45\%$) and dense ($D_r=85\%$) sands. The results were also compared to the uniform soil deposits. Figure 5.3a shows the evolution of the EPWP ratio in two adjacent elements of the chess-board like variable soil, one located in a loose soil patch (element 1) and the other in dense sand (element 2). From the results it was obvious that EPWP generation in loose sand pockets was faster than that in dense soil. The effects of water migration were also evident. The dense sand in the chess-board deposit reaches about 95% EPWP ratio, while at the same location in a uniform dense sand deposit the maximum EPWP ratio is about 25% (shown in Figures 5.3b).

Popescu and Chakraborty (2006) continued the above mentioned studies with the main focus on pore water migration between loose and dense soils. Two different heterogeneous patterns were considered to study the effects of the number of loose pockets, as shown in Figure 5.4: a chessboard-like pattern of loose and dense sands (Figure 5.4a) and a dense sand deposit with isolated loose sand pockets (Figure 5.4b). The evolution of EPWP ratio at locations *A* and *B* in heterogeneous soil is compared

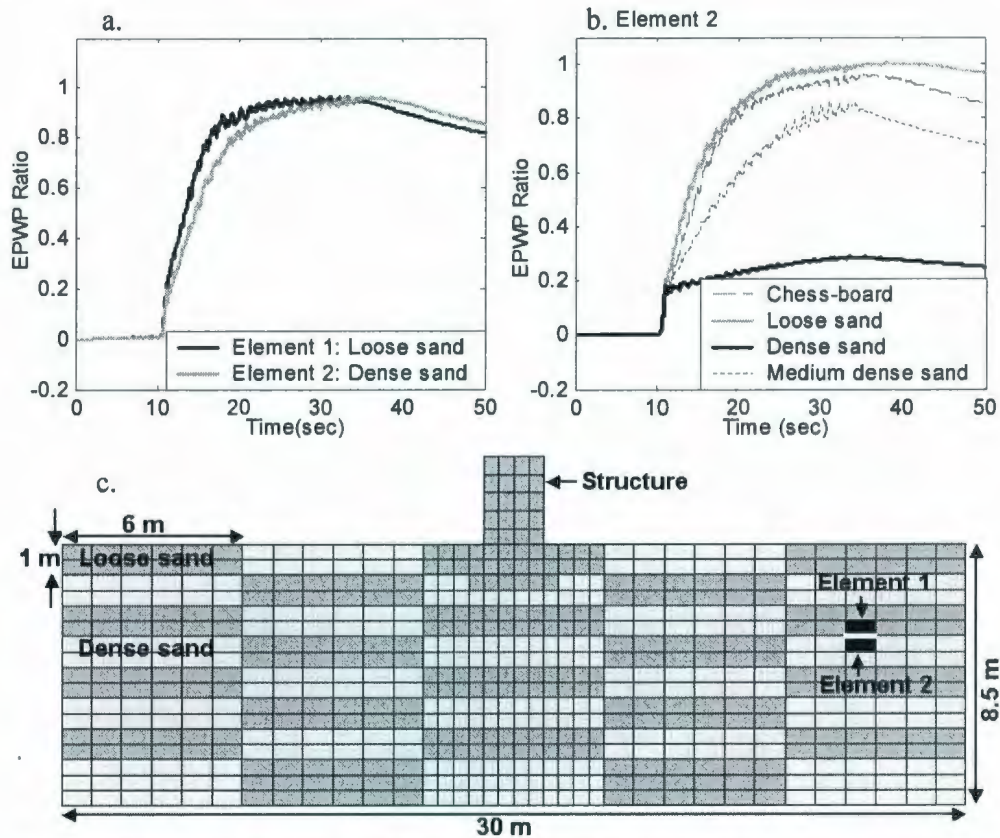


Figure 5.3: a. EPWP ratio time histories for the chess-board type heterogeneous soil computed at two adjacent locations in the free field (one in the loose soil: element 1, and the other in the dense soil: element 2); b. EPWP ratio in the free field in element 2; c. Finite element mesh (after Popescu et al., 2006).

in Figure 5.4c and d with computed EPWP ratios at the same locations in homogeneous soil deposits with various relative densities: (1) loose sand, with $D_r=45\%$ - same as the loose pockets in heterogeneous soil; (2) dense sand, with $D_r=85\%$ - same as the dense soils in heterogeneous soil; (3) medium dense sand, with $D_r=65\%$ - corresponding to the average relative density of the chessboard-like heterogeneous soil. The computed results are shown for the first 60 seconds of the analysis. The EPWP ratios calculated in the chessboard-like heterogeneous soil (dotted curves in Figure 5.4), are larger than those calculated in the medium dense soil uniform soil at all locations, including those in dense sands. At some locations (e.g., elements *A*) the EPWP ratios in the heterogeneous soil were closer to those computed

in loose sand than those computed in medium dense sand, which has an equivalent relative density with the heterogeneous soil. The general conclusion of these studies was that more EPWP is generated during cyclic loading in a heterogeneous soil deposit than in the corresponding uniform soil having geo-mechanical properties equivalent to the average properties of variable soil.

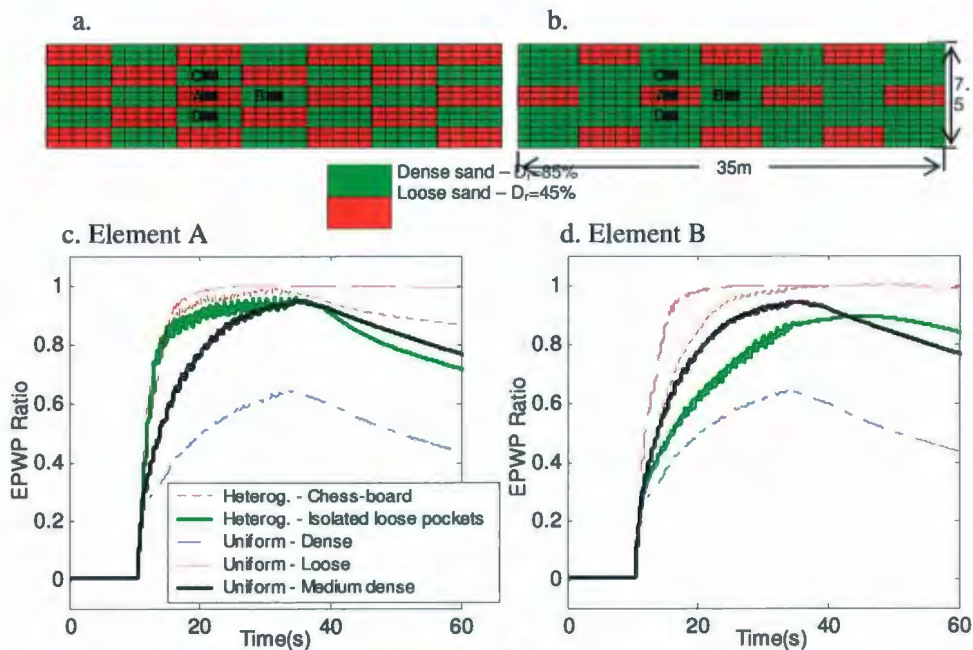


Figure 5.4: a. Finite element mesh: chess-board-like alternating loose and dense sands; b. Finite element mesh: isolated loose sand pockets in dense sand; Evolution of excess pore water pressure (EPWP) ratio with respect to the initial effective vertical stress at 2 locations in heterogeneous and uniform soil: c. Element A; d. Element B (after Popescu and Chakraborty, 2006).

5.3. Numerical Modelling of Centrifuge Tests

After the preliminary studies (those discussed in last section), a series of centrifuge tests were performed (results were discussed in Chapter 4) to investigate the liquefaction mechanisms for heterogeneous soil. Investigating liquefaction mechanisms for heterogeneous soil involves observing EPWP build up and water migration between neighbouring soil pockets with different relative densities. As it is

not practical to monitor experimental results at very close locations in the model during centrifuge tests, a numerical model was calibrated and validated based on centrifuge test results. The numerical model has been developed using the finite element computer code DYNAFLOW. The calibration of different parameters of the multi-yield plasticity soil constitutive model used in DYNAFLOW is discussed in the next section.

5.3.1. Calibration of the Numerical Model

The soil constitutive parameters of the multi-yield plasticity model can be divided into state parameters (obtained from general laboratory soil tests), low-strain elastic parameters (describing elastic deformability), yield and failure parameters (used for generating the nested yield surfaces), and dilation parameters (used to calculate the plastic volumetric strain). All the multi-yield plasticity model parameters except the dilation parameter (X_{pp}) can be estimated from results of conventional field (e.g. CPT, SPT) or laboratory soil tests. The dilation parameter, X_{pp} , is obtained by means of liquefaction strength analysis based on curve-fitting the experimental liquefaction strength curve using element tests (numerical simulations of undrained cyclic triaxial tests in this study).

Uthayakumar and Vaid (1998) identified the Fraser River sand grains as sub-angular to sub-rounded. Castro (1969) reported friction angle values for sub-rounded to sub-angular fine uniform sand with a relative density 30% in the range 31° to 34° and for a relative density of 80% between 37.25° and 41.25° . The friction angle at failure values reported in the literature for Fraser River sand is very scattered. As reported by Lunne et al. (1997), the *in-situ* friction angle of the Fraser River sand is in the range of 32 to 39 degrees. The results of monotonic laboratory tests performed at

University of British Columbia (UBC) show a very low friction angle of 27° for 40% relative density Fraser River sand (EIDMSL, 2003). The friction angle at failure, calculated from the results of the monotonic undrained triaxial tests performed on very loose ($D_r=20\%$) Fraser River sand by Vaid et al. (2001), is about 35° in compression and 39° in extension. A friction angle value of 37° has been reported by Vaid and Eliadorani (1998) for very loose Fraser River sand ($D_r=11\%$). Based on all the above results, a range of friction angle at failure values of 37° - 43° (shown in Table 5.2) were selected in the analyses for 30-80% relative densities of the soil. Linear interpolation (as reported by Castro, 1969) was used for calculating friction angle for the intermediate values of relative densities.

From earlier research on Fraser River sand (Vaid and Thomas, 1995) and other sands (Vaid and Chern, 1985) it has been observed that the value of **the dilation angle (in DYNAFLOW and in the thesis), referred also as critical state angle and as phase transformation angle**, does not depend upon the mode of loading, type of deformation or relative density. Based on laboratory tests performed under different conditions, a value of 34° has been obtained for Fraser River sand by Vaid et al. (2001). Based on a series of undrained triaxial compression test on loose ($D_r=11\%$) Fraser River sand specimen, Vaid and Eliadorani (1998) obtained a phase transformation angle of about 32° . Uthayakumar and Vaid (1998) reported a phase transformation angle value of 33° . The physical properties of the Fraser River sand used in this study are similar to the one reported by Vaid et al. (2001). Therefore, a phase transformation angle of 34° has been selected in this study for all relative densities.

In DYNAFLOW, the dependence of the low strain elastic shear (G) and bulk moduli (B) on the effective mean normal stress is taken as (DYNAFLOW, 2002):

$$G = G_0 \left(\frac{P}{P_0} \right)^n \quad \text{and,} \quad B = B_0 \left(\frac{P}{P_0} \right)^n \quad (5.1)$$

where p_0 is a reference effective confining stress, G_0 and B_0 are the low strain shear and bulk moduli values corresponding to p_0 , and n is a power exponent. A typical value of $n=0.5$ was recommended by Richart et al. (1970) for cohesionless soils.

In this numerical model, low strain shear modulus corresponds to the assumed range of soil deformation within the first yield surface. Two different symbols are used here for shear modulus: G_{\max} , shear modulus at very low strains (0.0001% to 0.01%); and G_0 , shear modulus at low strain (0.05 – 0.1%). Based on the results from resonant column test or *in-situ* shear wave velocity measurements, different correlations are derived by different researchers for calculating G_{\max} . The low strain shear modulus (G_0) can be estimated for 0.05% strain level using modulus degradation curve and G_{\max} value. Ishibashi and Zhang (1993) suggested that G_{\max} values can be utilized in computations with a rather high degree of confidence when actual measurements are not available. However, for Fraser River sand at 30% relative density, a value of shear modulus of about 28 MPa at a shear strain of 0.05% was inferred from the results of isotropically consolidated triaxial tests performed by Vaid and Eliadorani (2000). This low strain shear modulus value was used for estimating G_0 at other relative densities by extrapolating the value for 30% relative density using following relation (based on Belloti et al., 1986):

$$\frac{G_1}{G_2} = \frac{e^{1.39D_{r1}}}{e^{1.39D_{r2}}} \quad (5.2)$$

where G_1 is the low strain shear modulus at other relative density, G_2 is 28 MPa, D_{r1} is the other relative density (e.g. 40%, 70% etc) and D_{r2} is 30% relative density.

The typical ranges of Poisson's ratio for different types of sands are given in Table 5.3. For convenience in computer code implementation, Trautmann and Kulhawy (1987) presented the following relation:

$$\nu = 0.1 + 0.3\phi_{rel} \quad (5.3)$$

where $\phi_{rel} = \frac{(\phi - 25)}{(45 - 25)}$ = relative friction angle and its value is in between 0 and 1.

1. The Poisson's ratio used in this study for different relative densities (Table 5.2), were calculated using this relation. Those values are inside the recommended ranges mentioned in Table 5.3.

The parameter k_0 is used by DYNFLOW only for generating the deviatoric stress-strain backbone curves (e.g., Griffiths and Prevost, 1990) and the initial locations of yield surfaces in the stress space (Prevost, 1989). Its value depends on the type of consolidation (e.g., anisotropic or isotropic) employed in the laboratory soil tests used for calibrating the model parameters. In this study the dilation parameter (X_{pp}) is obtained based on the results from undrained triaxial tests done by Vaid et al. (2001) on anisotropically consolidated ($k_0=0.8$) Fraser River sand samples. Therefore, the coefficient of lateral stress was taken as 0.8 in the study.

The maximum deviatoric strain in compression, estimated from the drained triaxial test results reported by Eliadorani (2001) is about 10.67% for a Fraser River sample with a relative density of 27%. Chillarige et al. (1997) also documented drained triaxial test results on Fraser River sand, from which a very high (about 18%) maximum deviatoric strain can be calculated for very loose samples. Therefore, based on those test results a maximum deviatoric strain of 10% in compression and 8% in extension are considered for 30% relative density. The maximum deviatoric strains estimated for the other relative densities are shown in Table 5.2.

The coefficient of permeability is usually determined by performing constant and falling head permeability tests. Based on results of tests performed at UBC for 36 and 77% relative densities, the hydraulic conductivity values are calculated for other relative densities using following relation (based on Chapuis, 2004):

$$k_1 = k_2 \left(\frac{e_1^3}{(1+e_1)} \frac{(1+e_2)}{e_2^3} \right)^n \quad (5.4)$$

where e_1 , e_2 are the void ratios corresponding to k_1 and k_2 and n is calculated based on the coefficient of permeability results at 36 and 77% relative densities. All the estimated hydraulic conductivity values are modified next, to consider the effect of high viscosity fluid which was used in the centrifuge. This modification has been done using the fine tuning procedure (discuss later in Section 5.3.3) of the multi-yield surface plasticity model parameters.

After estimating all the other multi-yield plasticity parameters, the dilation parameter (X_{pp}) was estimated next by performing a liquefaction strength analysis as described by Popescu and Prevost (1993). This analysis is based on fitting the experimental liquefaction strength curve using finite element simulations of cyclic undrained triaxial tests (element tests). The dilation parameter (X_{pp}) was obtained based on the results from undrained triaxial tests done by Vaid et al. (2001) on anisotropically consolidated ($k_0=0.8$) Fraser River sand samples. This liquefaction strength curve was selected because it gave a set of parameters which mimic the centrifuge test results on uniform soil deposits (test 1) more accurately. The dilation parameter (shown in Table 5.2) was obtained based on the final number of cycles ($N_L=10$ in this case) required for liquefaction. A typical example of calculating X_{pp} from liquefaction strength curve and known soil relative density is shown in Figure 5.5.

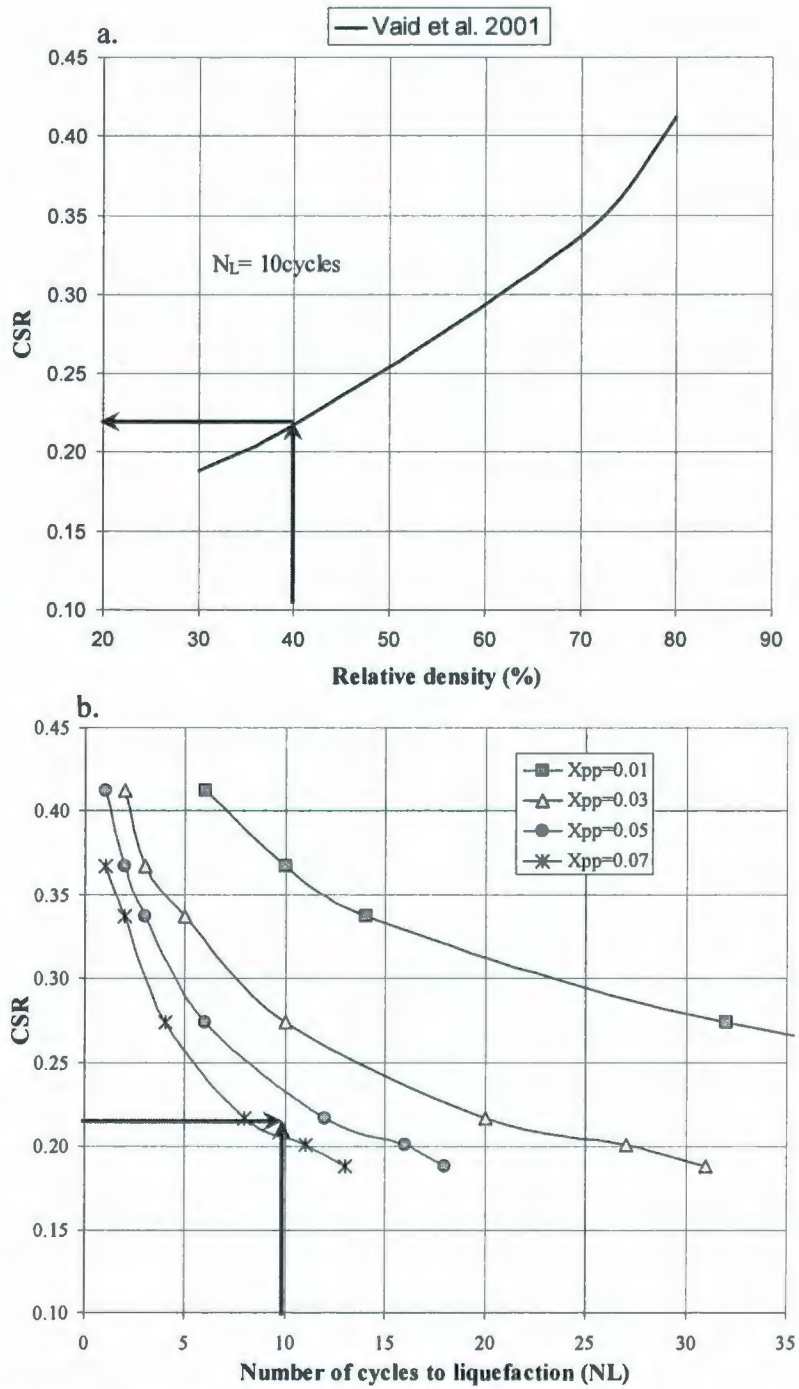


Figure 5.5: Liquefaction strength analysis: a. relation between soil relative density and cyclic stress ratio (CSR) which causes liquefaction in $N_L=10$ cycle (obtained from Vaid et al., 2001); b. illustrative example for calculating X_{pp} from element test. An example for calculating X_{pp} for 40% soil relative density is shown by arrows.

5.3.2. Finite Element Model

The finite element calculations were conducted in terms of effective stresses, using fully coupled solid-fluid equations and a multi-yield plasticity soil constitutive model for the treatment of saturated porous media. The structure and adjacent soil were analyzed using the plane strain assumption. A 20m deep, 44m long saturated sand deposit corresponding to the prototype scale dimensions of the centrifuge models was included in the analysis domain. The soil was discretized into two-phase bi-linear four node elements with four degrees of freedom (DOF) per node, two for solid phase and two for fluid phase kinematics. Finite element meshes used in the numerical simulation of centrifuge tests on homogeneous and heterogeneous soil together with the boundary conditions are shown in Figure 5.6. Smaller finite elements were used below the structure, to more accurately capture the stress gradients. The finite element dimensions were controlled in such a way that the locations of each pore water pressure transducer coincided with the mid point of an element, and accelerometer locations coincided with the node locations.

In the numerical model the structure was idealized as linear-elastic. The material properties are shown in Table 5.4. The two strip footings were modelled using one-phase bi-linear four node elements with two degrees of freedom per node, for the solid phase kinematics. The beams and columns were discretized using 2-node beam elements with three degrees of freedom per node (two for displacements and one for rotation). There were 36 beam elements used for modelling the frame structure. The beams and roof masses were applied as nodal masses on the horizontal beam at the first floor level. The beams and columns dimensions and mass densities were modified to model them using the plane strain assumption.

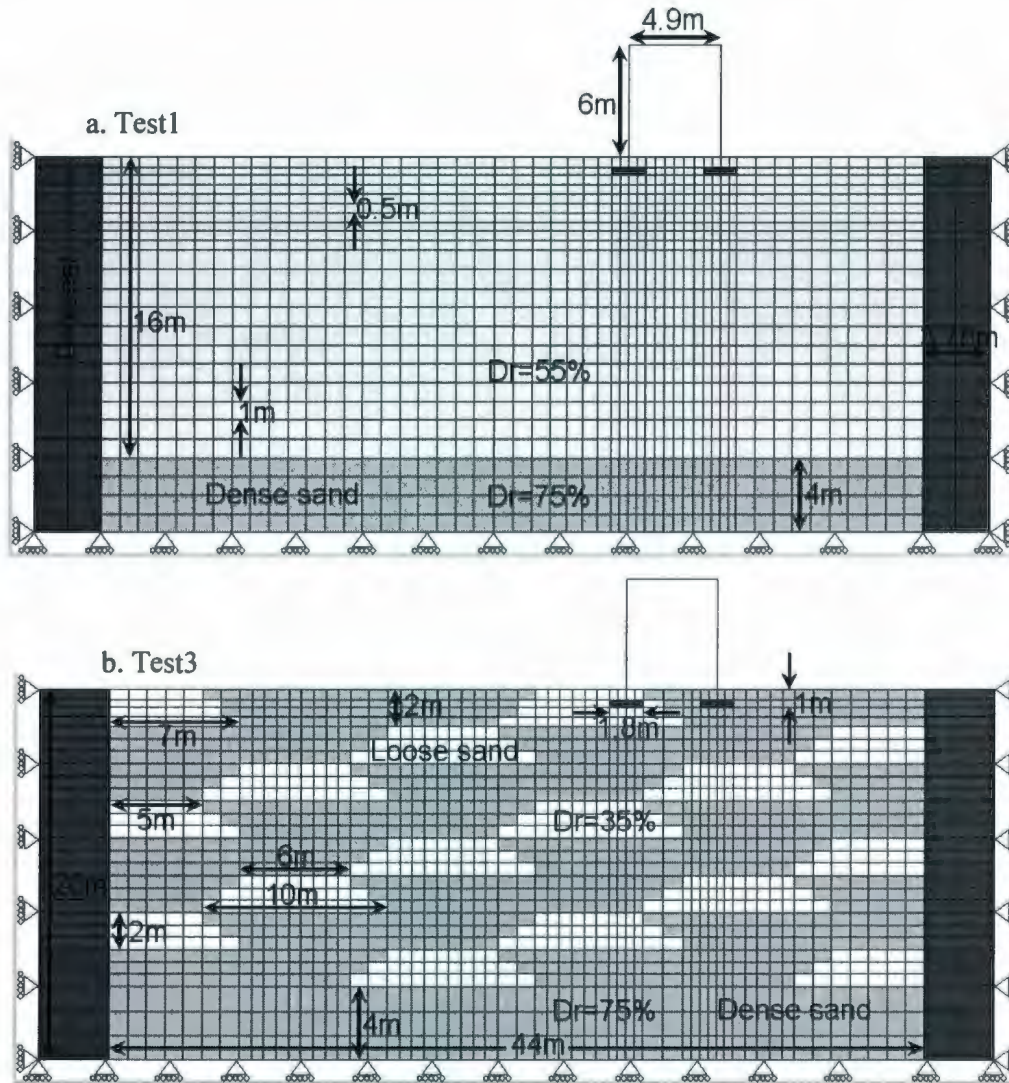


Figure 5.6: Finite element meshes used in the numerical simulation of centrifuge tests on homogeneous and heterogeneous soil.

The walls of the centrifuge box were rigid; therefore, the rigid boundary was applied for the finite element mesh boundaries of the analysis domain. The input ground motion was applied in a horizontal direction at the base and lateral boundary of the analysis domain, similar to the centrifuge experiment performed in a rigid box. Use of a rigid box in earthquake simulation centrifuge experiments induces a series of unwanted seismic waves that are generated by the reflection of seismic motion at each end wall of the box and are subsequently reflected back by the opposite wall. This

phenomenon, which might induce a behaviour in the model different from the real field, is partly attenuated by placing Duxseal (a relatively soft material) at each end wall of the box to create absorbing boundaries. Duxseal has been used in the centrifuge experiments to prevent seismic wave reflection from the lateral boundaries of the rigid centrifuge box and thus helping the soil deposit to behave like a semi-infinite medium. This material was also considered in the numerical analyses, and idealized as linear-elastic. It was assumed that those phenomena occurring in the centrifuge experiments (wave reflection due to simulation of rigid end walls and subsequent attenuation by Duxseal) were reproduced by the numerical model. The material properties obtained from the literature (e.g., Popescu et al., 2006) for Duxseal are listed in Table 5.4. Selective DOF slaving was used at the contact nodes to model the impervious surface between structure-soil, and soil-Duxseal. After the first phase of calibration (as discussed in Section 5.3.1), fine tuning of parameter values was done by back-analysis of test 1. This has been done by comparing the recorded and predicted test results for test1. Then the numerical model was verified and validated based in back-analysing of test 2 and 3.

5.3.3. Numerical Simulation of Centrifuge Tests: Model Validation

The numerical analyses were performed to simulate the centrifuge tests on homogeneous and heterogeneous soil using fully coupled solid-fluid equations and a multi-yield surface plasticity soil constitutive model implemented in DYNAFLOW. The centrifuge models were subjected to an acceleration field 70 times higher than the gravity field. The stresses increased accordingly (high stresses at the base of the model and low stresses at the top) due to this higher gravity field which caused non-uniform stress densification in an initially uniform relative density model. The amount

of stress densification was estimated based on a relation given by Park and Byrne (2004). The new relative densities after stress densification were verified during centrifuge tests by measuring the volume of soil in the box before the test and after the first spin and calculated the average soil densities of the model. The estimated relative densities (after stress densification) were considered in the numerical simulations. Soil constitutive parameters depending on relative density (such as porosity, hydraulic conductivity, friction angle at failure, dilation parameter, etc.) were recalculated at every elevation in the model according to the new values of relative density. Their ranges are shown in the last column of Table 5.2.

o **Analysis Results**

After estimating the dilation parameter from the liquefaction strength analysis, the next step was fine tuning of parameters. It was done by comparing numerically simulated results of test 1 (homogeneous soil) with experimental results. Some parameters (e.g., hydraulic conductivity) were adjusted until a satisfactory match was obtained. The numerical simulation results, obtained using the fine tuned multi-yield plasticity constitutive model parameters, are presented here with the results recorded in centrifuge tests. The recorded and computed EPWP ratios with respect to the initial vertical stress at four different locations in test 1 (2 locations below structure and 2 locations in the free field in homogeneous soil) are shown in Figure 5.7. Except for a location very close to the structure (i.e., P2), the numerical model accurately predicted the results recorded in the centrifuge test.

The next step was comparing numerical (using the fine tuned multi-yield model) and experimental results for heterogeneous soil to validate the numerical model. The recorded and computed EPWP ratios with respect to the initial vertical

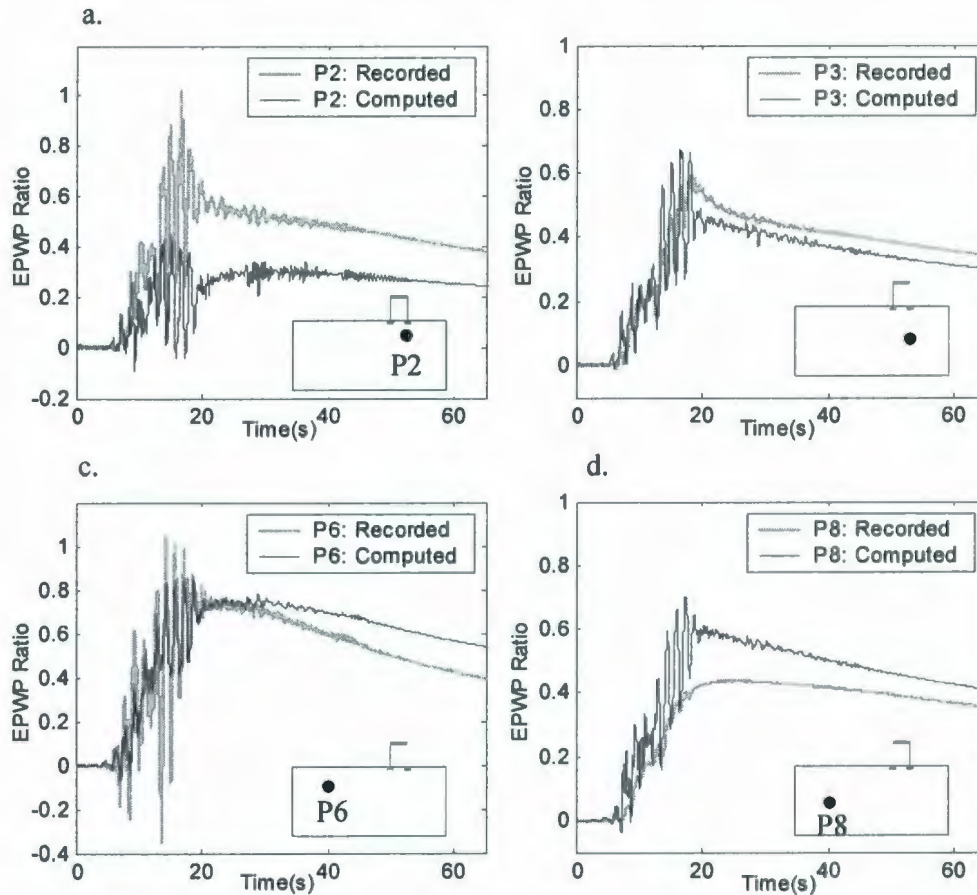


Figure 5.7: Recorded and computed excess pore water pressure (EPWP) ratio with respect to the initial effective vertical stress at 4 locations in test1 (medium dense homogeneous soil): a. Below structure at shallow depth: P2; b. Below structure at larger depth: P3; c. Free field at shallow depth: P6; d. Free field at larger depth: P8.

stress at four different locations in the free field in test 3 (on heterogeneous soil) are shown in Figure 5.8. Comparisons of recorded and computed EPWP ratios below the structure in heterogeneous soil are shown in Figure 5.9. From the results on the heterogeneous soil model it was observed that the numerical simulation results were in agreement (except P2) with the experimental results. The numerical model predicted more dilative behaviour for the soil at P2 than that observed in the centrifuge tests. This is believed to be due to presence of large static shear at that location because of the structure. This is a limitation of the model used in this research. In Dynaflo, this problem can be solved by using a double plastic potential

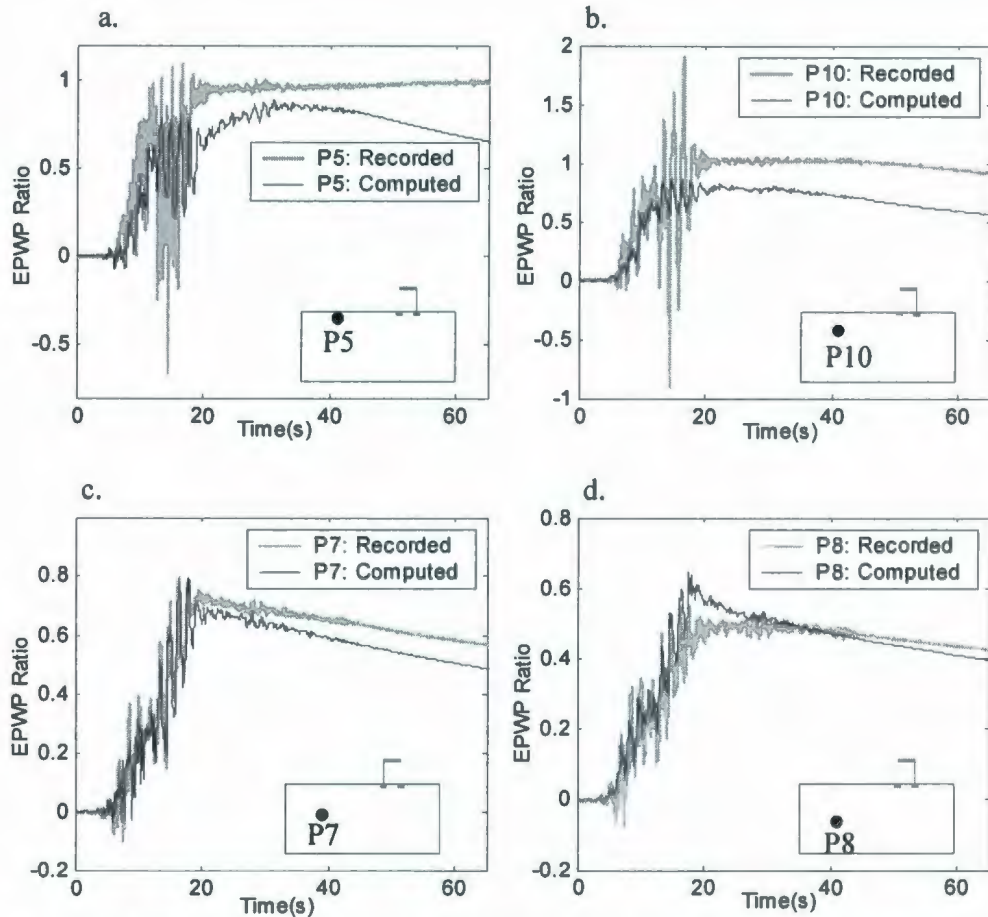


Figure 5.8: Recorded and computed excess pore water pressure (EPWP) ratio with respect to the initial effective vertical stress at 4 locations in the free field in test3 (heterogeneous soil): a. P5: Dense sand; b. P10: Loose sand; c. P7: Dense sand; d. P8: Loose sand.

model (not used in this research). However, the numerical model was deemed sufficiently accurate for the purpose of this study.

Figures 5.10a and b show the comparison of the EPWP ratio between homogeneous and heterogeneous soil, recorded after the end of earthquake ground motion during centrifuge tests. This result indicates a larger EPWP build-up in heterogeneous soil than in homogeneous soil (e.g. free field at 5m depth EPWP ratio in heterogeneous soil is 1 whereas in homogeneous soil it is 0.7). Similar results, obtained from numerical simulation of the centrifuge tests, are shown in Figure 5.10c and d. Although the heterogeneous soil deposit was on average denser than the

uniform soil, its liquefaction resistance was lower than that of the uniform soil. Similar conclusions were also observed from earlier numerical simulations of heterogeneous soil (e.g. Popescu and Chakraborty, 2006).

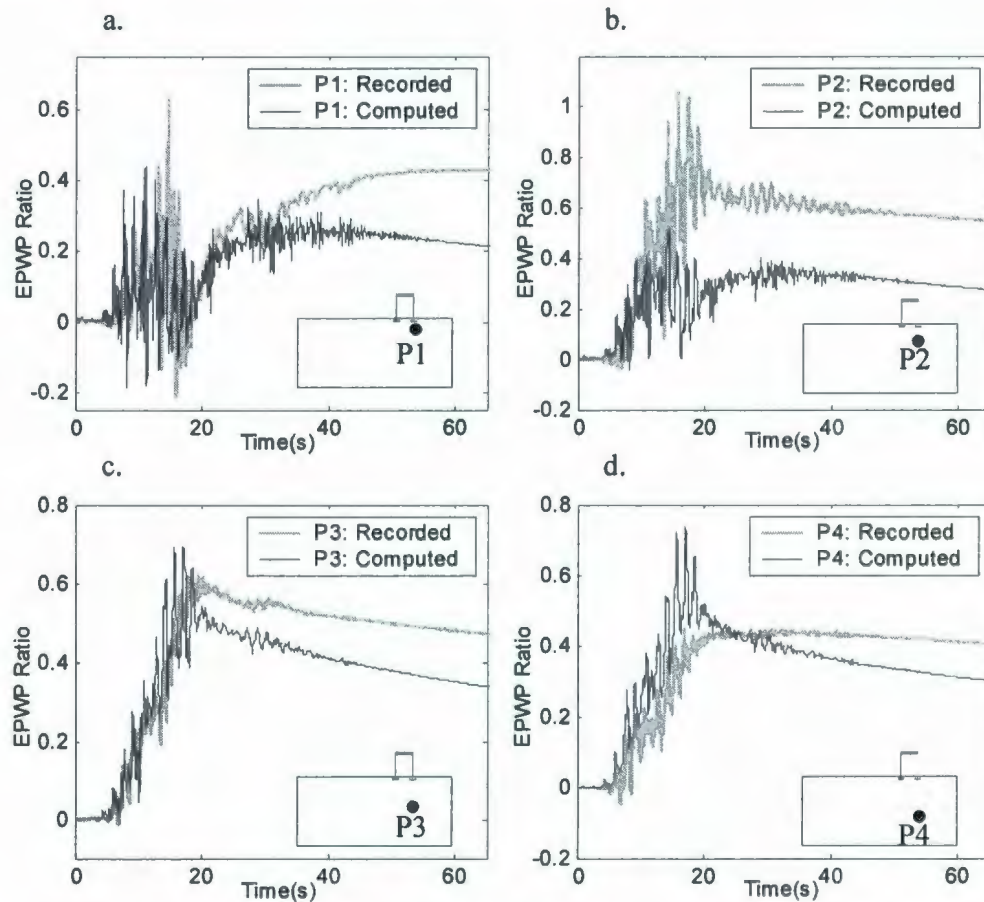


Figure 5.9: Recorded and computed excess pore water pressure (EPWP) ratio with respect to the initial effective vertical stress at 4 locations below structure in test3 (heterogeneous soil): a. P1: Dense sand; b. P2: Loose sand; c. P3: Dense sand; d. P4: Loose sand.

Settlements of the structure were also monitored during the tests. Recorded and computed settlements of the building in test 1 are shown in Figure 5.11. Similar comparisons for building settlements in test 3 (heterogeneous soil) are shown in Figure 5.12. It was observed that the structure resting on heterogeneous soil had settled more than that in uniform soil. A comparison of acceleration time histories in test 1 (homogeneous soil) recorded and computed at different depths in the free field

are shown in Figure 5.13. The acceleration record at *A7* shows very large high-

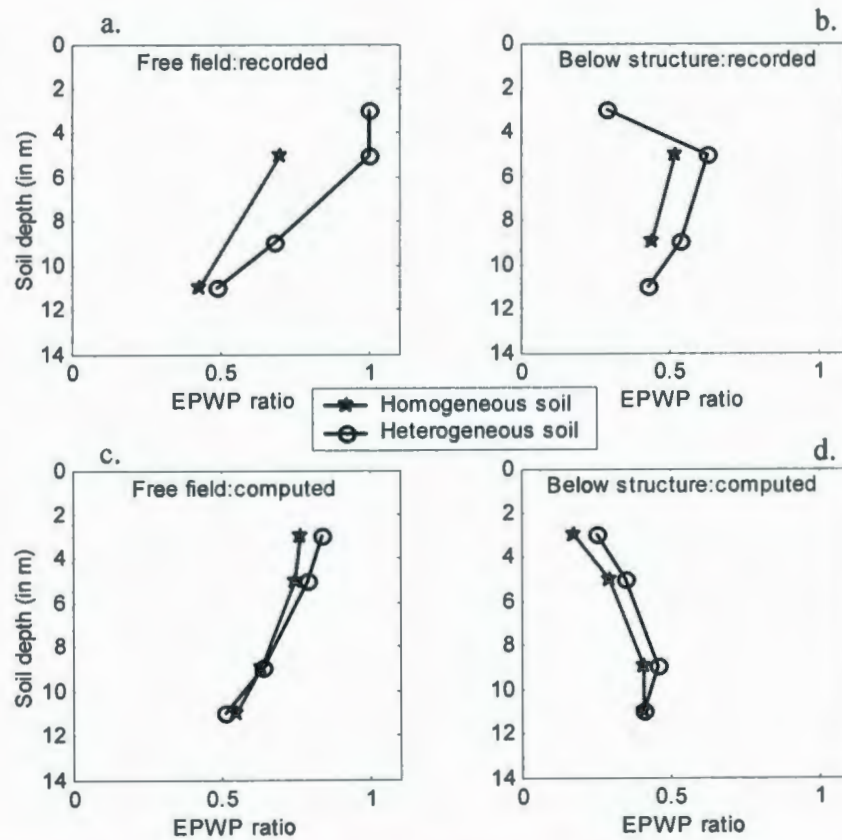


Figure 5.10: Comparison of excess pore water pressure (EPWP) ratio between homogeneous and heterogeneous soil at time $t=30s$ (depths at prototype scale).

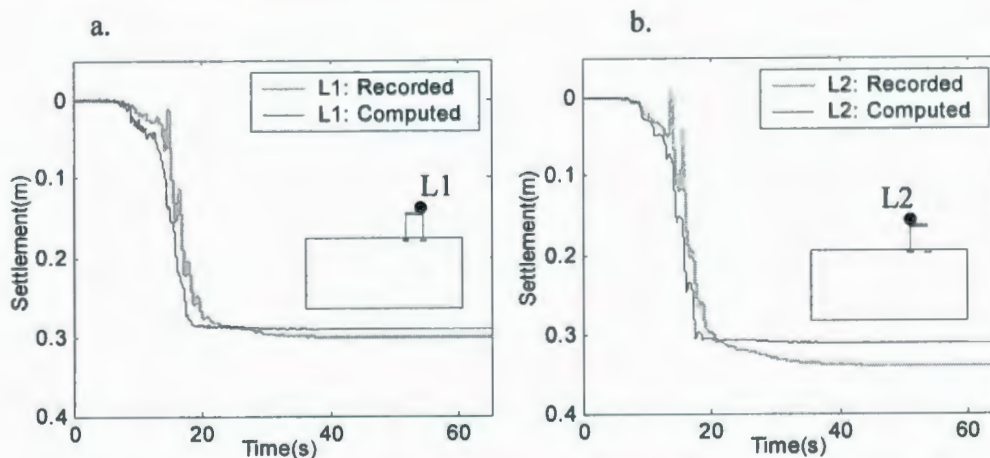


Figure 5.11: Recorded and computed settlement of building in test1 (homogeneous soil): a. L1; b. L2.

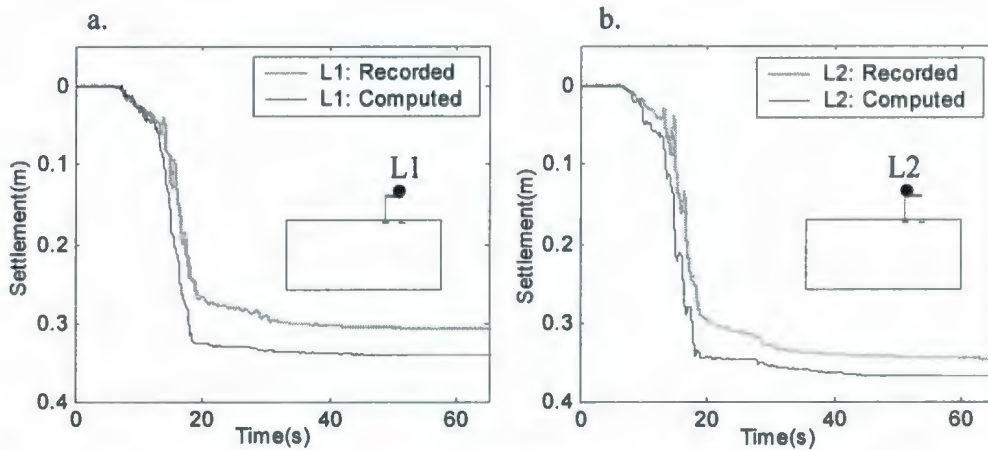


Figure 5.12: Recorded and computed settlement of building in test3 (heterogeneous soil): a. L1; b. L2.

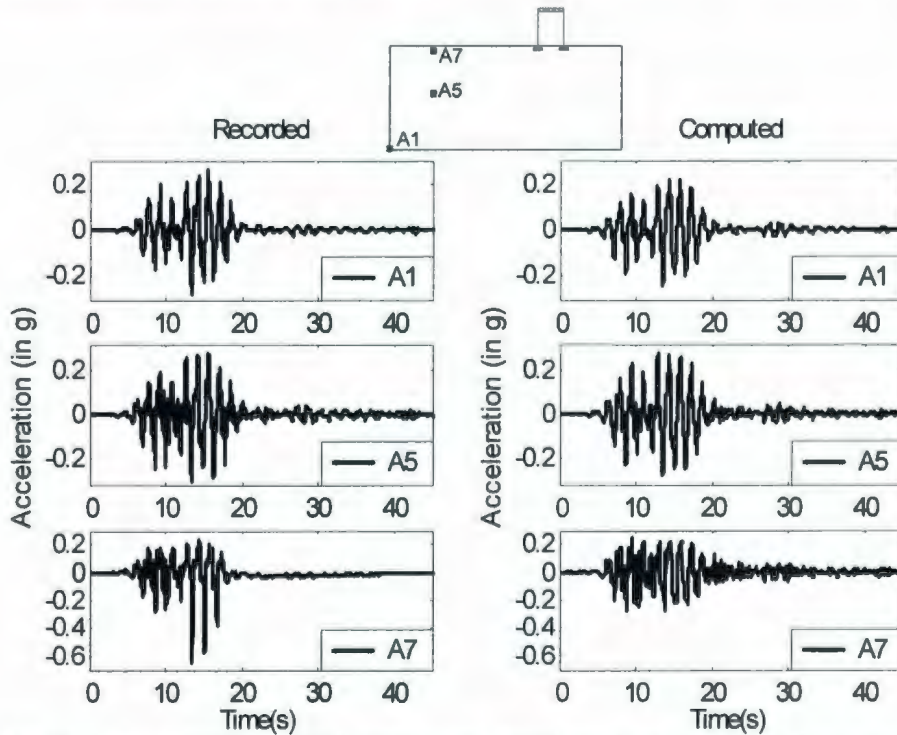


Figure 5.13: Recorded and computed accelerations in test1 (homogeneous soil).

frequency acceleration spikes during the strong ground motion. These spikes actually coincide with the negative pore pressure spikes during strong ground motion, and have been termed as de-liquefaction shock waves by Kutter and Wilson (1999). However the numerical model was not able to reproduce those dilation spikes recorded during centrifuge tests. Computed and recorded acceleration time histories in

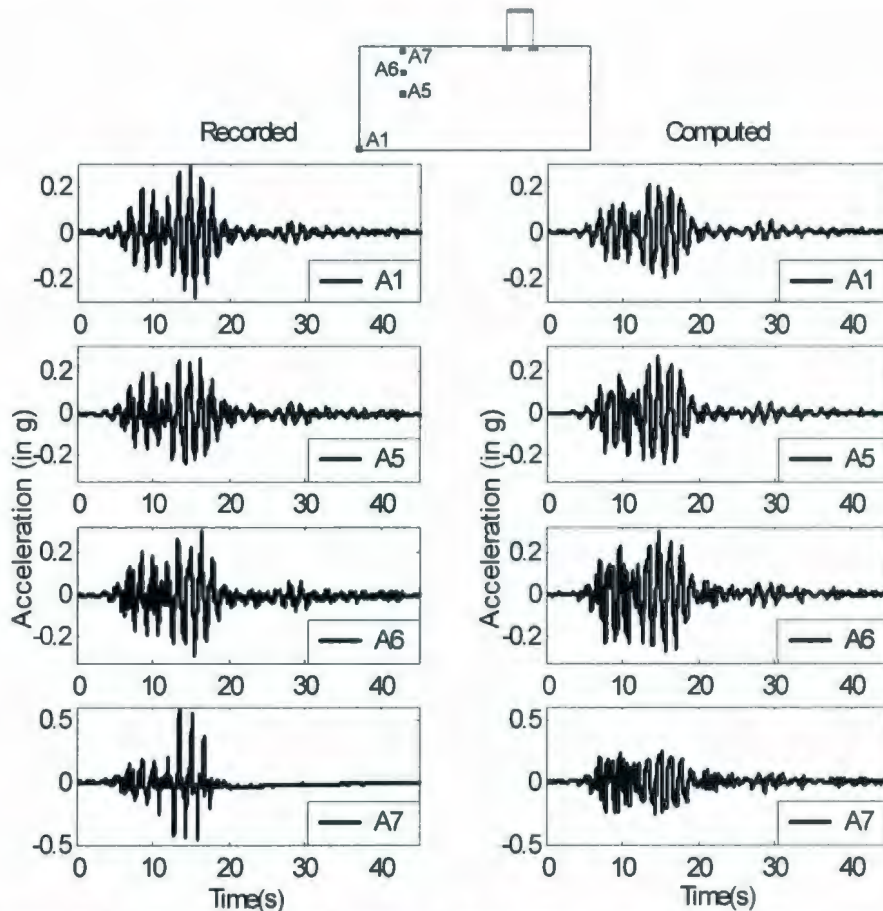


Figure 5.14: Recorded and computed accelerations in test3 (heterogeneous soil).

the heterogeneous soil model are shown in Figure 5.14. From the recorded and computed results it was observed that accelerations are attenuated in heterogeneous soil more than in homogeneous soil. The reason was believed to be the generation of a larger amount of EPWP in heterogeneous soil than uniform soil. The attenuation of seismic acceleration can be directly identified from the result shown in Figure 4.19 in page109.

5.4. Liquefaction Mechanism in Heterogeneous Soil: Results and Discussion

As discussed earlier in Chapter 2, based on numerical simulation results Popescu et al. (1997) stated that larger EPWP build-up is predicted in heterogeneous

soil than that in corresponding uniform soil. Later on, Popescu et al. (2006)

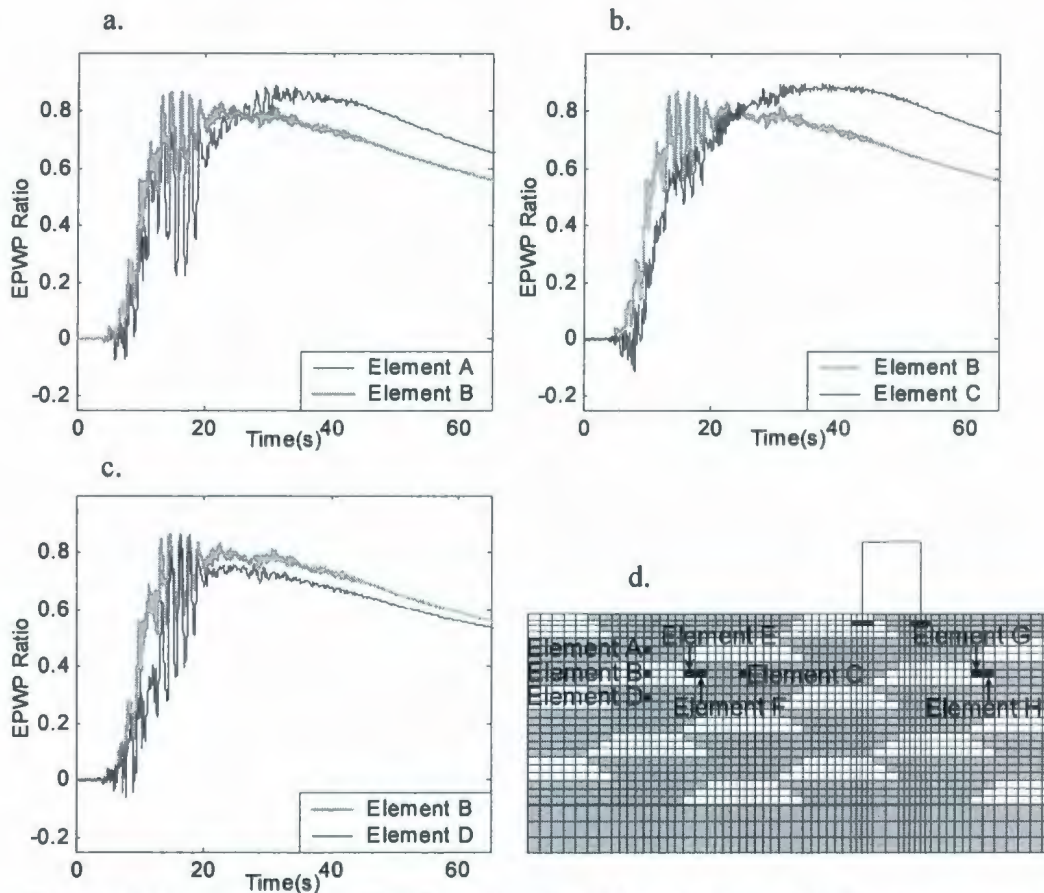


Figure 5.15: Computed EPWP ratio time histories in test3 (heterogeneous soil) in the middle of two adjacent dense and loose soil pockets in the free field: a. Element A: Dense soil vs. Element B: Loose soil; b. Element B: Loose soil vs. Element C: Dense soil; c. Element B: Loose soil vs. Element D: Dense soil; d. Finite element mesh with element locations.

investigated this phenomenon in detail by back-analysing two centrifuge experiments performed at Cambridge University, one with a loose sand layer and another with a single loose sand pocket. Popescu and Chakraborty (2006) extended this study to spatially variable soil by numerically analysing the hypothetical variable soil deposit. Some of those results were already briefly discussed in Section 5.2. The numerical and experimental studies indicated that the presence of loose pockets in heterogeneous soil would lead to earlier build-up of EPWP and local liquefaction in loose pockets. And ultimately, the pressure gradient between loose and dense sand zones would lead to water migration and softening of dense soil due to build-up of

significant EPWP. However, there is no large scale experimental verification available to date to the practicing engineering community to verify the above mentioned behaviour for truly heterogeneous soil. The geotechnical centrifuge experiments conducted on heterogeneous soil in the experimental part of this research program, are the first of this kind. The liquefaction phenomenon in heterogeneous soil was subsequently studied in more detail by closely analysing the results from numerical simulations.

To explain the liquefaction mechanisms for heterogeneous soil, computed results in terms of EPWP ratio with respect to the initial effective vertical stress are presented at four different locations shown in Figure 5.15: element B, located in the middle of a loose pocket in the free field, and elements A, C and D located in the dense sand area surrounding the loose pocket that contains element B. During an earthquake, EPWP builds-up faster in loose pockets (shown in Figure 5.15a, b and c). Then, due to a pressure gradient, water starts migrating toward neighbouring dense sand. Due to this water migration EPWP build up in dense soil continued until few seconds after the earthquake, which ultimately causes softening of dense sands. The effect of the presence of structure on this liquefaction mechanism in heterogeneous soil is shown in Figure 5.16. It shows the evolution of the EPWP ratio in two adjacent elements of the variable soil, one located in a loose soil pocket (element E and G – shown in Figure 5.15d) and the other in a dense sand zone (element F and H). The effects of water migration are more evident in the free field compared to the soil below the structure. All four elements presented here are at the same depth. However, due to presence of extra overburden pressure, soil did not liquefied below structure; whereas in the free field in dense soil (element F), EPWP reached almost equal to initial effective vertical overburden pressure at that location.

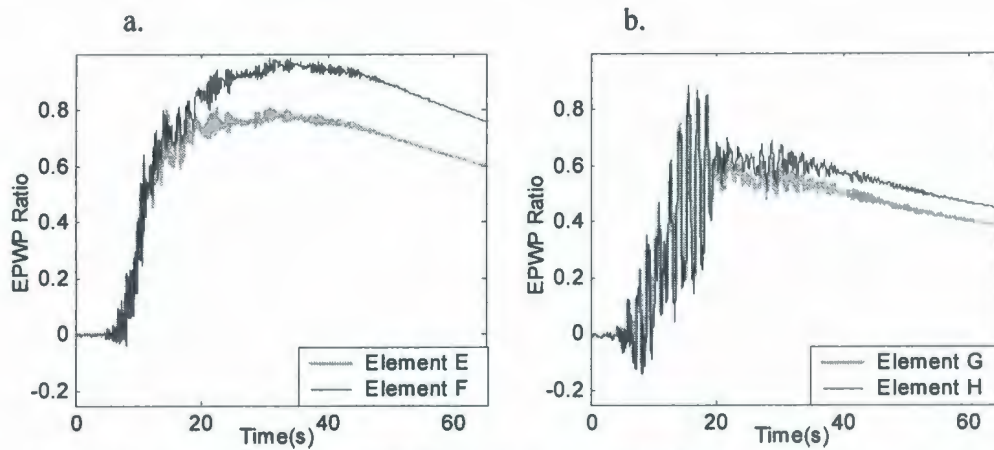


Figure 5.16: Computed EPWP ratio time histories in test3 (heterogeneous soil) computed at two adjacent locations: a. Free field (one in the loose soil: element E, and the other in the dense soil: element F); b. below structure (one in the loose soil: element G, and the other in the dense soil: element H); elements are shown in Figure 5.15(d).

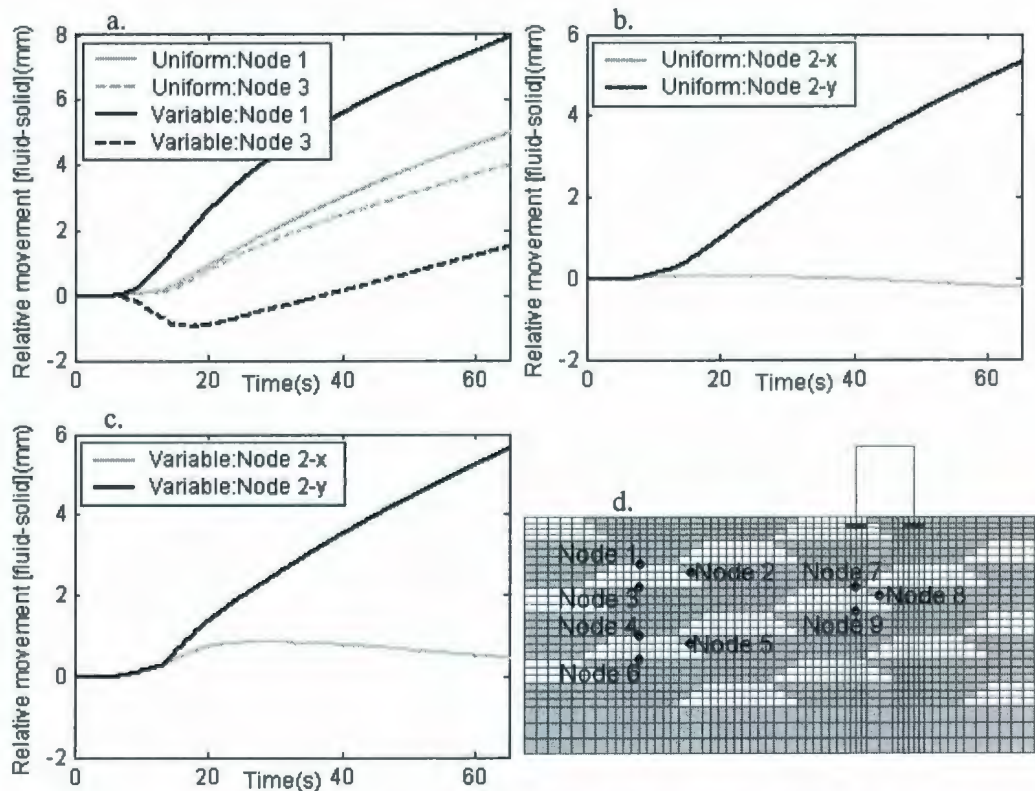


Figure 5.17: Computed relative movement of water in the free field (lower depth) with respect to the solid phase at the interface location between loose and dense sand in test on heterogeneous soil: a. vertical movement at two different nodes; b. horizontal (x) and vertical (y) movement at same node in homogeneous soil; c. horizontal (x) and vertical (y) movement at same node in heterogeneous soil. Positive relative displacements are upward (vertical) and left to right (horizontal); d. Finite element mesh with locations of nodes.

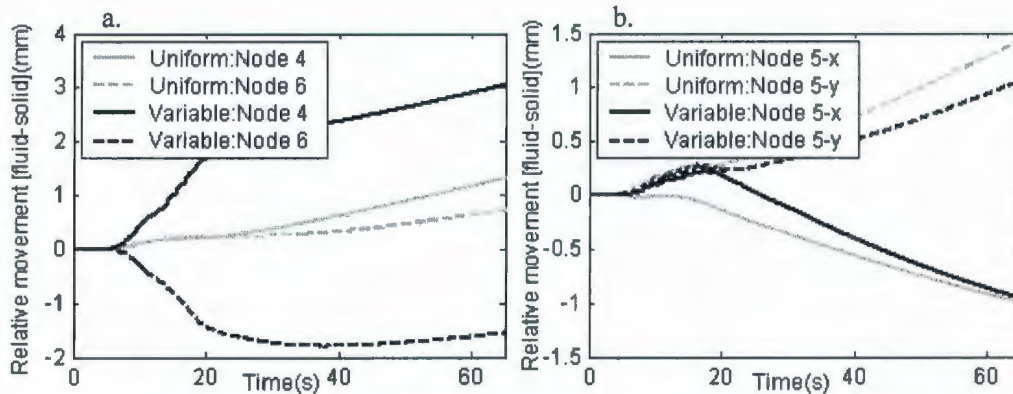


Figure 5.18: Computed relative movement of water in the free field (higher depth) with respect to the solid phase at the interface location between loose and dense sand in test on heterogeneous soil: a. vertical movement at two different nodes in homogeneous and heterogeneous soil; b. horizontal (x) and vertical (y) movement at same node in homogeneous and heterogeneous soil. Positive relative displacements are upward (vertical) and left to right (horizontal); nodes are shown in Figure 5.17(d).

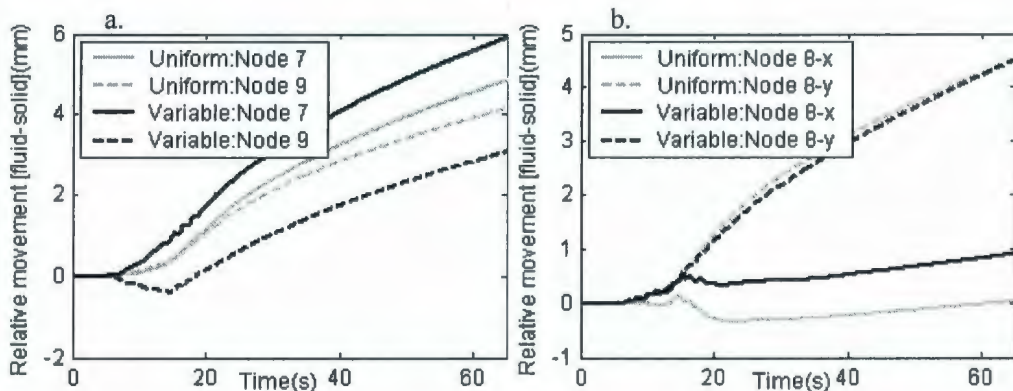


Figure 5.19: Computed relative movement of water below structure with respect to the solid phase at the interface location between loose and dense sand in test on heterogeneous soil: a. vertical movement at two different nodes in homogeneous and heterogeneous soil; b. horizontal (x) and vertical (y) movement at same node in homogeneous and heterogeneous soil. Positive relative displacements are upward (vertical) and left to right (horizontal); nodes are shown in Figure 5.17(d).

Simulation of water migration from loose to dense sand by the numerical model is illustrated in Figure 5.17, by computed time histories of relative water displacements, with respect to the solid phase at three locations at the interface between loose and dense sand zone. In the case of heterogeneous soil, it was observed

that during the earthquake water was migrating from loose to dense soil (shown in Figure 5.17 a). However, after the earthquake (at about 20s), water movement at node 3 was upward. It is because during EPWP dissipation water moves mainly in an upward direction. A comparison of the relative water movement in homogeneous soil with heterogeneous soil is also presented in Figure 5.17. From the results it is evident that the water was coming out from the loose soil pockets in heterogeneous soil and transmitting into the dense sand zones. This ultimately causes liquefaction in theoretically non-liquefiable dense sand. Similar comparisons at higher depth in the free field are shown in Figure 5.18. The comparisons of the relative water movement in heterogeneous soil (in the interface of a loose pocket) below structure are shown in Figure 5.19.

Contours of excess pore water pressure ratio with respect to the initial effective vertical overburden pressure, calculated at six different time instants for both the homogeneous and heterogeneous soil, are shown in Figure 5.20. EPWP ratio contours during strong shaking are shown in Figure 5.20a (test 1) and g (test 3). Until the end of strong shaking, significant amounts of EPWP were generated in the free field (Figure 5.20b, h) in both tests. However, as shaking progresses in heterogeneous soil, water starts migrating from the loose pockets to the surrounding dense soil. Therefore, a few seconds after the end of strong motion (at time=41s), larger areas in the free field of heterogeneous soil deposit liquefied (Figure 5.20l), due to the water migration. A value of EPWP ratio close to one indicates soil liquefaction. Figure 5.21 presents contours of computed volumetric strains at five different time instants for both homogeneous soil (Figure 5.21a, b, c, d, e) and heterogeneous soil (Figure 5.21f, g, h, i, j). It is interesting to note that the dense sand pockets exhibit a tendency of

dilation (positive volumetric strains at the end of shaking); however they liquefy due to water injection from neighbouring loose sands.

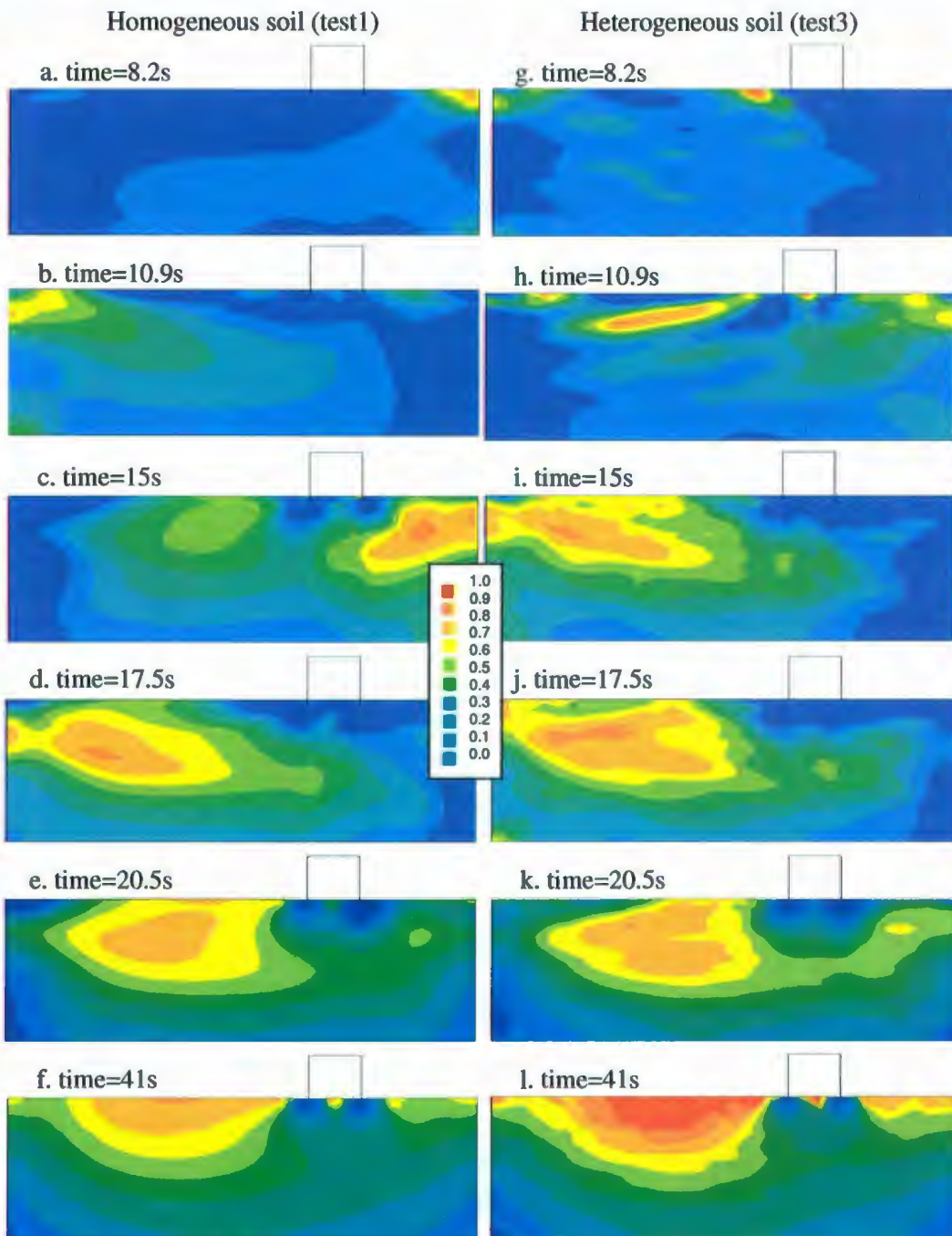


Figure 5.20: Evolution of predicted contours of excess pore water pressure ratios during tests on homogeneous and heterogeneous soil: a-f. in test1; g-l. in test3; The end of earthquake shaking is at time=20.5s.

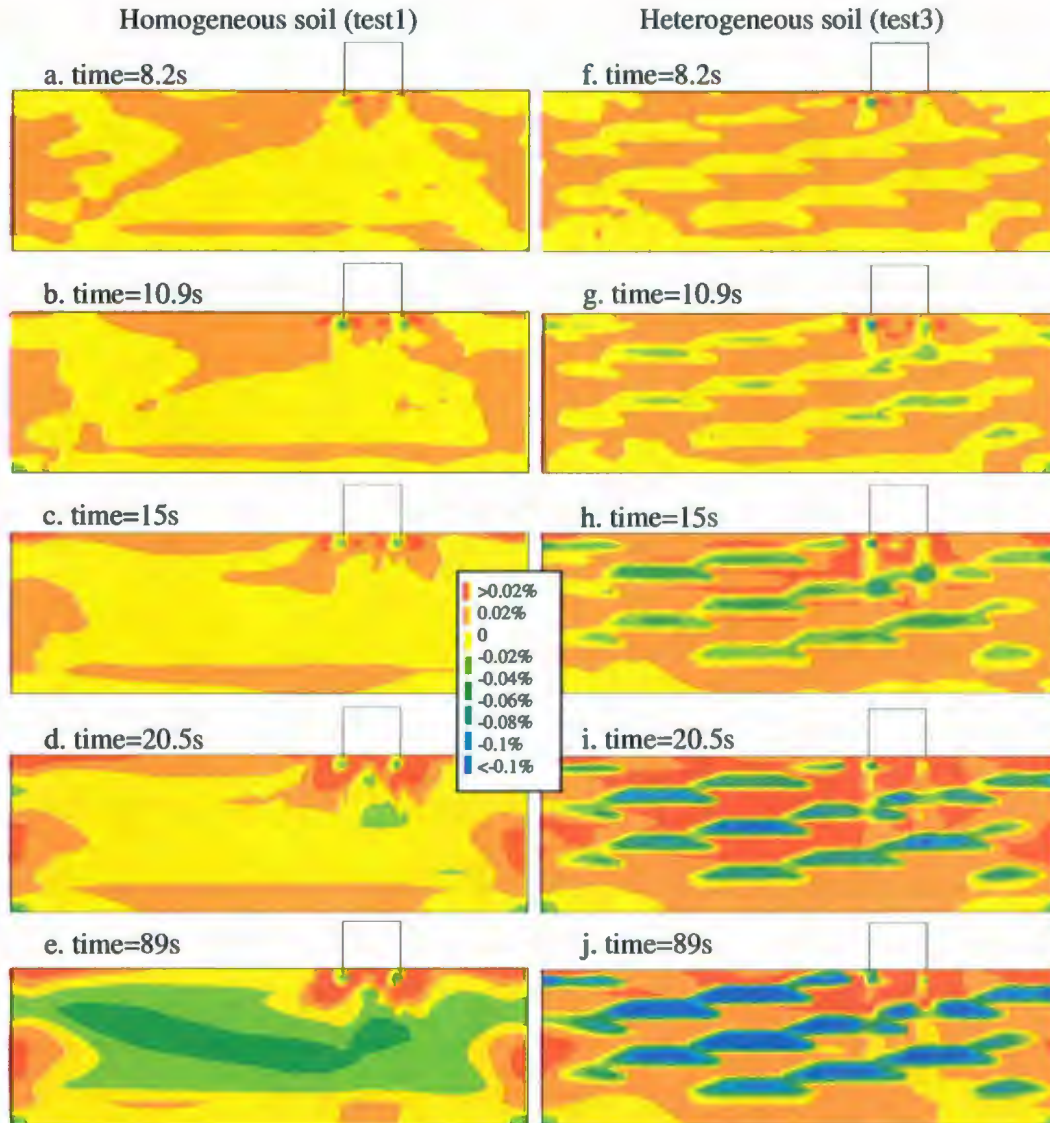


Figure 5.21: Evolution of predicted contours of volumetric strain: a-e. in test1; f-j. in test3 at the end of analysis (time=89s); The end of earthquake shaking is at time=20.5s; The end of analysis is at time=89s.

The failure mechanism illustrated by the maximum shear strain contours at the end of the analysis in Figure 5.22 is characteristic for local bearing capacity failures below the structure (shear strain larger than 12.5%) in both the homogeneous as well as in the heterogeneous soil. From the maximum shear strain contours in heterogeneous soil it was identified that the failure surface passes selectively through loose soils (location of loose pockets are shown in Figure 5.22b). This is similar to the

phenomenon observed by Popescu et al. (2005a) in the case of static bearing capacity failure in heterogeneous soil. Where it was observed that actual failure surface in heterogeneous soil deviated from its theoretical position and passed selectively through weaker soil zones and thus the average mobilized strength is reduced when compared to that of a corresponding uniform soil.

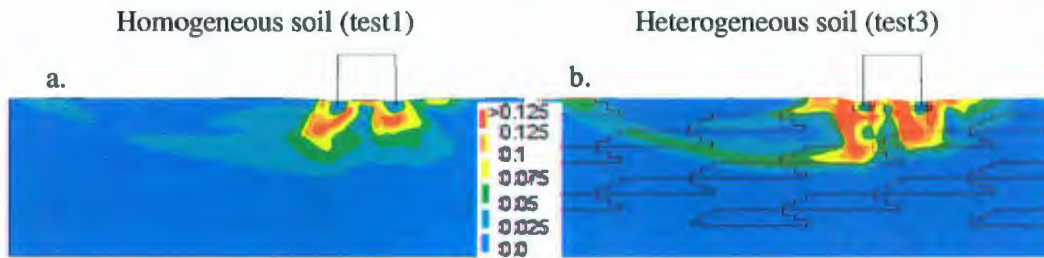


Figure 5.22: Predicted contours of maximum shear strain at the end of analysis (time= 89s): a. Test1; b. Test3 (locations of loose pockets are shown by red lines).

5.5. Summary and Conclusions

A series of centrifuge liquefaction tests were conducted to find out the seismic behaviour and liquefaction mechanisms for heterogeneous soil. The liquefaction phenomenon is explained in detail using the numerical simulation of those centrifuge tests. It was shown that this combined numerical and experimental study can be used as an efficient method to study and explain the liquefaction mechanism for heterogeneous soil. Based on a detailed analysis of numerical and centrifuge results, this study provides an explanation for an interesting and important behaviour detected in previous theoretical work, namely that more excess pore water pressure is generated by seismic loads in a heterogeneous soil than in an equivalent uniform soil. After closely observing the liquefaction mechanism (described in Section 5.4) in variable soil, it has been verified and concluded that EPWP is generated in loose pockets first. Next, the pressure gradient created between loose and dense sand zones

leads to water migration from loose to dense soil zones, resulting in softening of dense soil. This mechanism is also explained using the flowchart shown in Figure 5.23. The reason for liquefaction of the dense sand is the injection of water from loose pockets. This water migration, equivalent to water injection into the dense soil, leads to gradual softening and eventual liquefaction of a theoretically non-liquefiable material. From this study it is concluded that although the average relative density ($Dr^m=64\%$) of heterogeneous soil deposit (test 2 and test 3) was higher than that of the uniform ($Dr=55\%$) soil (test 1), liquefaction resistance was less than that of uniform soil due to water migration from loose to dense soil zones in heterogeneous soil deposits.

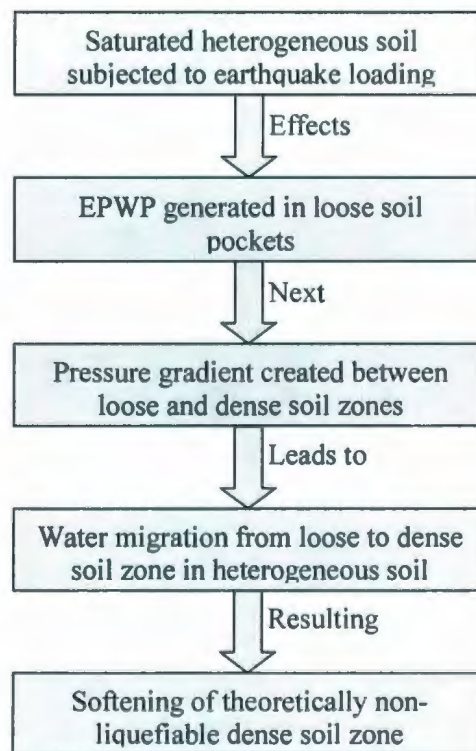


Figure 5.23: Flowchart showing liquefaction mechanism in heterogeneous soil.

From the experimental and numerical analyses it was observed that soil heterogeneity leads to more EPWP build-up than predicted for uniform soil. The average mobilized soil strength was also reduced due to deviation of failure surface

through loose sand pockets. The larger build-up of EPWP and reduction in average mobilized soil strength ultimately cause more damage (in terms of settlement) to the structure on heterogeneous soil as compared to homogeneous soil.

Finally, it should be mentioned that the heterogeneous soil deposits exemplified here exhibit large, sudden variations in relative density from one location to another, unlike natural soil deposits where those variations are gradual. Therefore, the results of this study may over-emphasize the effects of soil heterogeneity on liquefaction potential of spatially variable soils. However, as most laboratory soil testing procedures use uniform soil samples for assessing the liquefaction potential, their results may well be under-conservative when applied to natural soil deposits exhibiting inherent spatial variability of their properties.

Table 5.1: Experimental and numerical results of cyclic undrained triaxial tests on uniform and layered soil samples (for cyclic stress ratio CSR=0.166)

Type of soil sample	Number of cycles to liquefaction (N_L)	
	Experiment	Finite element analysis
Uniform sand	150	180
Uniform silt	90	98
Silt layer in sand sample	42	56

Table 5.2: Parameters of the multi-yield plasticity model used for the saturated soil

Type	Constitutive parameter	Symbol	Relative density			Relative density (with stress densification)
			Dr=35%	Dr=55%	Dr=75%	Dr= (33.6% - 75.05%)
State parameters	Mass density – solid	ρ^s	2710 kg/m ³	2710 kg/m ³	2710 kg/m ³	2710 kg/m ³
	Porosity	n^w	0.453	0.433	0.412	0.454 - 0.412
	Hydraulic conductivity	k	0.008862cm/s	0.00765cm/s	0.00651cm/s	0.00895cm/s – 0.00651cm/s
Low strain elastic parameters	Low strain elastic shear modulus	G_0	29.56MPa	39.04MPa	51.55MPa	29.0MPa - 51.59MPa
	Poisson's ratio	ν	0.289	0.325	0.361	0.286 - 0.361
	Power exponent	n	0.5	0.5	0.5	0.5
Yield and failure parameters	Friction angle at failure	ϕ	37.6 ⁰	40 ⁰	42.5 ⁰	37.43 ⁰ – 42.41 ⁰
	Maximum deviatoric strain (comp/ext)	ϵ_{dev}^{max}	9.6 (C)	8.0 (C)	6.4 (C)	9.7 – 6.4
			7.6 (E)	6.0 (E)	4.4 (E)	7.7 – 4.4
	Coefficient of lateral stress	k_0	0.8	0.8	0.8	0.8
Dilation parameters	Dilation angle	ψ	34 ⁰	34 ⁰	34 ⁰	34 ⁰
	Dilation parameter	X_{pp}	0.074	0.031	0.0111	0.0777 – 0.0111

Table 5.3: Poisson's ratio for different types of sand

Type of soil	Das, 2006	Kulhawy and Mayne, 1990
Loose sand	0.2-0.4	0.1-0.3
Medium Sand	0.25-0.4	-
Dense Sand	0.3-0.45	0.3-0.4
Silty sand	0.2-0.4	-

Table 5.4: Constitutive parameters for linear-elastic materials used in the numerical simulation

Constitutive parameter	Duxseal	Frame structures ⁽¹⁾
Mass density (kg/m ³)	1650	7813
Young's modulus (MPa)	8	203,000
Poisson's ratio	0.46	0.287

Notes: (1) mass calculated to obtain a bearing pressure in the prototype equivalent to the one in the centrifuge experiments

CHAPTER 6

Reliability Analysis of Structures on Heterogeneous Soil

6.1. Introduction

The first part of this research discussed the mechanism of liquefaction in heterogeneous soil. This has been done by means of geotechnical centrifuge tests and numerical modelling (discussed in previous chapters). After validating the numerical model, it has been used for a parametric study for finding the effects of soil heterogeneity on the structural responses. Dynamic analyses have been performed on various types of structures situated on heterogeneous soil. Based on the types of structures, this study is divided into two parts. The performance of a tower structure, where total settlements and base rotations are of primary interest, has been studied in the first part. In the second part, the performance of a frame structure (where total and differential settlements are of primary interest) has been studied. The results related to this study are presented in this chapter.

In the next section, a brief discussion about different steps of Monte Carlo simulations (used here) is presented. The reliability analysis of tower structure resting on heterogeneous soil is presented in Section 6.3. The research related to the reliability analysis of the frame structure resting on heterogeneous soil is discussed in Section 6.4. Geotechnical design recommendations are provided for structures on liquefiable heterogeneous soil deposits by directly including the effects of soil-structure interaction. Updated design guidelines are also provided on the spectral amplification of seismic

ground motion travelling through uniform and heterogeneous soil. Summary and conclusions from this study on different types of structures are presented in Section 6.5.

6.2. Monte Carlo Simulation

6.2.1. Methodology of Monte Carlo Simulation

A Monte Carlo simulation technique, using digital generation of non-Gaussian stochastic vector fields and nonlinear deterministic finite element analysis (using DYNFLOW) was used to calculate the effect of soil heterogeneity on the structural response of soil-structure system. The Monte Carlo simulation has the following four steps (Popescu, 1995):

1. Estimating the probabilistic characteristic of the spatial variability of index soil properties. Reasonable ranges of those probabilistic characteristics (e.g., marginal probability distribution functions, cross-correlation structure etc.) are used in this study based on the available information in the literature.
2. Digitally generating sample functions of a bi-variate, two-dimensional (2V-2D) non-Gaussian stochastic field, where each simulated sample function represents a possible realization of relevant index soil properties over the analysis domain.
3. Evaluating the soil constitutive model parameters at each location in the analysis domain using correlations with the index soil properties.
4. Performing deterministic non-linear finite element analyses, using stochastic input parameters obtained from the step three.

In step one, ranges for the probabilistic characteristic of the spatial variability of soil properties used in this study were estimated based on available data in the literature. After an extensive research, Phoon and Kulhawy (1999 a, b) documented some guidelines for ranges of probabilistic characteristics of geotechnical properties (e.g., coefficient of variance of cone tip resistance (q_n) for sand in natural deposits 20-60%). Those guidelines were used in this study. The step two of Monte Carlo simulation method is based on the spectral representation method. For the present study, 2D-2V (cone tip resistance q_n and soil classification index I_c) sample functions of random stochastic field were generated based on a prescribed cross-spectral density matrix and prescribed marginal probability distribution functions. For more details about this generation of sample functions, the reader is referred to Section 2.5.3.2 and Popescu et al. (1998). Sample functions of random stochastic fields in terms of q_n and I_c were generated over the analysis domain. In step three, the soil constitutive parameters are evaluated using some correlations with *in-situ* soil test indices (namely I_c and q_n at each location). The correlation formulae for estimating multi-yield plasticity model parameters based on q_n and I_c at each element centroid have been presented by Popescu (1995) and Popescu et al. (1997). Those formulae are for the multi-yield plasticity soil constitutive model with conical yield surface (more discussion about multi-yield plasticity soil constitutive model and conical yield surface can be found in Chapter 3 Section 3.2). They have been modified in this study for the model with rounded Mohr-Coulomb yield surfaces. Those correlations used here for calculating multi-yield plasticity model parameters are shown in Table 6.1. In step four, the values of different soil properties from step three (for each sample function and at each spatial location) are used as input in stochastic finite element

analyses. The analyses are performed for each sample function using the finite element computer code DYNAFLOW.

6.2.2. Stochastic Soil Properties

Soil heterogeneity is described in this study using the probabilistic characteristics of two index soil properties: overburden stress-normalized cone tip resistance, q_n , and soil classification index, I_c (Jefferies and Davies, 1993). The cone tip resistance is mainly related to the relative density and shear strength of the soil, while the soil classification index characterizes the soil type and is related to grain size and hydraulic conductivity. Modelling the two indices as the two components of a bi-variate stochastic field allows a more realistic simulation of the various soil properties that are derived from them, and are used in the liquefaction analysis. The probabilistic characteristics of the soil properties used in the first part of this study (with tower structure) are as follows (Popescu et al., 2005b):

1. For q_n : average value 6 MPa (corresponding to a relative density of 44% that is characteristic of a loose to medium dense sand), and coefficient of variation (CV_q) = 0.5. The selected marginal probability distribution function (PDF) is a Gamma PDF with parameters $\eta = 4$, $\lambda = 0.67$ and lower bound zero.
2. For I_c : average value 2, coefficient of variation of I_c (CV_I) = 0.15, symmetric Beta PDF bounded between 1 and 3, corresponding to a relatively clean, fine to medium coarse sand.
3. Squared exponential auto-correlation structure, common for both q_n and I_c (see Vanmarcke (1983) for a description of the auto-correlation model). The correlation distances are assumed as: $\theta_h = 8\text{m}$ in the horizontal direction and $\theta_v = 2\text{m}$ in the

vertical direction. These were selected based on the value in the literature (Phoon and Kulhawy (1999a), Popescu et al. (2005a), Fenton and Griffiths (2003)).

4. The cross-correlation coefficient between q_n and I_c is taken as $\rho = -0.58$ (Popescu, 1995).

Some of these soil properties resulted from the stochastic characterization of an actual site (Popescu, 1995). Most of the probabilistic characteristics of the soil properties (e.g. average value of I_c , CV_I , θ_h , θ_v , marginal PDF and cross-correlation coefficient between q_n and I_c) used in the second part of this study (with frame structure) are same as that in the first part of this study. The only change in the probabilistic characteristics is as follows:

1. q_n : Calculated based on soil (loose ($Dr=45\%$) /dense ($Dr=85\%$)) relative density and three CV_q (i.e., 0.2, 0.5 and 0.625) were used for loose soil and one CV_q (i.e., 0.5) was used for dense soil in the study.

6.3. Tower Structure on Heterogeneous Soil

6.3.1. General

A soil-structure system has its own characteristic frequency, which depends on material properties, geometry and degree of saturation of the soil. This characteristic frequency may decrease during dynamic excitation, due to degradation of the soil effective deformation moduli as a result of pore pressure build-up and/or large shear strains. Any mechanical system is more sensitive to dynamic loading as its characteristic frequency becomes closer to the frequency range corresponding to the maximum spectral

values of the excitation. Consequently, both the frequency content of seismic excitation and the evolution of structural frequency characteristics can make a significant difference in the dynamic response of geotechnical structures (Popescu, 2002).

The behaviour of a tower structure situated on a liquefiable soil deposit and subjected to horizontal seismic motion was studied here. The effects of soil variability are accounted for by considering 100 possible realizations of soil property distributions over the analysis domain. All these realizations are sample functions of a two-dimensional, two-variate non-Gaussian random field with prescribed probability characteristics (described in previous section). The two components of the random field represent two soil index properties resulting from piezocone (CPT) field tests, namely normalized cone tip resistance, q_n , and soil classification index, I_c . The effects of frequency content of the seismic motion are introduced by considering two different seismic design spectra recommended by the Uniform Building Code (1994) and corresponding to two different local soil conditions (soil underlying the analysis domain): type-1 spectrum, for rocks and stiff soils, and type-3 spectrum, for soft to medium stiff clays and sands. The seismic accelerations in each group have similar probabilistic characteristics, but differ in individual realizations (e.g. location of peak values). Moreover, the accelerations in each group are scaled to correspond to a wide range of seismic intensities.

All the factors mentioned before (soil variability including variations from one sample to another, seismic loading rate, including variations from one time history to another, and seismic acceleration intensity) are deemed to mimic a realistic design environment, where only some probabilistic characteristics of materials and loads may be known, but not their actual realizations. They induce a significant degree of variability in

the response, which is managed by means of fragility curves. Fragility curves are an illustrative way of expressing the probability of exceeding various thresholds in the response as a function of earthquake intensity.

6.3.2. Seismic Motions

The base input accelerations for this part of the research are generated using a procedure for non-stationary stochastic processes (Deodatis 1996a) capable of simulating seismic ground motion time histories that are compatible with prescribed response spectra and have a prescribed modulating function for amplitude variation. One hundred acceleration time histories are generated to be compatible to the type-1 response spectrum recommended by the Uniform Building Code (1994), and another hundred time histories are compatible with the type-3 response spectrum. Both response spectra are shown in Figure 6.1. All acceleration time histories in each group reflect the same target probabilistic characteristics (e.g. frequency content) and have identical modulating functions (i.e. the same duration of strong motion). The duration of the simulated earthquakes is about 12s, with about 10s of strong ground motion. The input acceleration time histories are then scaled according to predetermined Arias Intensity (Arias, 1970) values to uniformly cover a range between 0.19 and 2.1m/s. This Arias Intensity (I_A) is a measure of the total energy delivered per unit mass during an earthquake, and can be expressed as:

$$I_A = \frac{\pi}{2g} \int_0^T a^2(t) dt \quad (6.1)$$

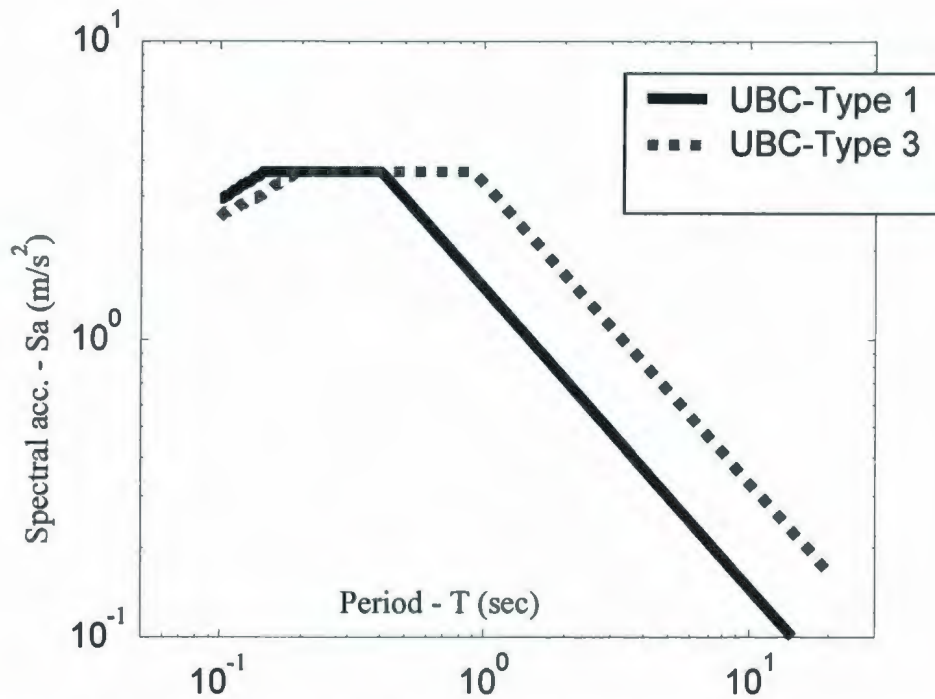


Figure 6.1: Comparison of the response spectra for the acceleration time histories used in the analysis.

where T_e is the total duration of the earthquake, $a(t)$ is the ground acceleration at time instant t , and g is the acceleration due to gravity in the same unit as a . For the frequency content and modulating function used in this study, this Arias Intensity range corresponds to a range of peak ground accelerations (PGA) from about 0.1g to about 0.4g.

6.3.3. Finite Element Model

For every sample function representing a possible realization of the index soil properties over the analysis domain, a nonlinear dynamic finite element (FE) analysis was performed using the multi-yield plasticity constitutive model (Prevost, 1985) implemented in DYNFLOW (Prevost, 2002). The finite element calculations were

conducted in terms of effective stresses, using fully coupled solid-fluid equations (discussed in more details in Chapter 3) for the treatment of saturated porous media. For each FE analysis, the soil parameters in each finite element were estimated based on the values of q_n and I_c at the element centroid, following the procedure described by Popescu et al. (1997). The constitutive parameter values used in the deterministic analyses are listed in Table 6.2. The probabilistic characteristics of soil properties are already mentioned in Section 6.2.2.

The structure and adjacent soil were analyzed using the plane strain assumption. A 12m deep, 72m long saturated sand layer underlying one metre of dry sand layer was included in the analysis domain. To accurately capture the soil spatial variability, the finite element dimensions were selected four times smaller than the correlation distances in all spatial directions. Smaller finite elements were used below the structure, to more accurately capture the stress gradients. Only the saturated sand was considered as variable in the stochastic analysis (the dry soil was assumed uniform). In the analyses the saturated soil was discretized into four-node quadrilateral continuum elements with four degrees of freedom per node (two for solid and two for fluid kinematics). For dry soil, one-phase elements with two degrees of freedom per node were used. There were 1008 two-phase elements used for saturated soil and 34 one-phase elements were used for dry soil. The structure (shown in Figure 6.2) was idealized as a single degree-of-freedom oscillator with a characteristic frequency of 1.4Hz, corresponding to a 7-story building. The foundation was 8m wide and placed at a depth of 1m. The factor of safety for bearing capacity under static conditions was about 13. The earthquake acceleration was applied at the base of the mesh in the horizontal direction. The base was assumed rigid and

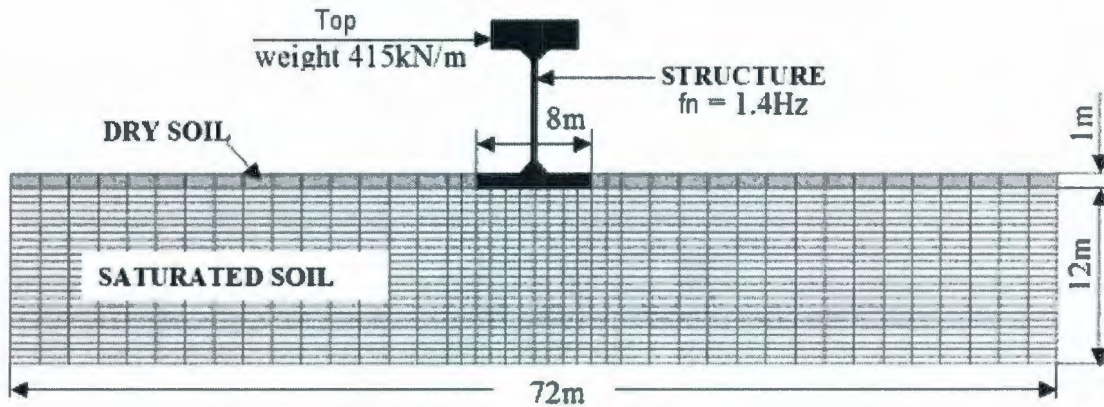


Figure 6.2: Finite element mesh of soil-structure model.

impervious. To simulate free field conditions at the lateral boundaries of the mesh, the degrees of freedom of all pairs of nodes situated at the same elevations at the lateral boundaries were slaved to each other in both spatial directions. Some preliminary analyses were performed (in 2004) to find the optimum mesh. Based on those analyses and the results reported in the literature it was concluded that the mesh used in Figure 6.2 was refined enough to capture proper interface action.

For each stochastic input analysis (involving a specific sample function of variable soil and a specific acceleration time history), a corresponding “deterministic” analysis was performed for comparison using soil properties that were uniform in the horizontal direction and whose values were equal to the average values of the soil properties in the stochastic analysis.

6.3.4. Results and Discussions

6.3.4.1. Pore Water Pressures, Deformations and Accelerations

Some of the analysis results are presented in Figures 6.3 through 6.7 in terms of EPWP ratios, maximum shear strains and deformed meshes. The EPWP ratio is the ratio

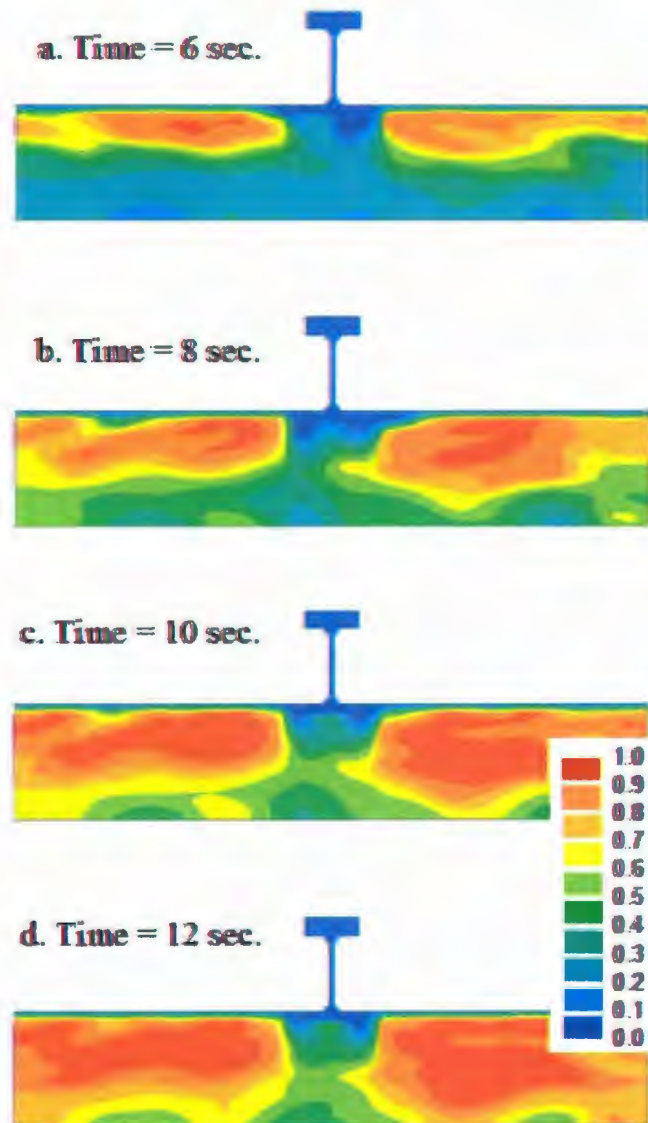


Figure 6.3: Excess pore water pressure contours for variable soil, seismic motion type 1, sample #51 (IA=1.15m/s, PGA=0.28g).

between the predicted excess pore water pressure at certain location and time instant, and the initial effective vertical stress at that location. A value of EPWP ratio close to one indicates soil liquefaction. Figure 6.3 presents the evolution of EPWP ratio for sample #51 subjected to type-1 seismic input, with $PGA = 0.28g$. The soil is predicted to liquefy in the free field, while much lower EPWP's are predicted below the structure. This is believed to be due to higher initial effective stress below the structure. Figure 6.4 presents

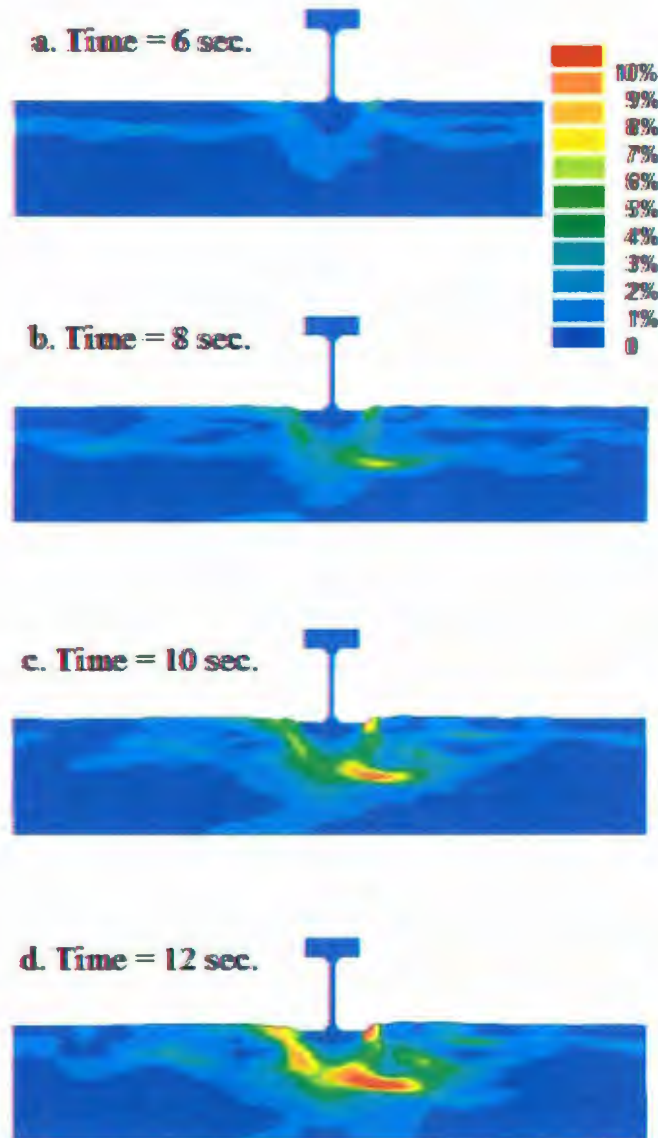


Figure 6.4: Maximum shear strain contours and deformed mesh for variable soil, seismic motion type 1, sample #51. Deformation magnification factor = 3.

the evolution of maximum shear strains for the same sample. The contours indicate a local bearing capacity failure mechanism, with some asymmetries, due to variability of soil strength. Dependence of the computed response on the seismic acceleration intensity is presented in Figure 6.5 in terms of maximum shear strain contours and deformed meshes at the end of the strong shaking period for four different soil samples subjected to type-1 seismic acceleration with various Arias Intensities (sample #25 with $I_A=0.67m/s$,

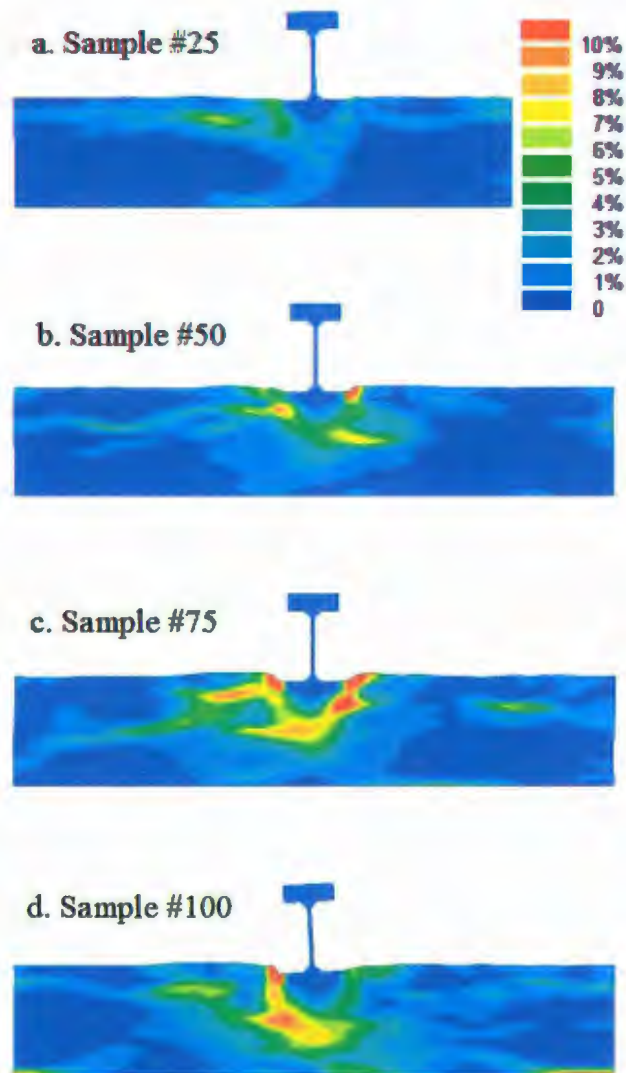


Figure 6.5: Maximum shear strain contours and deformed mesh at time T=10 sec. for variable soil, seismic motion type 1, and various soil samples and seismic motion intensities. Deformation magnification factor = 3.

sample #50 with $I_A=1.14\text{m/s}$, sample #75 with $I_A=1.62\text{m/s}$, and sample #100 with $I_A=2.1\text{m/s}$).

The effects of soil heterogeneity and seismic loading rate are illustrated in Figures 6.6 and 6.7 for sample #51 ($I_A=1.15\text{m/s}$, PGA approx 0.28g). For this level of seismic intensity the EPWP ratio (Figure 6.6) is more affected by the differences in loading rate

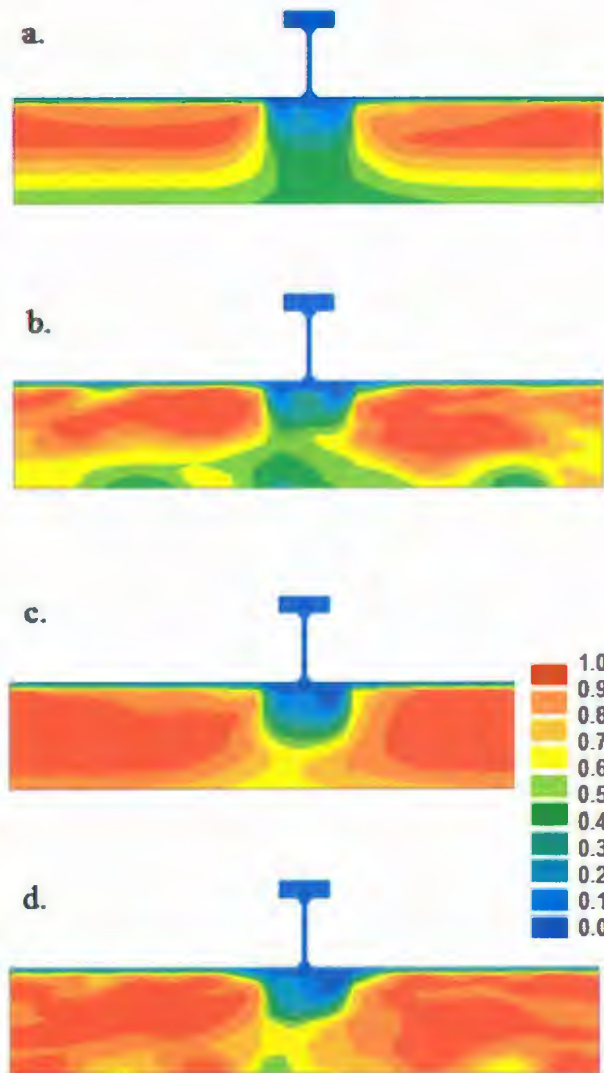


Figure 6.6: Excess pore water pressure contours for sample #51 at time T=10 sec: a. uniform soil, seismic motion type 1; b. variable soil, seismic motion type 1; c. uniform soil, seismic motion type 3; d. variable soil, seismic motion type 3.

(compare a. vs. c. and b. vs. d.) than by accounting (or not) for soil heterogeneity (a. vs. b. and c. vs. d.). Soil heterogeneity has stronger effects on EPWP at lower seismic intensity (Popescu et al. 2005c). However, there is not much difference in the induced EPWP responses in homogeneous and heterogeneous soil for higher earthquake

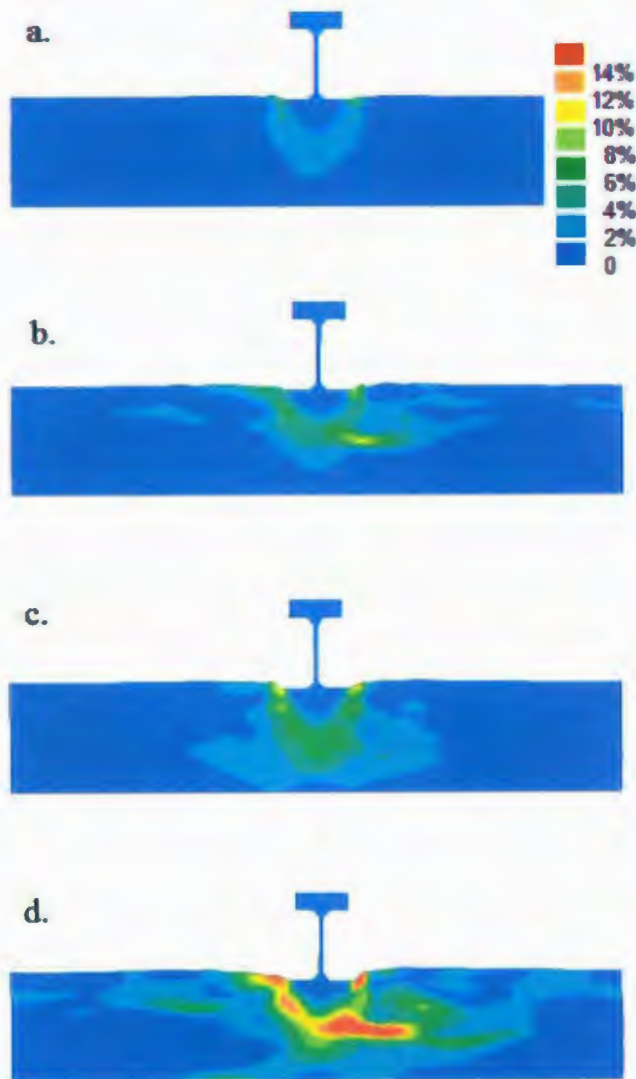


Figure 6.7: Maximum shear strain contours and deformed mesh for sample #51 at time $T=10$ sec: a. uniform soil, seismic motion type 1; b. variable soil, seismic motion type 1; c. uniform soil, seismic motion type 3; d. variable soil, seismic motion type 3. Deformation magnification factor = 3.

intensities especially for type 3 seismic inputs. This is because at higher intensity the EPWP reaches almost one in most of the areas in both the homogeneous and heterogeneous soil. Both the soil heterogeneity and the seismic loading rate are found to significantly influence the computed deformations (Figure 6.7). While the maximum strain contours indicate local bearing capacity failure for all cases, the heterogeneous soil

seems to be affected on a more extended area around the structure than the uniform soil. Due to softening of soil below the structure, the seismic motion is strongly attenuated, especially for large Arias Intensities (I_A), and the acceleration at the base of the structure has less specific energy compared to the input. This is illustrated in Figure 6.8, showing a plot of computed I_A for accelerations predicted at the base of structure vs. I_A of the input accelerations. This aspect of the seismic response is discussed in more detail by Chakraborty et al. (2004b) for tower structures on uniform soil and later, in Section 6.4.5 in this chapter for frame structure on uniform and variable soil. Regarding effects of soil heterogeneity, it can be concluded from the results presented in Figure 6.8 that soil variability leads to significantly larger attenuation of the seismic motion than uniform soil.

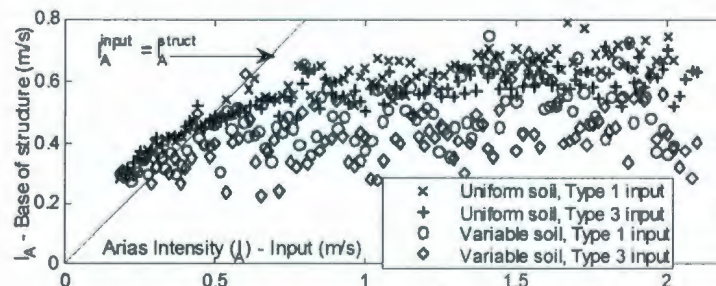


Figure 6.8: Comparison between Arias Intensities of base input accelerations and that of the computed accelerations at the base of the structure.

6.3.4.2. Maximum Structural Displacements

Computed maximum values of structure settlements and rotations are shown in Figure 6.9 for all the 400 cases analyzed. Those results represent earthquake effects in terms of rigid motion of the structure. The results in Figure 6.9 clearly indicate that both

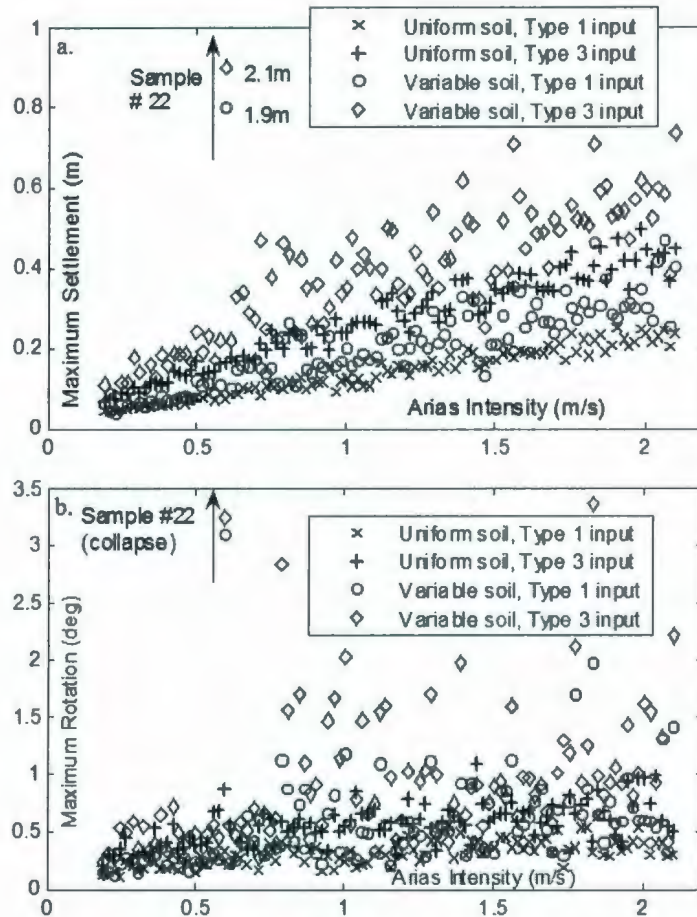


Figure 6.9: Predicted maximum values of structural responses: a. maximum settlement and b. base rotation, for all cases analyzed.

the seismic loading rate and the soil variability affect the structural response. For the entire range of seismic intensities, larger structural settlements and base rotations are predicted for type-3 than for type-1 seismic motion, and for heterogeneous soil than for uniform soil. The results for heterogeneous soil are more scattered due to presence of two uncertainty factors (seismic acceleration and random spatial distribution of soil strength). Complete collapse after 5 to 6s was predicted for sample #22 of heterogeneous soil for both types of seismic input. This was due to presence of an extended loose zone of soil immediately below the foundation. The computed maximum structural responses shown in Figure 6.9 are processed as fragility curves expressing the probability of exceeding

certain thresholds in the response (the procedure used for constructing the fragility curves is presented by Shinozuka et al. 2000).

6.3.4.3. Fragility Curves for the Response Variable

The fragility curves are expressed here in the form of two-parameter lognormal distribution functions. The procedure used for constructing fragility curves is already discussed in Chapter 2 (Section 2.6.5). The fragility curves presented here express the probability of exceeding certain thresholds in the response rather than certain damage levels. Figure 6.10 compares fragility curves for exceeding 20cm settlement and of 0.4 degree base rotations for all cases analyzed. For example, for a seismic input with Arias Intensity $I_A=1.0$, corresponding to a PGA of about 0.25g, one can infer from the fragility curves presented in Figure 6.10a that: (1) for a uniform soil, there are almost no chances of exceeding a 20cm settlement for type-1 seismic input and about 95% chance for type-3 input, and (2) for a variable soil with $CV=0.5$ the settlements would exceed 20 cm with a probability of about 55% for type-1 input and almost surely for type-3 input. Fragility curves for various levels of settlements and base rotations are presented in Figure 6.11 for one of the four cases analyzed (variable soil and type-3 seismic motion).

6.3.4.4. Combined Damage Curve

A fragility curve or fragility function is one way of expressing the probability of the degree of structural damage as a function of load intensity. This conditional probability is expressed by the following equation:

$$\text{Fragility function} = P(LS|AI=AI_i) \quad (6.2)$$

where LS is the limit state of damage level of the structure, AI is the load intensity (Arias Intensity) and AI_i is a realization of the load intensity. In this section a way of expressing combined damage probability is presented. For extremely important lifeline structures such as a nuclear reactor or a communication tower, where one and/or more

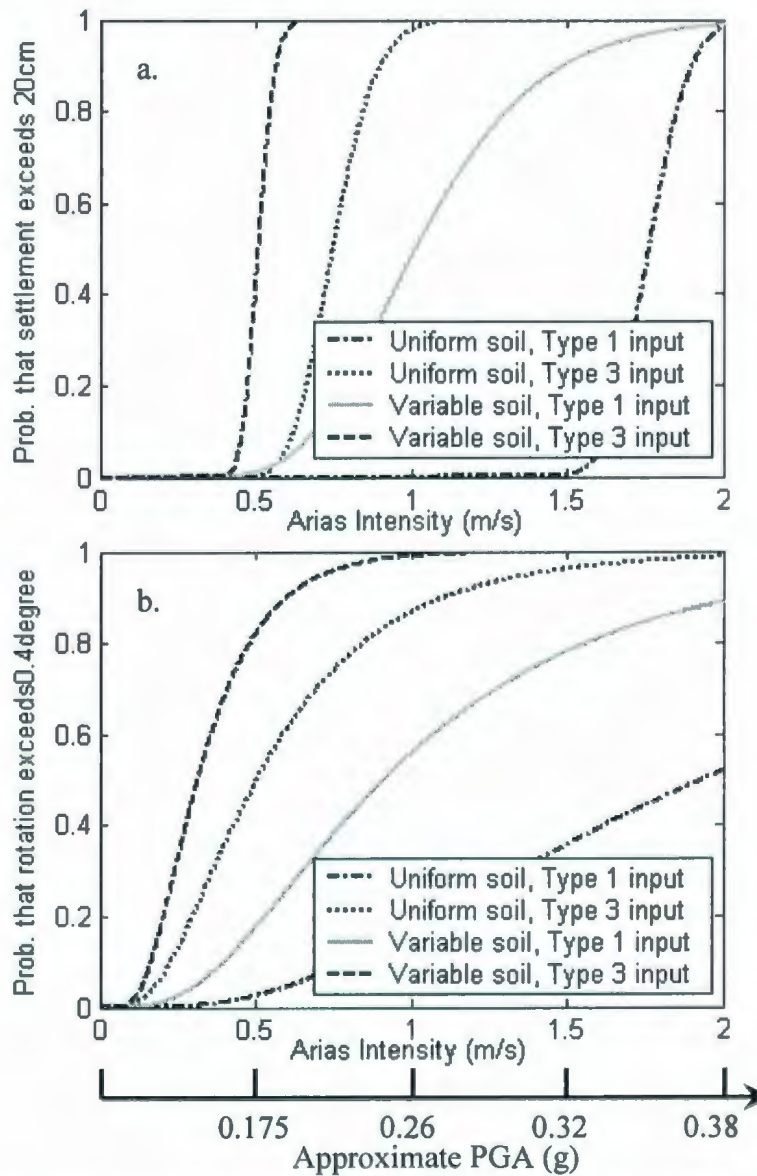


Figure 6.10: Comparison between analysis results for various cases in terms of fragility curves: a. settlements; b. rotations.

exceeding responses can cause partial or total failure of the structure, this type of damage curve can provide a quick assessment of the probability of damage. This method is based on a basic probability theory and is briefly discussed here.

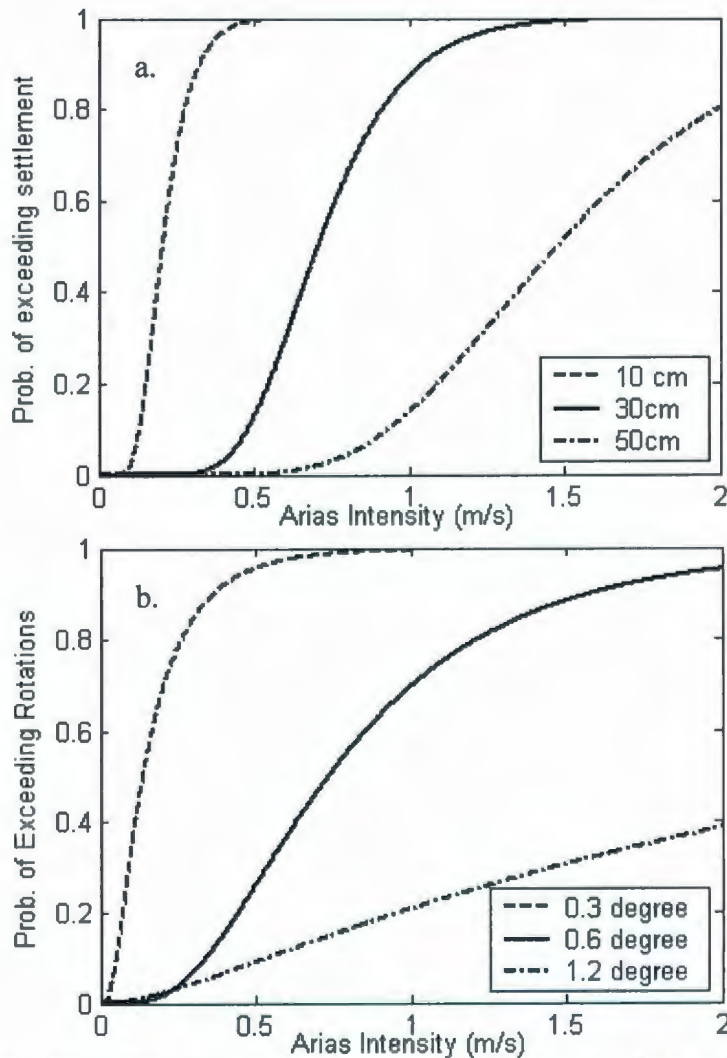


Figure 6.11: Fragility curves for structure on randomly variable soil deposit subjected to type 3 seismic motion: a. settlements; b. rotations.

Let the event S express the damage of the structure due to maximum settlement exceeding some given limits, and the event R express the damage of the structure due to maximum base rotation exceeding some given limits. It is also assumed that the damage of the structure can be due to maximum settlement, or maximum base rotation, or both

being exceeded. This is explained by the Venn diagram in Figure 6.12. The total sample space is shown by the rounded rectangle (C). Circles S and R are the events of failure of the structure due to maximum settlement and maximum base rotation exceeding

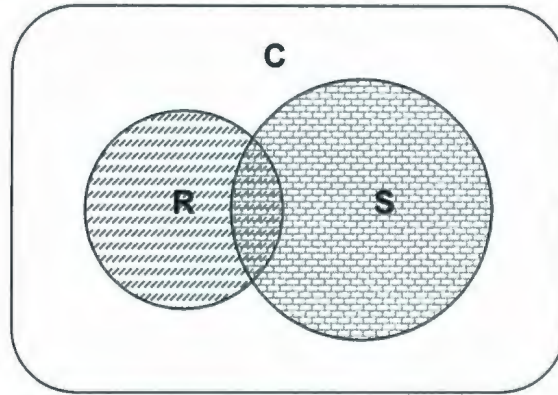


Figure 6.12: Venn diagram of damages.

corresponding permissible limits, respectively. Therefore, the space C is the event of no failure. Therefore, the probability of failure due to maximum settlement or maximum base rotation or both exceeding corresponding permissible limits is $P(S \cup R) = P(S) + P(R) - P(S \cap R)$, the union of S and R . And, the probability of failure due to both the maximum settlement and maximum base rotation exceeding permissible limits is $P(S \cap R)$, the intersection of S and R .

Based on the above theory, two types of combined damage curves are generated: Type-I and Type-II damage curves. The fragility function in the Type-I damage curve is the conditional probability of exceeding specific levels of S or R or both S and R , i.e. $(S \cup R)$. This conditional probability is expressed by the following equation:

$$\text{Type-I fragility function} = P(LS_{(S>S_i, UR>R_i)} | AI = AI_i) \quad (6.3)$$

where S is the maximum foundation settlement at arias intensity= AI_i , S_i is the limiting value of settlement (10cm, 15cm, and 20cm in this study; listed in Table 6.3), R is the maximum foundation rotation at arias intensity= AI_i , and R_i is the limiting value of

foundation rotation (0.3^0 , 0.4^0 , and 0.5^0 in this study, listed in Table 6.3). Similarly, the fragility function in the Type-II damage curve is the conditional probability of exceeding both the specific level of S and R , i.e. $(S \cap R)$ for a given load intensity. This conditional probability is expressed by the following equation:

$$\text{Type-II fragility function} = P(LS_{(S>S_i \cap R>R_i)} | AI = AI_i) \quad (6.4)$$

From the Type-I damage curve we can determine the probability of damage, due to maximum settlement exceeding a permissible settlement or maximum base rotation exceeding the permissible base rotation, or both exceeding their permissible limits. On the other hand, the Type-II damage curve expresses the probability of exceeding both the permissible settlement and base rotation. This type of fragility curve is important for those structures, where significant damage is only possible when both settlement and base rotation exceed their corresponding limiting values.

Figure 6.13 shows the Type-I combined damage curve. Figure 6.13a shows the Type-I damage curve for a level-2 damage limit. Similarly, Figure 6.13b shows the Type-I damage curve exceeding the level-3 permissible limit for settlement and level-2 limit for rotation. Figure 6.14 shows the Type-II combined damage curves. Figure 6.14a shows the Type-II curve for level-2 damage limits. Similarly Figure 6.14b shows Type-II curve for a level-3 damage limit for settlement and level-2 damage limit for rotation.

6.3.4.5. Design Recommendations

The performance of a tower structure resting on a strip footing has been studied in the previous sections. This numerical study supported some of the findings obtained from numerical and centrifuge test results reported in previous chapter. Such as: a) more

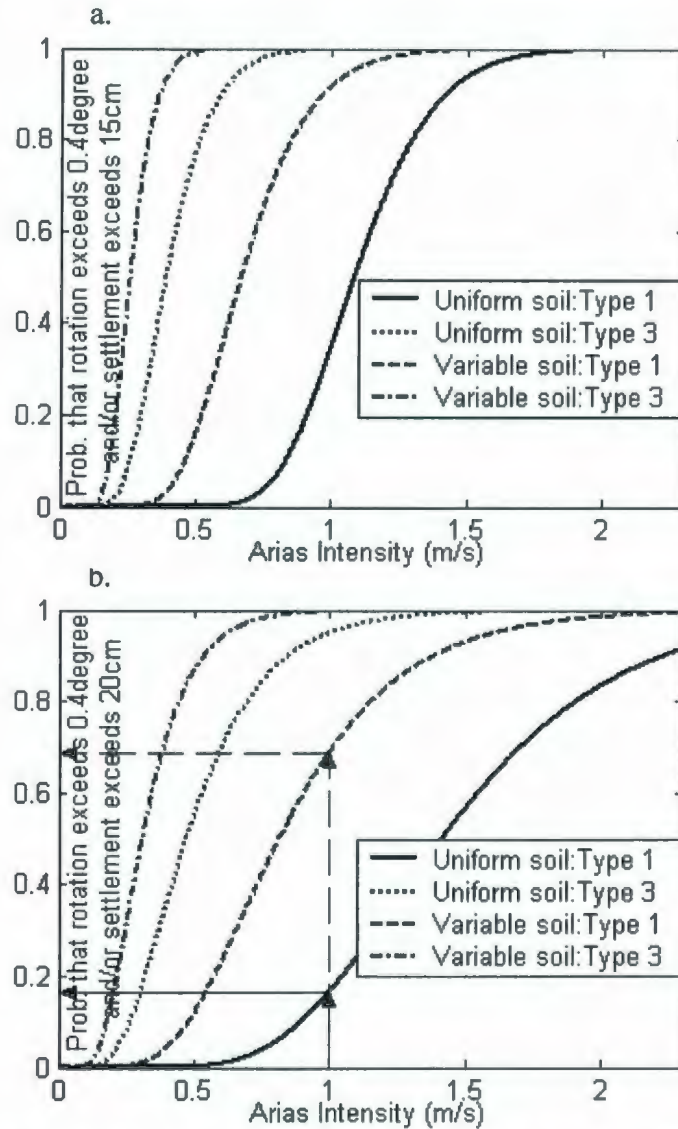


Figure 6.13: Type-I damage curve: probability of damage due to exceeding a. level-2 maximum settlement and/or level-2 maximum base rotation; b. level-3 maximum settlement and/or level-2 maximum base rotation.

EPWP build-up in heterogeneous soil than that in corresponding homogeneous soil; b) larger predicted structural damage when accounting for soil variability as compared to assuming homogeneous soil; and c) due to soil softening after build-up of pore pressures, the characteristic frequency of the soil-structure system goes down to values close to the dominant frequency of low frequency inputs (e.g. type-3 input in this study), and therefore considerably more structural damage is predicted for this type of seismic

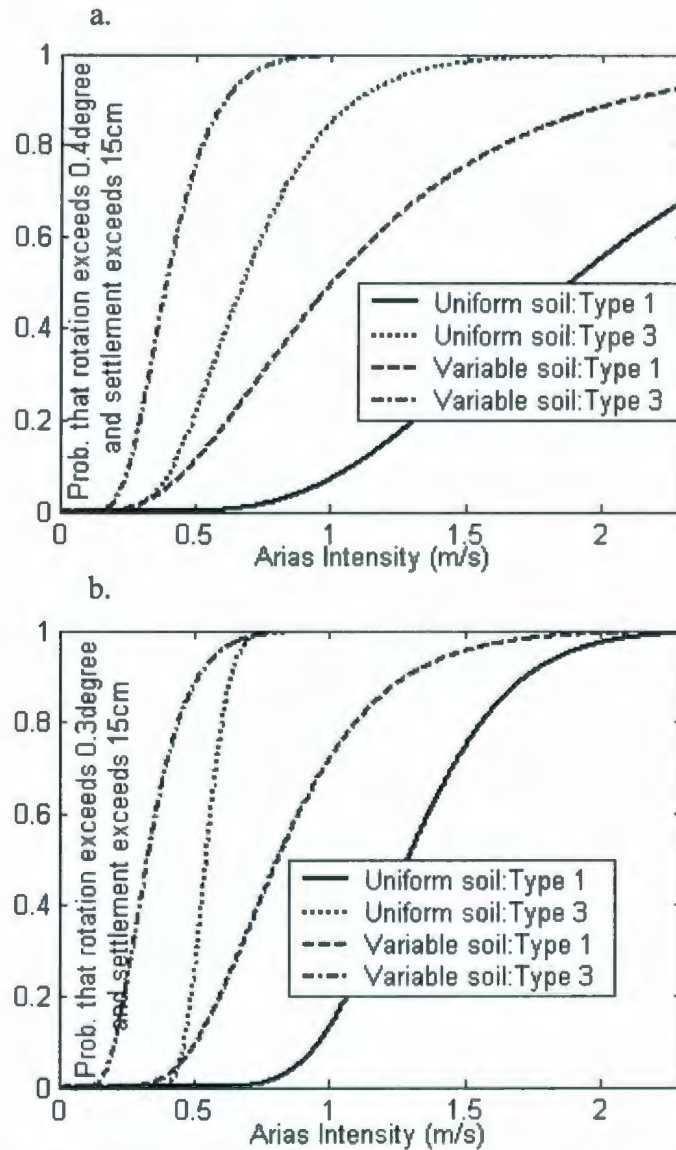


Figure 6.14: Type-II damage curve: probability of damage due to exceeding a. both level-2 maximum settlement and level-2 maximum base rotation; b. both level-2 maximum settlement and level-1 maximum base rotation.

motion. The analysis results are presented using the fragility curves and combined damage curves. These curves express the probability of exceeding certain thresholds in the response. The limiting Arias Intensity values for 1%, 5% and 10% probability of exceeding thresholds are presented in tabular form for design purpose for all the analysed cases. The limiting Arias Intensity is the value of I_A which has a certain probability of exceeding the thresholds of response in a particular soil conditions. The Arias Intensity

values for total settlements and rotations exceeding certain threshold levels are tabulated in Table 6.4 and 6.5 respectively. Fragility curves from where those Arias Intensity values estimated are shown in the Appendix-A. From the fragility curves it can be concluded that a structure situated on variable soil and subjected to type-3 input motion is the most vulnerable case among all the cases studied here.

How might these curves be useful for design? Suppose, for illustration purposes, that the Arias Intensity corresponding to the design earthquake is 1m/s , and that type-1 acceleration is warranted by deeper soil strata. Let's also assume that a limiting value for settlements is 20cm and the limiting value of base rotation is 0.4° . A certain degree of damage to the structure is possible when any of those limits are exceeded. Therefore, the Type-I combined damage curve (Figure 6.13b) can be used to calculate the probability of damage. From the damage curve for uniform soil and type-1 input acceleration, the probability of exceeding either limit is 17% . As soil properties in natural soil deposits randomly vary from one point to another, a fragility curve accounting for this aspect should be considered. For the degree of soil variability assumed in this study, the damage probability for the same structure results about 69% .

6.4. Frame Structure on Heterogeneous Soil

6.4.1. General

The last part of this study focuses on the reliability analysis of a frame structure resting on heterogeneous soil. The Monte Carlo simulation methodology is used for this purpose. Two different aspects of responses are studied here. First, the spectral

amplification of seismic ground motion has been determined for heterogeneous soil and uniform soil. Updated design guidelines are provided for spectral amplification of seismic ground motion. Next, equivalent uniform soil relative densities to be used in deterministic analysis have been determined for a wide range of heterogeneous soil, based on the results of structural damage. Here, total and differential settlements are of primary interest. These responses for the structure on heterogeneous soil are compared with the responses in a structure resting on uniform soil of various relative densities. Geotechnical design recommendations are provided for structures on liquefiable soil deposits, by directly including the effects of soil-structure interaction. Those recommendations can be used in design to consider the effects of small scale soil heterogeneity.

6.4.2. Seismic Input Acceleration Time Histories

The database of the strong motions used in this research includes a total of 90 seismograms recorded from different earthquakes worldwide in the last four decades. Bazzurro and Cornell (2004) concluded that using about 10 input seismograms (properly selected) will give sufficient accuracy in estimating median amplification function. The magnitude, location, earthquake name, and type of soil where the accelerations are recorded for the selected seismograms are shown in Table A.1. These seismograms were obtained from COSMOS virtual data centre (<http://db.cosmos-eq.org/scripts/default.plx>). These seismograms were recorded either in rock or very stiff soil, which represents the condition below the base of the finite element model (soil underlying the analysis domain). All the selected seismograms cover a wide range of earthquake input energy. The earthquake energy is expressed here in terms of Arias Intensity (Arias, 1970). The

Arias Intensity (I_A) was found to provide a better measure of earthquake severity than the peak ground acceleration (PGA) and root-mean-square acceleration (Koutsourelakis et al., 2002). The I_A is usually expressed in the unit of velocity (e.g. m/s). For ease in analysing the results, the input time histories were divided into 6 groups based on Arias Intensity: a) $I_A < 0.05\text{m/s}$, b) $0.05 \text{ m/s} \leq I_A < 0.1 \text{ m/s}$, c) $0.1 \text{ m/s} \leq I_A < 0.25 \text{ m/s}$, d) $0.25 \text{ m/s} \leq I_A < 0.5 \text{ m/s}$, e) $0.5 \text{ m/s} \leq I_A < 1.0 \text{ m/s}$ and f) $I_A > 1.0\text{m/s}$. Fifteen real free field recorded acceleration time histories were selected in each group of I_A . The calculated characteristics of the seismograms are shown in Table A.2. The response spectra with 5% damping for all the 90 acceleration time histories with the mean response spectrum (median of original value) are shown in Figure 6.15a. For the stochastic analysis, 18 input time histories (3 seismograms from each I_A group) are selected in such a way that the mean response spectrum of those 18 seismograms matches with the mean response spectrum for all 90 inputs. The response spectra with 5% damping for the selected 18 time histories for the stochastic analysis are shown in Figure 6.15b.

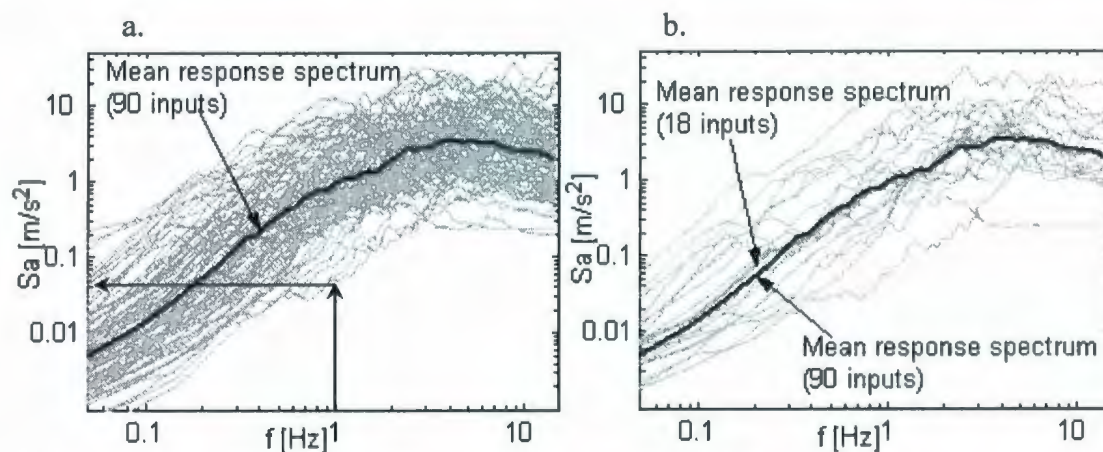


Figure 6.15: Response spectra at 5% damping of the selected records: a. for uniform soil; b. for variable soil. The arrows at 1Hz frequency in figure a) shows how $S_a(1.0)$ values in Figure 6.24 are obtained.

6.4.3. Finite Element Model

The finite element calculations are conducted in terms of effective stresses, using the multi-yield plasticity constitutive model (Prevost 1985) implemented in DYNFLOW (Prevost 2002). A 28m deep, 60m long saturated sand layer underlying a 2m deep dry sand layer is included in the analysis domain. Smaller finite elements are used below the structure, to more accurately capture the stress gradients. Only the spatial variability of saturated sand is considered in the stochastic analysis (the dry soil is assumed uniform, same as in the study for the tower structure). The finite element mesh is shown in Figure 6.16. Two different frame structures, with characteristic periods of 0.29s and 0.78s respectively, are considered in the analyses in this part of the research. While modelled as single frames in the finite element analysis, the fundamental periods of the two structures corresponds to a 3-storey and an 8-storey building. The structure is placed on two isolated footings of 2m width. The depth of the foundations is 2m. The

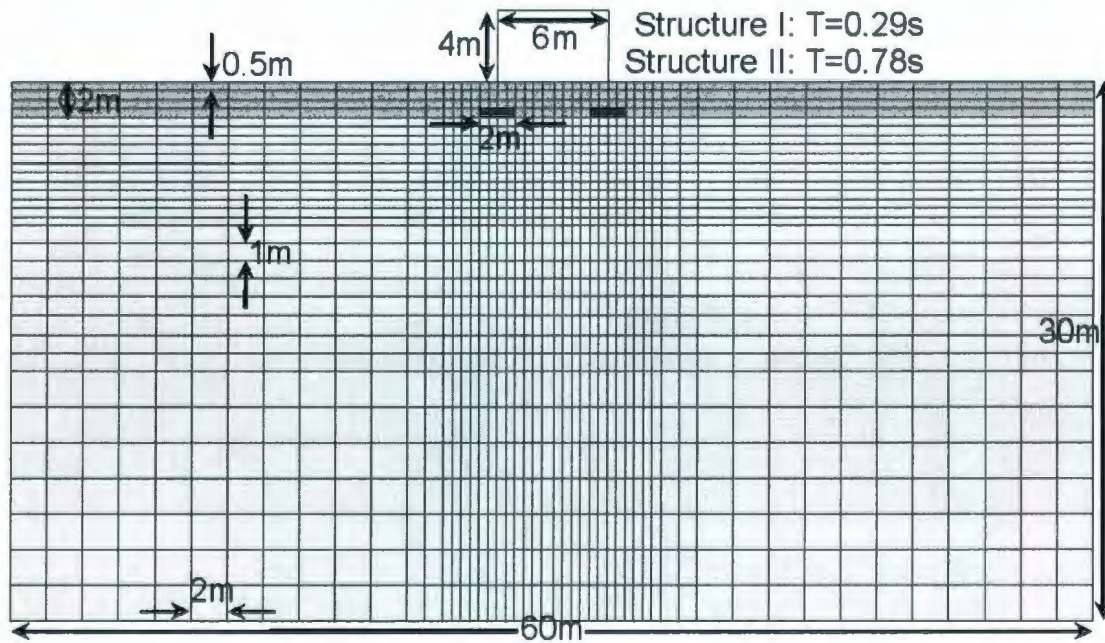


Figure 6.16: Finite element mesh of soil-structure model.

factor of safety for bearing capacity under static conditions is greater than 10 (in uniform soil). The earthquake acceleration is applied at the base of the mesh in the horizontal direction. The base is assumed rigid and impervious. To simulate free field conditions at the lateral boundaries of the mesh, the degrees of freedom of all pairs of nodes situated at the same elevations at the lateral boundaries are slaved to each other in both spatial directions.

The stochastic analyses were performed for the heterogeneous soil for two different average relative densities of the soil (i.e., 45% and 85%). A wide range for coefficient of variation (CV) of q_n are considered in the analysis (CV=0.2 to 0.625). For each stochastic input analysis (involving a specific sample function of variable soil and a specific acceleration time history), a corresponding “deterministic” analysis is performed for comparison using soil properties that are equal to the average values of the soil properties in the stochastic analysis. For each FE analysis, the soil parameters in each finite element are estimated based on the values of q_n and I_c at the element centroid, using the correlation formulas shown in Section 6.2.1. The structure and adjacent soil are modelled and analyzed using the plane strain assumption. The saturated soil is discretized into four-node quadrilateral continuum elements with four degrees of freedom per node (two for solid and two for fluid kinematics). For dry soil, one-phase elements with two degrees of freedom per node were used. There were 1350 two-phase elements used for saturated soil and 192 one-phase elements were used for dry soil. For the analyses with ground water level deeper than 30m (unsaturated soil), only one-phase elements (1542 number) were used. The structure was discretized using 2-node beam elements with three degrees of freedom per node (two for displacements and one for rotation). There were 34

beam elements used for modelling the frame structure. The structure mass is applied as nodal masses on the horizontal beam at the roof level.

6.4.4. Replacement Models for Settlements

6.4.4.1. Response Surface Method

Various researchers used a statistical methodology called design of experiments (DOE) as an efficient tool for identifying the most significant parameters contributing to a certain structural response and for modelling, among which: Azizian (2004) used Response Surface Method to model submarine slopes; Nobahar (2003) used factorial method with centre point and Face-Centred Central Composite Design (CCD). A more detailed description of the method used here was already presented in Chapter 2. In the preliminary phase of this study (not presented in this thesis), factorial design method was used for finding the significant factors, which control the responses. A two-level full factorial design gives a clear visual idea about which factor is significant for each response. Four important factors were selected for this study. In a 2-level full factorial design with four factors, 2^4 or 16 experiments are required. From the preliminary analysis it was observed that there was significant nonlinearity present in the models for the studied range of Arias Intensity. Therefore, a more advanced method (Face-Centred Central Composite Design) and four smaller ranges of Arias Intensity were used for formulating Response Surface models. Different levels of the factors in various response surface models presented here are shown in Table 6.6.

In Face-Centred Central Composite Design with four factors and without any replication, 30 design points and experiments are required. Each finite element analysis is

considered here as an experiment and each combination of factors are considered here as design points. Four models (Replacement Model-I, Replacement Model-II, Replacement Model-III, and Replacement Model-IV) are formulated without considering any replication. In the Monte Carlo simulation, 5 different sample functions were generated for each CV value to express the soil variability. Therefore, five replications (one with each sample functions) were used for Replacement Model-IIIA to consider the effect of the variable location of loose soil pockets in the heterogeneous soil with the same CV value. However, in the study there were two random quantities- realization of spatial variability of soil properties and realization of seismic acceleration. First source of randomness was considered in the Replacement Model-IIIA, but the realization of seismic acceleration time history was not considered in that model. Therefore another model (Replacement Model-IIIB) was constructed where both the random quantities were considered. In this Replacement Model-IIIB, ten different acceleration time histories and ten different sample functions were used in formulating that model. The design layout for the experiments with the responses obtained from finite element analyses for Replacement Model-I are presented (as an example) in Table 6.7. Similar results for other Replacement Models are shown in Appendix-A (Tables A.3-A.7).

6.4.4.2. Statistical Analysis of Results and Discussions

The results are analysed and discussed in this section. As mentioned earlier, the DOE was used as a tool to determine the significant factors and Response Surface Models for different responses. Design-Expert® software version 7.1.3 was used to statistically analyse the responses and fit the response surface model. The procedure for

formulating a response surface model and determining significant factors were already discussed in more detail in Section 2.6.6. These formulated models are only valid in the studied ranges (shown in Table 6.6) and can only be used in practical engineering applications to approximate complex behaviour in those ranges. Two different responses are considered here: maximum total settlements of left footing, and maximum differential settlements. The Analysis of Variance method (ANOVA) was used for determining whether the formulated models are appropriate or not. In some cases, the residuals of the responses were not uniformly distributed. In those cases, the responses were transformed. Natural log or inverse square root transformation for the responses of maximum total settlements and maximum differential settlements gives uniform distribution of the residuals. After analysing the results using Design-Expert® software version 7.1.3, different models were formulated for both the responses. The regression equations of Response Surface Models are presented in Tables 6.10. In case of both the responses (maximum total and differential settlements), all the four factors considered here, i.e. *A* (soil relative density), *B* (Coefficient of variation of q_n), *C* (Arias Intensity) and *D* (period of the structure), are significant. It has been observed that maximum total settlement goes down with increases in soil relative density when all the other three factors are constant. This is believed to be due to increase in soil resistance with the increase in soil relative density which ultimately reduces the total settlements in the structure. On the other hand, maximum total settlement goes up with increases in Arias Intensity (settlements increases here due to increase in input seismic energy), CV of q_n or fundamental period of the structure when other three factors are constant. The effects of different factors on

maximum differential settlements are same as that in the case of maximum total settlements.

It was found for Replacement Model-III, IIIA and IIIB that all three models (one without any replication and other two with replication) predicted almost similar results. Since five or ten sample functions are very low number of samples for a Monte Carlo simulation. This might affect the range of responses in Monte Carlo Simulation and might ultimately affect the accuracy of formulated response surface models. Therefore, further verifications of the model should be performed before using these models for calculating responses. There are a few limitations for these formulated models. They are as follows: a) these Response Surface models are only valid in the studied ranges of the factors; b) Replacement Model-I, Replacement Model-II, Replacement Model-III, Replacement Model-IIIA and Replacement Model-IV are formulated for a particular acceleration time history neglecting the randomness in seismic input. Therefore, these models are not valid (also observed in Section 6.4.4.3 while model validation) for all earthquakes. They are valid for a class of seismic motions (reference of seismic motions are shown in Table A.1) similar to the one used for deriving these models; c) Replacement Model-IIIA is formulated for structure-I only. Therefore, this model is valid for structure-I or structure with similar characteristic; d) a very limited number (1, 5 or 10) of sample functions are used here to consider the soil variability in the model. Therefore, it might induce some bias in the formulated models.

6.4.4.3. Validation of Response Surface Model (RSM)

After formulating all the RS models, all the models are validated for some input values of various factors which are not used for constructing that model. Each model is validated for 20 cases. The first 10 analyses for validation have been performed using one input acceleration time history (the one which was used for formulating that model) after scaling that in desired Arias Intensity and by changing the value of other factors.

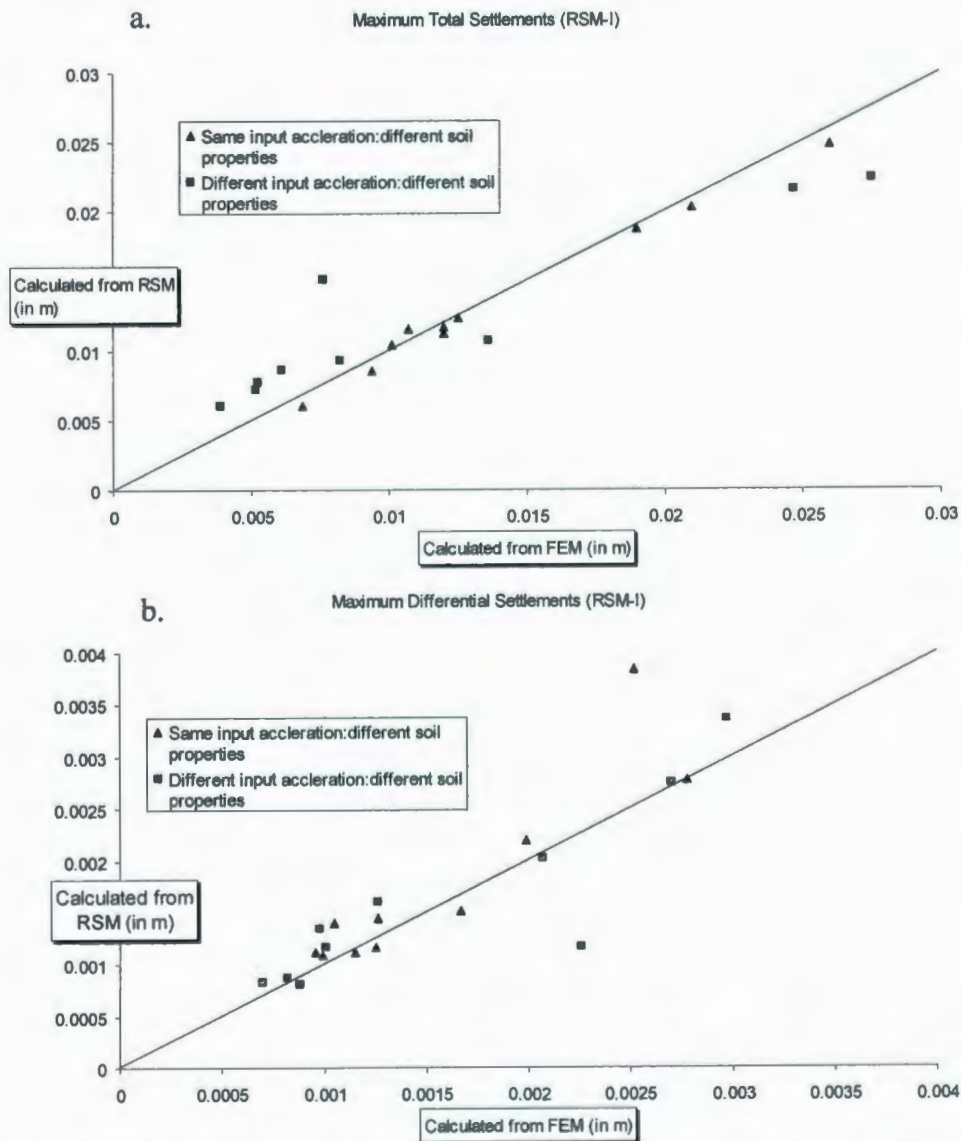


Figure 6.17: Scatter plot for the validation of Replacement Model-I.

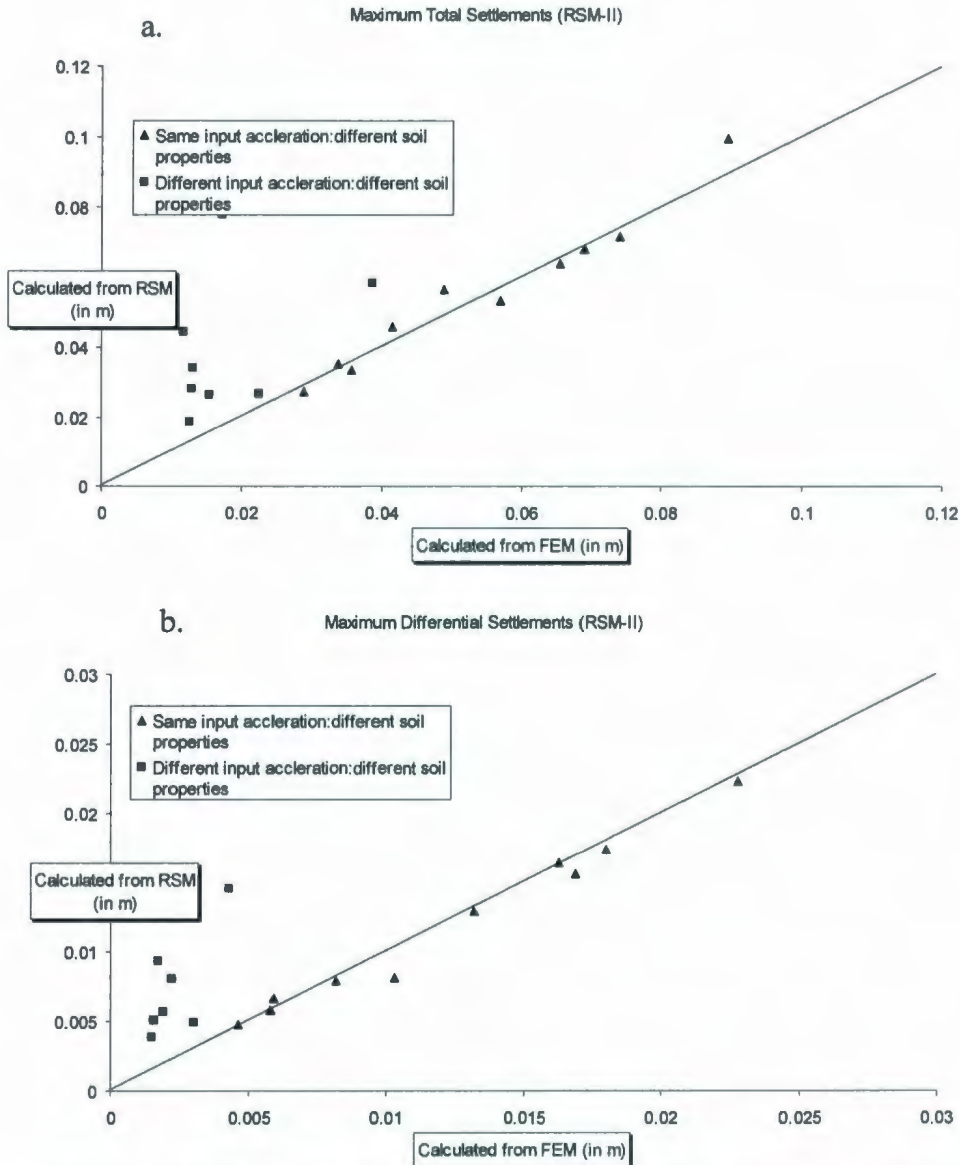


Figure 6.18: Scatter plot for the validation of Replacement Model-II.

Remaining 10 analyses have been performed using arbitrarily selected input time histories (the one which has an Arias Intensity very close to the value of selected Arias Intensity) after scaling for the design Arias Intensity. The input values of all the four factors are selected in such a way that they are distributed uniformly in the ranges used for formulating that model. The selected input values of all the factors and the results obtained from finite element analysis and Replacement Model-IV are presented (as an

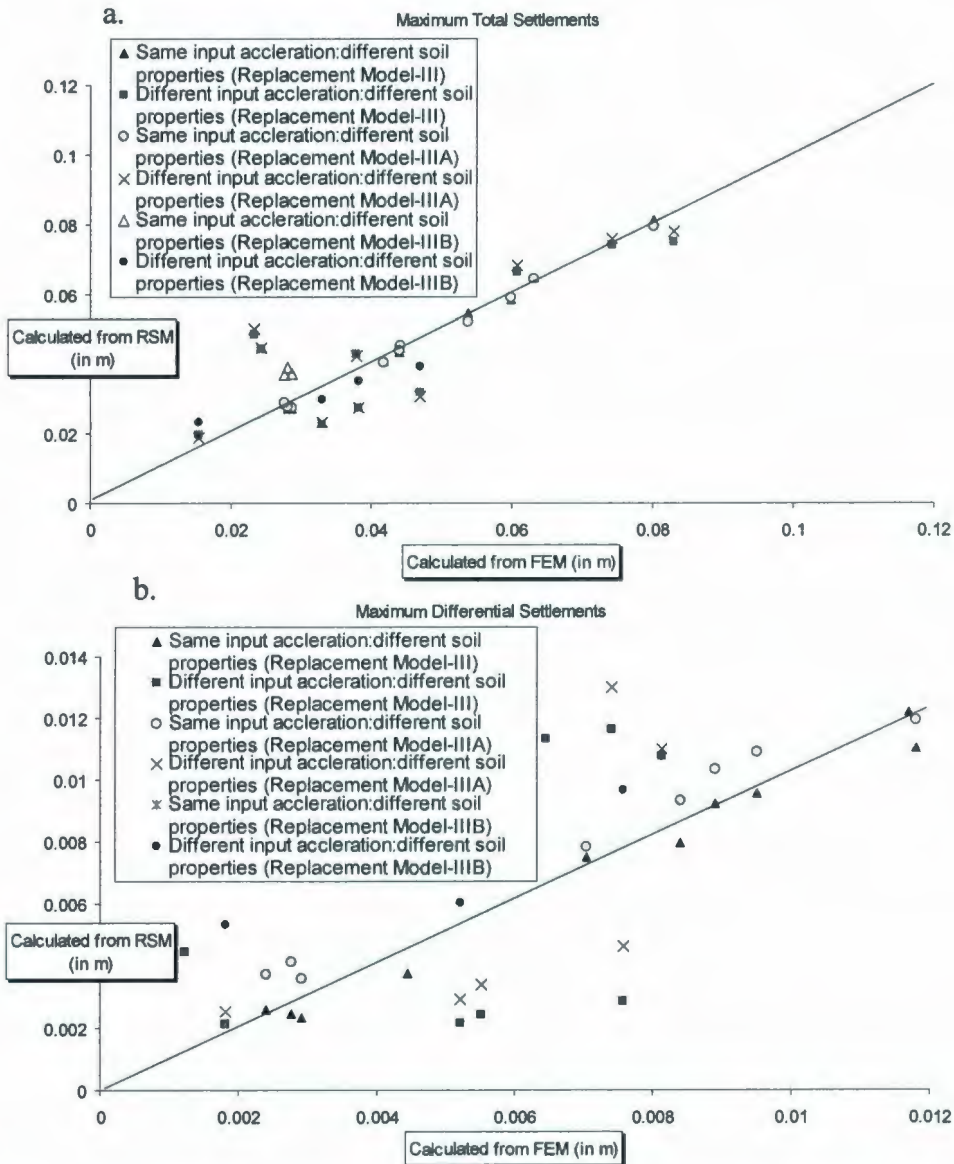


Figure 6.19: Scatter plot for the validation of Replacement Model-III, IIIA and IIIB.

example) in Table 6.9. Similar results for other Replacement Models are shown in Appendix-A (Tables A.8-A.10). The results are plotted in Figures 6.17 to 6.20 as a scatter plot between the results obtained from finite element analyses and that from Replacement models. From the model validation results it has been observed that, a) Replacement Models for predicting maximum total settlement is more accurate than that for calculating maximum differential settlements; b) In most cases, the Replacement Model is predicting

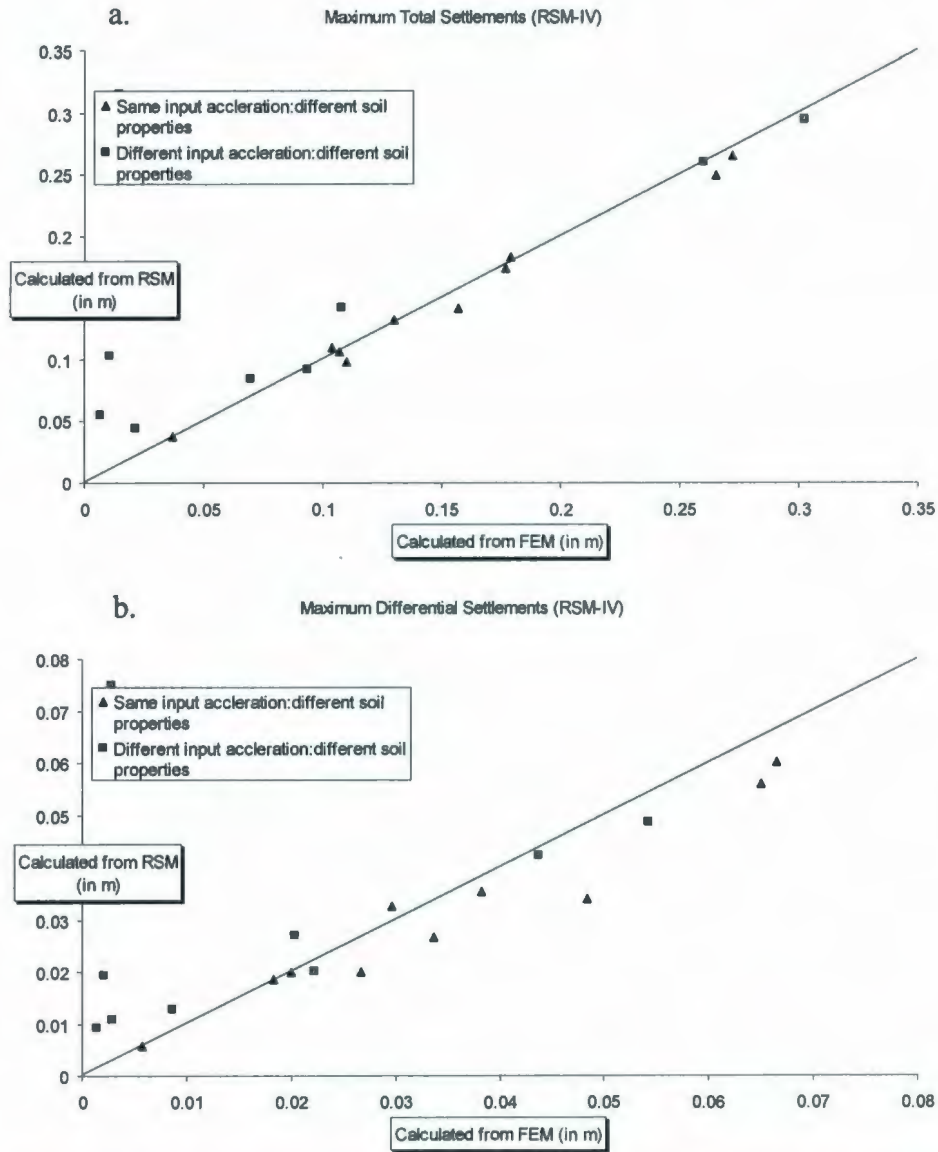


Figure 6.20: Scatter plot for the validation of Replacement Model-IV.

very close results as that obtained from finite element analysis with same (which is used for formulating that Replacement Model) input acceleration time history; c) in some cases for the analysis with different (which is not used for formulating that RSM) input acceleration time history, the predicted results from RSM is not always in agreement with that obtained from FE analyses. Most of presented models (Replacement Model-I, Replacement Model-II, Replacement Model-III, Replacement Model-IIIA and

Replacement Model-IV) are not able to consider the effect of time history to time history variation in frequency content and duration of the earthquakes. In some cases the error is as large as 50%-200%, especially in the case of lower magnitude of settlements. Therefore, these models are unable to accurately predict the maximum total and differential settlements for those cases.

6.4.5. Site Amplification Study

After determining the significant factors and replacement models using DOE, a parametric study on the spectral amplification of seismic ground motion was performed. The study was performed for the ranges of the previously mentioned (Section 6.4.4) four factors. The results for the structure, with a fundamental period of 0.29s and situated on a uniform soil relative density of 45%, are presented here as the base case results.

6.4.5.1. Base Case- Uniform Soil

For the base case (soil relative density=45%), 90 seismograms were used in the analyses. The effect of the soil condition was studied in terms of a site-specific, frequency dependent amplification function, $AF(f)$, where f is the oscillator frequencies of interest for engineering structure. For each analysis, the $AF(f)$ was computed by dividing the spectral acceleration ($Sa^{response}$) of the responses (at the base of the structure level) by the spectral acceleration of corresponding input acceleration time histories (Sa^{input}); i.e. $AF = (Sa^{response}) / (Sa^{input})$. The spectral accelerations were calculated for 5% damping. This $AF(f)$ was calculated for both in the free field (node 4, shown in Figure

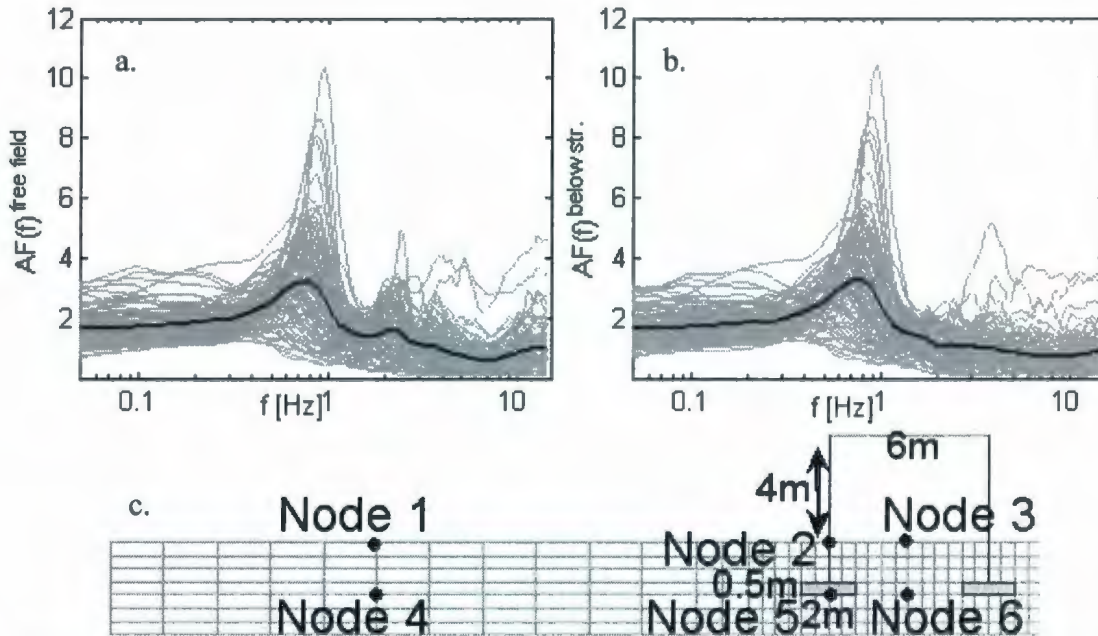


Figure 6.21: Amplification functions for loose saturated soil ($D_r=45\%$) site: a. Free field- Node4; b. Below structure- Node5; c. Partial finite element mesh showing output node locations.

6.21c) and below structure (node 5). The 90 amplification functions along with the mean curve (dark line in Figure 6.21) for base case ($D_r=45\%$) are shown in Figure 6.21. The two peaks are prominent (especially in the free field) at about 0.9Hz and 2Hz identified the first two resonant frequencies of the system.

The amplification functions are sorted based on Arias Intensity (AI) to visually identify the dependence of $AF(f)$ on these intensity measures of input acceleration time histories. They are divided into six different AI groups as mentioned earlier in Section 6.4.2. The mean of all these six groups, with the mean of all 90 cases, are shown in Figure B.1 (shown in Appendix B). It has been observed that a high value of amplification is observed for low intensity input time histories and vice versa. It is also observed that as the earthquake intensity increases the frequency where maximum AF occur, continuously shifted towards lower frequency. This is believed to be due to

reduction of characteristic frequency of the soil deposit with the increase in earthquakes intensity.

6.4.5.2. Effect of the Presence of Structure:

Figure 6.22 illustrated the comparison between Arias Intensity (I_A) of base input accelerations and that of the computed accelerations at the base of the foundation level. It expresses the total earthquake energy transfer from input to that at the base of the structure level. During an earthquake, due to build-up of EPWP in saturated soil, softening causes attenuation of seismic energy especially for large Arias Intensities. However, for the structures and soil types analyzed here there is no significant difference between free field Arias Intensity and that at the base of the structure (shown in Figure 6.22a). Results for the structure situated on loose saturated soil are shown in the Figure as an example. Similar results are also observed for structure resting on other type of soil studied here (e.g., structure on dense saturated or dry soil, structure on loose dry soil etc.). Therefore, it can be concluded that, there is no significant effect of the presence of structure on resulting Arias Intensity for the case analysed in this study. A possible explanation is that the dominant frequency of the structures analysed here are much higher than the dominant frequency of the soil deposit (after it softens due to build-up of EPWP). Therefore, the presence of structure is not causing any significant effect on modifying response Arias Intensity at the foundation level.

6.4.5.3. Effect of Water Table Depth:

The mean amplification functions (based on Arias Intensity groups), along with the mean curve of 90 amplification function for unsaturated loose ($D_r=45\%$) cohesionless soil, are shown in Figure B.2 (shown in Appendix B). From the comparison with Figure B.1 it has been observed that $AF(f)$ are higher in amplitude for unsaturated soil than that in saturated soil. Figure 6.22b shows the comparison of Arias Intensity (I_A) while seismic waves travelling through unsaturated and saturated cohesionless soils. In most of the analyses, Arias Intensity values in the free field responses in saturated soil are less than that in the unsaturated soil. Because, in unsaturated soil this reduction is due to soil nonlinearity only and in saturated soil this reduction is due to both the soil nonlinearity and build-up of EPWP. For higher Arias Intensity input earthquakes, where there is significant EPWP build-up in saturated soil, this difference is larger. For example, where input Arias Intensity is larger than $1.1m/s$ there is a significant reduction in the earthquake energy in the responses at the level of foundation for saturated soil. However, in unsaturated soil there is no significant reduction in earthquake energy in the responses.

6.4.5.4. Effect of Soil Relative Density:

The mean amplification functions (based on Arias Intensity groups), along with the mean curve of 90 amplification function for dense ($D_r=85\%$) saturated cohesionless soil, are shown in Figure B.3 (shown in Appendix B). From the comparison with Figure B.1, it has been observed that $AF(f)$ is higher in amplitude for dense soil than that in loose soil. Figure 6.22c shows the effect of soil relative density on the attenuation of Arias Intensity. As the soil relative density increases, the generation of EPWP is usually

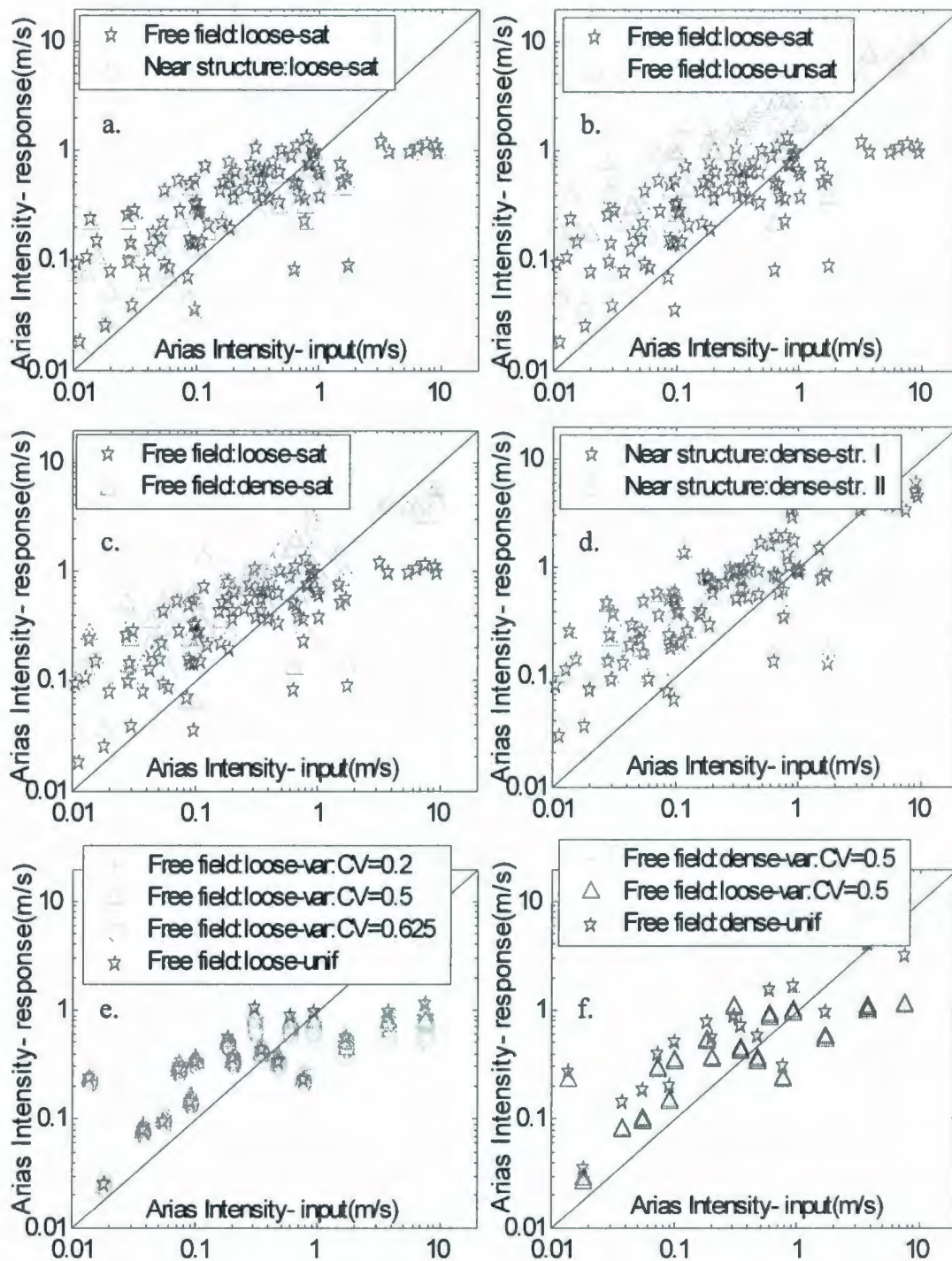


Figure 6.22: Comparison of Arias Intensity for different soil conditions- input vs. response at the foundation level: a. loose soil: free field vs. below structure; b. loose soil: saturated vs. unsaturated; c. loose vs. dense soil; d. structure I vs. structure II; e. loose saturated soil: uniform vs. variable; f. loose saturated variable soil vs. dense saturated uniform soil vs. dense saturated variable soil.

reduced for a particular magnitude of earthquake. Therefore, Arias Intensity reduction in the response for loose soil is larger than in dense soil, particularly for higher magnitude of earthquakes (e.g., $I_A > 0.8 \text{ m/s}$). It is apparent that the generation of larger EPWP is helping here by reducing the earthquake energy transmitted to the structure. However, there are other consequences of larger EPWP build-up (e.g., more structural total and differential settlements) which will be discussed later.

6.4.5.5. Effect of Fundamental Period of the Structure:

The structure-I, with a fundamental period of 0.29s, was used for all the other results presented so far. The effect of the fundamental period of the structure is presented here. The 90 amplification functions along with the mean curve for dense ($D_r=85\%$) cohesionless soil below structure II (fundamental period of structure=0.78s) are shown in Figure B.4 (shown in Appendix B). After comparing the results with Figure B.3, it has been observed that spectral amplification is reduced for structure II. The effects of the fundamental period of the structure on attenuation of Arias Intensity are shown in Figure 6.22d. However, there is no significant effect of the fundamental period of the structure in the attenuation of Arias Intensity for the range of structural characteristics used in this study.

6.4.5.6. Effect of Soil Variability:

As mentioned in Section 6.4.2, 18 seismic acceleration time histories are selected for stochastic analysis. Different values for CV of q_n (CV=0.2, 0.5 and 0.625 for loose

soil and 0.5 for dense soil) are considered in the amplification analysis. Five stochastic sample functions, for each CV value, are used in the Monte Carlo simulation. The amplification functions along with the mean curve for each case of variable soil are shown in Figure B.5 (shown in Appendix B). Regarding the effects of soil heterogeneity, it can be concluded from the results presented in Figure 6.22e and 6.22f that variable soil leads to significantly larger attenuation of the seismic motion than uniform soil. The Arias Intensity attenuation is stronger with the increasing in CV of q_n value.

Similar results on the comparison between peak acceleration (PA) of base input accelerations and that of the computed accelerations at the foundation level are shown in Figure 6.23. Here, the term 'peak acceleration' is used to express the absolute maximum acceleration at base input, or computed responses in the free field and below structure at 2m depth. The generation of EPWP affects the PA in the same way as it affects Arias Intensity. Due to the generation of larger EPWP, significant attenuation of PA has been observed (particularly for stronger earthquakes) in saturated loose uniform and heterogeneous soil.

6.4.5.7. Design Recommendations on Amplification of Seismic Ground Motion

Design recommendations in terms of amplification factors are presented in this section. In the Canadian building code (NBCC, 2005), the idea of using the short (0.2s) and long period (1.0s) amplification factor, F_a and F_v was adopted from National Earthquake Hazard Reduction Program (NEHRP). NEHRP originally used peak ground acceleration and velocity, but the most recent version of NEHRP uses spectral value at

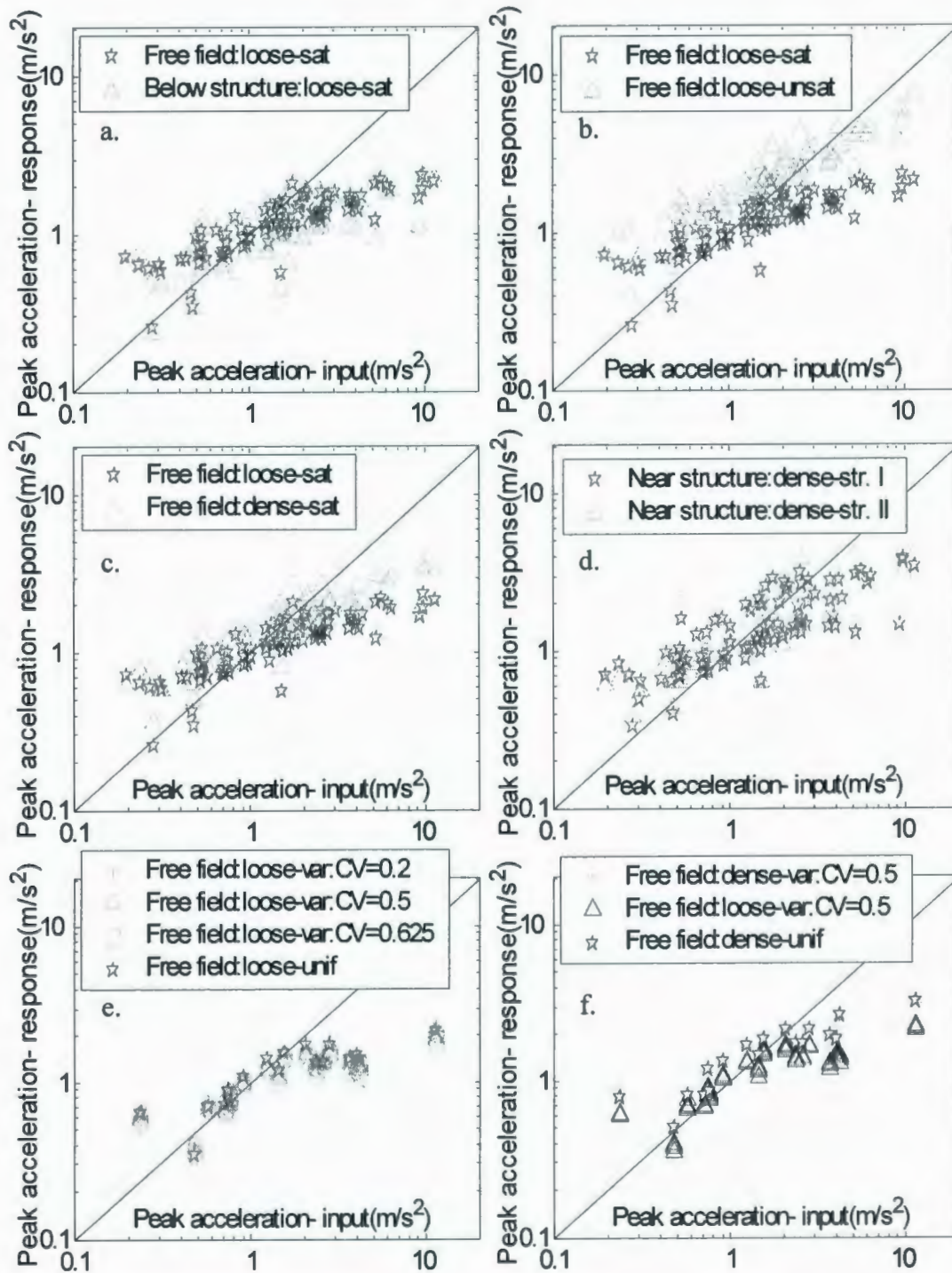


Figure 6.23: Comparison of peak acceleration for different soil conditions- input vs. response at the foundation level: a. loose soil: free field vs. below structure; b. loose soil: saturated vs. unsaturated; c. loose vs. dense soil; d. structure I vs. structure II; e. loose saturated soil: uniform vs. variable; f. loose saturated variable soil vs. dense saturated uniform soil vs. dense saturated variable soil.

various periods, which are also used in this study. Updated guidelines are presented for

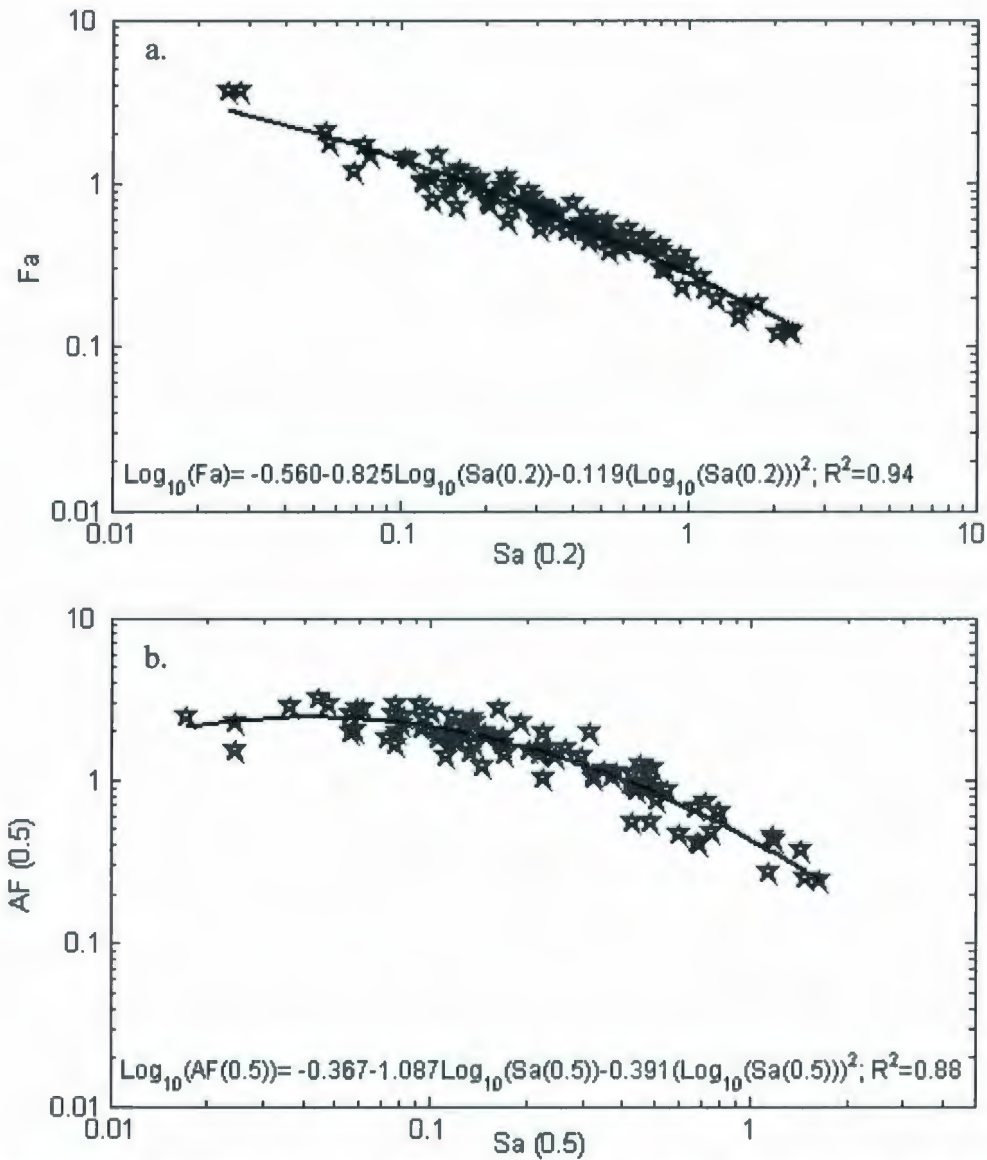


Figure 6.24: Regression equations of spectral amplification vs. input spectral acceleration for loose saturated, cohesionless soil: a. AF(0.2) or F_a vs input S_a at $T=0.2s$; b. AF(0.5) vs input S_a at $T=0.5s$. The star markers in the figure are showing the values obtained from 90 analyses performed on loose saturated soil.

those factors for different site conditions, based on fully coupled nonlinear time history analysis. Two different relative densities of the soil are considered here, 45% relative density corresponding to site class E (shear wave velocity (V_s) $<180\text{m/s}$) and 85% relative density corresponding to site class D (V_s between $180\text{-}360\text{ m/s}$) based on shear

wave velocity. The shear wave velocity for 45% and 85% soil relative densities are calculated based on following relation:

$$V_s = \sqrt{\frac{G_0}{\rho}} ; \quad (6.5)$$

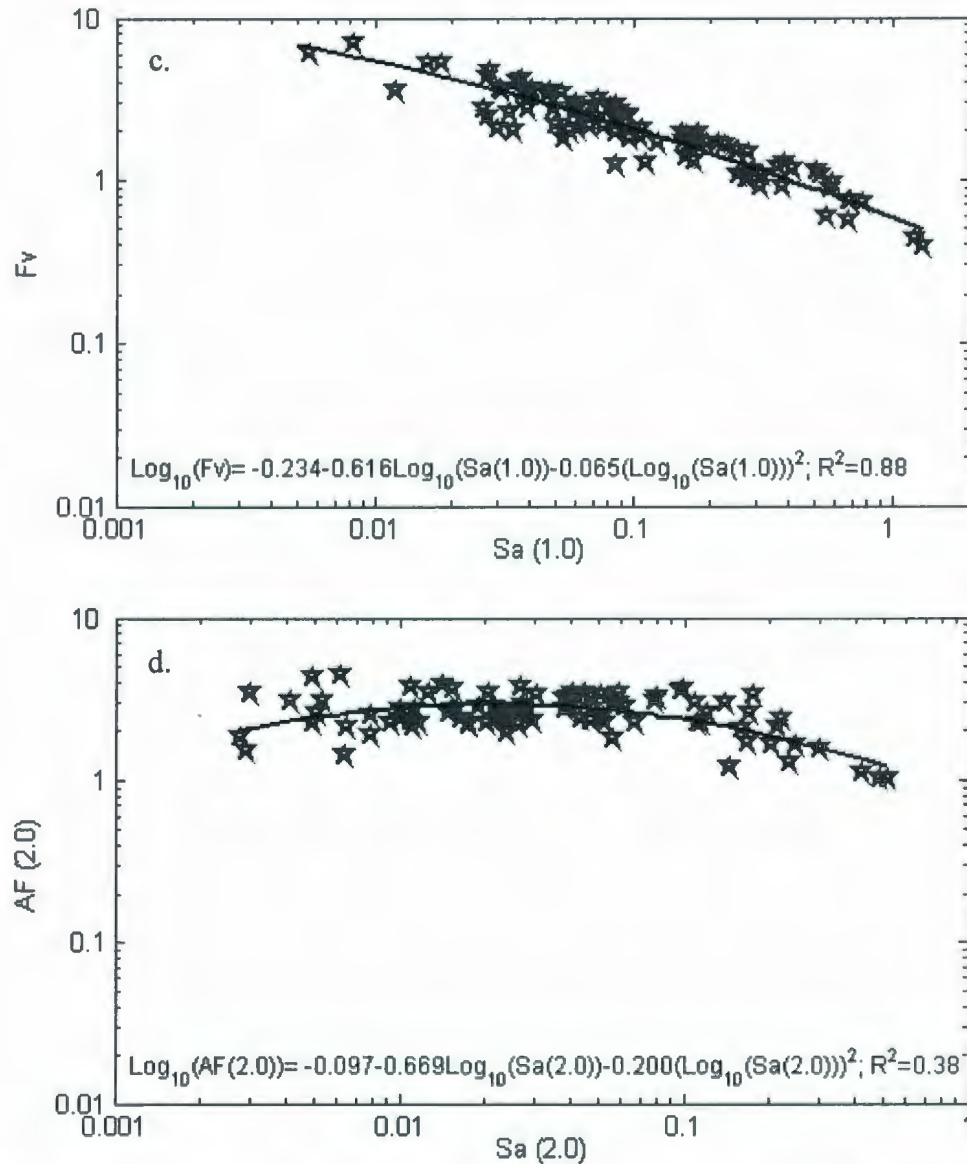


Figure 6.24 (cont.): Regression equations of spectral amplification vs. input spectral acceleration for loose saturated, cohesionless soil: a. $AF(0.2)$ or F_a vs input S_a at $T=0.2s$; b. $AF(0.5)$ vs input S_a at $T=0.5s$. The star markers in the figure are showing the values obtained from 90 analyses performed on loose saturated soil.

where G_0 is the low strain shear modulus, ρ is the mass density. There is a strong dependence of amplification factors on the input spectral acceleration. Therefore, the recommended values for amplification factors are given as functions of input spectral acceleration. Regression equations for calculating F_a and F_v (corresponding to $T=0.2s$ and $T=1.0s$ respectively) are presented here along with the equation for calculating the amplification factor at period=0.5 and 2.0s. The F_a and F_v values can be used for determining site specific response spectra in earthquake resistant design. The calculated spectral acceleration for 5% damping vs. amplification factors at four different periods: 0.2s, 0.5s, 1.0s, and 2.0s for saturated loose ($D_r=45\%$) cohesionless soil site are presented in Figure 6.24. The regression equations for calculating F_a and F_v are shown in the figures.

In Figure 6.24 and 6.25 F_a is the short period (0.2s) amplification factor, F_v is the long period (1.0s) amplification factor, $S_a(0.2)$ is the spectral acceleration of input for 5% damping at period=0.2s, and $S_a(1.0)$ is the spectral acceleration of input for 5% damping at period =1.0s (shown using arrows in Figure 6.15a for one acceleration input).

The effect of the water table was also studied here. Amplification factors are also calculated for unsaturated uniform loose soil. Figure 6.25 shows the relation of amplification factors with input spectral acceleration at the above mentioned four different periods. The regression equations for calculating F_a and F_v are shown in the Figure 6.25.

The amplification factors for a site comprised of dense ($D_r=85\%$) saturated cohesionless soil are presented in Figure 6.26. The regression equations for calculating F_a and F_v are as shown in the Figure 6.26. The amplification factors for an unsaturated dense

(Dr=85%) cohesionless soil site are presented in Figure 6.27. The regression equations for calculating F_a and F_v are shown in the Figure 6.27.

The effects of soil variability on amplification factors were also studied. Amplification factors for two different CV of q_n values (0.2 and 0.5) are provided. Figure

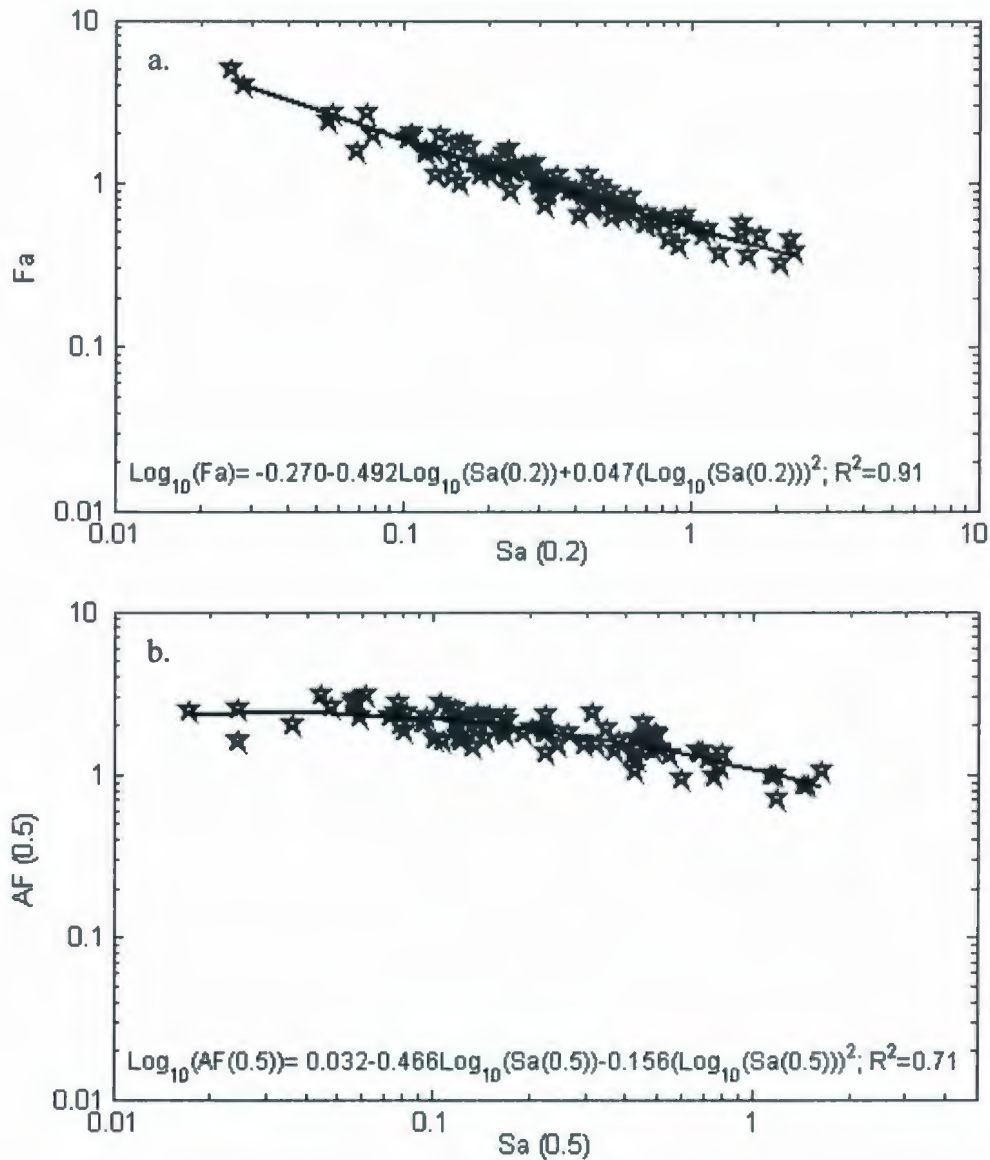


Figure 6.25: Regression equations of spectral amplification vs. input spectral acceleration for loose unsaturated cohesionless soil: a. AF(0.2) or F_a vs input S_a at $T=0.2$ s; b. AF(0.5) vs input S_a at $T=0.5$ s.

6.28 shows the relation of amplification factors with input spectral acceleration at the

above mentioned periods (0.2s, 0.5s, 1.0s, and 2.0s) for the loose variable soil with CV of q_n of 0.2. Similar results for the loose variable soil with CV of 0.5 are shown in Figure 6.29 (probabilistic characteristics of the soil properties are discussed in Section 6.2.2). The regression equations for calculating F_a and F_v are shown in the corresponding

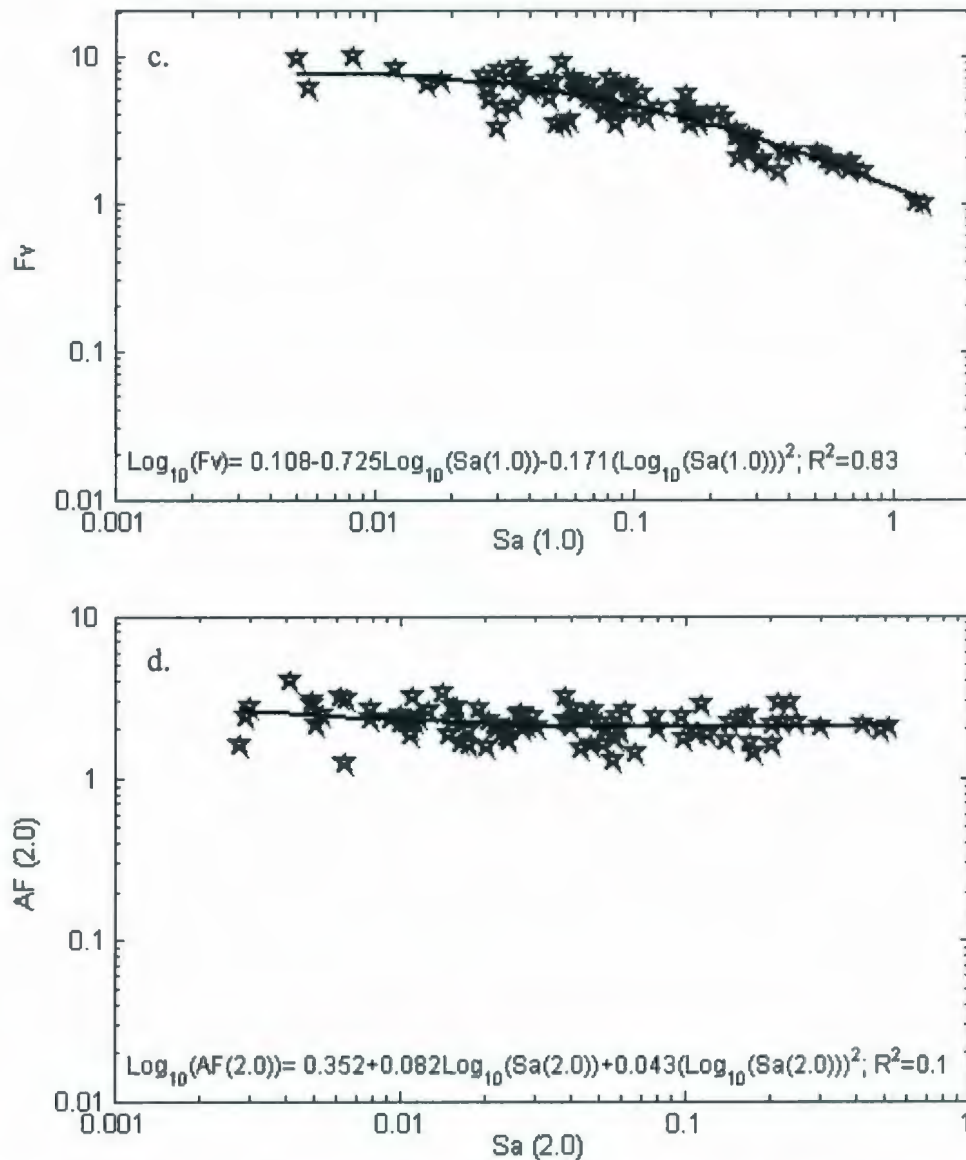


Figure 6.25 (cont.): Regression equations of spectral amplification vs. input spectral acceleration for loose unsaturated cohesionless soil: c. $AF(1.0)$ or F_v vs input S_a at $T=1.0s$; d. $AF(2.0)$ vs input S_a at $T=2.0s$.

Figures. From the results presented between Figure 6.24d and 6.29d it has been observed

that there is significant scatter present in the value for $AF(2.0)$. Therefore, the R-square value for the regression equations provided for $AF(2.0)$ are very low.

The comparison of the F_a and F_v results for cohesionless soil at two different relative densities are presented in Table 6.10. The results are compared with the

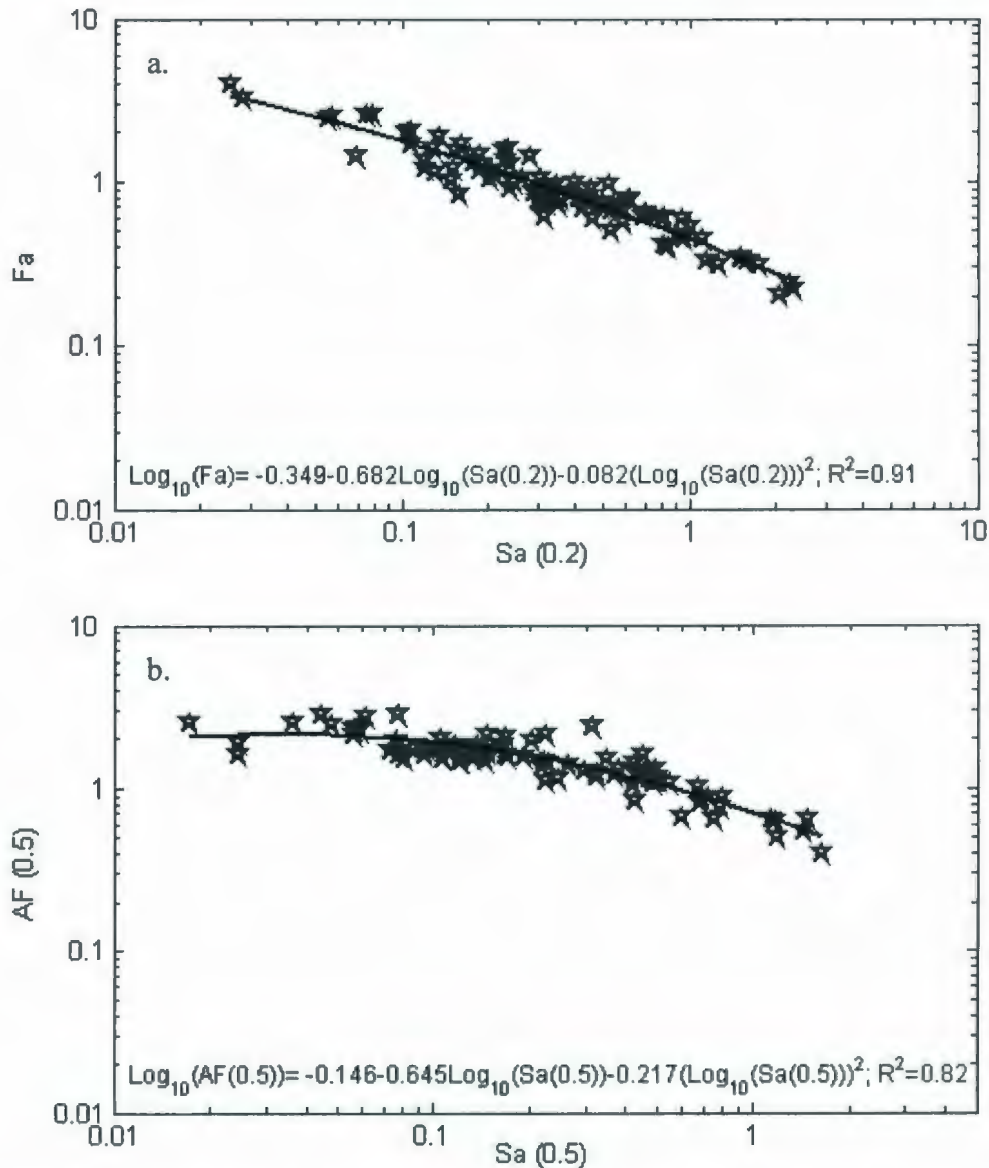


Figure 6.26: Regression equations of spectral amplification vs. input spectral acceleration for dense saturated cohesionless soil: a. $AF(0.2)$ or F_a vs input Sa at $T=0.2s$; b. $AF(0.5)$ vs input Sa at $T=0.5s$.

recommended values of spectral acceleration in the Canadian Building Code (NBCC

2005), and with other values from the literature. The comparison of spectral amplification between presented results for loose cohesionless soil and site class *E* in Canadian Building Code is illustrated by Figure 6.30. Similar comparison for dense cohesionless soil with the value for site class *D* in Canadian building Code is illustrated by Figure

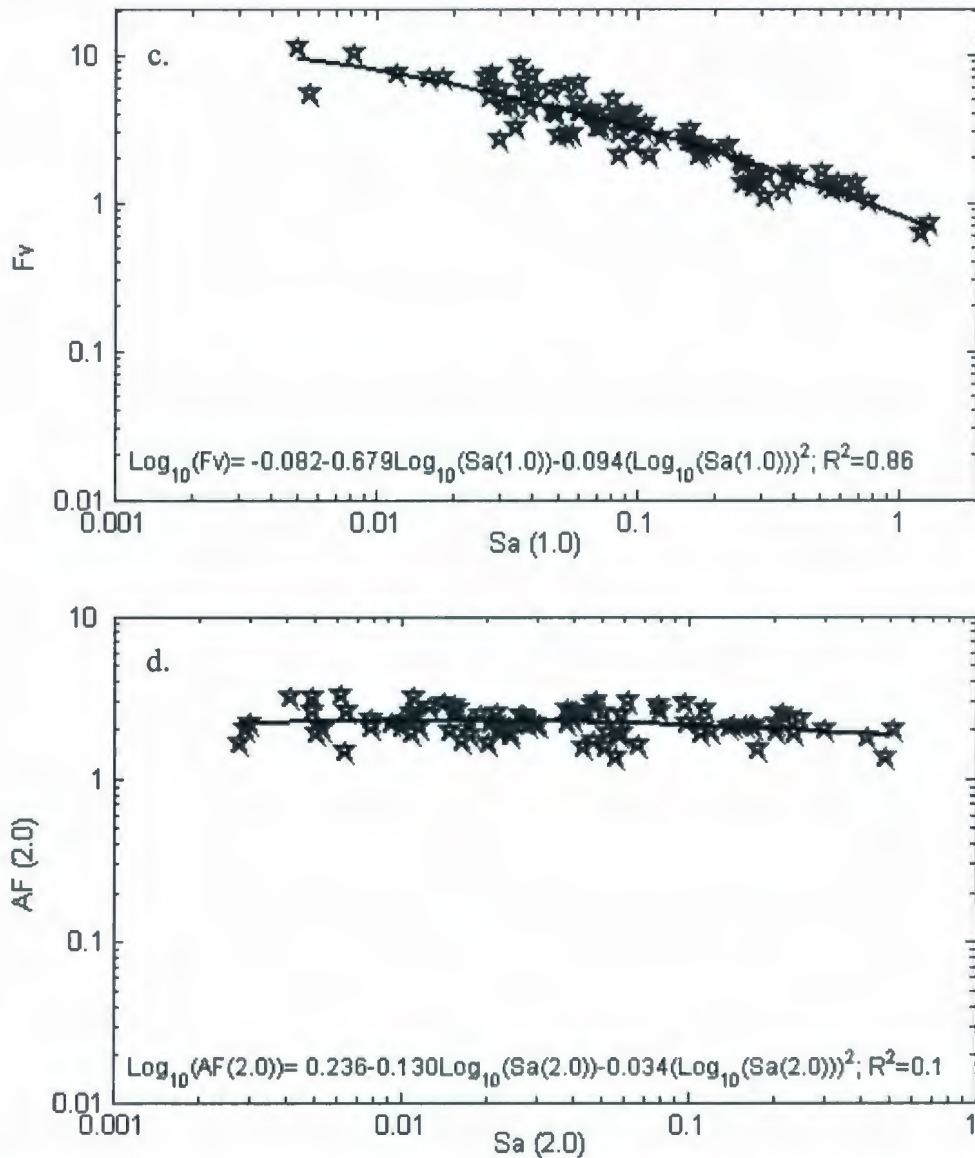


Figure 6.26 (cont.): Regression equations of spectral amplification vs. input spectral acceleration for dense saturated cohesionless soil: c. $AF(1.0)$ or F_v vs input S_a at $T=1.0s$; d. $AF(2.0)$ vs input S_a at $T=2.0s$.

6.31. The percentage change in the F_a and F_v values are compared with respect to that

value in Canadian Building Code. From the Table 6.10 it has been observed that there is a 40-47% (depending on the value of $S_a(1.0)$) change in F_a value when the soil is loose unsaturated compared to the values recommended in the Canadian Building Code for site class E. This variation in F_v value is about 20-118%. There is a 41-111% change in F_a

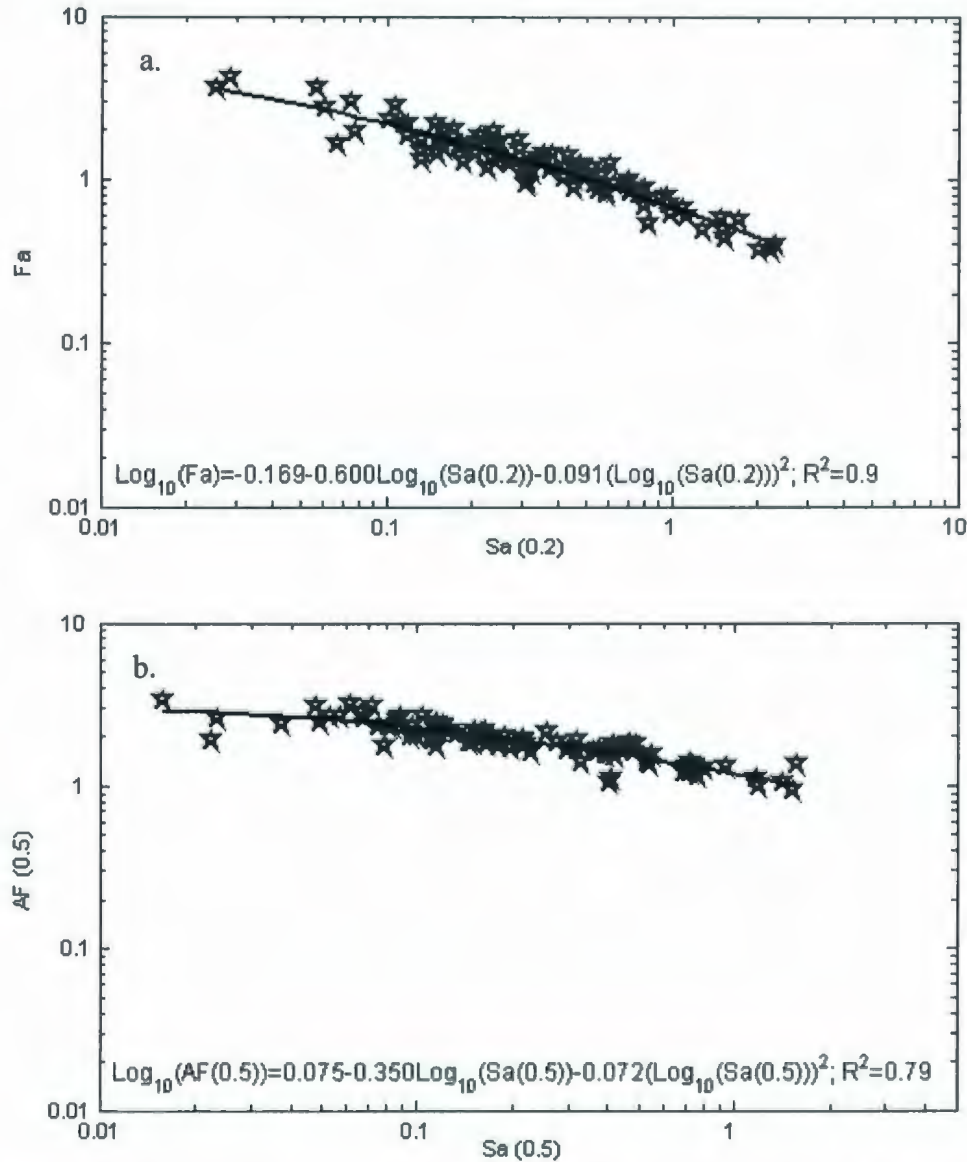


Figure 6.27: Regression equations of spectral amplification vs. input spectral acceleration for dense unsaturated cohesionless soil: a. $AF(0.2)$ or F_a vs input S_a at $T=0.2s$; b. $AF(0.5)$ vs input S_a at $T=0.5s$.

value when the soil is loose unsaturated compared to the values with loose saturated soil.

This variation in F_v values is even larger, where more than 121% change in the values has been estimated. In unsaturated dense cohesionless soil a 11-41% variation in F_a value and 106-181% variation in F_v value have been estimated compared to the values recommended in the Canadian Building Code for site class D. There is a 25-35%

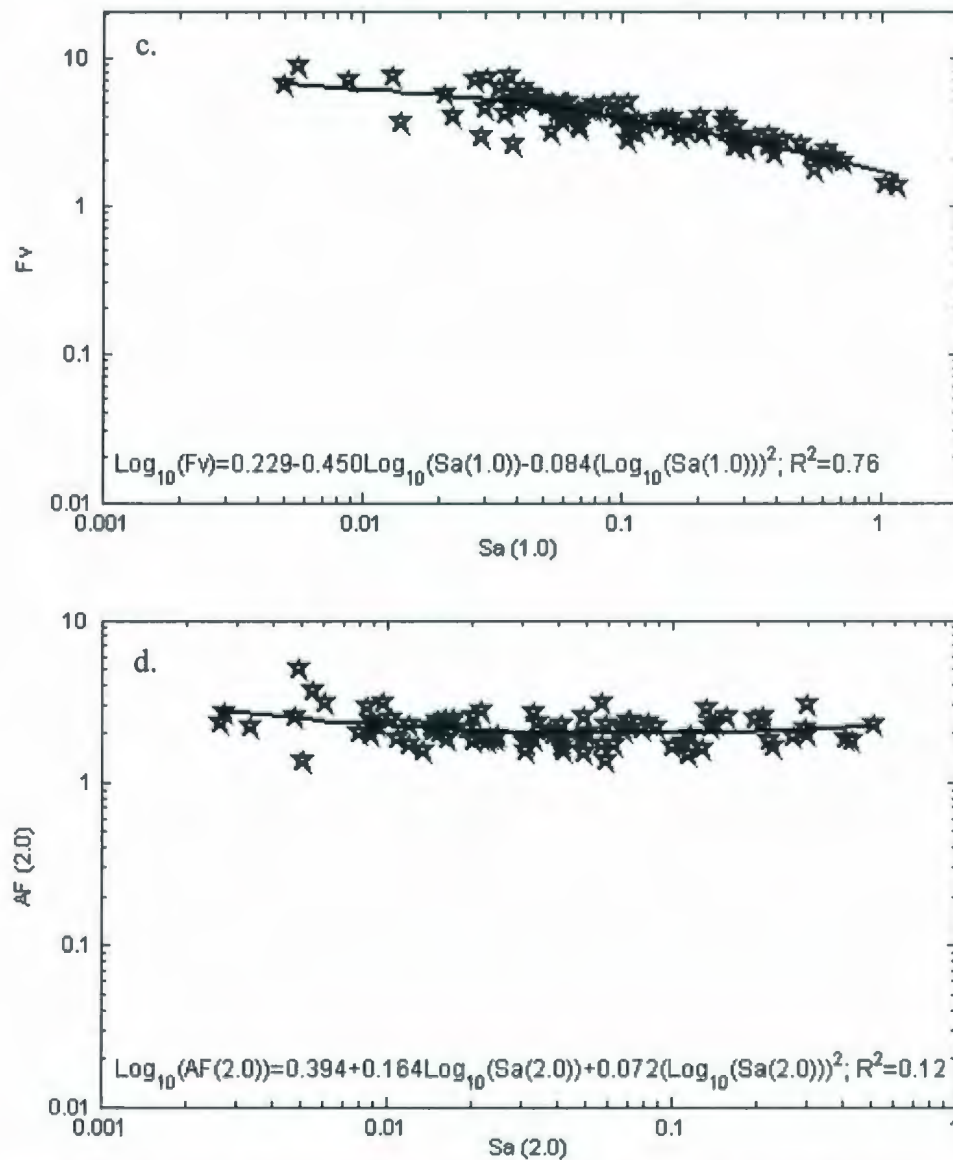


Figure 6.27 (cont.): Regression equations of spectral amplification vs. input spectral acceleration for dense unsaturated cohesionless soil: c. $AF(1.0)$ or F_v vs input Sa at $T=1.0s$; d. $AF(2.0)$ vs input Sa at $T=2.0s$.

variation in F_a value and 19-43% change in F_v value has been estimated in dense

saturated soil compared to the values in unsaturated dense soil. The comparison of amplification factors for a dense cohesionless soil with loose soil also can be estimated from Table 6.10. There is about 40% to 60% variation in the amplification factors for dense soil compared to that in loose uniform soil. The Canadian building code also

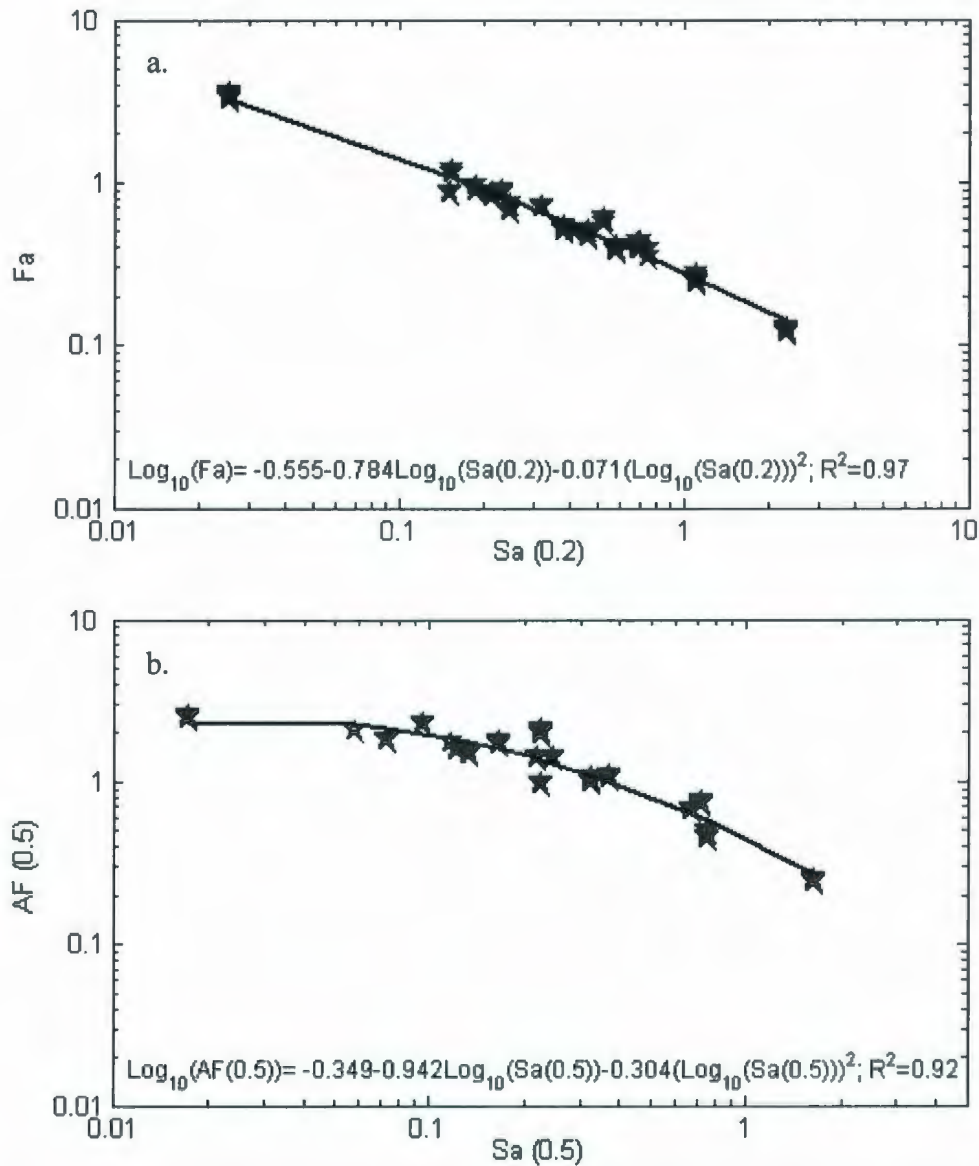


Figure 6.28: Regression equations of spectral amplification vs. input spectral acceleration for loose saturated heterogeneous soil (CV=0.2): a. AF(0.2) or F_a vs input S_a at $T=0.2$ s; b. AF(0.5) vs input S_a at $T=0.5$ s.

reported a variation up to about 62% between site class D and E. Bazzurro and Cornell

(2004) presented some recommended value for F_a and F_v . The presented results for a sandy site are shown in Table 6.10. The soil characteristics are very much close to dense saturated soil presented here. From the comparison it is observed that the value for F_a and

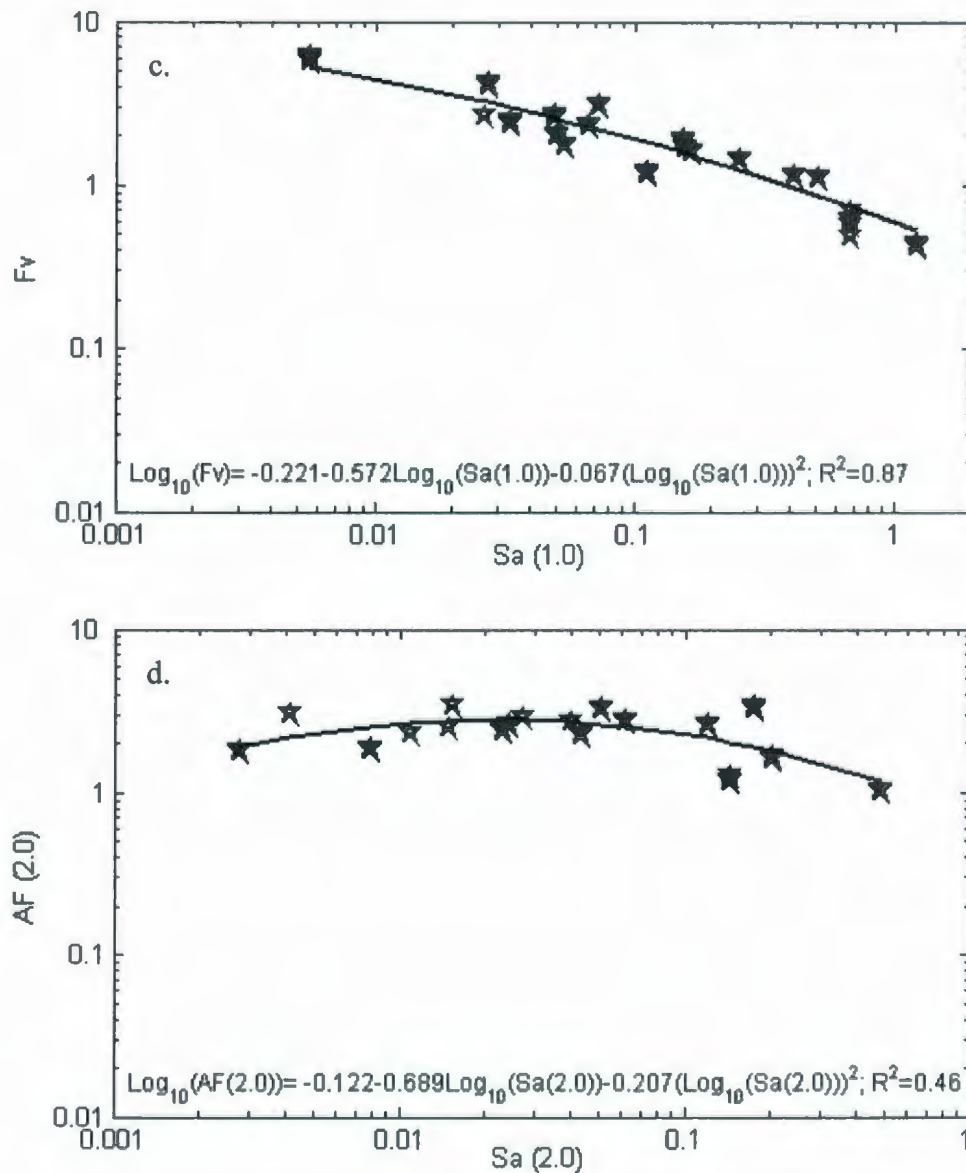


Figure 6.28 (cont.): Regression equations of spectral amplification vs. input spectral acceleration for loose unsaturated heterogeneous soil (CV=0.2): c. AF(1.0) or F_v vs input Sa at T=1.0s; d. AF(2.0) vs input Sa at T=2.0s.

F_v recommended by Bazzurro and Cornell (2004) are very much agreement with the results for dense saturated uniform soil presented here in this study.

It has been found in this study that there is small (less than 10%) change in the values of F_a and F_v for heterogeneous soil compared to that in uniform soil. Even for a variable saturated loose soil with CV of $q_n = 0.5$, < 2% change for the value in F_a and <

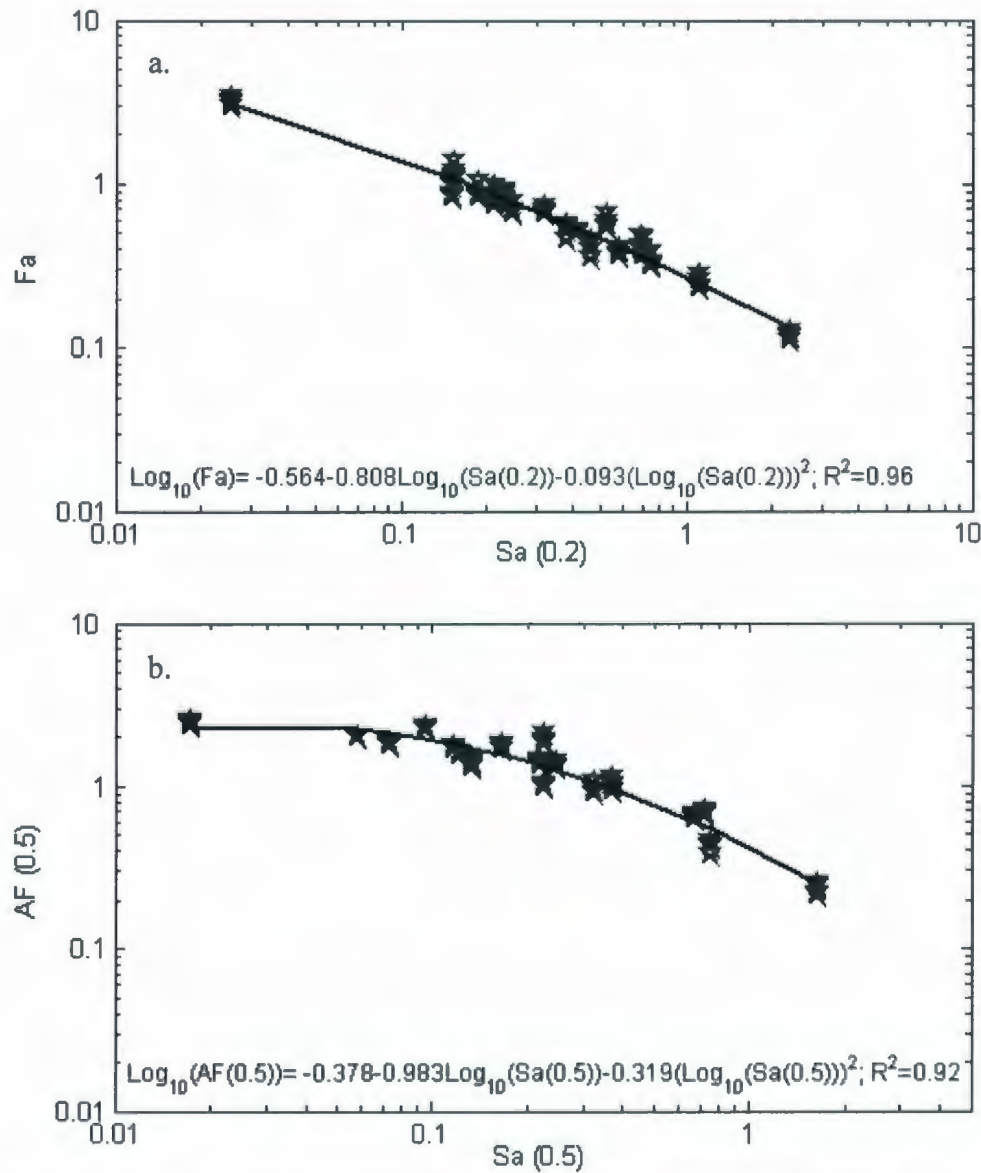


Figure 6.29: Regression equations of spectral amplification vs. input spectral acceleration for loose saturated heterogeneous soil (CV=0.5): a. AF(0.2) or F_a vs input Sa at T=0.2s; b. AF(0.5) vs input Sa at T=0.5s.

10% change for the value of F_v has been estimate compared to that in uniform saturated soil. The EPWP generation in heterogeneous soil is higher (shown in previous Chapters)

than that in uniform saturated soil. But, it does not affect here the F_a and F_v value in heterogeneous soil. One possible explanation can be obtained from the results presented in Figure 6.22e. Where it was found that attenuation of Arias Intensity was almost similar

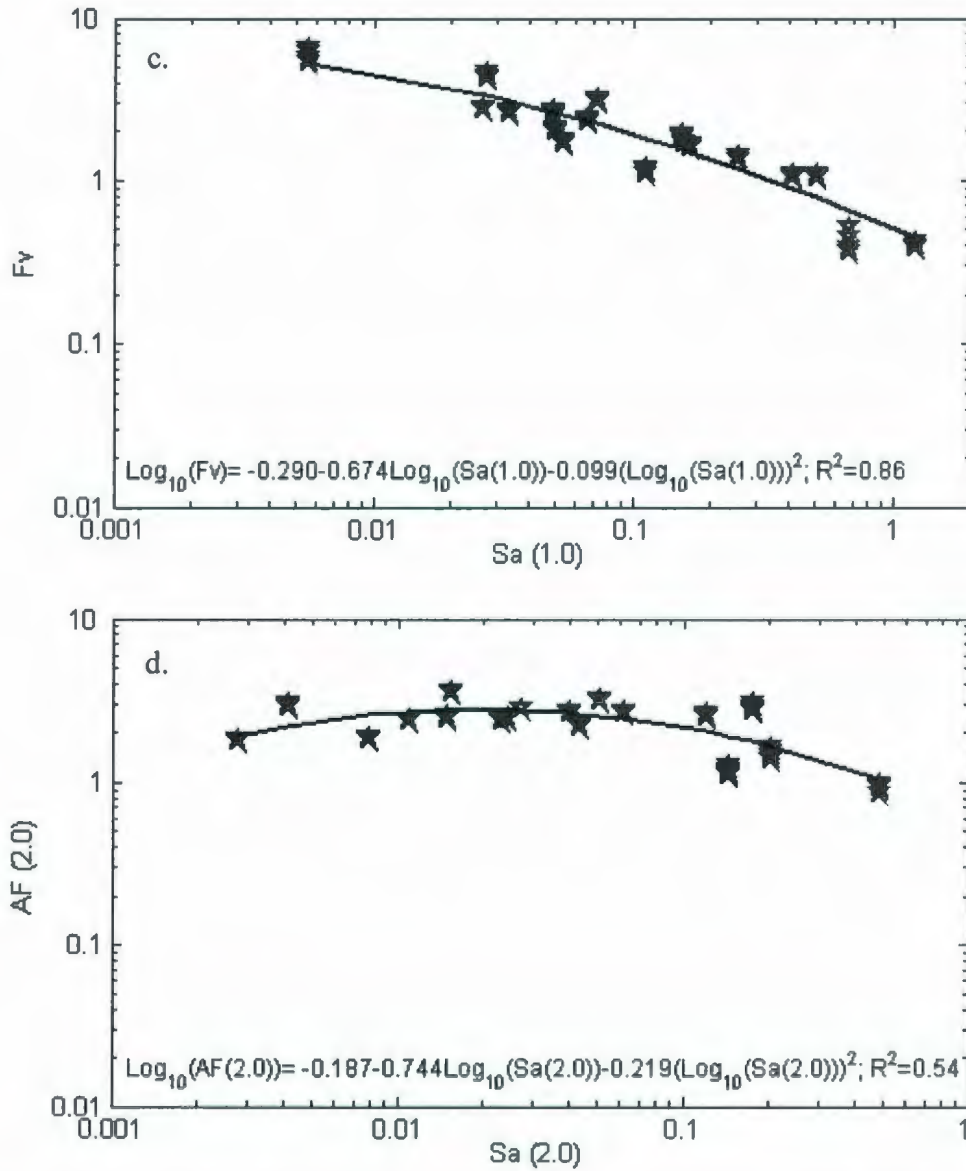


Figure 6.29 (cont.): Regression equations of spectral amplification vs. input spectral acceleration for loose saturated heterogeneous soil (CV=0.5): c. $AF(1.0)$ or F_v vs input Sa at $T=1.0s$; d. $AF(2.0)$ vs input Sa at $T=2.0s$.

in heterogeneous soil as compared to that in uniform soil, especially for low intensity earthquakes. This implies that, the earthquake energy level in the free field was almost

similar in variable soil compared to that in uniform soil. So, F_a and F_v value obtained here are almost similar. Therefore, it can be concluded that soil variability has no significant influence on the values of the amplification factors for the ranges of soil properties

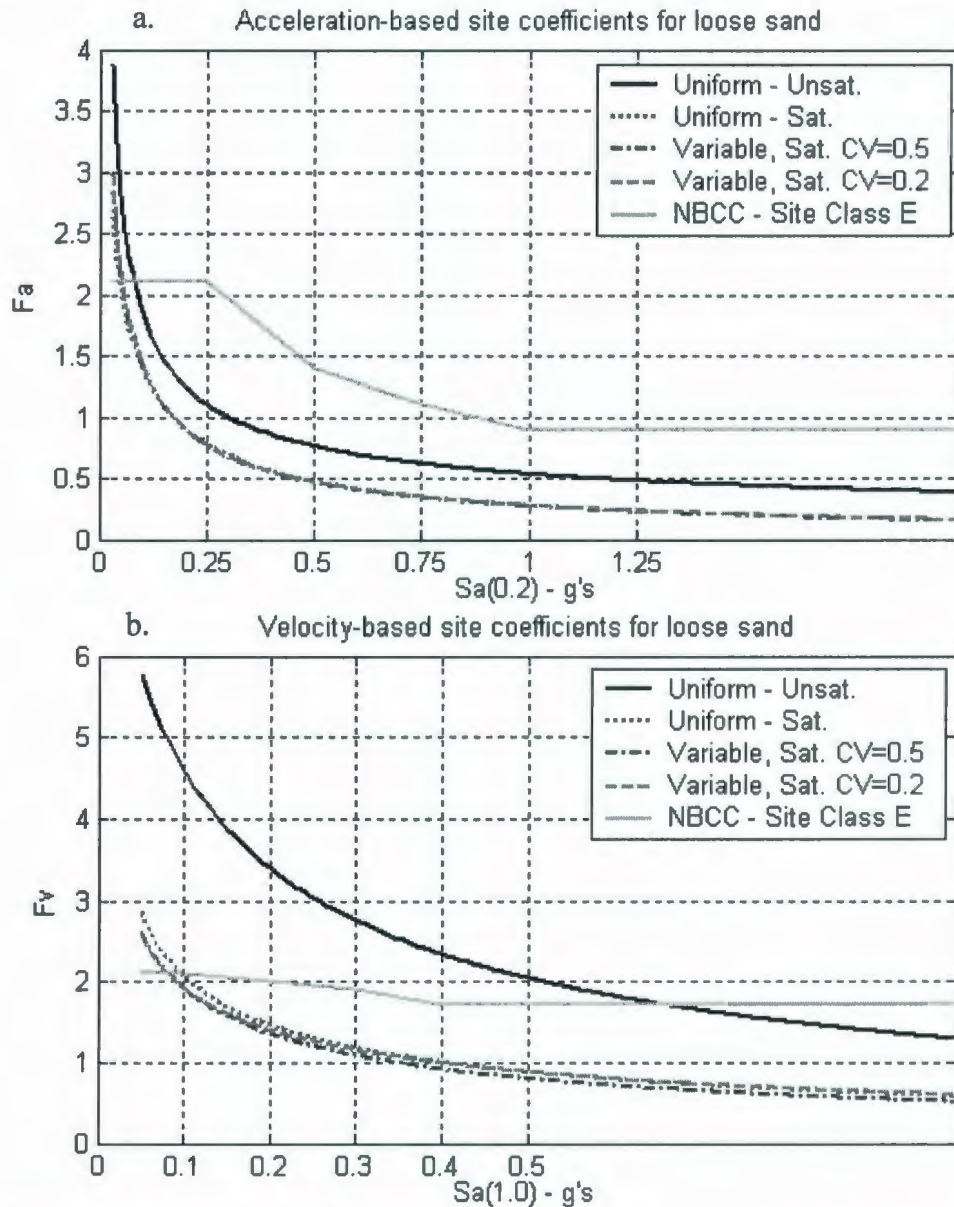


Figure 6.30: Comparison of spectral amplification vs. spectral acceleration for loose soil: a. AF(0.2) or F_a vs input S_a at $T=0.2s$; b. AF(1.0) or F_v vs input S_a at $T=0.5s$.

studied here (CV of $q_n = 0.2$ and 0.5). However, the comparison for unsaturated variable soil with unsaturated uniform soil is beyond the scope of this study.

On the other hand, the ground water depth has a huge influence on the amplification factors (shown in Table 6.10). There is an error larger than 40% might be induced in the value of amplification factors for not considering the effect of the ground

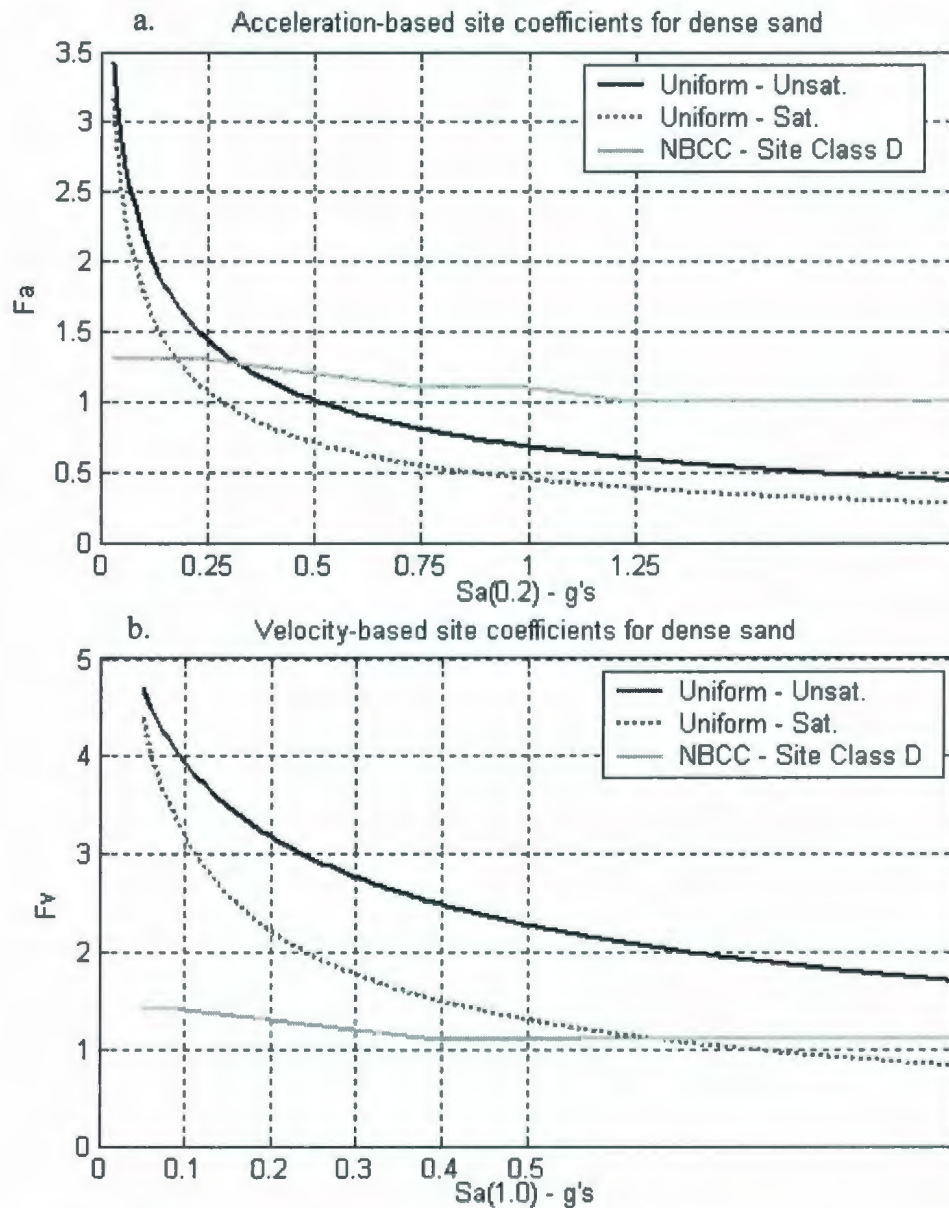


Figure 6.31: Comparison of spectral amplification vs. spectral acceleration for dense soil: a. AF(0.2) or F_a vs input S_a at $T=0.2s$; b. AF(1.0) or F_v vs input S_a at $T=0.5s$.

water level. So, nonlinear dynamic fully coupled site response analysis must be performed for saturated soil (which was performed in this study) instead of using

equivalent-linear methods such as the SHAKE program. It should be emphasized that the extra variability in the responses due to soil variability is not significant for the range of soil properties and variability studied here. However, the record-to-record variability of amplification factors is quite significant. The provided regression equations in Figures 6.24 to 6.29 for F_a and F_v are recommended to use for calculating short and long period amplification factors in site specific response analysis for designing an earthquake resistant structure. As mentioned earlier, in the study 90 acceleration time histories were used. The $S_a(0.2)$ values are inside the range of 0.01g to 2.5g and $S(1.0)$ values are inside the range of 0.005g to 1.5g. Therefore, the equations presented in Figures 6.24 to 6.29 are recommended for the above mentioned range of $S_a(0.2)$ and $S_a(1.0)$.

Based on relative density and corresponding shear wave velocity, the results for loose unsaturated cohesionless soil ($D_r=45\%$) can be used for site class E and those for dense unsaturated cohesionless soil ($D_r=85\%$) can be used for site class D in the Canadian Building Code. However, due to liquefaction susceptibility of saturated sand at moderate to large earthquakes, those saturated cohesionless soils are usually classified as site class F (NBCC, 2005). Therefore, the spectral amplification results for unsaturated cohesionless soil presented here can be directly compared with the values in Canadian Building Code (for site class D and E). The results for saturated soil for moderate to high earthquake intensities are recommended for site class F.

6.4.6. Results and Discussion

6.4.6.1. Maximum Structural Deformation Responses

Some of the results from Monte Carlo simulation in terms of structural deformation are presented here. The structure is modelled here as a single-storied frame. Two different fundamental periods of the structure (0.29s and 0.78s) were considered in the study. To achieve different fundamental periods of the structure, the floor mass at the roof level and the column dimensions were varied. So, the absolute values of maximum bending moment or maximum first story drift are not realistic. Therefore, the absolute values of maximum bending moments and maximum first story drift are not presented here. Only the ratio between the response in the structure resting on other type of soil and the structure resting on uniform loose saturated soil are presented here. Computed maximum induced bending moment ratio between structure on different types of soil and uniform soil are presented in Figure 6.32. It has been observed that as the soil variability increases, the variability in the maximum bending moment also increases. It has been also observed that as the soil below the structure becomes stronger (either due to an increase in soil relative density or due to lowering ground water level) the induced moment in the structure is increases. This can be explained based on the results presented in Figure 6.22 (comparison of Arias Intensity input vs. response at soil surface). The earthquake energy transmitted to the structure resting on dense soil is larger than that in loose soil, and stronger shaking induces more bending moment in the structure. Figure 6.33 show the computed maximum induced first story drift ratio between structure on different types of soil and on uniform loose saturated soil, respectively. Figure 6.34 shows the maximum base shear in the column. The effect of soil variability on base shear

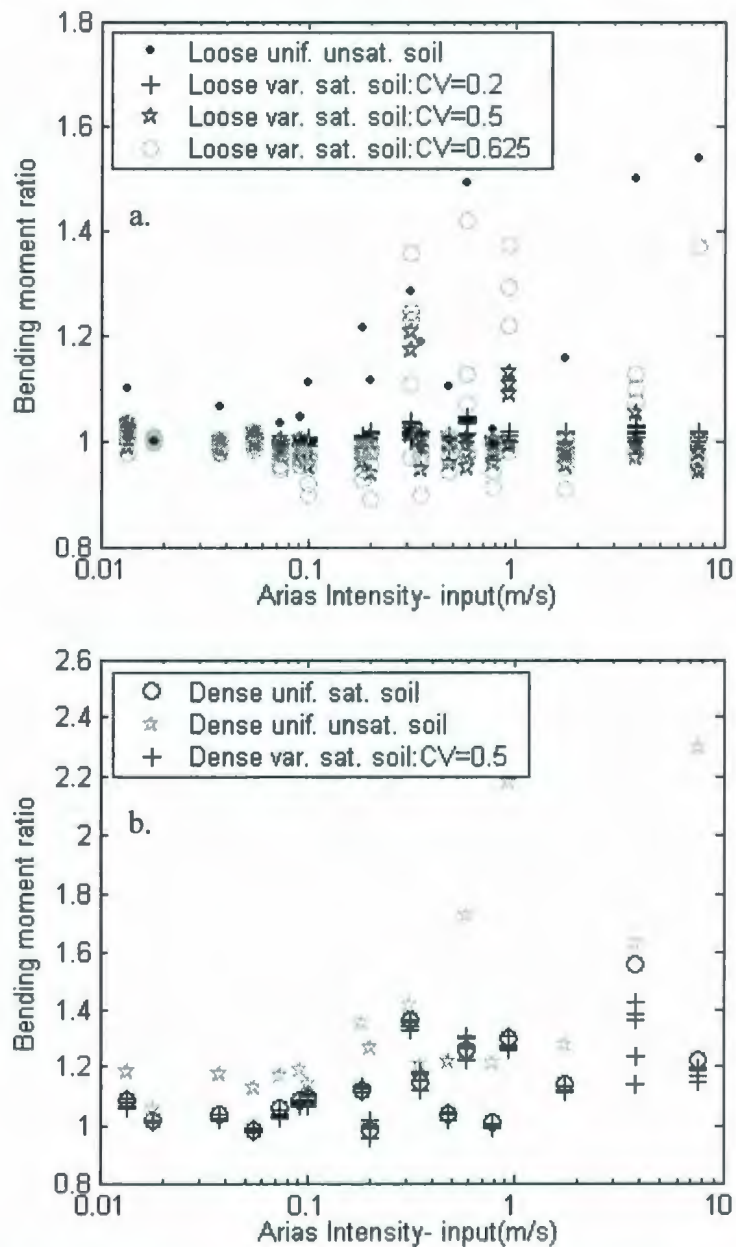


Figure 6.32: Maximum Bending Moment ratio (with respect to the structure on loose saturated soil) for different soil conditions. Where, bending moment ratio= maximum bending moment in the structure resting on other type of soil/maximum bending moment in the structure resting on loose saturated soil.

is illustrated in Figure 6.34a. It has been observed that as the soil variability increases, the maximum base shear in column is reduced. One possible explanation is that as soil variability increases the soil below the structure become weaker due to build up of more

EPWP. So it produces less resistance to the structure against rotation which ultimately induces less base shear in the column.

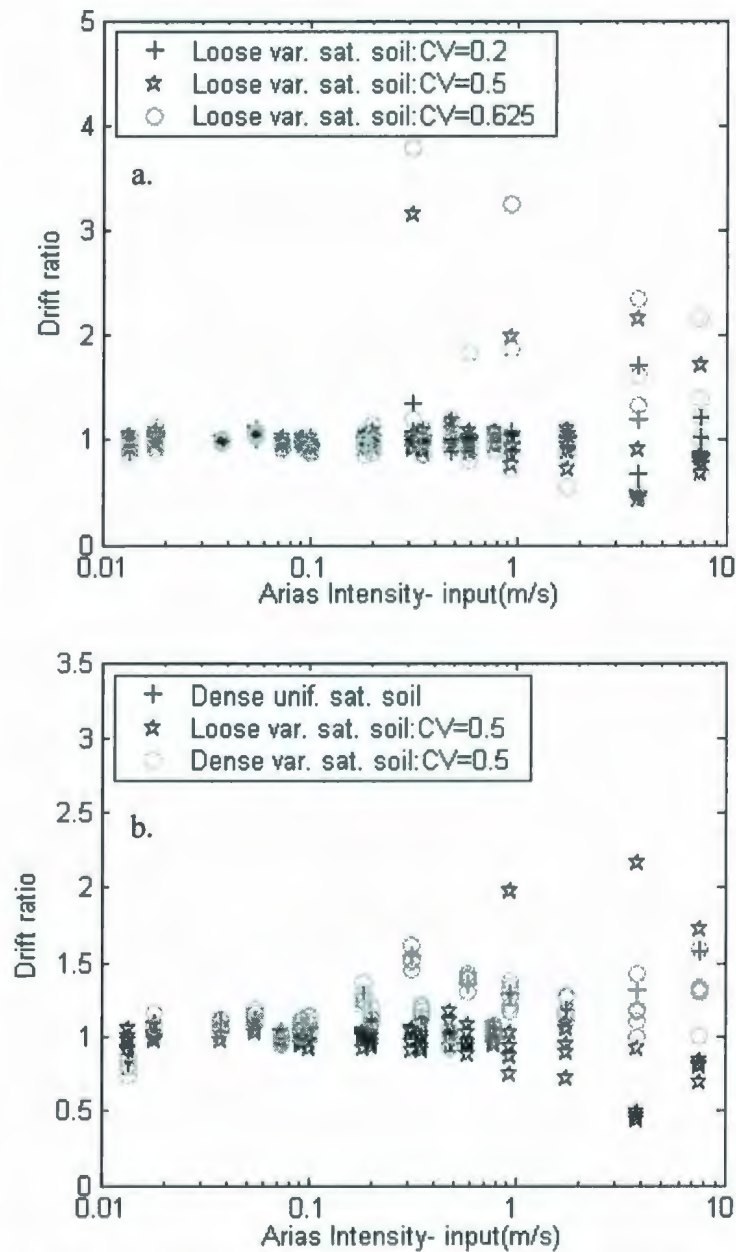


Figure 6.33: Maximum story drift ratio (with respect to the structure on loose saturated soil) for different soil conditions. Where, drift ratio= (maximum story drift at floor level in the structure resting on other type of soil/maximum story drift at floor level in the structure on loose saturated soil.

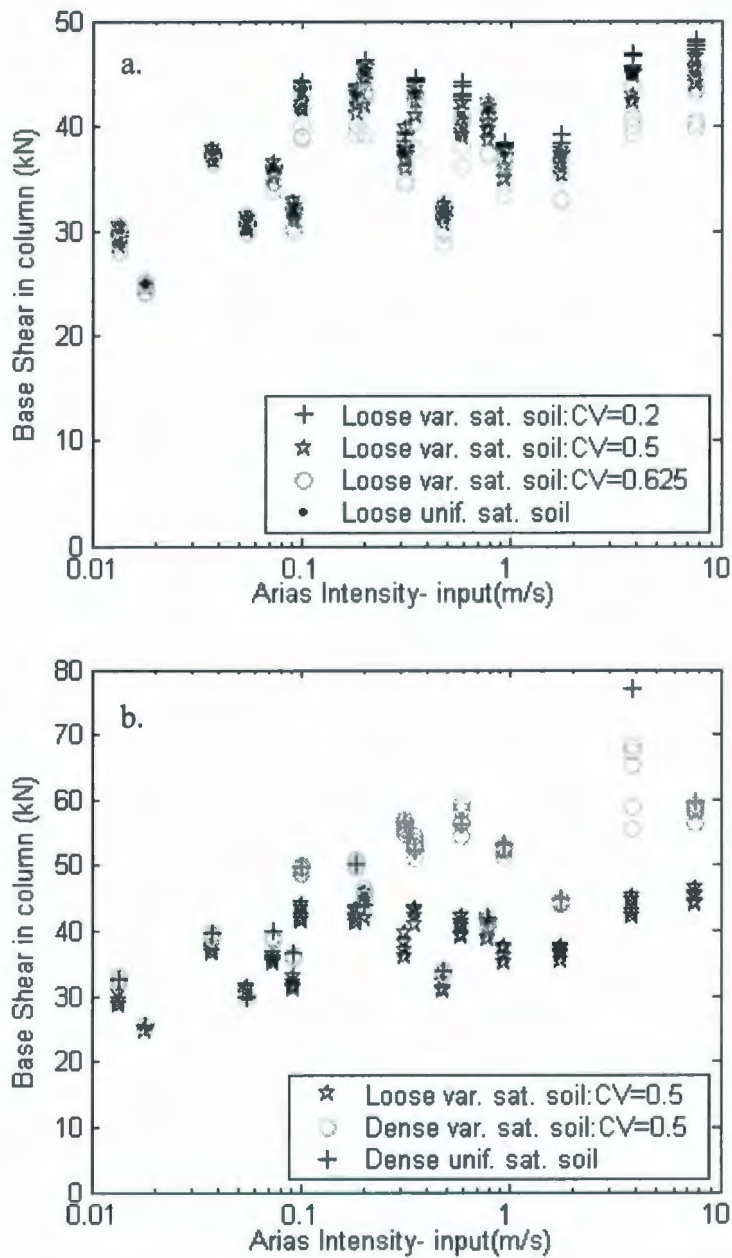


Figure 6.34: Maximum base shear ratio (with respect to the structure on loose saturated soil) for different soil conditions. Where, base shear ratio=(maximum base shear in the structure resting on other type of soil/maximum base shear at floor level in the structure on loose saturated soil).

Figure 6.35 illustrates the effect of earthquakes on structure in terms of maximum total settlements (shown here for the left footing). Effects of water table depth and soil

relative density on maximum settlement are shown in Figure 6.35a and 6.35b. Soil

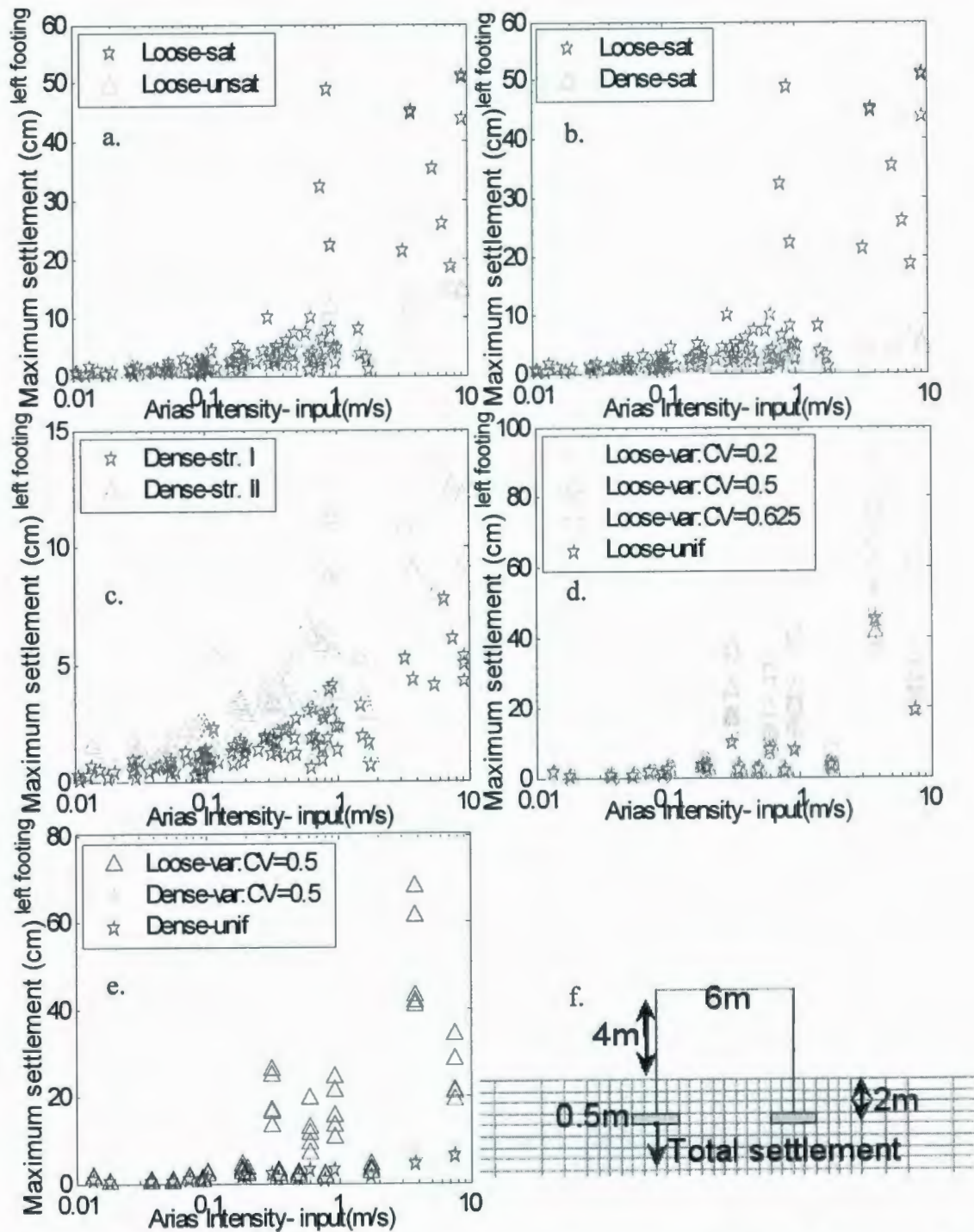


Figure 6.35: Scatter plot of maximum total settlement at left footing for different soil conditions below structure.

strength increases with increase in relative density and water table depth. Therefore,

maximum settlements are larger in loose saturated soil compare to that in unsaturated soil

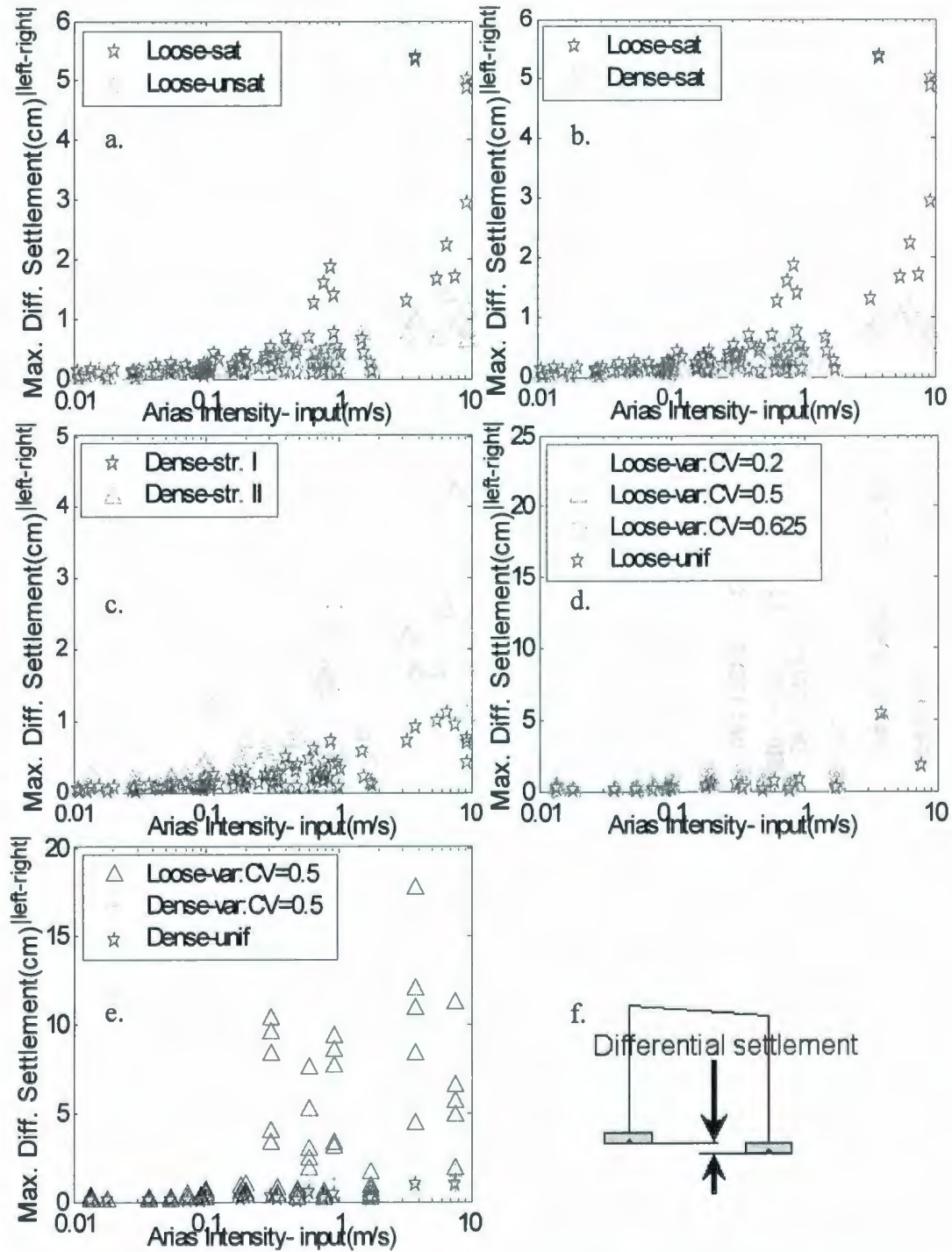


Figure 6.36: Scatter plot of maximum differential settlement for different soil conditions below structure.

or dense saturated soil. The fundamental period of structure-II is close to the fundamental

period of the site; therefore, more structural settlements (total and differential) are computed for Structure II (Figure 6.35c and 6.36c). The results for heterogeneous soil are more scattered due to the presence of two uncertainty factors (seismic acceleration and random spatial distribution of soil strength). The sample function-to-sample function variability in the computed maximum total settlement is increased with the increase in CV value. And also, for the entire range of seismic intensities larger total settlements are computed for larger CV.

Apart from earthquake intensity, the induced bending moment and deformation of the frame structure also depend upon maximum differential settlements. The maximum differential settlements are determined here by calculating the difference in total settlement at the mid point of both footings (shown in Figure 6.36f). Figures 6.36a and b show the effects of water table depth and soil strength on maximum differential settlements. Like total settlements, maximum differential settlements are also larger in the structure resting on loose saturated soil compare to unsaturated soil or dense saturated soil. Soil variability has a huge impact on maximum differential settlements. Larger differential settlements are computed in the structure on variable soil than that in uniform soil. The sample function to sample function variation in maximum differential settlements also increase with the increase in CV of q_n . As mentioned in Section 6.4.5.3, the larger build up of EPWP significantly reduced the earthquake energy transmitted to the structure. On the other hand, maximum total and differential settlements increase with the development of larger EPWP. This ultimately induces more structural total and

differential settlements. Therefore, the structure situated on loose variable soil suffered more structural deformation.

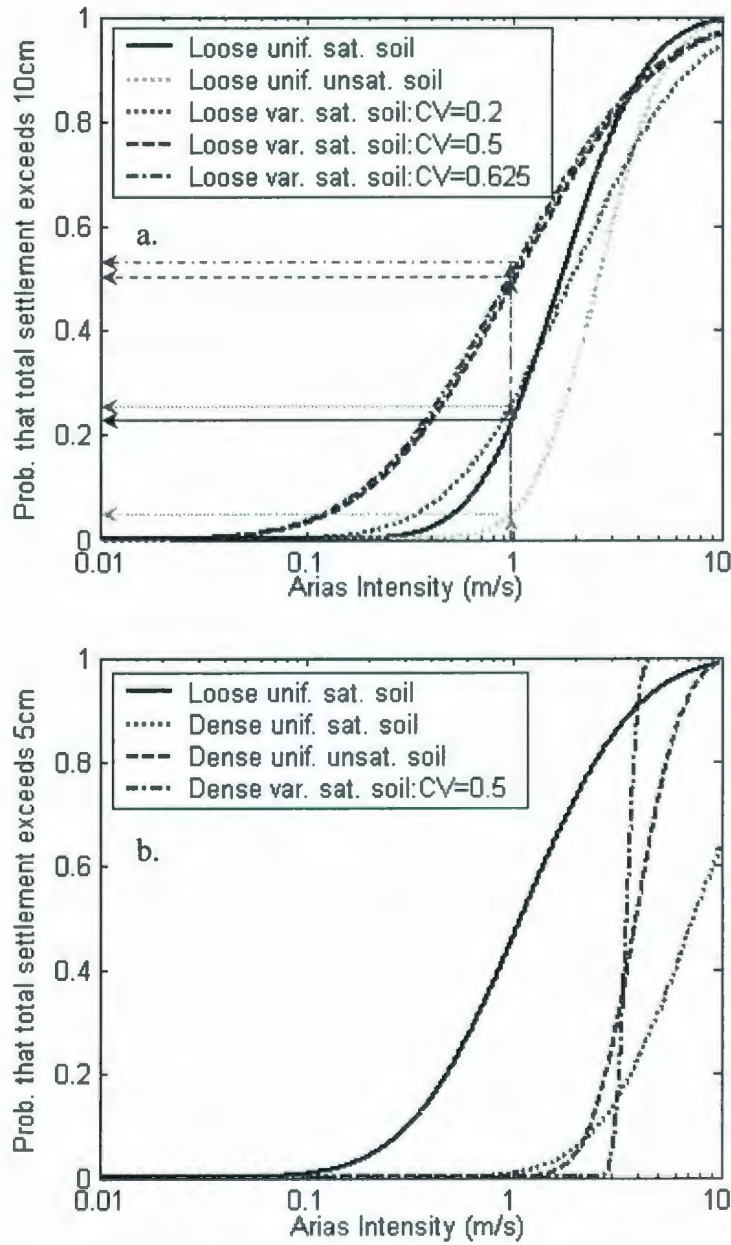


Figure 6.37: Fragility curves for maximum total settlement.

6.4.6.2. Fragility Curves

The computed maximum structural total and differential settlements are processed as fragility curves, expressing the probability of exceeding certain thresholds in the responses as a function of earthquake intensity. The procedure used for constructing the fragility curves, presented by Shinozuka et al. (2000), is already discussed in Chapter 2. Lambe and Whiteman (1969) provide some guidelines for allowable total and differential settlements for a frame structure. For the frame structure studied here, the permissible limits obtained based on the criteria suggested by Lambe and Whiteman (1969) are: total settlements of about 5-10cm and differential settlements of 3cm. Figure 6.37 compares fragility curves for exceeding a certain degree of structural total settlement for all cases analysed. For example, for an input with Arias Intensity of 1m/s, it can be inferred from the fragility curves presented in Figure 6.37a and 6.37b that:

a) There is about 2% probability of exceeding 10cm total settlement in loose uniform unsaturated soil, about 22% probability of exceeding 10cm total settlements in loose uniform saturated soil and about 25%, 50% and 53% chances for loose variable soil with $CV=0.2$, $CV=0.5$ and 0.625 respectively,

b) There is a very small probability ($<0.01\%$) of exceeding 5cm total settlement in dense uniform (both saturated and unsaturated) or variable soil, and about 50% chance for loose saturated uniform soil.

Figure 6.38 shows fragility curves for exceeding a certain degree of structural differential settlement for all analysed cases. Fragility curves for various levels of total and differential settlements (including those for the allowable limits) are presented in Figure 6.39 for loose saturated variable soil with $CV=0.5$. Some threshold levels for

constructing fragility curves are selected same as the allowable limits which were taken from the recommendations suggested by Lambe and Whiteman (1969). The fragility curves based on these allowable limits can be used for determining the limiting Arias Intensity which will cause a given probability of exceeding. The limiting Arias Intensity

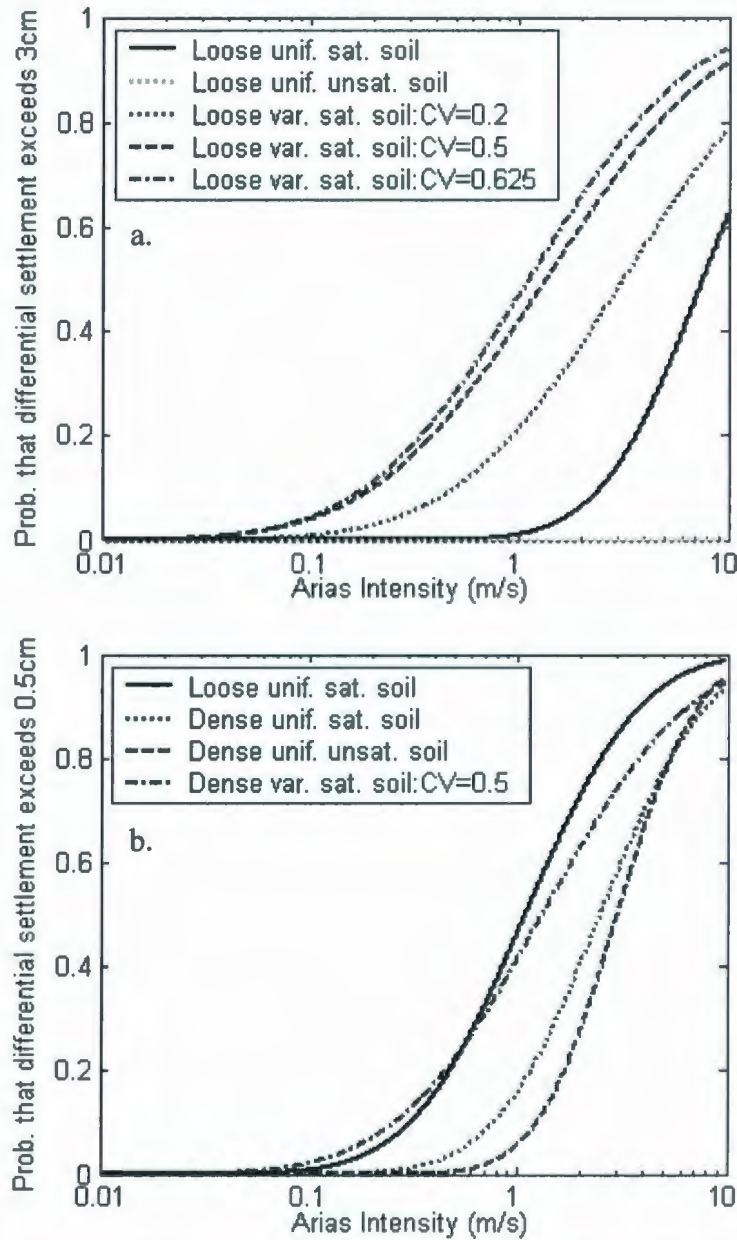


Figure 6.38: Fragility curves for maximum differential settlement.

values for 1%, 5% and 10% probability of exceeding various thresholds are presented in

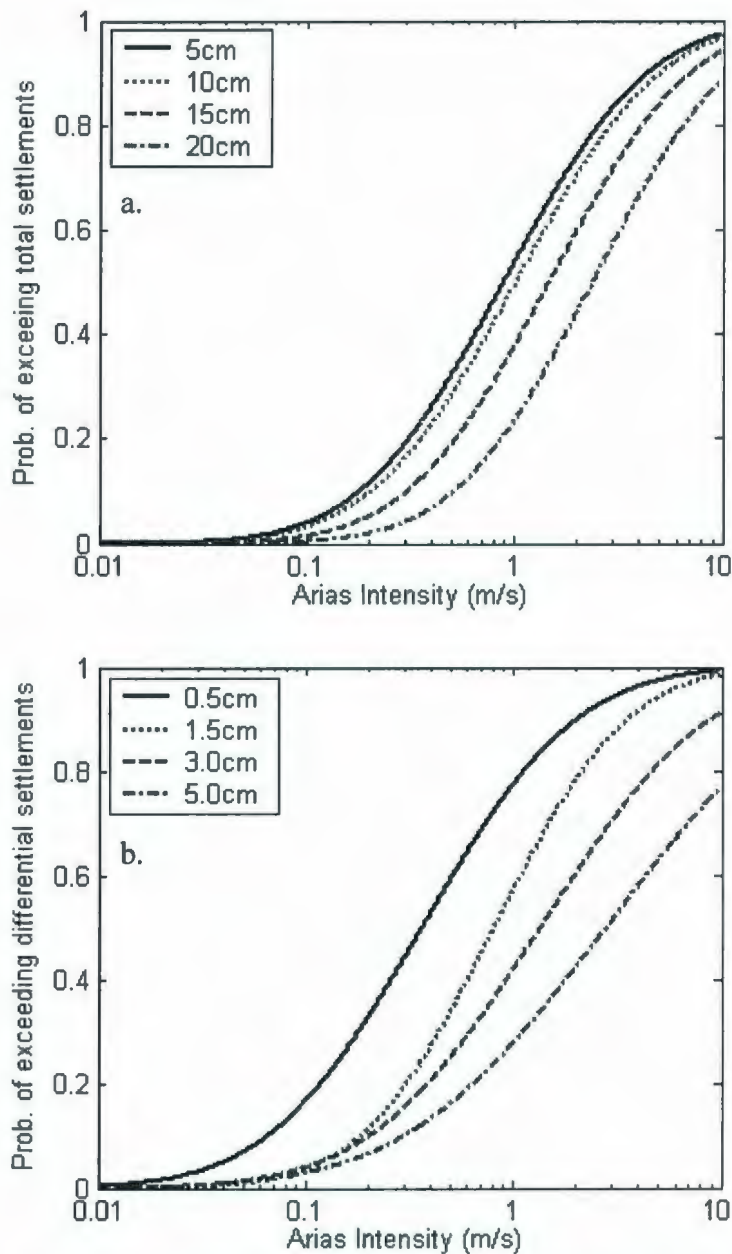


Figure 6.39: Fragility curves for structure on randomly variable loose saturated soil (COV=0.5) deposit subjected to 18 selected seismic motions: a. total settlement of left footing; b. differential settlement.

tabular form for design purpose for all the analysed cases. The Arias Intensity values for total and differential settlements exceeding certain threshold level are tabulated in Tables 6.11 and 6.12 respectively. The other fragility curves used for obtaining those Arias Intensity values are shown in the Appendix A.

Figure 6.40 shows the Type-I combined damage curve. The procedure used for constructing the combined damage curves is already discussed in Section 6.3.4.4. Figure 6.40a shows the Type-I damage curve for exceeding allowable limits of total and

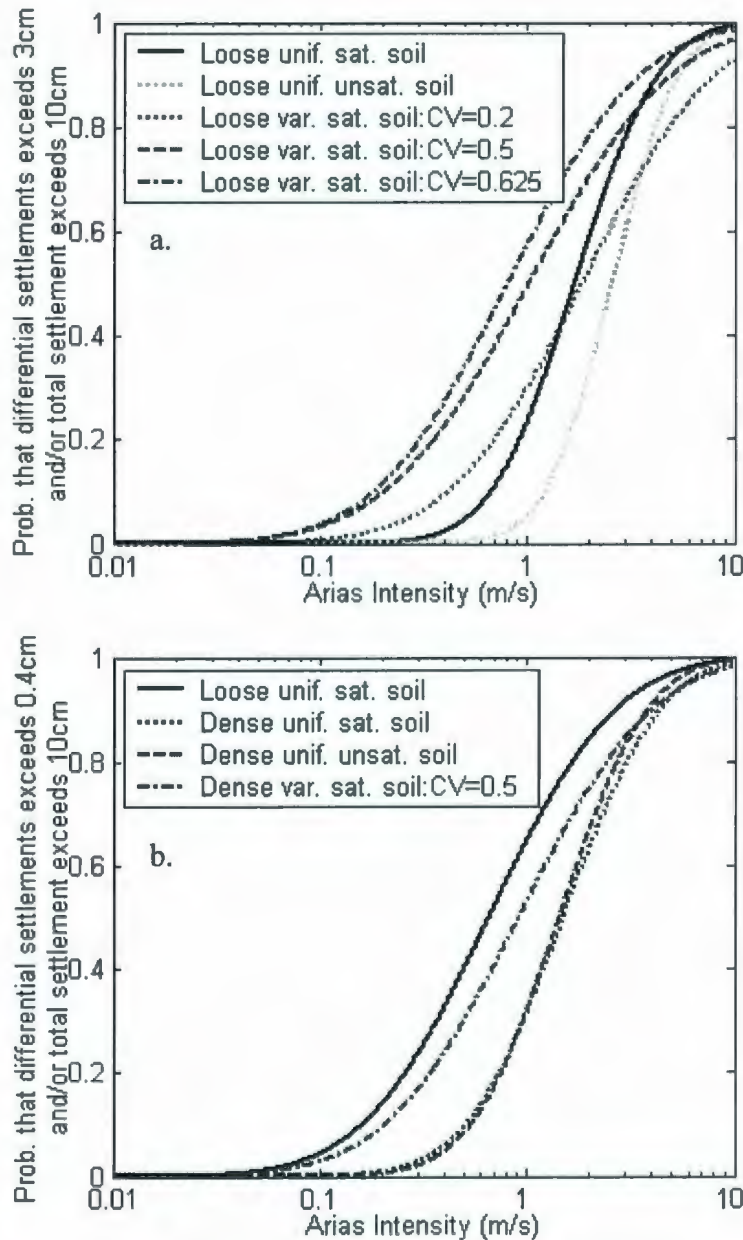


Figure 6.40: Type-I damage curve: probability of damage due to exceeding a. 10cm maximum total settlement and/or 3cm maximum differential settlement; b. 10cm maximum total settlement and/or 0.4cm maximum differential settlement.

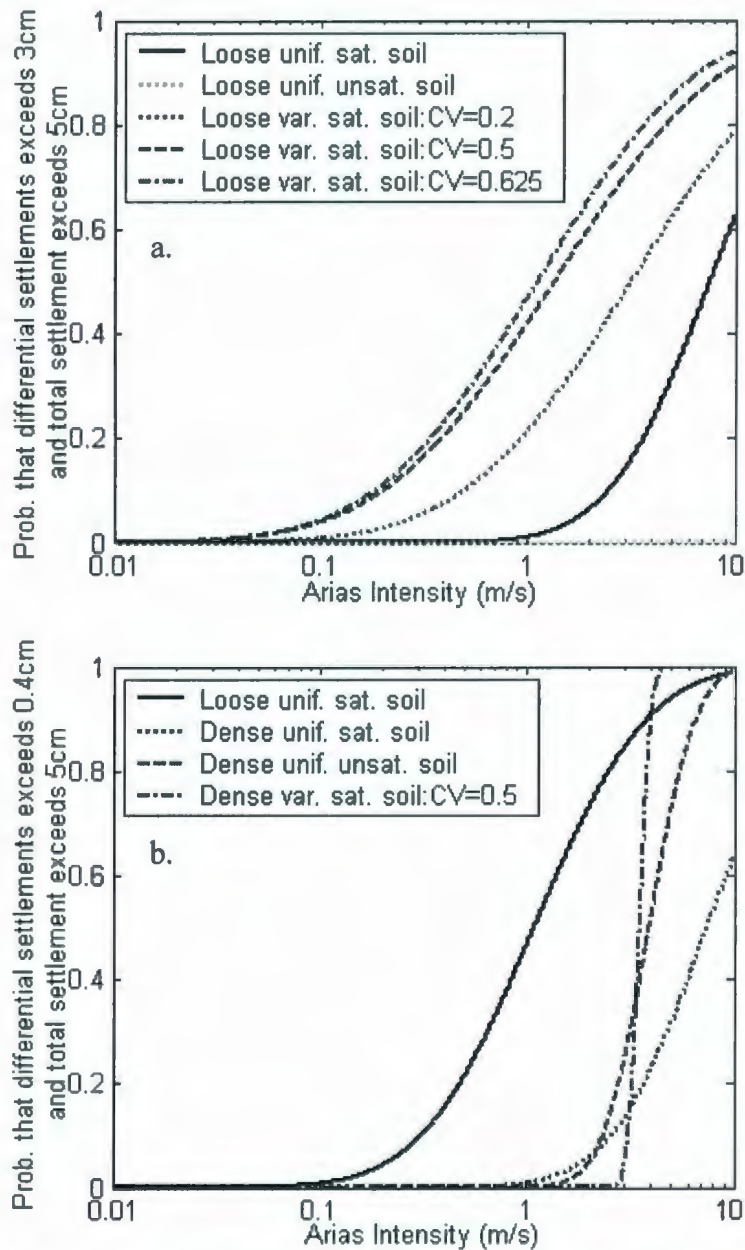


Figure 6.41: Type-II damage curve: probability of damage due to exceeding a. 5cm maximum total settlement and 3cm maximum differential settlement; b. 5cm maximum total settlement and 0.4cm maximum differential settlement.

differential settlements. Similarly, Figure 6.40b shows the Type-I damage curve for exceeding 0.4cm of differential settlements and the allowable limit of 10cm for total settlement. Figure 6.41 shows the Type-II combined damage curves. Figure 6.41a shows the Type-II curve for exceeding 3cm of differential settlements and 5cm of total

settlement. Similarly Figure 6.41b shows Type-II curve for exceeding 0.4cm of differential settlements and 5cm of total settlement.

6.4.6.3. Design Recommendations for Selecting an Equivalent Uniform Soil Strength

Based on the reliability analysis of frame structure presented in this Chapter, design recommendations are provided in this section. It has been observed that intensity of seismic ground motion, soil relative density, fundamental period of the structure and degree of soil variability all have significant influence on the predicted structural responses reported in this chapter. As shown in previous chapters (Chapter 4 and 5), soil heterogeneity leads to more EPWP build up than that in uniform soil. This ultimately causes more structural damage in terms of total and differential settlements. The fragility curves, combined damage curves and tables (Tables 6.11 and 6.12) provided in the previous section also can be used in design.

Based on the results of maximum total and differential settlements of the structure resting on heterogeneous soil, guidelines are provided here on selecting an equivalent uniform soil relative density (Dr^e). This equivalent uniform soil relative density represents the uniform soil density which will result in an equivalent response to that obtained for a structure on variable soil. The objective of this study was to find the fraction of the actual average relative density of the heterogeneous soil that, when used in a conventional analysis assuming uniform soil properties, would provide a response that is “equivalent” with that from Monte Carlo simulations. The meaning of “equivalent” response depends on what is the response parameter considered in the analysis- it may be

equivalent EPWP build-up, equivalent average settlements, equivalent total and differential settlements or equivalent base rotation.

A series of time history analyses has been performed on the soil-structure models where the structure was placed on uniform soil deposits with various soil relative densities. The relative densities of those uniform soil deposits were selected in such a way that they are the fraction of the actual average relative density of the heterogeneous soil (i.e., $Dr^e = F \times Dr^m$; where Dr^m is the average relative density of the heterogeneous soil, F is the fraction of the actual average relative density of the heterogeneous soil). The responses obtained for structure on heterogeneous soil are compared next with these analyses results.

Figure 6.42 shows the comparison between maximum total settlements at the left footing of the structure resting on loose variable soil ($Dr_m=45\%$) and that calculated for uniform soil. From the results it is observed that a uniform soil with a relative density 90% of average relative density of the heterogeneous soil results in total settlements at the left footing similar to those in variable soil with $CV=0.2$. For variable soil with $CV=0.5$, a relative density 80% of average relative density of the heterogeneous soil induces conservative maximum total settlements in most of the earthquakes. However, in some cases (e.g., $I_A=0.3m/s$) they are less than that computed in variable soil. Since it is very unlikely to get a natural soil deposit with relative density $<35\%$, the results for uniform soil with 70% of average relative density of the heterogeneous loose soil are not presented here. Similar comparisons for maximum differential settlements in structure on loose soil are shown in Figure 6.43. Due to the presence of loose pockets in the soil below the structure, maximum differential settlements in heterogeneous soil are much

higher than that in uniform soil in most cases. Even with small variability (CV=0.2),

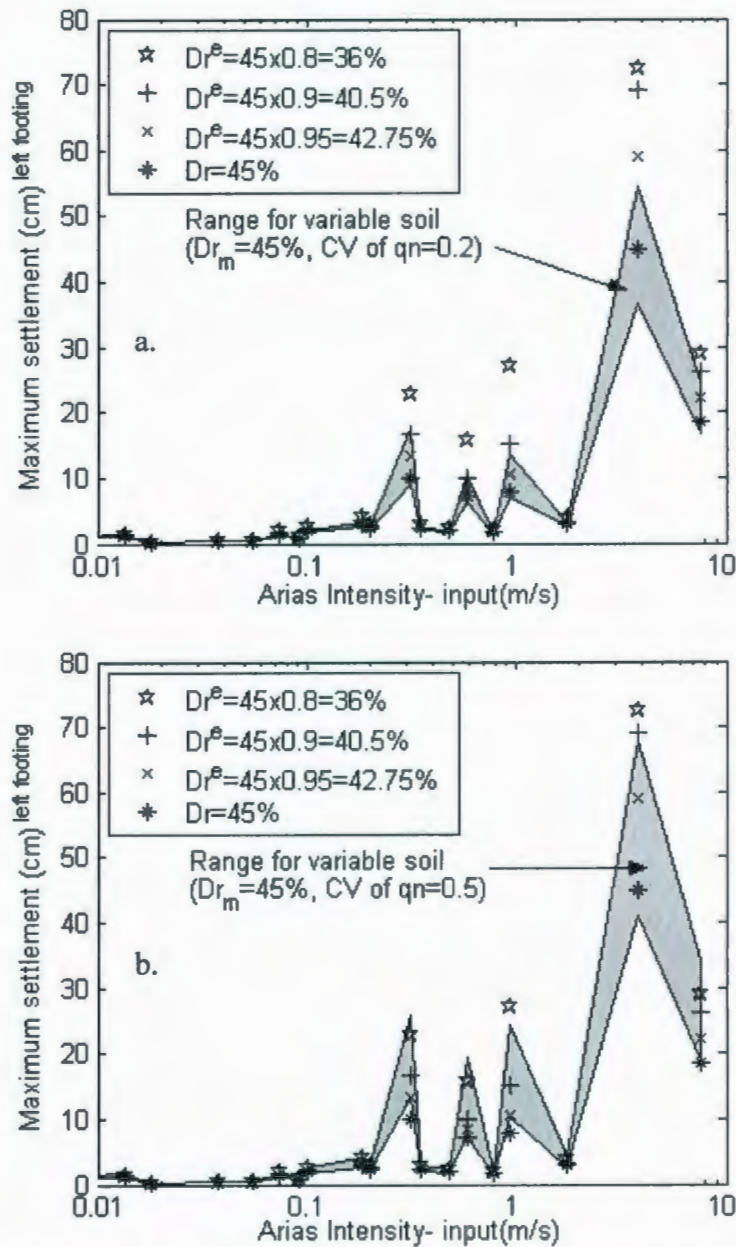


Figure 6.42: Comparison for maximum total settlements for the structure on loose heterogeneous soil and equivalent uniform soil.

about 2-3 times larger maximum differential settlements are recorded in heterogeneous soil than that in corresponding uniform soil.

The comparison of responses (for maximum total and differential settlements) between the structure on heterogeneous dense sand with $CV=0.5$ and uniform soil are

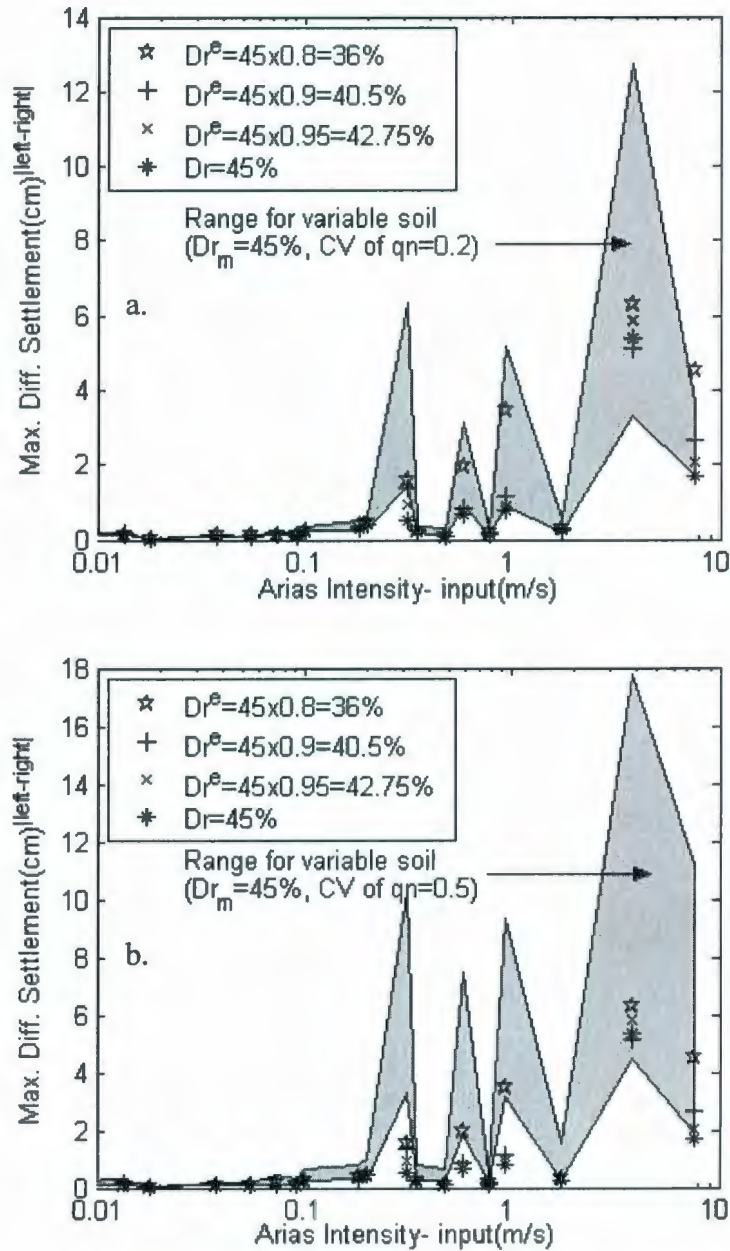


Figure 6.43: Comparison for maximum differential settlements for the structure on loose heterogeneous soil and equivalent uniform soil.

shown in Figure 6.44. All these results are briefly tabulated in Table 6.13. From the maximum total settlement comparison, it is found that a relative density 70% of average

relative density of the heterogeneous soil is conservative enough to produce similar responses as that in heterogeneous dense soil with $CV=0.5$. However, for maximum

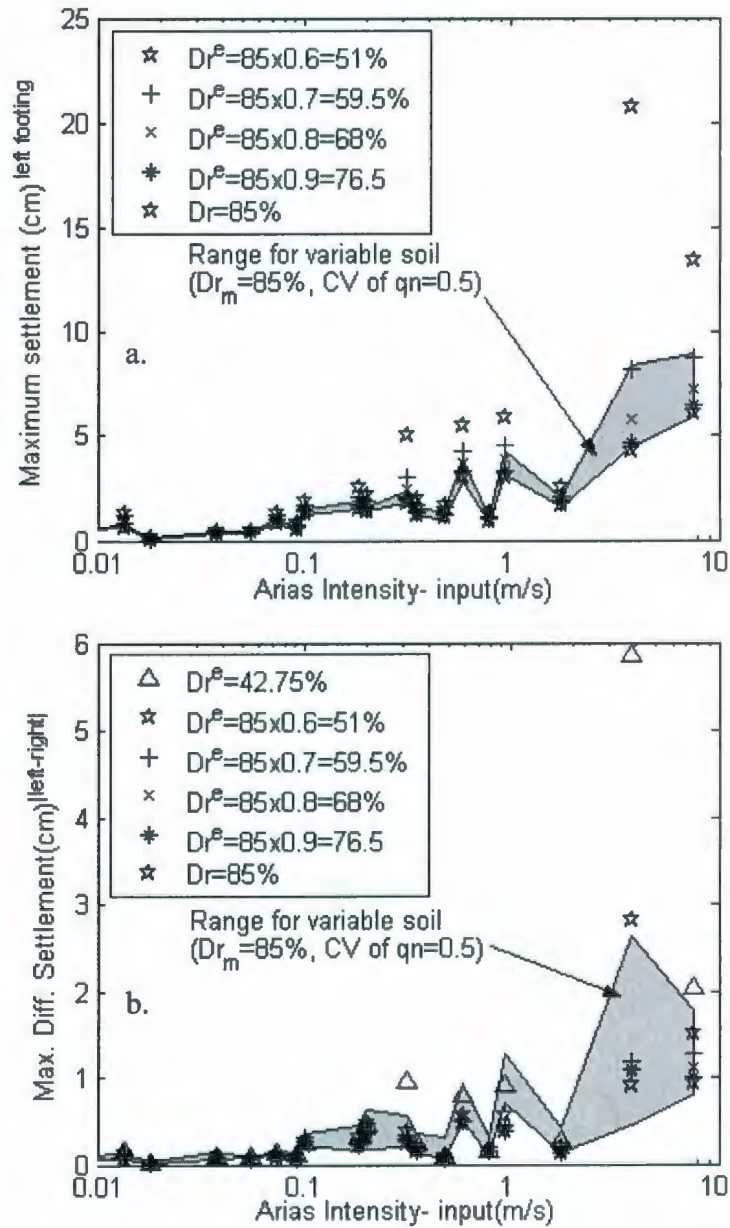


Figure 6.44: Comparison for maximum settlements for the structure on dense heterogeneous soil and equivalent uniform soil.

differential settlements, even about 50% equivalent uniform soil relative density ($Dr^e=42.75\%$) is not conservative enough to produce similar responses than that in heterogeneous soil. Therefore, it can be concluded that using equivalent relative density

will not be able to reproduce the same results as obtained from the structure on heterogeneous soil. Therefore, soil heterogeneity must be taken into consideration to accurately determine differential settlements in the frame structure. Without considering the presence of loose pockets in the soil below structure, it is not possible to accurately calculate the differential settlements in frame structure.

6.5. Summary and Conclusions

Both the spatial variability of soil properties and the frequency content of the seismic motion have a major role in predicted structural responses. In the first part of this study (Section 6.3), it was observed that for the type of soil considered here, UBC type-3 input acceleration time histories induce more damage to the structure than type-1 input acceleration. Due to soil softening after build-up of EPWP, the characteristic frequency of the soil-structure system goes down to the value close to the dominant frequency of low frequency inputs (e.g. type 3 input in this study). Therefore, considerably more structural damage is predicted for that type of seismic motion. It is also concluded that soil variability adversely affects the performance of the structure. The probability of damage of the structure situated on variable soil is higher compared to that of a structure situated on a uniform soil with the soil properties that are the average soil properties of the variable soil. The design guidelines based on this part of the study are presented in Section 6.3.4.5 (Table 6.4, 6.5 and Figure 6.10, 6.11, 6.13, 6.14). The combined damage curves, constructed based on basic probability theory, are useful for the initial reliability analysis of structures. The number of Monte Carlo simulations used here was much smaller than the theoretical number of simulations required for proper assessment of

result range boundaries. This was due to the significant computational effort required by each FE analysis (each analysis was taking about 2 hours using a dual core 2 @2.16GHz, 2MB ram computer). From previous similar studies (Bazzurro and Cornell, 2004; Nobahar, 2003) it was, however, found that 100 sample functions (as used here) are sufficient for correctly inferring the mean and standard deviation of the resulting quantities.

In the second part of this study, the results related to the analysis of a frame structure have been presented. The design guidelines for spectral amplification factors (F_a and F_v) have been provided for different types of soil conditions. Regression equations (in Figures 6.24 to 6.29) are provided for loose saturated and unsaturated soil (equivalent to site class E) and dense saturated and unsaturated soil (equivalent to site class D). A comparison of these amplification factors with the value in Canadian Building Code and previous studies (e.g., Bazzurro and Cornell, 2004) are shown in Table 6.10. Effects of soil variability on amplification factors were also studied. The effect of soil variability has been found to be not very significant in the studied ranges for calculating the values of spectral amplification factors. There is a less than 10% change in the values of F_a and F_v for heterogeneous soil compared to that in uniform soil. Separate regression equations are provided for heterogeneous soil with CV of $q_n = 0.2$ and 0.5 for calculating F_a and F_v . For intermediate CV values provided regression equations can be used with sufficient accuracy. However, water table depth has a significant influence on amplification factors. If the ground water level goes up, it decreases the soil strength and therefore amplification factors are decreased. So amplification factors in saturated soil are lower

than those in unsaturated soil. Therefore, not considering the effect of ground water table depth might induce significant errors in the values of amplification factors.

A statistical methodology called design of experiments (DOE) was used for obtaining significant parameters and replacement Response Surface model for calculating total and differential settlements. Various Response Surface models were formulated in the studied ranges of different factors and presented in Section 6.4.4 in more detail. The equations for Response Surface models are presented in Section 6.4.4.2 (Table 6.8). These Response Surface models can be used in the studied range of various factors for approximately calculating responses (total and differential settlements) in the structure. The results of reliability analysis for the frame structure situated on heterogeneous soil are presented in form of fragility curves and combined damage curves. The limiting Arias Intensity values for 1%, 5% and 10% probability of exceeding various thresholds for total and differential settlements are presented in tabular form (Tables 6.11 and 6.12) for all the analysed cases. The limiting Arias Intensity is the value of I_A which induces a certain probability of exceeding the thresholds of responses for particular soil conditions. These tabulated results can be used for design purposes.

In the last part of this study, relative density of an equivalent uniform soil deposit was recommended based on the results of maximum total settlements. This equivalent uniform soil relative density is the relative density of a uniform soil deposit which will produce an “equivalent” structural response to that in the case of structure on heterogeneous soil. It is concluded that for a loose soil with $CV=0.2$, 90% of average relative density of the heterogeneous soil is conservative enough to represent total settlements in heterogeneous soil. For $CV=0.5$, 70% of average relative density of the

heterogeneous soil is conservative enough to represent heterogeneous soil. However, accurate calculation for maximum differential settlements is not possible by using this equivalent relative density of uniform soil. This concept is not considering the presence of loose pockets which actually controls the differential settlements of a structure situated on heterogeneous soil. Therefore, soil heterogeneity must be taken into consideration to accurately determine the differential settlements in the frame structure.

Table 6.1: The correlations used for estimating parameters and the values of the multi-yield plasticity model parameters used in the analysis

Constitutive parameter	Values/Correlations	Reference
Mass density – solid	2660 kg/m ³	Been et al. (1991)
Soil relative density (Dr)	$Dr = \sqrt{\frac{q_n}{305P_{atm}}}$, where P _{atm} is the atmospheric pressure (100kPa)	Kulhawy and Maine (1990)
Void ratio (e)	$e = e_{max} - Dr(e_{max} - e_{min})$, where e _{max} and e _{min} are maximum and minimum void ratio	-
Porosity (n)	$n = \frac{e}{1+e}$	-
Hydraulic conductivity	$k = 1.2 \frac{e^3}{(1+e)} C_u^{0.735} D_{10}^{0.89}$, C _u is the uniformity coefficient, D ₁₀ is in mm and are calculated using following relation: $D_{10} = 0.015 + \left(\frac{11.619}{I_c + 10.293} \right)^{28.06629}$	Das (1994)

Table 6.1(contd.): The correlations used for estimating parameters and the values of the multi-yield plasticity model parameters used in the analysis

Low strain elastic shear modulus	$G_0 = 70 \frac{(2.17 - e)^2}{(1 + e)} \left(\frac{P'_0}{P_{atm}} \right)^{0.5}$	Hardin and Richard (1963)
Poisson's ratio	0.35	Popescu et al. (1997)
Power exponent	0.5	Popescu et al. (1997)
Friction angle at failure	$\phi = \tan^{-1} \left[0.1 + 0.38 \log \frac{q_c}{\sigma'_{v0}} \right]$, q_c is the cone penetration resistance, σ'_{v0} is the initial effective vertical stress	Robertson and Campanella (1983)
Maximum deviatoric strain (comp/ext)	0.07/0.04	Been et al. 1991
Coefficient of lateral stress	0.7	Jefferies et al. (1988)
Stress-strain curve coefficient	$\alpha = 0.217 - 0.027C_u + 0.037D_{max}$, D_{max} is the maximum particle size	Hayashi et al. (1992)
Dilation angle	31°	Been and Jefferies (1985)
Dilation parameter	$\log \left(\frac{X_{pp}}{0.7} \right) = 7.071 - 11.38 \times \left(0.1 \frac{15 + q_c \sqrt{P'_a} / (\sigma'_{v0})^{0.386}}{25 - q_c \sqrt{P'_a} / (\sigma'_{v0})^{0.386}} \right)^{0.132}$ 0.7 - to account for Mohr-Coulomb yield surface effect	Popescu (1995), Popescu et al. (2005)

Table 6.2: The parameters of the multi-yield plasticity model, and the values used for the saturated soil in the deterministic analysis

Constitutive parameter	Symbol	Value	Type
Mass density – solid	ρ^s	2660 kg/m ³	State parameters
Porosity	n^w	0.435	
Hydraulic conductivity	k	0.000264m/s	
Low strain elastic shear modulus	G_0	19.4MPa	Low strain elastic parameters
Poisson's ratio	ν	0.35	
Power exponent	n	0.5	
Friction angle at failure ⁽¹⁾	ϕ	37.2 ⁰43.7 ⁰	Yield and failure parameters
Maximum deviatoric strain (comp/ext)	ϵ_{dev}^{max}	0.07/0.04	
Coefficient of lateral stress	k_0	0.7	
Stress-strain curve coefficient	α	0.2756	
Dilation angle	ψ	31 ⁰	Dilation parameters
Dilation parameter ⁽¹⁾	X_{pp}	0.035....0.04	

Note: (1) Variable with depth, function of overburden stress.

Table 6.3: The damage levels used in the study for generating combined damage curves

Response parameter	Damage level	Value
Maximum permissible settlement (S _t)	Level – 1 damage	10cm
	Level – 2 damage	15cm
	Level – 3 damage	20cm
Maximum permissible base rotation (R _t)	Level – 1 damage	0.3 ⁰
	Level – 2 damage	0.4 ⁰
	Level – 3 damage	0.5 ⁰

Table 6.4: Minimum Arias Intensities corresponding to several probabilities of exceeding three threshold levels of total settlements for a tower structure constructed on liquefiable uniform or variable soil

Analysis condition →		Uniform soil, Type 1 input	Uniform soil, Type 3 input	Variable soil, Type 1 input	Variable soil, Type 3 input
Threshold level	Exceeding probability	Arias Intensity (m/s)			
10cm	1%	0.484	0.237	0.418	0.092
	5%	0.540	0.251	0.444	0.116
	10%	0.572	0.258	0.459	0.132
20cm	1%	1.538	0.535	0.504	0.419
	5%	1.601	0.590	0.619	0.444
	10%	1.635	0.622	0.690	0.457
30cm	1%	>2.3 ⁽¹⁾	0.875	0.699	0.348
	5%	>2.3 ⁽¹⁾	0.965	0.929	0.428
	10%	>2.3 ⁽¹⁾	1.017	1.082	0.478

Note: (1) Values are outside the analysis domain of Arias Intensity.

Table 6.5: Minimum Arias Intensities corresponding to several probabilities of exceeding three threshold levels of base rotation for a tower structure constructed on liquefiable uniform or variable soil

Analysis condition →		Uniform soil, Type 1 input	Uniform soil, Type 3 input	Variable soil, Type 1 input	Variable soil, Type 3 input
Threshold level	Exceeding probability	Arias Intensity (m/s)			
0.3 ⁰	1%	0.234	0.073	0.234	0.024
	5%	0.344	0.103	0.313	0.04
	10%	0.424	0.124	0.365	0.052
0.4 ⁰	1%	0.388	0.118	0.204	0.098
	5%	0.621	0.181	0.316	0.137
	10%	0.798	0.226	0.400	0.165
0.6 ⁰	1%	1.586	0.176	0.186	0.181
	5%	1.997	0.318	0.345	0.272
	10%	2.259	0.435	0.481	0.339

Note: (1) Outside the analysis domain of Arias Intensity.

Table 6.6: Different factors used in Face-Centred Central Composite Design and their high and low levels

Models	Factors	Unit	Low level	High level
Replacement Model-I	A: Soil relative density	%	45	85
	B: Coefficient of variation of q_n	-	0.2	0.5
	C: Arias Intensity	m/s	0.01	0.1
	D: Fundamental period of the structure	sec	0.29	0.78
Replacement Model-II	A: Soil relative density	%	45	85
	B: Coefficient of variation of q_n	-	0.2	0.5
	C: Arias Intensity	m/s	0.075	0.5
	D: Fundamental period of the structure	sec	0.29	0.78
Replacement Model-III, IIIA	A: Soil relative density	%	45	85
	B: Coefficient of variation of q_n	-	0.2	0.5
	C: Arias Intensity	m/s	0.5	1.5
	D: Fundamental period of the structure	sec	0.29	0.78
Replacement Model-IIIB	A: Soil relative density	%	45	85
	B: Coefficient of variation of q_n	-	0.2	0.5
	C: Arias Intensity	m/s	0.5	1.5
Replacement Model-IV	A: Soil relative density	%	45	85
	B: Coefficient of variation of q_n	-	0.2	0.5
	C: Arias Intensity	m/s	1.0	4.0
	D: Fundamental period of the structure	sec	0.29	0.78

Table 6.7: Design layout for Response Surface Model-I using Face-Centred Central Composite Design and calculated (from FE analysis) responses

Run #	A- Relative Density (%)	B- CV	C- Arias Intensity (m/s)	D- Period of Structure (sec)	Response: 1	Response: 2
					Maximum total settlement at left footing (m)	Maximum differential settlements (m)
1	85.00	0.50	0.010	0.29	3.539E-03	8.916E-04
2	65.00	0.50	0.055	0.78	1.745E-02	1.882E-03
3	65.00	0.35	0.010	0.29	3.309E-03	5.428E-04
4	65.00	0.35	0.100	0.78	2.164E-02	1.997E-03
5	85.00	0.50	0.010	0.78	5.359E-03	1.225E-03
6	45.00	0.50	0.100	0.29	1.795E-02	2.753E-03
7	85.00	0.20	0.100	0.29	9.540E-03	1.008E-03
8	85.00	0.50	0.100	0.78	2.016E-02	2.088E-03
9	65.00	0.35	0.010	0.78	6.464E-03	9.620E-04
10	45.00	0.20	0.010	0.78	7.555E-03	1.339E-03
11	45.00	0.50	0.100	0.78	2.670E-02	5.298E-03
12	65.00	0.35	0.055	0.29	9.075E-03	9.653E-04
13	85.00	0.20	0.010	0.29	2.569E-03	4.621E-04
14	85.00	0.50	0.100	0.29	1.079E-02	9.425E-04
15	45.00	0.20	0.100	0.78	2.548E-02	3.514E-03
16	65.00	0.35	0.055	0.78	1.568E-02	1.890E-03
17	45.00	0.20	0.010	0.29	3.650E-03	7.547E-04
18	85.00	0.20	0.010	0.78	3.918E-03	6.132E-04
19	65.00	0.20	0.055	0.78	1.532E-02	1.845E-03
20	45.00	0.35	0.055	0.78	1.938E-02	2.895E-03
21	45.00	0.50	0.010	0.78	7.693E-03	2.222E-03
22	65.00	0.50	0.055	0.29	1.009E-02	9.276E-04
23	85.00	0.20	0.100	0.78	1.849E-02	1.490E-03
24	85.00	0.35	0.055	0.29	7.527E-03	7.098E-04
25	45.00	0.50	0.010	0.29	3.927E-03	1.129E-03
26	45.00	0.35	0.055	0.29	1.238E-02	1.174E-03
27	65.00	0.20	0.055	0.29	8.645E-03	9.977E-04
28	65.00	0.35	0.100	0.29	1.261E-02	1.560E-03
29	45.00	0.20	0.100	0.29	1.652E-02	1.731E-03
30	85.00	0.35	0.055	0.78	1.453E-02	1.467E-03

Note: Soil relative density, coefficient of variation of q_n , and Arias Intensity are numerical factors and fundamental period of the structure is a categorical factor in this study.

Table 6.8: Equations for Response Surface Models

Models	Maximum total settlements (TS) of left footing in m	Maximum differential settlements (DS) in m
Replacement Model-I	<p>T_n=0.29: $TS=7.862E-03 -2.281E-04Dr +3.997E-03CV +0.3039AI -1.405E-03Dr.AI +1.487E-06Dr^2 -0.9142AI^2, R^2=0.99$</p> <p>T_n=0.78: $TS=1.031E-02 -2.281E-04Dr +3.997E-03CV +0.3729AI -1.405E-03Dr.AI +1.487E-06Dr^2 -0.9142AI^2, R^2=0.99$</p>	<p>T_n=0.29: $Ln(DS) = -6.999 - 0.012Dr + 1.117CV + 14.31AI - 0.090Dr.AI, R^2 = 0.9$</p> <p>T_n=0.78: $Ln(DS) = -6.409 - 0.012Dr + 1.117CV + 14.31AI - 0.090Dr.AI, R^2 = 0.9$</p>
Replacement Model-II	<p>T_n=0.29: $Ln(TS)= -2.313 -0.040Dr -1.541CV +4.222AI -0.01Dr.CV +1.895CV.AI +1.689E-04Dr^2 +3.424CV^2 -4.318AI^2, R^2=0.99$</p> <p>T_n=0.78: $Ln(TS)= -1.820 -0.037Dr -1.541CV +4.222AI -0.01Dr.CV +1.895CV.AI +1.689E-04*Dr^2 +3.424*CV^2 -4.318*AI^2, R^2=0.99$</p>	<p>T_n=0.29: $Ln(DS) = -4.865 - 0.011Dr - 2.97CV + 3.212AI + 1.475CV.AI + 4.619CV^2 - 3.605AI^2, R^2 = 0.98$</p> <p>T_n=0.78: $Ln(DS) = -3.875 - 1.509E - 02Dr - 2.97CV + 4.345AI + 1.475CV.AI + 4.619CV^2 - 3.605AI^2, R^2 = 0.98$</p>

Table 6.8 (contd.): Equations for Response Surface Models

<p>Replacement Model-III</p>	<p>Tn=0.29: $Ln(TS) = -2.490 - 0.041Dr - 0.718CV + 1.214AI - 0.005Dr.AI + 0.352CV.AI + 1.938E-04Dr^2 + 1.597CV^2 - 0.255AI^2$, $R^2=0.99$</p> <p>Tn=0.78: $Ln(TS) = -2.17 - 0.036Dr - 0.718CV + 1.214AI - 4.809E-03Dr.AI + 0.352CV.AI + 1.938E-04Dr^2 + 1.597CV^2 - 0.255AI^2$, $R^2=0.99$</p>	<p>Tn=0.29: $DS = +1.048E - 02 - 2.183E - 04Dr - 0.015CV + 5.075E - 03AI - 5.277E - 05Dr.AI + 1.631E - 06Dr^2 + 0.022CV^2$, $R^2 = 0.96$</p> <p>Tn=0.78: $DS = +0.016 - 2.643E - 04Dr - 0.01CV + 7.573E - 03AI - 5.277E - 05Dr.AI + 1.631E - 06Dr^2 + 0.022CV^2$, $R^2 = 0.96$</p>
<p>Replacement Model-IIIA</p>	<p>Tn=0.29: $1/\sqrt{(TS)} = 2.939 + 0.119Dr - 1.887CV - 2.849AI - 4.256E-04Dr^2 + 0.666AI^2$, $R^2=0.95$</p> <p>Tn=0.78: $1/\sqrt{(TS)} = 2.493 + 0.091Dr - 1.193CV - 2.433AI - 4.256E-04Dr^2 + 0.666AI^2$, $R^2=0.95$</p>	<p>Tn=0.29: $1/\sqrt{(DS)} = +3.142 + 0.535Dr - 15.610CV - 5.356AI - 2.366E - 03Dr^2$, $R^2 = 0.84$</p> <p>Tn=0.78: $1/\sqrt{(DS)} = +1.719 + 0.353Dr - 5.514CV - 2.347AI - 2.366E - 03Dr^2$, $R^2 = 0.84$</p>
<p>Replacement Model-IIIB</p>	<p>Tn=0.29: $1/\sqrt{(TS)} = -2.728 + 0.26Dr - 1.732CV - 3.334AI - 1.388E - 03Dr^2 + 0.902AI^2$, $R^2 = 0.99$</p>	<p>Tn=0.29: $\sqrt{(DS)} = 0.292 - 8.930E - 03Dr + 0.312CV + 0.117AI - 3.038E - 03Dr.CV - 6.278E - 04Dr.AI + 6.653E - 05Dr^2 - 0.021AI^2$, $R^2 = 0.99$</p>

Table 6.8 (contd.): Equations for Response Surface Models

Replacement Model-IV	<p>Tn=0.29: $Ln(TS) = -7.227E-02 - 9.626E-02Dr + 1.019CV + 0.741AI + 4.986E-04Dr^2 - 8.728E-02AI^2$, $R^2=0.99$</p> <p>Tn=0.78: $Ln(TS) = +0.378 - 9.345E-02Dr + 1.019CV + 0.741AI + 4.986E-04Dr^2 - 0.087AI^2$, $R^2=0.99$</p>	<p>Tn=0.29: $Ln(DS) = -4.294 - 6.175E-02Dr + 2.583CV + 1.156AI - 5.410E-02Dr.CV - 0.410CVAI + 4.046E-04Dr^2 + 7.675CV^2 - 0.141AI^2$, $R^2 = 0.95$</p> <p>Tn=0.78: $Ln(DS) = -3.061 - 6.175E-02Dr + 1.072CV + 1.156AI - 5.410E-02Dr.CV - 0.410CV.AI + 4.046E-04Dr^2 + 7.675CV^2 - 0.141AI^2$, $R^2 = 0.95$</p>
----------------------	---	--

Where, Dr= Soil relative density and its value ranging from 45% to 85%, CV= Coefficient of variation of q_c and its value ranging from 0.2 to 0.5, AI= Arias Intensity in m/s and its value depends on the range for corresponding model.

Table 6.9: Validation of Response Surface Model-IV

Dr (%)	CV	Arias Intensity (m/s)	period of the structure (sec)	Input acceleration file no	Maximum Total Settlements (m)		Maximum Differential Settlements (m)	
					Calculated From FE Analysis	Calculated From RSM	Calculated From FE Analysis	Calculated From RSM
79	0.31	2.7	0.78	ac098	0.10400	0.10960	0.02000	0.01994
67	0.27	1.995	0.78	ac098	0.10700	0.10671	0.01830	0.01859
52	0.43	2.714	0.78	ac098	0.27200	0.26570	0.06500	0.05595
69	0.46	3.19	0.78	ac098	0.17700	0.17375	0.03830	0.03548
54	0.48	1.693	0.29	ac098	0.11000	0.09808	0.03370	0.02674
58	0.48	3.565	0.29	ac098	0.15700	0.14160	0.04840	0.03410
57	0.35	3.821	0.29	ac098	0.13000	0.13218	0.02670	0.01991
52	0.47	2.362	0.78	ac098	0.26500	0.24917	0.06650	0.06025
70	0.34	1.145	0.29	ac098	0.03710	0.03740	0.00575	0.00565
62	0.34	3.088	0.78	ac098	0.17900	0.18355	0.02960	0.03261
83	0.31	2.908	0.29	ac096	0.00670	0.05543	0.00136	0.00926
76	0.41	2.041	0.78	ac096	0.01030	0.10265	0.00207	0.01941
83	0.49	1.688	0.29	ac094	0.02130	0.04396	0.00286	0.01098
52	0.26	3.477	0.78	ac098	0.26000	0.26048	0.04370	0.04237
70	0.33	3.826	0.29	ac097	0.06950	0.08444	0.00861	0.01295
47	0.49	3.727	0.29	ac097	0.57000	0.23582	0.11500	0.05890
70	0.46	3.398	0.29	ac098	0.09330	0.09193	0.02220	0.02027
49	0.31	3.132	0.78	ac098	0.30200	0.29470	0.05420	0.04868
70	0.22	3.705	0.78	ac097	0.10800	0.14270	0.02030	0.02715
46	0.46	2.303	0.78	ac096	0.01430	0.31599	0.00274	0.07502

Note: This model was formulated using input acceleration file # ac098.

Table 6.10: Comparison of the short (0.2s) and long period (1.0s) amplification factors, F_a and F_v results for different types of soil

Sa(0.2)	Short period (0.2s) amplification factor, F_a									
	Site class E (NBCC 2005)	Sandy site (Bazzurro and Cornell, 2004)	Uniform saturated loose soil ($D_r=45\%$)		Uniform unsaturated loose soil ($D_r=45\%$)		Variable saturated loose soil ($D_{r_m}=45\%$, $CV=0.2$)		Variable saturated loose soil ($D_{r_m}=45\%$, $CV=0.5$)	
			Value	(% change) _E	Value	(% change) _E	Value	(% change) _E	Value	(% change) _E
0.25	2.1	1.489	0.783	-62.711	1.106	-47.342	0.778	-62.968	0.773	-63.187
0.5	1.4	0.962	0.476	-65.980	0.763	-45.471	0.472	-66.267	0.468	-66.563
0.75	1.1	0.703	0.348	-68.365	0.620	-43.617	0.348	-68.369	0.343	-68.832
1	0.9	0.549	0.276	-69.370	0.537	-40.290	0.278	-69.065	0.273	-69.703
1.25	0.9	0.446	0.229	-74.584	0.482	-46.450	0.233	-74.068	0.227	-74.750
Sa(1.0)	Long period (1.0s) amplification factor, F_v									
	Site class E (NBCC 2005)	Sandy site (Bazzurro and Cornell, 2004)	Uniform saturated loose soil ($D_r=45\%$)		Uniform unsaturated loose soil ($D_r=45\%$)		Variable saturated loose soil ($D_{r_m}=45\%$, $CV=0.2$)		Variable saturated loose soil ($D_{r_m}=45\%$, $CV=0.5$)	
			Value	(% change) _E	Value	(% change) _E	Value	(% change) _A	Value	(% change) _E
0.1	2.1	3.016	2.071	-1.391	4.592	118.657	1.925	-8.322	1.929	-8.157
0.2	2.0	2.255	1.460	-27.024	3.396	69.824	1.402	-29.919	1.358	-32.108
0.3	1.9	1.811	1.174	-38.186	2.755	44.988	1.149	-39.525	1.085	-42.902
0.4	1.7	1.517	1.001	-41.119	2.340	37.623	0.992	-41.640	0.917	-46.043
0.5	1.7	1.305	0.881	-48.153	2.044	20.224	0.882	-48.095	0.801	-52.860

Note: D_r = Soil relative density, CV = Coefficient of variation of q_n ,

$$(\% \text{ change})_E = \left(\frac{F_a \text{ or } F_v \text{ in other type of soil} - F_a \text{ or } F_v \text{ recommended by NBCC for site class E}}{F_a \text{ or } F_v \text{ recommended by NBCC for site class E}} \right) \times 100\%$$

Table 6.10 (contd.): Comparison of the short (0.2s) and long period (1.0s) amplification factors, F_a and F_v results for different types of soil

Sa(0.2)	Short period (0.2s) amplification factor, F_a								
	Site class D (NBCC 2005)	Site class E (NBCC 2005)	Sandy site (Bazzurro and Cornell, 2004)		Uniform saturated loose soil (Dr=45%)	Uniform saturated dense soil (Dr=85%)		Uniform unsaturated dense soil (Dr=85%)	
			Value	(% change) _D		Value	(% change) _D	Value	(% change) _D
0.25	1.3	2.1	1.489	14.507	0.783	1.078	-17.059	1.445	11.120
0.5	1.2	1.4	0.962	-19.824	0.476	0.707	-41.074	1.009	-15.947
0.75	1.1	1.1	0.703	-36.056	0.348	0.544	-50.562	0.803	-26.973
1	1.1	0.9	0.549	-50.108	0.276	0.448	-59.254	0.678	-38.350
1.25	1	0.9	0.446	-55.394	0.229	0.384	-61.578	0.592	-40.798
Sa(1.0)	Long period (1.0s) amplification factor, F_v								
	Site class D (NBCC 2005)	Site class E (NBCC 2005)	Sandy site (Bazzurro and Cornell, 2004)		Uniform saturated loose soil (Dr=45%)	Uniform saturated dense soil (Dr=85%)		Uniform unsaturated dense soil (Dr=85%)	
			Value	(% change) _D		Value	(% change) _D	Value	(% change) _D
0.1	1.4	2.1	3.016	115.441	2.071	3.190	127.871	3.934	180.997
0.2	1.3	2.0	2.255	73.451	1.460	2.225	71.150	3.181	144.690
0.3	1.2	1.9	1.811	50.924	1.174	1.770	47.469	2.764	130.316
0.4	1.1	1.7	1.517	37.876	1.001	1.492	35.646	2.483	125.748
0.5	1.1	1.7	1.305	18.651	0.881	1.301	18.283	2.276	106.897

$$(\% \text{ change})_D = \left(\frac{F_a \text{ or } F_v \text{ in other type of soil} - F_a \text{ or } F_v \text{ recommended by NBCC for site class D}}{F_a \text{ or } F_v \text{ recommended by NBCC for site class D}} \right) \times 100\%$$

Table 6.11: Arias Intensities (in m/s) corresponding to various exceedance probabilities for various threshold levels of structural settlements and various soil conditions

	Threshold level											
	5cm			10cm			15cm			20cm		
Exceeding probability →	1%	5%	10%	1%	5%	10%	1%	5%	10%	1%	5%	10%
Soil condition												
Loose, uniform, saturated	0.11	0.215	0.308	0.313	0.514	0.669	0.403	0.625	0.789	0.297	0.550	0.763
Loose, uniform, unsaturated	0.143	0.261	0.361	0.668	0.992	1.225	7.711	8.249	8.551	>10.0 ⁽¹⁾	>10.0 ⁽¹⁾	>10.0 ⁽¹⁾
Loose, variable, saturated CV=0.2	0.049	0.114	0.179	0.171	0.346	0.504	0.386	0.651	0.86	0.589	1.143	1.628
Loose, variable, saturated CV=0.5	0.049	0.114	0.179	0.056	0.130	0.205	0.085	0.195	0.305	0.148	0.333	0.513
Dense, uniform, saturated	1.062	1.878	2.544	>10.0 ⁽¹⁾								
Dense, uniform, unsaturated	1.537	2.021	2.339	>10.0 ⁽¹⁾								
Dense, variable, saturated CV=0.5	2.807	2.998	3.105	>10.0 ⁽¹⁾								

Note: (1) Outside the analysis domain of Arias Intensity.

Table 6.12: Arias Intensities (in m/s) corresponding to various exceedance probabilities for various threshold levels of structural settlements and various soil conditions

	Threshold level											
	0.5cm			1.5cm			3cm			5cm		
Exceeding probability →	1%	5%	10%	1%	5%	10%	1%	5%	10%	1%	5%	10%
Soil condition												
Loose, uniform, saturated	0.110	0.213	0.306	0.452	0.733	0.949	0.979	1.781	2.449	0.695	2.050	3.650
Loose, uniform, unsaturated	0.333	0.552	0.722	>10.0 ⁽¹⁾								
Loose, variable, saturated CV=0.2	0.028	0.072	0.118	0.089	0.207	0.326	0.109	0.291	0.492	0.105	0.543	1.302
Loose, variable, saturated CV=0.5	0.016	0.039	0.064	0.054	0.119	0.181	0.042	0.116	0.200	0.047	0.155	0.294
Dense, uniform, saturated	0.295	0.550	0.767	>10.0 ⁽¹⁾								
Dense, uniform, unsaturated	0.597	0.957	1.231	>10.0 ⁽¹⁾								
Dense, variable, saturated CV=0.5	0.068	0.162	0.257	1.053	1.860	2.520	>10.0 ⁽¹⁾					

Note: (1) Outside the analysis domain of Arias Intensity.

Table 6.13: Practical recommendations on equivalent uniform soil relative density (Dr^e)

Soil type	Average relative density (Dr^m %)	Coefficient of variation of q_n	Response Variable	$F^{(1)} = \frac{Dr^e}{Dr^m}$
Loose saturated variable soil	45	0.2	Total settlements	0.90
Loose saturated variable soil	45	0.5		0.70 ⁽²⁾
Dense saturated variable soil	85	0.5		0.70

Note: (1) F is the fraction of the actual average relative density of the heterogeneous soil.

(2) Results are not presented in the thesis (since uniform soil relative density < 35%)

CHAPTER 7

Concluding Remarks

7.1. Summary and Conclusions

This chapter presents a summary of the research conducted, the conclusions reached and the suggestions for future work. It is usually found that most of the soil properties of a natural deposit not only vary in the vertical direction but could also vary in the horizontal direction even within a so-called 'uniform' soil layer. From past numerical research it was observed that in the case of seismically induced excess pore water pressure (EPWP) generation, more EPWP is generated during an earthquake in a heterogeneous soil deposit than in a homogeneous soil with equivalent average geomechanical properties. However, to date there are very limited number of experimental verifications available to the practicing engineering community to help in recognizing, quantifying and accepting the above-mentioned behaviour of heterogeneous soils. Therefore, the main aim of this thesis was to identify and explain the liquefaction mechanisms for heterogeneous soil. The second objective was to provide recommendations for structural foundation designs.

This study has two main parts. In the first part, the liquefaction mechanisms for heterogeneous soil were studied in detail using numerical (finite element analysis) and physical (geotechnical centrifuge tests) modelling. A series of three centrifuge tests were performed (one on homogeneous soil and two on heterogeneous soil). The test on homogeneous soil was performed on a soil deposit with the soil relative density lower

than the average relative density of heterogeneous soil. The results were monitored and measured throughout the test duration to explain the liquefaction mechanisms for heterogeneous soil. The liquefaction mechanism was explained by observing EPWP build-up and water migration between neighbouring soil zones with different relative densities. However, it is not practical to monitor experimental results at very close proximity in the model. Therefore, a numerical model was calibrated and validated from the centrifuge test results (described in Section 5.3.3 in Chapter 5) on uniform soil first. Then, the liquefaction mechanism in heterogeneous soil (discussed in detail in Section 5.4) was studied in more detail using the numerical simulation results.

In the second part of this research, the effects of soil heterogeneity on structural response were studied using Monte Carlo simulation. Two different types of structures were considered in the analysis: a tower structure (where maximum total settlement and base rotation were of primary interest) and a frame structure (where maximum total and differential settlements were of primary interest). The reliability analysis of a tower structure resting on heterogeneous soil is presented in Section 6.3. The design recommendations based on this part of the study are presented in Section 6.3.4.5. The research related to the reliability analysis of the frame structure resting on heterogeneous soil is discussed in Section 6.4. Quantitative and qualitative guidelines were provided, based on the analysis results. A design of experiments approach was then used for formulating replacement Response Surface models for calculating total and differential settlements. These are presented in Section 6.4.4.2 (shown in Table 6.8). These equations can be used in the studied range of various factors for approximately calculating structural responses (total and differential settlements). Updated design guidelines were

also provided for the spectral amplification of seismic ground motion. Based on the nonlinear dynamic fully-coupled finite element site response analysis, regression equations for the short (0.2s) and long period (1.0s) amplification factors, F_a and F_v were provided. Regression equations (shown in Figure 6.24-6.29) are provided for calculating spectral amplification factors in loose saturated and unsaturated soil and dense saturated and unsaturated soil. Effects of soil variability on amplification factors were also studied (discussed in detail in Section 6.4.5.6). The effect of soil variability on spectral amplification factors has been found to be not very significant in the studied ranges. The Monte Carlo simulation results for the frame structure on variable soil are presented in Section 6.4.6.2 in form of fragility curves and combined damage curves. The Tables 6.11 and 6.12, fragility curves and combined damage curve presented in Section 6.4.6.2 can be used for design purposes. Based on the results of maximum total settlements (discussed in details in Section 6.4.6.3) in the last part of this study, the relative density of an equivalent uniform soil deposit was recommended for use in simplified seismic analysis.

A detailed summary was given at the end of each chapter. Based on the entire research, the following conclusions can be drawn:

1. Recorded centrifuge test results (presented in Section 4.6.3 in Chapter 4) support the conclusion of previous numerical findings that more EPWP is generated in a heterogeneous soil than in the corresponding homogeneous soil. Although the average relative density of heterogeneous soil deposit (test 2 and test 3) were higher than that in uniform soil deposit model (test 1), the liquefaction resistance was lower than that of the uniform soil. The higher EPWP ratio generated in the free field compared to that below the

structure showed that the presence of a structure causes a higher liquefaction resistance in the soil.

2. After analysing the numerical and experimental results (in Chapter 5), it was concluded that the EPWP is generated in the loose sand pockets first. Next, due to the pressure gradient created between loose and dense sand zones in the heterogeneous soil, water migrates from loose to dense soil zones. This ultimately results in softening of the dense sand by reducing the effective stress, due to the build-up of EPWP.
3. A structure placed on heterogeneous soil may experience larger differential settlements and base rotations than one placed on a homogeneous soil deposit with equivalent (average) properties. Overall, it can be concluded that soil variability adversely affects the seismic performance of the structure.
4. From the Monte Carlo simulation results it was concluded that both the spatial variability of soil properties and the frequency content of the seismic motion have a major role in the structural response.
5. Based on a limited number of sample functions from Monte Carlo simulation, an equivalent uniform relative density was suggested for the heterogeneous soil in Chapter 6 (Section 6.4.6.3). Depending on the result of maximum total settlements at the left footing of the structure, it was concluded that for a soil with CV of $q_n = 0.2$, 90% of average relative density of the heterogeneous soil is found to be conservative enough to represent heterogeneous soil. For CV of $q_n = 0.5$, 70% of average relative

density of the heterogeneous soil is conservative enough to represent heterogeneous soil. However, where differential settlements are important (e.g., a frame structure on heterogeneous soil), accurate calculation for differential settlements are not possible using the relative density of the equivalent uniform soil deposit. The actual spatial locations of soil pockets are very important for quantifying the differential settlements. Therefore, random soil heterogeneity must be taken into consideration to determine differential settlements in the frame structure. However, the location of soil pockets in a randomly heterogeneous soil is not known, and therefore Monte Carlo simulation and statistical analysis of results are required for estimating differential settlements.

6. Some design guidelines for spectral amplification factors (the short (0.2s) and long period (1.0s) amplification factors, F_a and F_v) have been provided for different types of soil conditions (discussed in more detail in Section 6.4.5.6). Provided regression equations (shown in Figure 6.24-6.29) can be used for seismic design purposes. From the study it is concluded that soil heterogeneity does not have much influence on the values of amplification factors for the range of soil properties studied here. However, there is a very significant influence of water table depth. Therefore, not considering the effect of water table depth might induce significant errors in the values of amplification factors.
7. The combined numerical and experimental methods can be used as an efficient tool for including the soil-structure interaction effect during an

earthquake shaking and to model the structure resting on a natural soil deposit. Moreover, the numerical model used in this research can accurately reproduce experimental phenomena observed during liquefaction of heterogeneous soil, and therefore, it can be used to expand the scope of experimental results and provide design recommendations.

7.2. Scope of future study

Based on the research presented in the thesis, the following are recommendations for future study:

1. **Extend the study with numerical modelling:** The calibrated numerical model can be used for further research in simulating the behaviour of heterogeneous soil. For example, the effect of the absolute value and ratio of horizontal and vertical correlation distance, span of the frame structure on quantifying structural differential settlement can be studied. While determining relative density of equivalent uniform soil (in Section 6.4.6.3), the effect of earthquake intensity on the relative density value was not considered. A separate study on this factor on relative density of the equivalent uniform soil deposit can be performed. The present study has been performed for a structure situated on level heterogeneous soil deposit. However, further studies can be possible where the structure is situated on sloping ground. This numerical study on heterogeneous soil can also be extended on submerged and waterfront slopes made of heterogeneous soil.

2. **Extend the study with physical modelling:** The centrifuge experimental study can be extended for identifying the liquefaction mechanism to other type of cohesionless soils with different physical properties. Also, some advanced imaging techniques can be used in the centrifuge (on flight) to measure the relative water velocity during earthquake shaking. Accurate determination of actual relative density just before applying ground motion in the model can be done using some advanced techniques.
3. **Extend the study with Design of Experiments:** In the present study, various response surface models were formulated for various response variables. More factors (e.g., more structural types and layouts), more response variables and increased number of samples in Monte Carlo simulation (only 1, 5 and 10 samples were used in this study) can be selected to formulate more accurate response surface models. These models can be used for predicting the approximate responses inside the analysis domain.
4. **Further study of the constitutive model:** The numerical model predicted, in general more dilative behaviour for the soil below the structure than that observed in the centrifuge tests (both uniform and heterogeneous soil model). Therefore, there is a need for further research on the development of an efficient constitutive model which can more accurately reproduce the behaviour of the soil with static shear.
5. **Extrapolate the study for liquefaction mitigation:** The present study can be extended for mitigating liquefaction hazards in the heterogeneous

soil. Effectiveness of various mitigation methods (e.g. stone column, dynamic compaction, vibroflotation etc) in heterogeneous soil can be studied in more detail using the calibrated and validated numerical model and centrifuge tests.

REFERENCES

1. Aboim, C., Scott, R.F., Lee, J.R., and Roth, W.H. (1986). "Centrifuge earth dam studies: earthquake tests and analysis", *Report to the National Science Foundation*. Grant No. CEE-7926691. Dames and Moore. Los Angeles. California.
2. Andrus, R.D., and Stokoe, K.H. (1997). "Liquefaction resistance based on shear wave velocity", *In Proc. NCEER Workshop on Evaluation of Liquefaction Resistance of Soils*, National Centre for Earthquake Eng. Res., State Univ. of New York at Buffalo, pp. 89-128.
3. Andrus, R.D., and Stokoe, K.H. (2000). "Liquefaction resistance of soils from shear-wave velocity", *Journal of Geotechnical and Geo-environmental Engineering, ASCE*, vol. 126(11), pp. 1015-25.
4. Arias, A. (1970). "A measure of earthquake intensity", *Seismic design for nuclear power plants*, Edited by R.J. Hansen. MIT Press. Cambridge, Mass., pp. 438-483.
5. Arulanandan, K., Canclini, J., and Anandarajah, A. (1982). "Stimulation of earthquake motions in centrifuge", *Journal of Geotechnical Engineering Division, ASCE*, vol. 108, pp. 730-742.
6. Arulanandan, K., Muraleetharan, K.K., and Yogachandran, C. (1997). "Seismic response of soil deposits in San Francisco marina district," *Journal of Geotechnical and Geo-environmental Engineering, ASCE*, Vol. 123(10), October, pp. 965-974.
7. Arulanandan, K., and Scott, R.F., editors, (1993). *In Proc. International Conference on Verification of Numerical Procedures for the Analysis of soil liquefaction problems*, vol. 1, Balkema, Rotterdam.
8. Arulanandan, K., and Scott, R., F., editors, (1994). *In Proc. International Conference on Verif. Numerical Procedures for the Analysis of soil liquefaction problems*, vol. 2, Balkema, Rotterdam.
9. Arya, A.S., Nandakumaran, P., Puri, V.K., and Mukerjee, S., (1978). "Verification of liquefaction potential by field blast tests", *In Proc. 2nd International Conference on Microzonation*, Seattle, USA.

10. Atigh, E. and Byrne, P.M. (2004). "Liquefaction flow of submarine slopes under partially undrained condition: an effective stress approach", *Canadian Geotechnical Journal*, vol. 41, pp. 154-65.
11. Azizian, A. (2004). "Seismic Analysis of Submarine Slopes: Retrogressive and Three-Dimensional Effects", *Ph.D. Thesis*, Memorial University of Newfoundland, St. John's, NL, Canada.
12. Bazzurro, P., and Cornell, C.A. (2004). "Ground-motion amplification in nonlinear soil sites with uncertain properties", *Bulletin of the Seismological Society of America*, vol. 94(6), pp. 2090-109.
13. Belloti, R., Ghionna, V., Jamiolkowski, M., Lancellotta, R., and Manfredini, G. (1986). "Deformation characteristics of cohesionless soils from in-situ tests", *In: Use of In-Situ Tests in Geotechnical Engineering*, Clemence SP, editor, pp. 47-73.
14. Been, K., Jefferies, M.G. (1985). "A state parameter for sands", *Geotechnique*, vol. 35(2), pp. 99-112.
15. Been, K., Jefferies, M.G., Hachey, J. (1991). "The critical state of sands", *Geotechnique*, vol. 41(3), pp. 365-81.
16. Been, K., Jefferies, M.G., Crooks, L.H.A., and Rothenburg, L. (1987). "The cone penetration test in sand: Part II, general inference of state", *Geotechnique*, vol. 37(3), pp. 285-99.
17. Biot, M.A. (1955). "Theory of elasticity and consolidation for a porous anisotropic solid", *Journal of Applied Physics*, vol. 26, pp. 182-185.
18. Biot, M.A. (1962). "Mechanics of deformation and acoustic propagation in porous media", *Journal of Applied Physics*, vol. 33(4), pp. 1482-98.
19. Bolton, M.D., Gui, M.W., Garnier, J., Corte, J.F., Bagge, G., Laue, J., and Renzi, R. (1998). "Centrifuge modelling of cone penetration tests". In T Kimura et al. (eds), *Centrifuge 1998*, pp. 155-60, Rotterdam, Balkema.
20. Bolton, M.D., Gui, M.W., Garnier, J., Corte, J.F., Bagge, G., Laue, J., and Renzi, R. (1999). "Centrifuge cone penetration tests in sand". *Geotechnique*, vol. 49(3), pp. 543-52.

21. Budiman J.S., Mohammadi J., and Bandi S. (1995). "Effect of large inclusions on liquefaction of sand". In *Proc. Conference in Geotechnical Engineering Division, Geotechnical Special Publication, ASCE*, vol. 56, pp. 48-63.
22. Castro, G. (1969). "Liquefaction of sands". *Ph.D. thesis, Harvard University*; Cambridge.
23. Castro, G., and Poulos, J. (1977). "Factors affecting liquefaction and cyclic mobility", *Journal of the Geotechnical Engineering Division, ASCE*, vol. 103(6), pp. 501-16.
24. C-CORE. (2005). "Earthquake induced damage mitigation from soil liquefaction", *Data Report- centrifuge test CT7, C-CORE Report R-04-095-145*.
25. Chakraborty, P., Jafari Mehrabadi, A., and Popescu, R. (2004a). "Effect of low-permeability soil layers on the stability of submarine slopes", In *proc. 57th Canadian Geotechnical Conference and 5th Joint-IAH-CNC-CGS conference*, Quebec city, October 24-27, Hilton-Quebec.
26. Chakraborty, P., Popescu, R., and Prevost, J.H. (2004b). "Tower structure on liquefiable soil excited by random seismic input", In *proc. 9th ASCE Specialty Conference on Probabilistic Mechanics and Structural Reliability*, Albuquerque, NM, July 26-28.
27. Chapuis, R.P. (2004). "Predicting the saturated hydraulic conductivity of sand and gravel using effective diameter and void ratio", *Canadian Geotechnical Journal*, Vol. 41(5), pp. 787-95.
28. Cho, G.C., Lee, J.S., and Santamarina, J.C. (2004). "Spatial variability in soils: high resolution assessment with electrical needle probe", *Journal of Geotechnical and Geo-environmental Engineering, ASCE*, August, pp. 843-50.
29. Chillarige, A.V., Robertson, P.K., Morgenstern, N.R., and Christian, H.A. (1997). "Evaluation of the in situ state of Fraser River sand", *Canadian Geotechnical Journal*, vol. 34, pp. 510-19.
30. Christian, J.T. (2004). "Geotechnical engineering reliability: how well do we know what we are doing?", *Journal of geotechnical and geo-environmental engineering, ASCE*, vol. 130 (10), pp. 985-1003.
31. Cooke, H.G. (2000). "Ground improvement for liquefaction mitigation at existing highway bridges", *PhD Thesis, Virginia Polytechnic Institute and State University*.

32. COSMOS virtual data centre, <http://db.cosmos-eq.org/scripts/default.plx> .
33. Creager, W.P., Justin, J.D., and Hinds, J. (1945). "Engineering for dams", *John Wiley & Sons, Inc.*
34. Cundall, P. A. (1995). "FLAC user's manual, version 3.3", *Itasca Consulting Group Inc.*, Minneapolis, MN. (as cited in Puebla et al., 1997).
35. Das, B.M. (2006). "Principles of Geotechnical Engineering", *Thompson Canada Ltd*, Sixth edition.
36. Dief, H.M. (2000). "Evaluating the liquefaction potential of soils by the energy method in the centrifuge", *PhD thesis*, Case Western Reserve University.
37. Deodatis, G. (1996a). "Nonstationary stochastic vector processes: seismic ground motion application", *Probabilistic Engineering Mechanics*, vol. 11(3), pp. 149-67.
38. Deodatis, G. (1996b). "Simulation of ergodic multi-variate stochastic process", *Journal of Engineering Mechanics*, vol. 122(8), pp. 778-87.
39. Deodatis, G., Saxena, V., and Shinozuka, M. (2000). "Effect of spatial variability of ground motion on bridge fragility curve", *In proc. 8th ASCE Specialty conference on the Probabilistic Mechanics and Structural Reliability*, University of Notre Dame, July 24-26.
40. Der Kiureghian, A., and Ke, J.B. (1988). "The stochastic finite element method in structural reliability", *Probabilistic Engineering Mechanics*, vol. 3(2), pp. 83-91.
41. Dobry, R., Taboada, V., and Liu, L. (1995). "Centrifuge modeling of liquefaction effects during earthquakes", *In proc. 1st International Conference on Earthquake Geotechnical Engineering (IS-Tokyo)*, Ishihara Ed. Balkema Rotterdam, Vol. 3, 1291-1324.
42. Duncan, J.M. (2000). "Factors of safety and reliability in geotechnical engineering", *Journal of Geotechnical and Geo-environmental engineering, ASCE*, vol. 126(4), pp. 307-16.
43. Elkateb, T., Chalaturnyk, R., and Robertson, P.K. (2003a). "An overview of soil heterogeneity: quantification and implications on geotechnical field problems", *Canadian Geotechnical Journal*, vol. 40, pp.1-15.

44. Elkateb, T., Chalaturnyk, R., and Robertson, P.K. (2003b). "Simplified geo-statistical analysis of earthquake-induced ground response at the Wildlife site, California, USA", *Canadian Geotechnical Journal*, vol. 40, pp.16-35.
45. Eliadorani, A. (2001). "The effect of drainage conditions on liquefaction response of sands", *In Proc. 54th Canadian Geotechnical Conference* September, Calgary, Alberta, Canada.
46. Fenton, G.A., and Griffiths, D.V. (2003). "Bearing capacity prediction of spatially random c – f soils", *Canadian Geotechnical Journal*, vol. 40, pp. 54-65.
47. Fenton, G.A., and Vanmarcke, E.H. (1998). "Spatial variation in liquefaction risk", *Geotechnique*, vol. 48(6), pp. 819-31.
48. Fiegel, G.L., and Kutter, B.L. (1992). "Liquefaction mechanism for layered soil", *Journal of Geotechnical Engineering, ASCE*, Vol. 120(4), pp. 737-55.
49. Fiegel, G.L., and Kutter, B.L. (1994). "Liquefaction for layered soils", *Journal of Geotechnical and Geo-environmental engineering, ASCE*, Vol. 120(4), pp. 737-55.
50. Finn, W.D.L., Emery, J.J., and Gupta, Y.P. (1971). "A shaking table study of the liquefaction of saturated sands during earthquake", *Third European Symposium on Earthquake Engineering*, Bulgaria, pp. 253-62.
51. Finn, W.D.L. (1988). "Dynamic analysis in geotechnical engineering," *In Proc. Earthquake Engineering and Soil Dynamics II - Recent Advances in Ground Motion Evaluation, ASCE Geotechnical Engineering Division*, Park City, Utah, June, 523-91 (as cited in Finn et al., 1994).
52. Finn, W.D.L. (1991). "Estimating how embankment dams behave during earthquakes", *Water Power and Dam Construction*, London, April, 17-22. (as cited in Finn et al., 1994).
53. Focht, J.A., and Focht III, J.A. (2001). "Factor of safety and reliability in geotechnical engineering (Discussion)", *Journal of Geotechnical and Geo-environmental Engineering, ASCE*, vol. 127(8), pp. 704-06.
54. Ghosh, B., and Madabhushi, S.P.G. (2003). "Effects of localized soil inhomogeneity in modifying seismic soil-structure interaction", *In Proc. 16th ASCE Engineering Mechanics Conference*, Seattle, WA, July.

55. Griffiths, D.V., and Fenton, G.A. (2000). "Influence of soil strength spatial variability on the stability of an undrained clay slope by finite elements", *Slope Stability 2000, Geotechnical Special Publications No. 101, ASCE*, pp. 184-93.
56. Griffiths, D.V., Fenton, G.A., and Manoharan, N. (2002). "Bearing capacity of rough rigid strip footing on cohesive soil: Probabilistic study", *Journal of Geotechnical and Geo-environmental Engineering, ASCE*, vol. 128 (9), pp. 743-55.
57. Griffiths, D.V., and Prevost, J.H. (1990). "Stress strain curve generation from simple triaxial parameters", *International Journal for Numerical and Analytical Methods in Geomechanics*, vol. 14, pp. 587-94.
58. Grigoriu, M. (1998). "Simulation of stationary non-Gaussian translation processes", *Journal of Engineering Mechanics*, Vol. 124(2), pp. 121-26.
59. Haldar, A., and Mahadevan, S. (2000). "Probability, reliability and statistical methods in engineering design", *John Wiley & sons, Inc.*
60. Harder, L. F., Jr., and Seed, H. B., (1986). "Determination of penetration resistance for coarse-grained soils using the Becker hammer drill", *Earthquake Engineering Research Centre, Rep. UCB/EERC-86/06, University of California at Berkeley.*
61. Hardin, B.O., Richard, F.E. (1963). "Elastic wave velocities in granular soils", *ASCE Journal of the Soil Mechanics and Foundations Division*; vol. 89(SM1), pp. 33-65.
62. Hausler, E. A. (2002). "Influence of ground improvement on settlement and liquefaction: a study based on field case history evidence and dynamic geotechnical centrifuge tests", *PhD thesis, University of California, Berkeley.*
63. Hayashi, H., Honda, M., and Yamada, T. (1992). "Modelling of nonlinear stress strain relations of sands for dynamic response analysis", *In Proc. 10th World Conf. on Earthquake Engineering, Madrid, Balkema, Rotterdam, Vol. 11, pp. 6819-25.*
64. Hazen, A. (1930). "Water supply", *In American Civil Engineers Handbook.*
65. Ishibashi, I., and Zhang, X. (1993). "Unified dynamic shear moduli and damping ratios of sand and clay", *Soils and Foundations*; vol. 33(1), pp. 182-91.
66. Iwasaki, T., Tatsuoka, F., Tokida K., and Yasuda, S. (1978), "A practical method for assessing soil liquefaction potential based on case studies at various sites in Japan", *In Proc. 2nd International Conference on Microzonation for Safer construction-Research and Applications, San Francisco, USA, Vol. 2.*

67. Jafari-Mehrabadi, A. (2006). "Seismic liquefaction countermeasures for waterfront slopes", *PhD thesis*, Memorial University of Newfoundland.
68. Jafferries, M.G., and Davies, M.P. (1993). "Use of CPTu to estimate equivalent SPT N_{60} ", *Geotechnical Testing Journal*, vol. 16(4), pp. 458-68.
69. Jafferries, M.G., Rogers, B.T., Stewart, H.R., Shinde, S., James, D., and Williams-Fitzpatrick, S. (1988). "Island construction in the Canadian Beaufort Sea", *In Proc. ASCE Spec. Conf. Hydr. Fills*, Fort Collins, CO, pp. 816-83.
70. Jaky, J. (1948). "Pressure in soils", *In Proc. 2nd ICSMFE*, vol. 1, pp. 103-09.
71. Jones, A.L., Kramer, S.L., and Arduino, P. (2002). "Estimation of uncertainty in geotechnical properties for performance-based earthquake engineering", *Pacific Earthquake Engineering Research Centre*, December.
72. Juang, C.H., Jiang, T., and Andrus, R.D. (2002). "Assessing probability-based methods for liquefaction potential evaluation", *Journal of Geotechnical and Geo-environmental engineering*, ASCE, vol. 128(7), pp. 580-89.
73. Kafali, C., and Grigoriu, M. (2004). "Seismic fragility analysis", *In proc. 9th ASCE Specialty Conference on Probabilistic Mechanics and Structural Reliability*, July 26-28, Albuquerque, NM.
74. Keanne C.M., and Prevost. J.H. (1989). "An analysis of earthquake data observed at the wildlife liquefaction array site, Imperial County, California", *In Proc. 2nd US-Japan Workshop on Liquefaction, Large Ground Deformations and Effects on Lifelines*, New York, pp. 39-53.
75. Kokusho, T. (1999). "Formation of water film in liquefied sand and its effect on lateral spread", *Journal of Geotechnical and Geo-environmental Engineering*, ASCE, Vol. 125(10), pp. 817-26.
76. Kokusho, T. (2000a). "Mechanism for water film generation and lateral flow in liquefied sand layer", *Soils and Foundations*, Vol. 40(5), pp. 99-111.
77. Kokusho, T. (2000b). "Emergence of water film in liquefied sand and its role in lateral flow", *In Proc. 12th World Conference on Earthquake Engineering*, Auckland, New Zealand.

78. Kokusho, T., and Kojima, T. (2002). "Mechanism for post liquefaction water film generation in layered sand", *Journal of Geotechnical and Geo-environmental engineering, ASCE*, Vol. 18(2), pp. 129-37.
79. Konrad J.M., and Dubeau S. (2002). "Cyclic strength of stratified soil samples". In *Proc. 55th Canadian Geotechnical Conference: Ground and Water: Theory to Practice*, October, Niagara Falls, ON, pp. 89-94.
80. Koutsourelakis, S., Prevost, J.H., and Deodatis, G. (2001). "Stochastic approach to the design of a simple structure under the risk of liquefaction", In *Proc. of ICOSSAR 2001, International conference on Structural Safety and Reliability*, Newport Beach, California, USA, June 17-21.
81. Koutsourelakis, S., Prevost, J.H., and Deodatis, G. (2002). "Risk assessment of an interacting structure-soil system due to liquefaction", *Earthquake Engineering and Structural Dynamics*, vol. 31, pp. 851-79.
82. Kulhawy, F.H., Jackson, C.S., and Mayne, P.W. (1989). "First-order estimation of k_0 in sands and clays", In K.H. Kulhawy, editor, *Foundation engineering: current principles and practices*, ASCE, pp. 121-34.
83. Kulhawy, F.H., and Mayne, P.W. (1990). "Manual on estimating soil properties for foundation design", *Final Report 1493-6, EL-6800*, Electric Power Research Institute, Palo Alto, CA.
84. Kutter, B.L. (1983). "Deformation of centrifuge models of clay embankments due to 'bumpy road' earthquakes", *Soil Dynamics and Earthquake Engineering*, Vol. 2(4), pp. 199-205.
85. Kutter B.L., and Wilson D.W. (1999). "De-liquefaction shock waves", In *Proc. 7th U.S Japan Workshop on earthquake resistant design of life line facilities and countermeasures against liquefaction*, pp. 295-310.
86. Lambe, T.W., and Whitman, R.V. (1969). "Soil mechanics", *John Wiley & Sons, Inc.*
87. Laue, J. (2002). "Centrifuge technology", Constitutive and centrifuge modelling: two extremes, Ed. By Sarah Springman, Bhawani Singh, *Proceedings of an international workshop*, Centro Stefano Franscini, Monte Verita, Ascona, pp. 75-104.
88. Lee, J.S. (2003). "High resolution geophysical techniques for small-scale soil model testing", *PhD thesis*, Georgia Institute of Technology.

89. Li, Z., Kutter, B.L., Wilson, D.W., Sprott, K., Lee, J.S., and Santamarina, J.C. (2005). "Needle probe application for high-resolution assessment of soil spatial variability in the centrifuge", *Geo-Frontiers 2005*, Austin, Texas, January 24-26.
90. Li, X.S., Shen, C.K., and Wang, Z.L. (1998). "Fully coupled inelastic site response analysis for 1986 Lotung earthquake", *Journal of Geotechnical and Geo-environmental Engineering*, vol. 124, No. 7, pp. 560-73.
91. Li, X.S., Wang, Z.L., and Shen, C.K. (1992). "SUMDES, A nonlinear procedure for response analysis of horizontally-layered sites subjected to multidirectional earthquake loading," *Department of Civil Engineering*, University of California, Davis, CA. (as cited in Li et al., 1998).
92. Lunne, T., Robertson, P.K., and Powell, J. (1997). "Cone Penetration Testing in Geotechnical Practice", *Blackie Academic and Professional*.
93. Lye, L.M. (2002). "Design of Experiments in civil engineering: are we still in the 1920's?", *Annual Conference of the Canadian Society for Civil Engineering*, GE069, pp. 1-10.
94. Lye, L.M. (2003). "Some applications of statistical Design of Experiment methodology in civil engineering", *Annual Conference of the Canadian Society for Civil Engineering*, GCD-115, pp. 1-10.
95. Madabhushi, S.P.G., and Schofield, A.N. (1993). "Centrifuge modeling of tower structure on saturated sands subjected to earthquake perturbations", *Geotechnique*, vol. 43(4), pp. 555-65.
96. Madabhushi, S.P.G., and Zeng, X. (1998). "Seismic response of gravity quay walls II: numerical modeling", *Journal of Geotechnical and Geo-environmental Engineering*, ASCE, Vol. 124(5), May, pp. 418-27.
97. Marcuson, W.F. III. (1978). "Definition of terms related to liquefaction", *Journal of Geotechnical Engineering Division, ASCE*, vol. 104(9), pp. 1197-1200.
98. Montgomery, D.C. (1997). "Design and analysis of experiments", *John Wiley & Sons*, New York.
99. Morris, D.V. (1979). "The centrifugal modeling of dynamic soil-structure interaction and earthquake behaviour", *PhD thesis*, University of Cambridge.

100. Mroz, Z. (1967). "On the Description of Anisotropic Work-hardening", *Journal of the mechanics and Physics of Solids*, vol. 15, pp. 163-75.
101. NAVFAC, (1982). "Naval Fac. Eng. Command", Soil Mechanics (DM 7.1), Alexandria.
102. National Building Code of Canada (NBCC). (2005), Canadian commission on building and fire codes, *National Research Council of Canada*, Ottawa.
103. Nobahar, A. (2003). "Effects of soil spatial variability on soil-structure interaction", *PhD thesis*, Memorial University of Newfoundland.
104. Nobahar, A., and Popescu, R. (2000). "Spatial variability of soil properties - effects on foundation design", *In Proc. 53rd Canadian Geotechnical Conference*, Montreal, Quebec, vol. 2, pp.1139-44.
105. Nobahar, A., and Popescu, R. (2001). "Some effects of soil heterogeneity on bearing capacity of shallow foundations", *In Proc. ASCE Spec. Conf. 2001: A Geo-Odyssey*, Blacksburg, VA.
106. Ochiai, H. (1977). "The estimated equation of the coefficient of earth pressure at rest k_0 for sand by using N-value", *JSSMFE*, vol. 17(3), pp. 93-101.
107. Ohtomo, K., and Shinozuka, M. (1990). "Two-dimensional spatial severity of liquefaction", *In Proc. 8th Japan Earthquake Engineering Symposium*, Tokyo.
108. Paice, G.M., Griffiths, G.V., and Fenton, G.A. (1996). "Finite element modeling of settlement on spatially random soil", *Journal of Geotechnical Engineering, ASCE*, vol. 122, pp. 777-80.
109. Park, S. S, and Byrne, P. M. (2004). "Stress densification and its evaluation", *Canadian Geotechnical Journal*, vol. 41(1), pp. 181-86.
110. Phillips, R., Coulter, S.E., and Tu, M. (2004). "Earthquake simulator development for the C-CORE geotechnical centrifuge", *In proc. 57th Canadian Geotechnical Conference and 5th Joint-IAH-CNC-CGS conference*, Quebec city, October 24-27, Hilton-Quebec.
111. Phoon, K.K., and Kulhawy, F.H. (1999a). "Characterization of geotechnical variability", *Canadian Geotechnical Journal*, vol. 36, pp. 612-24.
112. Phoon, K.K., and Kulhawy, F.H. (1999b). "Evaluation of geotechnical property variability", *Canadian Geotechnical Journal*, vol. 36, pp. 625-39.

113. Popescu, R. (1995). "Stochastic variability of soil properties: data analysis, digital simulation, effects on system behaviour", *PhD thesis*. Princeton University.
114. Popescu, R. (2002). "Influence of seismic loading rate on soil liquefaction". *Canadian Geotechnical Journal*, vol. 39(2), pp. 331-44.
115. Popescu, R., and Chakraborty, P. (2006). "Liquefaction Mechanism For Heterogeneous Soils", *In Proc. Sea to Sky Geotechnique 2006 - 59th Canadian Geotechnical Conference and 7th Joint CGS/IAH-CNC Groundwater Specialty Conference* October 1-4, Vancouver, BC, Canada.
116. Popescu, R., and Prevost, J.H. (1993). "Centrifuge validation of a numerical model for dynamic soil liquefaction", *Soil Dynamics and Earthquake Engineering*, vol. 12(2), pp. 73-90.
117. Popescu, R., and Prevost, J.H. (1995). "Comparison between VELACS numerical 'class A' predictions and centrifuge experimental soil test results", *Soil Dynamics and Earthquake Engineering*, vol. 14(2), pp. 79-92.
118. Popescu, R., Deodatis, G., and Nobahar, A. (2005a). "Effects of soil heterogeneity on bearing capacity", *Probabilistic Engineering Mechanics*, vol. 20(4), pp. 324-41.
119. Popescu, R., Chakraborty, P., and Prevost, J.H. (2005b). "Fragility curves for tall structure on stochastically variable soil", *In Proc. 9th Int. Conf. on Structural Safety and Reliability (ICOSSAR)*, Rome, June.
120. Popescu, R., Prevost, J.H., and Deodatis, G. (1996). "Influence of spatial variability of soil properties on seismically induced soil liquefaction", *In Proc. Uncertainty in the Geologic Environment: From Theory to Practice*, ASCE, Madison, Wisconsin, pp. 1098-1112.
121. Popescu, R., Prevost, J.H., and Deodatis, G. (1997). "Effects of spatial variability on soil liquefaction: some design recommendations", *Geotechnique*, vol. 47(5), pp. 1019-36.
122. Popescu, R., Prevost, J.H., and Deodatis, G. (1998a). "Spatial variability of soil properties: Two case studies", *Geotechnical Earthquake Engineering and Soil Dynamics, Geotechnical Special Publication No.-75*, ASCE, Seattle, pp. 568-79.

123. Popescu, R., Deodatis, G., and Prevost, J.H. (1998b). "Simulation of non-Gaussian homogeneous stochastic vector fields", *Probabilistic Engineering Mechanics*, vol. 13(1), pp. 1-13.
124. Popescu, R., Prevost, J.H., and Deodatis, G. (2005c) "3D effects in seismic liquefaction of stochastically variable soil deposits", *Geotechnique*, vol. 55(1), pp. 21-31.
125. Popescu, R., Prevost, J.H., Deodatis, G., and Chakraborty, P. (2006). "Dynamics of nonlinear porous media with applications to soil liquefaction", *Journal of Soil Dynamics and Earthquake Engineering*, vol. 26(6-7), pp. 648-65.
126. Prakash, S. (1981). "Soil dynamics", *McGraw-Hill Book Company*.
127. Prévost, J.H. (1982). "Nonlinear transient phenomena in saturated porous media", *Computer Methods in Applied Mechanics and Engineering*, vol. 30, pp. 3-18.
128. Prévost, J.H. (1985). "Wave propagation in fluid-saturated porous media: An Efficient Finite Element Procedure", *Soil Dynamics and Earthquake Engineering*, vol. 4(4), pp. 183-202.
129. Prevost, J.H. (1989). "DYNA1D a computer program for nonlinear seismic site response analysis", *Technical documentation NCEER-89-0025*, Technical report, Department of civil engineering and operational Research, Princeton University.
130. Prevost, J.H. (2002). "DYNAFLOW - A nonlinear transient finite element analysis program", Version 02, *Technical Report*, Department of Civil and Environmental Engineering, Princeton University, Princeton, NJ.
<http://www.princeton.edu/~dynaflow/>
131. Prévost, J.H., and Keane, C.M. (1989). "Shear stress-strain curve generation from simple material parameter", *Journal of Geotechnical Engineering, ASCE*, vol. 116(8), pp. 1255-63.
132. Prevost, J.H., and Popescu, R. (1996). "Constitutive relations for soil materials", *The Electrical journal of Geotechnical Engineering*, vol. 1.
133. Prevost, J.H., and Scanlon, R.H. (1983). "Dynamic soil-structure interaction: centrifugal modeling", *Soil Dynamics and Earthquake Engineering*, vol. 2, pp. 212-21.

134. Puebla, H., Byrne, P.M., and Phillips, R. (1997). "Analysis of CANLEX liquefaction embankments, prototype and centrifuge models", *Canadian Geotechnical Journal*, vol. 34, pp. 641-57.
135. Rathje, E.M., Abrahamson, N.A., and Bray, J.D. (1998). "Simplified frequency content estimates of earthquake ground motion", *Journal of Geotechnical and Geo-environmental Engineering, ASCE*, vol. 124(2), pp. 150-59.
136. Renzi, R., Corte, J.F., Rault, G., Bagge, G., Gui, M.W., and Laue, J. (1994). "Cone penetration tests in the centrifuge: experience of five laboratories", In C.F. Leung et al. (eds), *Centrifuge 94*, pp. 77-82, Rotterdam, Balkema.
137. Rice, S.O. (1954). "Mathematical analysis of random noise", In ed. N. Wax, *Selected Papers on Noise and Stochastic Processes*, Dover.
138. Richart, F.E.Jr., Hall, J.R.Jr., and Woods, R.D. (1970). "Vibrations of soils and foundations", *Prentice Hall*, Englewood Cliffs.
139. Riemer, M.F., and Seed, H.B. (1997). "Factors affecting apparent position of steady-state line", *Journal of Geotechnical and Geo-environmental engineering, ASCE*, vol.- 123 (3), pp. 281-88.
140. Robertson, P.K., and Campanella, R.G. (1985). "Liquefaction potential of sand using CPT", *Journal of Geotechnical Engineering Division, ASCE*, vol. 111(3), March.
141. Robertson, P.K., and Wride, C.E. (1998). "Evaluating cyclic liquefaction potential using the cone penetration test." *Canadian Geotechnical Journal*, vol. 35(3), pp. 442-52.
142. Schmertmann, J.H. (1975). "Measurement of in-situ shear strength", In Proc. ASCE Spec. Conf. on In-situ Meas. Soil Prop., vol. 2, pp. 57-138.
143. Schofield, A.N. (1980). "Cambridge geotechnical centrifuge operations", *Geotechnique*, vol. 30(3), pp. 227-68.
144. Seed, H.B., and De-Alba, P. (1986). "Use of SPT and CPT tests for evaluating the liquefaction resistance of sands", In Proc. *Use of In-situ Tests in Geotechnical engineering, ASCE*, New York, pp. 281-302.

145. Seed, H.B., and Idriss, I.M. (1970). "A simplified procedure for evaluating soil liquefaction potential", *Earthquake Engineering Research Centre*, report no EERC 70-9, November.
146. Seed, H.B., Idriss, I.M., and Arango, I. (1983). "Evaluation of liquefaction potential using field performance data", *Journal of Geotechnical Engineering Division, ASCE*, vol. 109(3), March.
147. Seed, H.B., and Lee, K.L. (1966). "Liquefaction of saturated sands during cyclic loading", *Journal of Soil Mechanics and Foundation Engineering Division, ASCE*, vol. 92(6), pp. 105-34.
148. Shahabi, A.A., Das, B.M., and Tarquin, A.J. (1984). "An empirical relation for coefficient of permeability of sands". In: *Proceedings of the 4th. Australia-New Zealand Conference on Geomechanics*, Vol. 1, pp. 54-57.
149. Shinozuka, M. (1972). "Monte Carlo solution of structural dynamics", *Computers and Structures*, vol. 2(5+6), pp. 855-74.
150. Shinozuka, M. (1998). "Statistical analysis of bridge fragility curves", In *Proc. U.S. - Italy Workshop on Protective Systems for Bridges*, New York, 26-28 April, pp. 249-56.
151. Shinozuka, M. (2000). "Development of bridge fragility curves based on the damage data", In *Proc. of International Workshop on Annual Commemoration of Chi-Chi Earthquake*, Volume-II - Technology Aspect, 18-20 September, Taipei, Taiwan, pp. 14-25.
152. Shinozuka, M., and Jan, C.M. (1972). "Digital simulation of random process and its applications", *Journal of Sound and Vibration*, vol. 25(1), pp. 111-28.
153. Shinozuka, M. (1974). "Digital simulation of random processes in engineering mechanics with the aid of FFT technique", In ed. S. T. Ariaratnam and H. H. E. Leipholz, *Stochastic Problems in Mechanics*, University of Waterloo press, pp. 277-86.
154. Shinozuka, M., and Dasgupta, G. (1986). "Stochastic finite element methods in dynamics", In *Proc. 3rd Conference of Dynamic Response of Structures*, ASCE, University of California, L.A., CA, pp. 44-54.

155. Shinozuka, M., and Deodatis, G. (1996). "Simulation of multi-dimensional Gaussian stochastic fields by spectral representation", *Applied Mechanics Reviews, ASME*, vol. 49(1), pp. 29-53.
156. Shinozuka, M., Feng, M.Q., Lee, J., and Naganuma, T. (2000). "Statistical analysis of fragility curves", *Journal of Engineering Mechanics, ASCE*, vol. 126(12), pp. 1224-31.
157. Shinozuka, M., and Kishimoto, S. (1989). "Development of fragility curve for liquefaction", *In Proc. of ICOSSAR 89, the 5th International Conference on Structural Safety and Reliability*, San Francisco, August 7-11.
158. Tantalla, J.M., Prevost, J.H. and Deodatis, G. (2001). "Spatial variability of soil properties in slope stability analysis: fragility curve generation", *In Proc. of ICOSSAR 2001, International Conference on Structural Safety and Reliability*, Newport Beach, California, USA, June 17-21.
159. Tarzaghi, K., and Peck, R.B., (1967). "Soil Mechanics in Engineering Practice", *John Wiley & Sons, Inc.*
160. Tatsouka, F., Zhou, S., Sato, T., and Shibuya, S. (1990). "Evaluation method of liquefaction potential and its application", *Report on seismic hazards on the ground in urban areas*, Ministry of Education of Japan, Tokyo, pp. 75-109 (In Japanese).
161. Taylor, R.N. (1995). "Geotechnical centrifuge technology", *Blackie Academic & Professional*, New York.
162. Trautmann, C.H., and Kulhawy, F.H. (1987). "CUFAD- A computer program for compression and uplift foundation analysis and design", *Report EL-4540-CCM*, vol. 16, *Electric power research institute* October, Palo Alto.
163. Uniform Building Code. (1994). *International Conference of Building Officials*, ICBO, Whittier, CA, vol. 2.
164. US Army Corps of Engineers. (1992). "Bearing capacity of soils", *Report No. E M 1110-1-1905*.
165. Uthayakumar, M., and Vaid, Y.P. (1998). "Static liquefaction of sands under multiaxial loading", *Canadian Geotechnical Journal*, vol. 35(2), pp. 273-83.

166. Vaid, Y.P., and Eliadorani, A. (1998). "Instability and liquefaction of granular soils under undrained and partially drained states", *Canadian Geotechnical Journal*, vol. 35(6), pp. 1053-62.
167. Vaid, Y.P., and Eliadorani, A. (2000). "Undrained and drained (?) stress-strain response", *Canadian Geotechnical Journal*, vol. 37(5), pp. 1126-30.
168. Vaid, Y.P., and Chern, J.C. (1985). "Cyclic and monotonic undrained response of saturated sands", *Advances in the testing soils under cyclic condition ASCE*, pp. 120-47.
169. Vaid, Y.P., and Sivathayalan, S. (1996). "Static and cyclic liquefaction potential of Fraser Delta sand in simple shear and triaxial tests", *Canadian Geotechnical Journal*, Vol. 33(2), pp. 281-89.
170. Vaid, Y.P., and Sivathayalan, S. (2000). "Fundamental factors affecting liquefaction susceptibility of sands", *Canadian Geotechnical Journal*, Vol. 37(3), pp. 592-606.
171. Vaid, Y.P., Stedman, J.D., and Sivathayalan, S. (2001) "Confining stress and static shear effects in cyclic liquefaction", *Canadian Geotechnical Journal*, vol. 38(3), pp. 580-91.
172. Vaid, Y.P., and Thomas, J. (1995). "Liquefaction and post liquefaction behaviour of sand", *Journal of Geotechnical Engineering ASCE*, vol. 121, pp. 163-73.
173. Vanmarcke, E.H. (1977). "Probabilistic modelling of soil profiles", *Journal of Geotechnical Engineering Division*, vol. 103(11), pp. 1227-46.
174. Vanmarcke, E.H. (1983). "Random fields: analysis and synthesis", *The MIT Press*.
175. Weissman, K., and Prevost, J.H. (1989). "Centrifugal modeling of dynamic soil-structure interaction", *Technical Report NCEER-89-0040*, Princeton University.
176. Wijewickreme, D., Sriskandakumar, Somasundaram, Byrne, P. (2005). "Cyclic loading response of loose air-pluviated Fraser River sand for validation of numerical models simulating centrifuge tests", *Canadian Geotechnical Journal*, Vol. 42(2), pp. 550-61.

177. Yamaguchi, N., and Yamazaki, F. (2000). "Fragility curves for buildings in Japan based on damage surveys after the 1995 Kobe earthquake", *In Proc. of the 12th World Conference on Earthquake Engineering*, Auckland, New Zealand, 8pages, CD-ROM.
178. Yamazaki, F., and Shinozuka, M. (1988). "Digital generation of non-Gaussian stochastic fields", *Journal of Engineering Mechanics, ASCE*, vol. 114(7), pp. 1183-97.
179. Yang, J.N. (1972). "Simulation of random envelop processes", *Journal of sound and Vibration*, vol. 25(1), pp. 73-85.
180. Yang, J.N. (1973). "On the normality and accuracy of simulated random process", *Journal of Sound and Vibration*, vol. 26(3), pp. 417-28.
181. Yang, T.F. (1996). "Effect of gravel drainage on the remedy of soil liquefaction", *PhD thesis*, University of Colorado at Boulder.
182. Yoshimine, M., Ishihara, K., and Vargas, W. (1998). "Effects of principal stress direction and intermediate principal stress on undrained shear behaviour of sand", *Soils and Foundations*, vol. 38(3), pp. 177-86.
183. Yoshimine, M., Robertson, P.K., and Wride, C.E. (1999). "Undrained shear strength of clean sands to trigger flow liquefaction", *Canadian Geotechnical Journal*, vol. 36(5), pp. 891-906.
184. Youd, T.L., and Perkins, D.M. (1978). "Mapping of liquefaction induced ground failure potential", *Journal of Geotechnical Engineering Division, ASCE*, vol. 104(4), p. 433-46.
185. Youd, T.L., Idriss, I.M., Andrus, R.D., Arango, I., Castro, G., Christian, J.T., Dobry, R., Finn, W.D.L., Harder, L.F. Jr., Hynes, M. E., Ishihara, K., Koester, J.P., Laio, S.S.C., Marcuson, III, W.F., Martin, G.R., Mitchell, J.K., Moriwaki, Y., Power, M.S., Robertson, P.K., Seed, R.B., and Stokoe, II, K.H. (2001). "Liquefaction resistance of soils: summary report from the 1996 NCEER and 1998 NCEER/NSF workshops on evaluation of liquefaction resistance of soils" *Journal of Geotechnical and Geo-environmental Engineering, ASCE*, vol. 127(10), pp. 817-33.
186. Zangeneh, N., Azizian, A., Lye, L., and Popescu, R. (2002). "Application of Response Surface Methodology in numerical geotechnical analysis", *In: Proceedings of the 55th Canadian Geotechnical Conference*, pp. 321 – 329.

187. Zelikson, A., Devaure, B., and Badel, D. (1981). "Scale modelling of soil Structure Interaction During Earthquake Using a Programmed Series of Explosions During Centrifugation", *In Proc. of the International Conference on Recent Advances in Geotechnical Earthquake Engineering and Soil Dynamics*, University of Missouri Rolla. Vol. 1, pp 361-66.

APPENDIX A

Table A.1: Earthquake data base used in the analyses with frame structure

No.	Input acce- ration file no	Earthquake	Date (mm/dd/yy)	Recording Station	Closest Distance to Fault (km)	Focal Depth (km)	Magnitude	Recording Direction	Soil Type
1	ac016	CHICHI	09/25/99	HWA026	58.9	16.0	6.3	0 ⁰	S_B
2	ac017	N.E. INDIA	05/08/97	PYNURSLA	67.1	34	6	59 ⁰	rock
3	ac018	CHICHI	09/25/99	HWA056	51.5	16	6.3	0 ⁰	S_B
4	ac019	CHICHI	09/25/99	KAU008	135.6	16	6.3	0 ⁰	S_D
5	ac020	CHICHI	09/25/99	HWA046	60.3	16	6.3	0 ⁰	S_B
6	ac021	N.E. INDIA	08/05/97	NONGPOH	124.1	34	6.0	40 ⁰	rock
7	ac022	CHAMOLI (NW HIMALAYA)	07/04/99	GOPESHWAR	16.2	10	4.6	290 ⁰	rock
8	ac023	PARKFIELD, CA	09/28/04	COALINGA, FIRE STATION 39	36.6	7.9	6.0	0 ⁰	rock

9	ac024	CHAMOLI (NW HIMALAYA)	03/28/99	UTTARKASHI	100.6	15	6.6	72 ⁰	rock
10	ac025	CHAMOLI (NW HIMALAYA)	03/28/99	JOSHIMATH	26	15	6.6	80 ⁰	rock
11	ac026	N.E. INDIA	05/08/97	NONGSTOIN	125.0	34	6.0	65 ⁰	rock
12	ac027	CHICHI	09/20/99	CHY099	86.8	8.0	6.2	0 ⁰	S_D
13	ac028	N.E. INDIA	05/08/97	SHILLONG	90.1	34	6.0	40 ⁰	rock
14	ac029	CHAMOLI (NW HIMALAYA)	03/28/99	TEHRI	89.7	15	6.6	297 ⁰	rock
15	ac030	CHICHI	09/22/99	HWA020	34.9	10	6.2	0 ⁰	S_D
16	ac031	IMPERIAL VALLEY	10/15/79	STOREHOUSE, PLASTER CITY	29.5	9.96	6.9	135 ⁰	Stiff soil
17	ac032	UTTARKASHI	10/19/91	TEHRI	50.6	10.0	7.0	297 ⁰	rock
18	ac033	CHICHI	09/22/99	CHY099	105.5	10	6.2	0 ⁰	S_D
19	ac034	N.E. INDIA	08/05/97	UMSNING	106.8	34	6.0	45 ⁰	rock
20	ac035	CHAMBA, INDIA	03/24/95	CHAMBA	34	33.0	4.9	90 ⁰	soil

21	ac036	CHICHI	09/25/99	CHY099	92.7	16.0	6.3	0 ⁰	S_D
22	ac037	HECTOR MINE	10/16/99	WHITEWATER TROUT FARM	76.0	5.0	7.1	155 ⁰	Stiff soil
23	ac038	ANZA	06/12/05	ANZA ARRAY- TULE CANYON	17.4	14.1	5.6	360 ⁰	rock
24	ac039	CHICHI	09/22/99	TCU055	49.0	10	6.2	0 ⁰	S_D
25	ac040	HECTOR MINE, CA	10/16/99	SBA: FIRE STATION #4	107	5.0	7.1	360 ⁰	Stiff soil
26	ac041	COALINGA	07/09/83	SKUNK HOLLOW	12.6	9.0	5.4	360 ⁰	Stiff soil
27	ac042	CHICHI	09/20/99	TCU109	34.8	8.0	6.2	0 ⁰	S_D
28	ac043	N.E. INDIA	08/05/97	UMMULONG	78.4	34	6.0	87 ⁰	rock
29	ac044	CHAMOLI (NW HIMALAYA)	03/28/99	GHANSIALI	75.3	15	6.6	0 ⁰	rock
30	ac045	CHICHI	09/22/99	CHY035	58.2	10	6.2	0 ⁰	S_D
31	ac046	LOMA PRIETA EARTHQUAK E	10/18/89	CALAVERAS ARRAY	31.0	17.48	7.1	270 ⁰	rock
32	ac047	CHICHI	09/20/99	TCU067	28.5	8.0	6.2	0 ⁰	S_D

33	ac048	CHICHI	09/22/99	TCU067	41.5	10	6.2	0 ⁰	S_D
34	ac049	UTTARKASHI , INDIA	10/19/91	BARKOT	55.8	10.0	7.0	10 ⁰	rock
35	ac050	CHICHI	09/22/99	KAU020	109.1	10	6.2	0 ⁰	S_D
36	ac051	COALINGA	07/09/83	BURNETT CONSTRUCTION	15.9	9.0	5.4	360 ⁰	Stiff soil
37	ac052	CHICHI	09/20/99	TCU072	22.5	8.0	6.2	0 ⁰	S_D
38	ac053	CHICHI	09/22/99	TCU051	51.3	10	6.2	0 ⁰	S_D
39	ac054	CHICHI	09/22/99	TCU123	54.2	10	6.2	0 ⁰	S_D
40	ac055	NORTHRIDGE	01/17/94	855 ARCADIA AVE	39.6	17.5	6.8	262 ⁰	Stiff soil
41	ac056	CHICHI	09/20/99	CHY036	36.4	8.0	6.2	0 ⁰	S_D
42	ac057	NORTHRIDGE	01/17/94	MT. WILSON - CALTECH SEISMIC STATION	36.7	17.5	6.8	90 ⁰	rock
43	ac058	CHICHI	09/22/99	TCU106	55.8	10	6.2	0 ⁰	S_D
44	ac059	CHICHI	09/20/99	TCU076	14.7	8.0	6.2	0 ⁰	S_D
45	ac060	LOMA PRIETA	10/18/89	UPPER CRYSTAL SPRINGS RES.	31.6	17.48	7.1	0 ⁰	rock
46	ac061	LOMA PRIETA	10/18/89	HAYWARD - BART STATION	46.3	17.48	7.1	310 ⁰	Stiff soil

47	ac062	CHICHI	09/25/99	CHY088	65.7	16.0	6.3	90 ⁰	S_D
48	ac063	CHAMOLI (NW HIMALAYA)	03/28/99	GOPESHWAR	17.3	15	6.6	290 ⁰	rock
49	ac064	LOMA PRIETA	10/18/89	SAN FRANCISCO BAY- DUMBARTON BRIDGE	26.7	17.48	7.1	357 ⁰	Stiff soil
50	ac065	ALASKA	05/02/71	ADAK, NAVAL BASE	78.9	43.0	7.1	90 ⁰	rock
51	ac066	LOMA PRIETA EARTHQUAK E	10/18/89	CALAVERAS ARRAY	35	17.48	7.1	90 ⁰	rock
52	ac067	NORTHRIDGE	01/17/94	535 SOUTH WILSON AVE	33.7	17.5	6.8	360 ⁰	Stiff soil
53	ac068	CHICHI	09/22/99	CHY024	48.7	10	6.2	90 ⁰	S_D
54	ac069	PETROLIA/CA PE MENDOCINO	04/25/92	EEL RIVER VALLEY ARRAY, USGS STATION	60.6	9.6	7.1	60 ⁰	rock

		EARTHQUAK E		1112					
55	ac070	CHICHI	09/25/99	TCU129	24.8	16.0	6.3	0 ⁰	S_D
56	ac071	NORTHRIDGE	18/01/94	LOS ANGELES, GRIFFITH OBSERVATORY	22.9	17.5	6.8	360 ⁰	rock
57	ac072	PETROLIA/CA PE MENDOCINO EARTHQUAK E	04/25/92	EEL RIVER VALLEY ARRAY, USGS STATION 1112	60.6	9.6	7.1	330 ⁰	rock
58	ac073	SAN FERNANDO	02/09/71	GRIFFITH PARK OBSERVATORY	25.5	13	6.6	270 ⁰	rock
59	ac074	CHICHI	09/22/99	CHY024	48.7	10	6.2	0 ⁰	S_D
60	ac075	CHICHI	09/25/99	CHY088	65.7	16.0	6.3	0 ⁰	S_D
61	ac076	PETROLIA/CA PE MENDOCINO EARTHQUAK E	04/25/92	EEL RIVER VALLEY ARRAY, USGS STATION 1584	20.9	9.6	7.1	360 ⁰	rock

62	ac077	CHICHI	09/20/99	TCU079	8.5	8.0	6.2	0 ⁰	S_D
63	ac078	PETROLIA/CA PE MENDOCINO EARTHQUAK E	04/25/92	EEL RIVER VALLEY ARRAY, USGS STATION 1584	20.9	9.6	7.1	270 ⁰	rock
64	ac079	UTTARKASHI , INDIA	10/19/91	BHATWARI	21.7	10.0	7.0	85 ⁰	rock
65	ac080	ANZA EQ	06/12/05	RARICK SPRINGS	15.9	14.1	5.6	270 ⁰	rock
66	ac081	UTTARKASHI , INDIA	10/19/91	UTTARKASHI	34	10.0	7.0	345 ⁰	rock
67	ac082	COALINGA	07/09/83	COALINGA, OIL CITY	10.0	9.0	5.4	360 ⁰	Stiff soil
68	ac083	CHICHI	09/20/99	TCU129	12.8	8.0	6.2	0 ⁰	S_D
69	ac084	LOMA PRIETA	10/18/89	SUNNYVALE, COLTON AVE	18.1	17.48	7.1	360 ⁰	Stiff soil
70	ac085	KOBE	01/16/95	KOBE UNIVERSITY	0.9	17.9	6.9	90 ⁰	rock
71	ac086	NORTHRIDGE EARTHQUAK	01/17/94	LOS ANGELES - CITY TERRACE	35.8	17.5	6.8	90 ⁰	rock

		E							
72	ac087	KOBE	01/16/95	FUKUSHIMA	17.9	17.9	6.9	90 ⁰	-
73	ac088	LOMA PRIETA	10/18/89	EMERYVILLE, 6363 CHRISTIE GR	67.7	17.48	7.1	260 ⁰	Stiff soil
74	ac089	LOMA PRIETA	10/18/89	STANFORD UNIVERSITY	20.5	17.48	7.1	360 ⁰	-
75	ac090	CHICHI	09/25/99	TCU078	11.5	16.0	6.3	0 ⁰	S_D
76	ac091	CHICHI	09/22/99	TCU129	38.9	10	6.2	0 ⁰	S_D
77	ac092	NORTHRIDGE	01/17/94	UCSB/USC PORTABLE SITE	19.5	17.5	6.8	270 ⁰	rock
78	ac093	NORTHRIDGE	01/18/94	LOS ANGELES, GRIFFITH OBSERVATORY	22.9	17.5	6.8	270 ⁰	rock
79	ac094	LOMA PRIETA	10/18/89	GILROY #1 - GAVILAN COLLEGE	2.8	17.48	7.1	90 ⁰	rock
80	ac095	LOMA PRIETA	10/18/89	UCSC/ LICK OBSERVATORY	18.8	17.48	7.1	90 ⁰	rock
81	ac096	ANZA EQ	06/12/05	RARICK SPRINGS	15.9	14.1	5.6	360 ⁰	rock
82	ac097	CHICHI	09/20/99	TCU079	11	6.76	7.6	0 ⁰	S_D

83	ac098	NORTHRIDGE	01/17/94	JENSEN FILTRATION PLANT	8.6	17.5	6.8	22 ⁰	rock
84	ac099	CHICHI	09/20/99	TCU079	8.5	8.0	6.2	90 ⁰	S_D
85	ac100	CHICHI	09/20/99	TCU129	2.2	6.76	7.6	90 ⁰	S_D
86	ac101	CHICHI	09/20/99	TCU129	12.8	8.0	6.2	90 ⁰	S_D
87	ac102	NORTHRIDGE	01/17/94	JENSEN FILTRATION PLANT	8.6	17.5	6.8	292 ⁰	rock
88	ac103	SAN FERNANDO	02/09/71	PACOIMA DAM	3.5	13	6.6	164 ⁰	rock
89	ac104	CHICHI	09/20/99	TCU071	4.9	6.76	7.6	90 ⁰	S_D
90	ac105	CHICHI	09/20/99	TCU071	4.9	6.76	7.6	0 ⁰	S_D

Note: S_B → Site Geology: rock (1997 UBC), S_D → Site Geology: stiff soil (1997 UBC)

Table A.2: Properties of various selected seismograms used in the finite element analysis

No	Arias Intensity (m/s) [Arias, 1970]	Maximum acceleration (in g)	Mean period (s) [Rathje et al. (1998)]	Predominant period (s) [Rathje et al. (1998)]	Smoothed predominant period (s) [Rathje et al. (1998)]	Dominant period (s) [Vanmarcke and Lai (1986)]
1	0.011	0.031	0.863	0.24	0.297	0.282
2	0.011	0.028	0.086	0.098	0.159	0.123
3	0.013	0.041	0.548	0.236	0.192	0.191
4	0.014	0.024	2.045	1.078	0.929	0.737
5	0.016	0.032	1.244	0.402	0.35	0.346
6	0.018	0.049	0.099	0.181	0.159	0.157
7	0.020	0.053	0.230	0.238	0.331	0.48
8	0.028	0.027	1.310	0.126	0.409	0.366
9	0.028	0.053	0.198	0.202	0.29	0.179
10	0.029	0.071	0.225	0.148	0.191	0.273
11	0.030	0.048	0.111	0.204	0.173	0.187
12	0.031	0.020	2.334	2.486	1.26	1.262
13	0.038	0.072	0.154	0.224	0.277	0.158
14	0.042	0.054	0.212	0.301	0.314	0.313
15	0.044	0.056	0.573	0.34	0.226	0.11
16	0.051	0.053	0.197	0.189	0.268	0.231
17	0.054	0.073	0.216	0.307	0.256	0.221
18	0.054	0.044	1.521	0.487	0.41	0.585
19	0.054	0.077	0.143	0.131	0.221	0.135
20	0.060	0.125	0.168	0.222	0.239	0.316
21	0.071	0.054	1.757	0.495	0.505	0.812
22	0.073	0.059	0.784	0.343	0.267	0.181
23	0.084	0.169	0.265	0.11	0.092	0.086
24	0.087	0.095	0.436	0.151	0.155	0.132

25	0.088	0.051	1.324	0.306	0.484	0.375
26	0.091	0.147	0.459	0.236	0.159	0.157
27	0.096	0.066	1.266	0.462	0.463	0.419
28	0.097	0.155	0.091	0.086	0.109	0.099
29	0.097	0.073	0.120	0.175	0.188	0.193
30	0.099	0.075	0.711	0.218	0.248	0.184
31	0.100	0.076	0.918	0.421	0.364	0.255
32	0.104	0.206	0.837	0.214	0.155	0.266
33	0.108	0.099	0.561	0.172	0.198	0.159
34	0.109	0.095	0.125	0.109	0.229	0.128
35	0.117	0.055	1.994	0.518	0.675	0.754
36	0.125	0.141	0.611	0.224	0.221	0.211
37	0.158	0.154	0.814	0.435	0.246	0.296
38	0.163	0.146	0.381	0.155	0.156	0.134
39	0.165	0.104	0.794	0.218	0.179	0.222
40	0.182	0.092	0.282	0.171	0.393	0.385
41	0.182	0.084	1.788	0.407	0.665	0.927
42	0.192	0.133	0.119	0.22	0.193	0.165
43	0.199	0.126	0.487	0.119	0.139	0.155
44	0.202	0.156	0.959	0.234	0.281	0.134
45	0.207	0.103	0.502	0.52	0.546	0.453
46	0.253	0.158	0.203	0.212	0.241	0.236
47	0.279	0.134	1.163	0.295	0.377	0.416
48	0.282	0.199	0.400	0.652	0.414	0.443
49	0.310	0.127	0.546	0.722	0.552	0.74
50	0.313	0.208	0.517	0.132	0.189	0.134
51	0.322	0.194	0.985	0.201	0.315	0.306
52	0.348	0.164	0.745	0.202	0.281	0.255
53	0.350	0.239	0.539	0.235	0.212	0.18
54	0.356	0.155	1.180	0.389	0.425	0.469

55	0.399	0.186	0.420	0.156	0.177	0.144
56	0.400	0.163	0.954	0.509	0.304	0.168
57	0.422	0.150	1.390	0.431	0.507	0.477
58	0.475	0.171	0.261	0.213	0.367	0.247
59	0.481	0.263	0.443	0.153	0.19	0.16
60	0.493	0.259	1.178	0.286	0.308	0.613
61	0.589	0.209	1.421	0.453	0.533	0.478
62	0.626	0.262	0.612	0.245	0.208	0.257
63	0.647	0.179	1.827	0.344	0.772	0.608
64	0.670	0.253	0.219	0.28	0.335	0.218
65	0.632	0.530	0.196	0.069	0.076	0.068
66	0.688	0.242	0.148	0.243	0.257	0.185
67	0.777	0.376	0.348	0.132	0.118	0.124
68	0.777	0.396	0.482	0.195	0.18	0.162
69	0.783	0.219	1.134	0.209	0.52	0.477
70	0.807	0.310	0.697	0.416	0.38	0.314
71	0.855	0.263	0.310	0.164	0.193	0.202
72	0.874	0.216	1.174	0.926	0.66	0.89
73	0.912	0.260	2.191	1.188	0.705	0.893
74	0.935	0.288	1.149	0.307	0.381	0.284
75	0.990	0.386	0.752	0.212	0.28	0.221
76	1.010	0.279	0.374	0.169	0.159	0.144
77	1.032	0.379	0.386	0.311	0.251	0.227
78	1.500	0.289	0.850	0.5	0.303	0.184
79	1.538	0.442	0.208	0.381	0.275	0.185
80	1.727	0.409	0.118	0.154	0.205	0.162
81	1.775	0.946	0.202	0.072	0.075	0.071
82	3.815	0.425	0.853	0.471	0.39	0.42
83	3.251	0.572	0.941	0.354	0.311	0.288
84	3.815	0.425	0.853	0.286	0.343	0.226

85	9.177	1.002	0.648	0.387	0.462	0.476
86	5.496	0.623	0.648	0.189	0.197	0.2
87	6.541	0.997	1.036	0.315	0.295	0.38
88	7.645	1.170	0.282	0.386	0.241	0.249
89	9.276	0.532	0.824	0.351	0.49	0.464
90	9.418	0.652	0.644	0.249	0.213	0.193

Table A.3: Design layout for Response Surface Model-II using Face-Centred Central Composite Design and calculated (from FE analysis) responses

Run #	A- Relative Density (%)	B- CV	C- Arias Intensity (m/s)	D- Period of Structure (sec)	Response: 1	Response: 2
					Maximum total settlement at left footing (m)	Maximum differential settlements (m)
1	85.00	0.50	0.075	0.29	1.178E-02	2.803E-03
2	65.00	0.50	0.287	0.78	7.454E-02	1.830E-02
3	65.00	0.35	0.075	0.29	1.557E-02	3.018E-03
4	65.00	0.35	0.500	0.78	8.044E-02	2.099E-02
5	85.00	0.50	0.075	0.78	2.487E-02	5.697E-03
6	45.00	0.50	0.500	0.29	1.052E-01	3.907E-02
7	85.00	0.20	0.500	0.29	2.625E-02	5.424E-03
8	85.00	0.50	0.500	0.78	7.403E-02	2.132E-02
9	65.00	0.35	0.075	0.78	3.055E-02	6.739E-03
10	45.00	0.20	0.075	0.78	4.709E-02	1.007E-02
11	45.00	0.50	0.500	0.78	1.674E-01	4.373E-02
12	65.00	0.35	0.287	0.29	2.956E-02	5.379E-03
13	85.00	0.20	0.075	0.29	1.064E-02	2.452E-03
14	85.00	0.50	0.500	0.29	3.286E-02	6.045E-03
15	45.00	0.20	0.500	0.78	1.123E-01	2.585E-02
16	65.00	0.35	0.287	0.78	6.370E-02	1.457E-02
17	45.00	0.20	0.075	0.29	2.375E-02	4.402E-03
18	85.00	0.20	0.075	0.78	2.208E-02	5.080E-03
19	65.00	0.20	0.287	0.78	5.941E-02	1.357E-02
20	45.00	0.35	0.287	0.78	1.544E-02	3.565E-03
21	45.00	0.50	0.075	0.78	5.277E-02	1.108E-02
22	65.00	0.50	0.287	0.29	3.467E-02	5.856E-03
23	85.00	0.20	0.500	0.78	5.880E-02	1.608E-02
24	85.00	0.35	0.287	0.29	2.089E-02	4.615E-03
25	45.00	0.50	0.075	0.29	2.612E-02	4.819E-03
26	45.00	0.35	0.287	0.29	4.524E-02	5.617E-03
27	65.00	0.20	0.287	0.29	2.769E-02	5.082E-03
28	65.00	0.35	0.500	0.29	3.743E-02	5.955E-03
29	45.00	0.20	0.500	0.29	6.123E-02	7.606E-03
30	85.00	0.35	0.287	0.78	4.617E-02	1.223E-02

Note: Soil relative density, Coefficient of variation of q_n , and Arias Intensity are numerical factors and Fundamental period of the structure is a categorical factor in this study.

Table A.4: Design layout for Response Surface Model-III (without replication) using Face-Centred Central Composite Design and calculated (from FE analysis) responses

Run #	A- Relative Density (%)	B- CV	C- Arias Intensity (m/s)	D- Period of Structure (sec)	Response: 1	Response: 2
					Maximum total settlement at left footing (m)	Maximum differential settlements (m)
1	85.00	0.50	0.50	0.29	1.723E-02	1.684E-03
2	65.00	0.50	1.00	0.78	5.984E-02	1.003E-02
3	65.00	0.35	0.50	0.29	2.030E-02	2.342E-03
4	65.00	0.35	1.50	0.78	6.093E-02	1.054E-02
5	85.00	0.50	0.50	0.78	3.406E-02	6.396E-03
6	45.00	0.50	1.50	0.29	8.950E-02	2.226E-02
7	85.00	0.20	1.50	0.29	2.085E-02	2.564E-03
8	85.00	0.50	1.50	0.78	5.429E-02	9.385E-03
9	65.00	0.35	0.50	0.78	3.791E-02	6.166E-03
10	45.00	0.20	0.50	0.78	4.966E-02	8.238E-03
11	45.00	0.50	1.50	0.78	1.161E-01	1.534E-02
12	65.00	0.35	1.00	0.29	2.750E-02	2.476E-03
13	85.00	0.20	0.50	0.29	1.438E-02	1.806E-03
14	85.00	0.50	1.50	0.29	2.732E-02	2.552E-03
15	45.00	0.20	1.50	0.78	8.532E-02	1.393E-02
16	65.00	0.35	1.00	0.78	5.036E-02	8.902E-03
17	45.00	0.20	0.50	0.29	2.917E-02	2.927E-03
18	85.00	0.20	0.50	0.78	2.900E-02	5.480E-03
19	65.00	0.20	1.00	0.78	4.667E-02	7.887E-03
20	45.00	0.35	1.00	0.78	7.627E-02	1.059E-02
21	45.00	0.50	0.50	0.78	5.774E-02	1.099E-02
22	65.00	0.50	1.00	0.29	3.313E-02	3.434E-03
23	85.00	0.20	1.50	0.78	4.408E-02	8.793E-03
24	85.00	0.35	1.00	0.29	1.910E-02	2.221E-03
25	45.00	0.50	0.50	0.29	3.385E-02	3.439E-03
26	45.00	0.35	1.00	0.29	4.533E-02	3.560E-03
27	65.00	0.20	1.00	0.29	2.450E-02	2.418E-03
28	65.00	0.35	1.50	0.29	3.246E-02	2.606E-03
29	45.00	0.20	1.50	0.29	5.106E-02	6.580E-03
30	85.00	0.35	1.00	0.78	4.054E-02	8.032E-03

Table A.5: Design layout for Response Surface Model-III (with 5-replication) using Face-Centred Central Composite Design and calculated (from FE analysis) responses

Run #	A- Relative Density (%)	B- CV	C- Arias Intensity (m/s)	D- Period of Structure (sec)	Response: 1	Response: 2
					Maximum total settlement at left footing (m)	Maximum differential settlements (m)
1	65	0.35	1.5	0.29	3.246E-02	2.606E-03
2	45	0.35	1	0.29	6.641E-02	1.822E-02
3	65	0.2	1	0.29	2.450E-02	2.418E-03
4	85	0.5	1.5	0.78	6.257E-02	1.763E-02
5	65	0.5	1	0.78	5.504E-02	8.811E-03
6	65	0.2	1	0.29	2.838E-02	3.134E-03
7	45	0.5	0.5	0.29	3.455E-02	6.232E-03
8	45	0.5	1.5	0.29	5.450E-02	3.966E-02
9	45	0.2	0.5	0.78	5.245E-02	5.899E-03
10	85	0.5	1.5	0.29	2.561E-02	4.243E-03
11	45	0.35	1	0.29	4.695E-02	6.515E-03
12	65	0.35	0.5	0.29	1.800E-02	4.053E-03
13	85	0.35	1	0.29	2.132E-02	2.305E-03
14	65	0.35	0.5	0.29	2.023E-02	2.518E-03
15	65	0.35	0.5	0.78	3.592E-02	7.192E-03
16	45	0.5	0.5	0.78	4.930E-02	2.107E-02
17	65	0.2	1	0.29	2.541E-02	2.366E-03
18	45	0.5	1.5	0.78	1.879E-01	8.363E-02
19	65	0.35	1.5	0.29	3.307E-02	3.878E-03
20	85	0.5	0.5	0.78	3.928E-02	1.198E-02
21	65	0.35	0.5	0.78	3.801E-02	7.587E-03
22	45	0.5	1.5	0.78	1.161E-01	1.534E-02
23	85	0.35	1	0.29	1.798E-02	1.941E-03
24	65	0.35	0.5	0.78	3.791E-02	6.166E-03
25	45	0.2	1.5	0.78	8.532E-02	1.393E-02
26	45	0.5	0.5	0.29	3.385E-02	3.439E-03
27	85	0.5	1.5	0.78	5.152E-02	1.216E-02
28	45	0.35	1	0.78	6.708E-02	1.997E-02
29	65	0.35	0.5	0.78	4.541E-02	1.056E-02
30	85	0.2	0.5	0.78	3.256E-02	8.709E-03
31	85	0.2	0.5	0.78	2.806E-02	7.008E-03
32	85	0.5	0.5	0.29	1.493E-02	3.023E-03
33	65	0.35	0.5	0.29	2.339E-02	2.580E-03
34	65	0.2	1	0.78	5.382E-02	1.029E-02
35	85	0.2	0.5	0.78	2.930E-02	7.261E-03

36	85	0.2	1.5	0.29	1.987E-02	2.012E-03
37	65	0.35	1.5	0.29	2.842E-02	7.850E-03
38	85	0.5	0.5	0.78	2.897E-02	7.313E-03
39	65	0.35	1	0.78	6.045E-02	1.310E-02
40	85	0.2	0.5	0.29	1.445E-02	1.974E-03
41	45	0.35	1	0.78	7.214E-02	8.858E-03
42	45	0.35	1	0.29	4.533E-02	3.560E-03
43	45	0.2	0.5	0.29	3.076E-02	3.525E-03
44	45	0.2	1.5	0.78	8.105E-02	1.951E-02
45	85	0.2	1.5	0.29	2.121E-02	2.004E-03
46	45	0.2	1.5	0.29	5.094E-02	5.272E-03
47	65	0.35	1.5	0.78	6.093E-02	1.054E-02
48	45	0.5	1.5	0.29	8.948E-02	2.260E-02
49	65	0.2	1	0.78	4.744E-02	7.764E-03
50	45	0.5	1.5	0.78	1.194E-01	1.973E-02
51	65	0.5	1	0.78	5.588E-02	9.302E-03
52	85	0.5	1.5	0.78	5.429E-02	9.385E-03
53	45	0.5	0.5	0.78	8.036E-02	2.432E-02
54	65	0.5	1	0.78	4.745E-02	1.754E-02
55	65	0.35	1	0.29	2.750E-02	2.476E-03
56	45	0.5	1.5	0.78	8.440E-02	3.696E-02
57	85	0.5	0.5	0.78	3.229E-02	8.240E-03
58	85	0.2	1.5	0.29	2.313E-02	2.601E-03
59	65	0.5	1	0.29	2.533E-02	9.163E-03
60	85	0.5	1.5	0.78	4.523E-02	1.347E-02
61	65	0.35	1.5	0.78	7.134E-02	1.456E-02
62	45	0.5	1.5	0.29	7.429E-02	1.698E-02
63	85	0.5	0.5	0.29	1.723E-02	1.684E-03
64	85	0.35	1	0.29	1.923E-02	2.287E-03
65	85	0.2	0.5	0.29	1.470E-02	1.520E-03
66	85	0.2	1.5	0.29	2.085E-02	2.564E-03
67	65	0.35	1	0.29	2.639E-02	2.523E-03
68	45	0.5	0.5	0.78	5.558E-02	7.751E-03
69	45	0.2	1.5	0.29	4.648E-02	1.440E-02
70	65	0.35	1	0.78	5.007E-02	8.505E-03
71	65	0.35	1.5	0.29	3.811E-02	6.238E-03
72	65	0.5	1	0.78	7.318E-02	1.995E-02
73	65	0.35	1	0.29	3.152E-02	4.084E-03
74	45	0.5	0.5	0.78	5.774E-02	1.099E-02
75	85	0.35	1	0.78	3.727E-02	9.262E-03
76	45	0.2	0.5	0.29	2.917E-02	2.927E-03
77	45	0.2	1.5	0.78	8.501E-02	7.784E-03
78	85	0.5	0.5	0.78	3.406E-02	6.396E-03
79	45	0.5	0.5	0.29	2.850E-02	9.861E-03
80	45	0.2	1.5	0.78	1.139E-01	2.748E-02

81	45	0.5	1.5	0.29	1.977E-01	1.120E-01
82	65	0.2	1	0.78	4.509E-02	9.521E-03
83	85	0.2	1.5	0.78	4.318E-02	9.143E-03
84	65	0.35	1	0.78	4.759E-02	7.911E-03
85	85	0.2	0.5	0.29	1.592E-02	1.392E-03
86	45	0.35	1	0.78	9.994E-02	2.652E-02
87	45	0.2	0.5	0.29	2.873E-02	3.092E-03
88	45	0.2	0.5	0.78	4.910E-02	6.111E-03
89	65	0.35	0.5	0.78	3.476E-02	8.233E-03
90	65	0.35	1	0.29	2.738E-02	3.369E-03
91	85	0.2	0.5	0.29	1.380E-02	1.490E-03
92	85	0.2	0.5	0.78	2.811E-02	5.512E-03
93	85	0.5	1.5	0.78	4.874E-02	1.056E-02
94	65	0.5	1	0.29	3.152E-02	4.503E-03
95	45	0.2	0.5	0.29	2.782E-02	4.997E-03
96	85	0.5	1.5	0.29	2.527E-02	1.536E-03
97	65	0.5	1	0.29	3.199E-02	3.143E-03
98	65	0.5	1	0.29	3.313E-02	3.434E-03
99	45	0.5	1.5	0.29	8.950E-02	2.226E-02
100	65	0.2	1	0.29	2.401E-02	2.057E-03
101	65	0.35	1.5	0.78	5.913E-02	9.054E-03
102	65	0.2	1	0.78	4.667E-02	7.887E-03
103	45	0.2	0.5	0.78	4.966E-02	8.238E-03
104	85	0.2	1.5	0.29	2.070E-02	2.931E-03
105	65	0.5	1	0.29	3.908E-02	8.609E-03
106	65	0.5	1	0.78	5.984E-02	1.003E-02
107	45	0.5	0.5	0.78	5.780E-02	8.400E-03
108	85	0.35	1	0.29	1.823E-02	3.287E-03
109	85	0.5	0.5	0.29	1.652E-02	2.302E-03
110	65	0.35	0.5	0.29	2.030E-02	2.342E-03
111	85	0.2	1.5	0.78	4.411E-02	1.041E-02
112	85	0.5	1.5	0.29	2.177E-02	6.043E-03
113	65	0.35	0.5	0.29	1.951E-02	1.954E-03
114	45	0.35	1	0.29	3.860E-02	1.225E-02
115	85	0.5	1.5	0.29	2.732E-02	2.552E-03
116	45	0.2	1.5	0.78	8.766E-02	9.959E-03
117	45	0.35	1	0.78	7.573E-02	1.189E-02
118	85	0.2	1.5	0.78	4.905E-02	1.254E-02
119	85	0.2	1.5	0.78	4.174E-02	1.005E-02
120	85	0.35	1	0.29	1.910E-02	2.221E-03
121	45	0.2	1.5	0.29	8.326E-02	2.500E-02
122	45	0.2	0.5	0.78	6.166E-02	1.134E-02
123	85	0.5	0.5	0.29	1.904E-02	2.658E-03
124	45	0.2	0.5	0.29	3.567E-02	5.398E-03
125	45	0.5	0.5	0.29	3.629E-02	5.398E-03

126	85	0.35	1	0.78	4.054E-02	8.032E-03
127	65	0.2	1	0.29	2.450E-02	2.418E-03
128	45	0.5	0.5	0.29	4.544E-02	1.091E-02
129	65	0.2	1	0.78	4.500E-02	7.921E-03
130	85	0.5	1.5	0.29	3.014E-02	6.103E-03
131	45	0.35	1	0.78	7.627E-02	1.059E-02
132	65	0.35	1	0.78	4.569E-02	1.274E-02
133	65	0.35	1	0.78	5.036E-02	8.902E-03
134	45	0.35	1	0.29	4.416E-02	6.112E-03
135	65	0.35	1	0.29	2.396E-02	5.761E-03
136	85	0.2	0.5	0.78	2.900E-02	5.480E-03
137	85	0.35	1	0.78	4.511E-02	1.203E-02
138	85	0.35	1	0.78	3.715E-02	9.197E-03
139	45	0.2	1.5	0.29	5.342E-02	4.770E-03
140	85	0.2	1.5	0.78	4.408E-02	8.793E-03
141	45	0.2	0.5	0.78	4.782E-02	1.120E-02
142	65	0.35	1.5	0.78	5.281E-02	1.665E-02
143	65	0.35	1.5	0.78	5.659E-02	8.794E-03
144	45	0.2	1.5	0.29	5.106E-02	6.580E-03
145	45	0.5	1.5	0.78	1.082E-01	2.062E-02
146	65	0.35	1.5	0.29	3.167E-02	3.083E-03
147	85	0.35	1	0.78	3.992E-02	1.001E-02
148	85	0.2	0.5	0.29	1.438E-02	1.806E-03
149	85	0.5	0.5	0.78	3.072E-02	7.818E-03
150	85	0.5	0.5	0.29	1.554E-02	1.613E-03

Table A.6: Design layout for Response Surface Model-IV using Face-Centred Central Composite Design and calculated (from FE analysis) responses

Run #	A- Relative Density (%)	B- CV	C- Arias Intensity (m/s)	D- Period of Structure (sec)	Response: 1	Response: 2
					Maximum total settlement at left footing (m)	Maximum differential settlements (m)
1	85.00	0.50	1.00	0.29	3.174E-02	6.238E-03
2	65.00	0.50	2.50	0.78	1.867E-01	4.775E-02
3	65.00	0.35	1.00	0.29	3.891E-02	6.328E-03
4	65.00	0.35	4.00	0.78	1.932E-01	3.229E-02
5	85.00	0.50	1.00	0.78	5.905E-02	1.086E-02
6	45.00	0.50	4.00	0.29	2.374E-01	5.163E-02
7	85.00	0.20	4.00	0.29	5.451E-02	9.165E-03
8	85.00	0.50	4.00	0.78	1.554E-01	3.193E-02
9	65.00	0.35	1.00	0.78	7.436E-02	1.275E-02
10	45.00	0.20	1.00	0.78	1.337E-01	1.640E-02
11	45.00	0.50	4.00	0.78	4.440E-01	9.068E-02
12	65.00	0.35	2.50	0.29	7.212E-02	1.300E-02
13	85.00	0.20	1.00	0.29	2.431E-02	3.596E-03
14	85.00	0.50	4.00	0.29	7.809E-02	1.660E-02
15	45.00	0.20	4.00	0.78	3.749E-01	5.150E-02
16	65.00	0.35	2.50	0.78	1.395E-01	2.240E-02
17	45.00	0.20	1.00	0.29	7.387E-02	6.126E-03
18	85.00	0.20	1.00	0.78	4.675E-02	8.811E-03
19	65.00	0.20	2.50	0.78	1.253E-01	2.225E-02
20	45.00	0.35	2.50	0.78	3.245E-01	6.021E-02
21	45.00	0.50	1.00	0.78	1.937E-01	4.824E-02
22	65.00	0.50	2.50	0.29	1.028E-01	3.247E-02
23	85.00	0.20	4.00	0.78	1.151E-01	2.520E-02
24	85.00	0.35	2.50	0.29	4.645E-02	6.874E-03
25	45.00	0.50	1.00	0.29	1.119E-01	3.663E-02
26	45.00	0.35	2.50	0.29	1.896E-01	3.674E-02
27	65.00	0.20	2.50	0.29	6.431E-02	7.745E-03
28	65.00	0.35	4.00	0.29	9.693E-02	1.451E-02
29	45.00	0.20	4.00	0.29	2.204E-01	2.430E-02
30	85.00	0.35	2.50	0.78	9.234E-02	1.683E-02

Table A.7: Design layout for Response Surface Model-IIIB (with 10-replication) using Face-Centred Central Composite Design and calculated (from FE analysis) responses

Run #	A- Relative Density (%)	B- CV	C- Arias Intensity (m/s)	Response: 1	Response: 2
				Maximum total settlement at left footing (m)	Maximum differential settlements (m)
1	45	0.2	0.5	2.770E-02	2.882E-03
2	45	0.2	0.5	7.250E-02	8.002E-03
3	45	0.2	0.5	2.320E-02	2.865E-03
4	45	0.2	0.5	1.160E-02	1.652E-03
5	45	0.2	0.5	1.770E-01	5.154E-02
6	45	0.2	0.5	4.300E-02	3.637E-03
7	45	0.2	0.5	3.000E-02	2.332E-03
8	45	0.2	0.5	6.980E-02	1.683E-02
9	45	0.2	0.5	2.990E-02	3.020E-03
10	45	0.2	0.5	3.770E-02	5.972E-03
11	85	0.2	0.5	1.520E-02	2.249E-03
12	85	0.2	0.5	2.530E-02	5.221E-03
13	85	0.2	0.5	1.320E-02	2.098E-03
14	85	0.2	0.5	7.400E-03	7.722E-04
15	85	0.2	0.5	2.120E-02	5.001E-03
16	85	0.2	0.5	2.080E-02	2.806E-03
17	85	0.2	0.5	1.420E-02	9.825E-04
18	85	0.2	0.5	2.390E-02	3.651E-03
19	85	0.2	0.5	1.540E-02	2.037E-03
20	85	0.2	0.5	2.120E-02	4.432E-03
21	45	0.5	0.5	3.120E-02	4.665E-03
22	45	0.5	0.5	8.390E-02	1.199E-02
23	45	0.5	0.5	2.830E-02	6.515E-03
24	45	0.5	0.5	1.210E-02	1.831E-03
25	45	0.5	0.5	2.210E-01	8.334E-02
26	45	0.5	0.5	5.640E-02	1.389E-02
27	45	0.5	0.5	3.450E-02	5.383E-03
28	45	0.5	0.5	1.420E-01	7.001E-02
29	45	0.5	0.5	3.380E-02	5.947E-03
30	45	0.5	0.5	4.120E-02	1.669E-02
31	85	0.5	0.5	1.770E-02	2.360E-03
32	85	0.5	0.5	2.900E-02	5.691E-03
33	85	0.5	0.5	1.550E-02	3.377E-03
34	85	0.5	0.5	7.270E-03	8.508E-04
35	85	0.5	0.5	2.190E-02	8.310E-03
36	85	0.5	0.5	2.450E-02	3.761E-03

37	85	0.5	0.5	1.540E-02	1.113E-03
38	85	0.5	0.5	3.100E-02	7.372E-03
39	85	0.5	0.5	1.660E-02	1.997E-03
40	85	0.5	0.5	2.170E-02	7.192E-03
41	45	0.2	1.5	4.500E-02	2.982E-03
42	45	0.2	1.5	2.020E-01	1.495E-02
43	45	0.2	1.5	4.020E-02	7.124E-03
44	45	0.2	1.5	1.820E-02	1.828E-03
45	45	0.2	1.5	4.380E-01	5.412E-02
46	45	0.2	1.5	9.730E-02	1.118E-02
47	45	0.2	1.5	5.870E-02	6.264E-03
48	45	0.2	1.5	2.550E-01	7.966E-02
49	45	0.2	1.5	5.290E-02	7.611E-03
50	45	0.2	1.5	7.290E-02	2.401E-02
51	85	0.2	1.5	2.180E-02	3.909E-03
52	85	0.2	1.5	4.220E-02	1.107E-02
53	85	0.2	1.5	1.970E-02	3.061E-03
54	85	0.2	1.5	1.040E-02	1.509E-03
55	85	0.2	1.5	3.850E-02	9.989E-03
56	85	0.2	1.5	3.090E-02	4.418E-03
57	85	0.2	1.5	2.040E-02	1.827E-03
58	85	0.2	1.5	3.890E-02	8.237E-03
59	85	0.2	1.5	2.410E-02	3.701E-03
60	85	0.2	1.5	3.050E-02	4.965E-03
61	45	0.5	1.5	5.920E-02	4.803E-03
62	45	0.5	1.5	2.200E-01	2.395E-02
63	45	0.5	1.5	6.440E-02	2.682E-02
64	45	0.5	1.5	1.970E-02	2.267E-03
65	45	0.5	1.5	5.520E-01	7.650E-02
66	45	0.5	1.5	1.670E-01	6.953E-02
67	45	0.5	1.5	7.370E-02	1.409E-02
68	45	0.5	1.5	3.600E-01	1.006E-01
69	45	0.5	1.5	6.860E-02	1.604E-02
70	45	0.5	1.5	8.320E-02	6.219E-02
71	85	0.5	1.5	2.680E-02	4.160E-03
72	85	0.5	1.5	4.890E-02	1.235E-02
73	85	0.5	1.5	2.420E-02	5.235E-03
74	85	0.5	1.5	1.050E-02	1.693E-03
75	85	0.5	1.5	4.120E-02	1.704E-02
76	85	0.5	1.5	4.270E-02	8.757E-03
77	85	0.5	1.5	2.370E-02	2.676E-03
78	85	0.5	1.5	5.780E-02	1.967E-02
79	85	0.5	1.5	2.730E-02	4.046E-03
80	85	0.5	1.5	3.170E-02	9.633E-03
81	45	0.35	1	4.000E-02	3.128E-03

82	45	0.35	1	1.680E-01	1.672E-02
83	45	0.35	1	3.570E-02	6.970E-03
84	45	0.35	1	1.620E-02	1.957E-03
85	45	0.35	1	3.450E-01	6.602E-02
86	45	0.35	1	8.650E-02	1.885E-02
87	45	0.35	1	4.930E-02	6.775E-03
88	45	0.35	1	2.100E-01	9.019E-02
89	45	0.35	1	4.510E-02	7.497E-03
90	45	0.35	1	5.910E-02	2.462E-02
91	85	0.35	1	2.020E-02	3.263E-03
92	85	0.35	1	3.580E-02	8.859E-03
93	85	0.35	1	1.850E-02	3.438E-03
94	85	0.35	1	9.020E-03	1.225E-03
95	85	0.35	1	3.020E-02	9.588E-03
96	85	0.35	1	2.770E-02	2.996E-03
97	85	0.35	1	1.840E-02	1.410E-03
98	85	0.35	1	3.570E-02	8.041E-03
99	85	0.35	1	2.110E-02	2.796E-03
100	85	0.35	1	2.690E-02	6.153E-03
101	65	0.2	1	2.480E-02	3.551E-03
102	65	0.2	1	5.120E-02	8.653E-03
103	65	0.2	1	2.160E-02	3.388E-03
104	65	0.2	1	1.030E-02	1.578E-03
105	65	0.2	1	4.580E-02	1.082E-02
106	65	0.2	1	3.640E-02	3.595E-03
107	65	0.2	1	2.430E-02	1.805E-03
108	65	0.2	1	4.890E-02	9.902E-03
109	65	0.2	1	2.660E-02	3.625E-03
110	65	0.2	1	3.280E-02	5.407E-03
111	65	0.5	1	3.090E-02	3.441E-03
112	65	0.5	1	6.430E-02	1.322E-02
113	65	0.5	1	2.770E-02	6.493E-03
114	65	0.5	1	1.140E-02	1.195E-03
115	65	0.5	1	5.490E-02	2.725E-02
116	65	0.5	1	5.130E-02	1.360E-02
117	65	0.5	1	2.980E-02	4.349E-03
118	65	0.5	1	8.760E-02	3.355E-02
119	65	0.5	1	3.230E-02	5.282E-03
120	65	0.5	1	3.560E-02	1.253E-02
121	65	0.35	0.5	2.050E-02	2.796E-03
122	65	0.35	0.5	3.780E-02	5.838E-03
123	65	0.35	0.5	1.820E-02	3.227E-03
124	65	0.35	0.5	8.470E-03	1.010E-03
125	65	0.35	0.5	3.020E-02	7.552E-03
126	65	0.35	0.5	2.900E-02	3.445E-03
127	65	0.35	0.5	1.870E-02	1.459E-03

128	65	0.35	0.5	3.990E-02	8.436E-03
129	65	0.35	0.5	2.090E-02	2.521E-03
130	65	0.35	0.5	2.590E-02	6.356E-03
131	65	0.35	1.5	3.090E-02	3.719E-03
132	65	0.35	1.5	6.910E-02	1.302E-02
133	65	0.35	1.5	2.800E-02	5.127E-03
134	65	0.35	1.5	1.330E-02	1.278E-03
135	65	0.35	1.5	7.820E-02	2.481E-02
136	65	0.35	1.5	4.990E-02	8.583E-03
137	65	0.35	1.5	3.240E-02	3.418E-03
138	65	0.35	1.5	7.340E-02	1.901E-02
139	65	0.35	1.5	3.370E-02	5.054E-03
140	65	0.35	1.5	4.060E-02	8.298E-03
141	65	0.35	1	2.670E-02	3.548E-03
142	65	0.35	1	5.510E-02	1.048E-02
143	65	0.35	1	2.380E-02	4.279E-03
144	65	0.35	1	1.070E-02	1.384E-03
145	65	0.35	1	4.820E-02	1.615E-02
146	65	0.35	1	3.980E-02	5.732E-03
147	65	0.35	1	2.620E-02	2.567E-03
148	65	0.35	1	5.780E-02	1.430E-02
149	65	0.35	1	2.830E-02	4.204E-03
150	65	0.35	1	3.360E-02	7.635E-03

Table A.8: Validation of Response Surface Model-I

Dr (%)	CV	Arias Intensity (m/s)	Period of the structure (sec)	Input acceleration file no	Maximum Total Settlements (in m)		Maximum Differential Settlements (in m)	
					Calculated From FE Analysis	Calculated From RSM	Calculated From FE Analysis	Calculated From RSM
79	0.31	0.024	0.78	ac045	0.00938	0.00857	0.00099	0.00109
67	0.27	0.012	0.78	ac045	0.00687	0.00600	0.00096	0.00112
52	0.43	0.068	0.78	ac045	0.02100	0.02036	0.00278	0.00278
69	0.46	0.073	0.78	ac045	0.01900	0.01877	0.00199	0.00221
54	0.48	0.056	0.29	ac045	0.01200	0.01170	0.00105	0.00140
58	0.48	0.067	0.29	ac045	0.01250	0.01235	0.00126	0.00145
57	0.35	0.053	0.29	ac045	0.01010	0.01039	0.00115	0.00112
52	0.47	0.097	0.78	ac045	0.02600	0.02484	0.00252	0.00384
70	0.34	0.087	0.29	ac045	0.01070	0.01151	0.00125	0.00118
62	0.34	0.031	0.78	ac045	0.01200	0.01123	0.00167	0.00152
83	0.31	0.075	0.29	ac037	0.00823	0.00932	0.00088	0.00081
76	0.41	0.055	0.78	ac034	0.00762	0.01508	0.00126	0.00160
83	0.49	0.099	0.29	ac046	0.01360	0.01072	0.00226	0.00117
52	0.26	0.013	0.78	ac018	0.00515	0.00726	0.00098	0.00135
70	0.33	0.051	0.29	ac031	0.00609	0.00861	0.00082	0.00087
47	0.49	0.025	0.29	ac022	0.00523	0.00776	0.00101	0.00117
70	0.46	0.028	0.29	ac024	0.00388	0.00606	0.00070	0.00084
49	0.31	0.075	0.78	ac037	0.02470	0.02161	0.00270	0.00275
70	0.22	0.098	0.78	ac044	0.01150	0.02064	0.00207	0.00202
46	0.46	0.073	0.78	ac037	0.02750	0.02244	0.00297	0.00336

Note: This model was formulated using input acceleration file # ac045.

Table A.9: Validation of Response Surface Model-II

Dr (%)	CV	Arias Intensity (m/s)	period of the structure (sec)	Input acceleration file no	Maximum Total Settlements (in m)		Maximum Differential Settlements (in m)	
					Calculated From FE Analysis	Calculated From RSM	Calculated From FE Analysis	Calculated From RSM
79	0.31	0.494	0.78	ac076	0.06550	0.06392	0.01800	0.01739
67	0.27	0.265	0.78	ac076	0.05690	0.05347	0.01320	0.01294
52	0.43	0.22	0.78	ac076	0.07400	0.07181	0.01690	0.01558
69	0.46	0.099	0.78	ac076	0.03570	0.03343	0.00818	0.00788
54	0.48	0.134	0.29	ac076	0.02890	0.02734	0.00463	0.00475
58	0.48	0.458	0.29	ac076	0.04900	0.05670	0.01030	0.00812
57	0.35	0.434	0.29	ac076	0.04150	0.04606	0.00591	0.00663
52	0.47	0.316	0.78	ac076	0.08950	0.09953	0.02280	0.02230
70	0.34	0.47	0.29	ac076	0.03380	0.03529	0.00583	0.00581
62	0.34	0.318	0.78	ac076	0.06900	0.06825	0.01630	0.01641
83	0.31	0.249	0.29	ac061	0.01260	0.01875	0.00152	0.00389
76	0.41	0.327	0.78	ac066	0.03870	0.05840	0.00429	0.01455
83	0.49	0.349	0.29	ac068	0.01290	0.02825	0.00193	0.00566
52	0.26	0.481	0.78	ac074	0.02580	0.09861	0.00163	0.02523
70	0.33	0.296	0.29	ac064	0.02260	0.02674	0.00300	0.00490
47	0.49	0.293	0.29	ac064	0.18100	0.05720	0.08650	0.00763
70	0.46	0.241	0.29	ac061	0.01540	0.02626	0.00159	0.00508
49	0.31	0.093	0.78	ac041	0.01170	0.04453	0.00172	0.00932
70	0.22	0.128	0.78	ac051	0.01310	0.03411	0.00222	0.00805
46	0.46	0.187	0.78	ac057	0.01720	0.07792	0.00181	0.01585

Note: This model was formulated using input acceleration file # ac076.

Table A.10: Validation of Response Surface Model-III

Dr (%)	CV	Arias Intensity (m/s)	period of the structure (sec)	Input acceleration file no	Maximum Total Settlements (in m)			Maximum Differential Settlements (in m)		
					Calculated From FE Analysis	Calculated From RSM (without replication)	Calculated From RSM (with 5-replication)	Calculated From FE Analysis	Calculated From RSM (without replication)	Calculated From RSM (with 5-replication)
79	0.31	1.196	0.78	ac105	0.04410	0.04466	0.04534	0.00841	0.00796	0.00932
67	0.27	0.844	0.78	ac105	0.04400	0.04341	0.04384	0.00704	0.00751	0.00782
52	0.43	0.744	0.78	ac105	0.05980	0.05831	0.05898	0.00951	0.00958	0.01089
69	0.46	1.049	0.78	ac105	0.05370	0.05460	0.05224	0.00890	0.00925	0.01032
54	0.48	1.05	0.29	ac105	0.04180	0.04092	0.04054	0.00445	0.00376	0.00693
58	0.48	0.594	0.29	ac105	0.02860	0.02721	0.02730	0.00277	0.00248	0.00414
57	0.35	0.708	0.29	ac105	0.02800	0.02716	0.02777	0.00291	0.00232	0.00359
52	0.47	1.209	0.78	ac105	0.08020	0.08135	0.07962	0.01170	0.01221	0.01462
70	0.34	1.373	0.29	ac105	0.02760	0.02861	0.02879	0.00240	0.00261	0.00375
62	0.34	1.493	0.78	ac105	0.06310	0.06473	0.06429	0.01180	0.01102	0.01192
83	0.31	1.48	0.29	ac093	0.03300	0.02270	0.02331	0.00521	0.00216	0.00293
76	0.41	0.857	0.78	ac086	0.03780	0.04296	0.04229	0.00490	0.00754	0.00883
83	0.49	0.697	0.29	ac081	0.01550	0.01965	0.01873	0.00181	0.00213	0.00253
52	0.26	1.165	0.78	ac092	0.06080	0.06639	0.06810	0.00813	0.01076	0.01101
70	0.33	1.256	0.29	ac093	0.03810	0.02732	0.02741	0.00552	0.00245	0.00341
47	0.49	1.009	0.29	ac091	0.02330	0.04843	0.04993	0.00123	0.00448	0.00999
70	0.46	1.327	0.29	ac093	0.04700	0.03190	0.03062	0.00757	0.00288	0.00462
49	0.31	1.217	0.78	ac093	0.08300	0.07494	0.07802	0.00741	0.01162	0.01300
70	0.22	1.015	0.78	ac091	0.02440	0.04446	0.04471	0.00155	0.00788	0.00787
46	0.46	0.862	0.78	ac086	0.07430	0.07414	0.07607	0.00646	0.01133	0.01413

Note: This model was formulated using input acceleration file # ac0105.

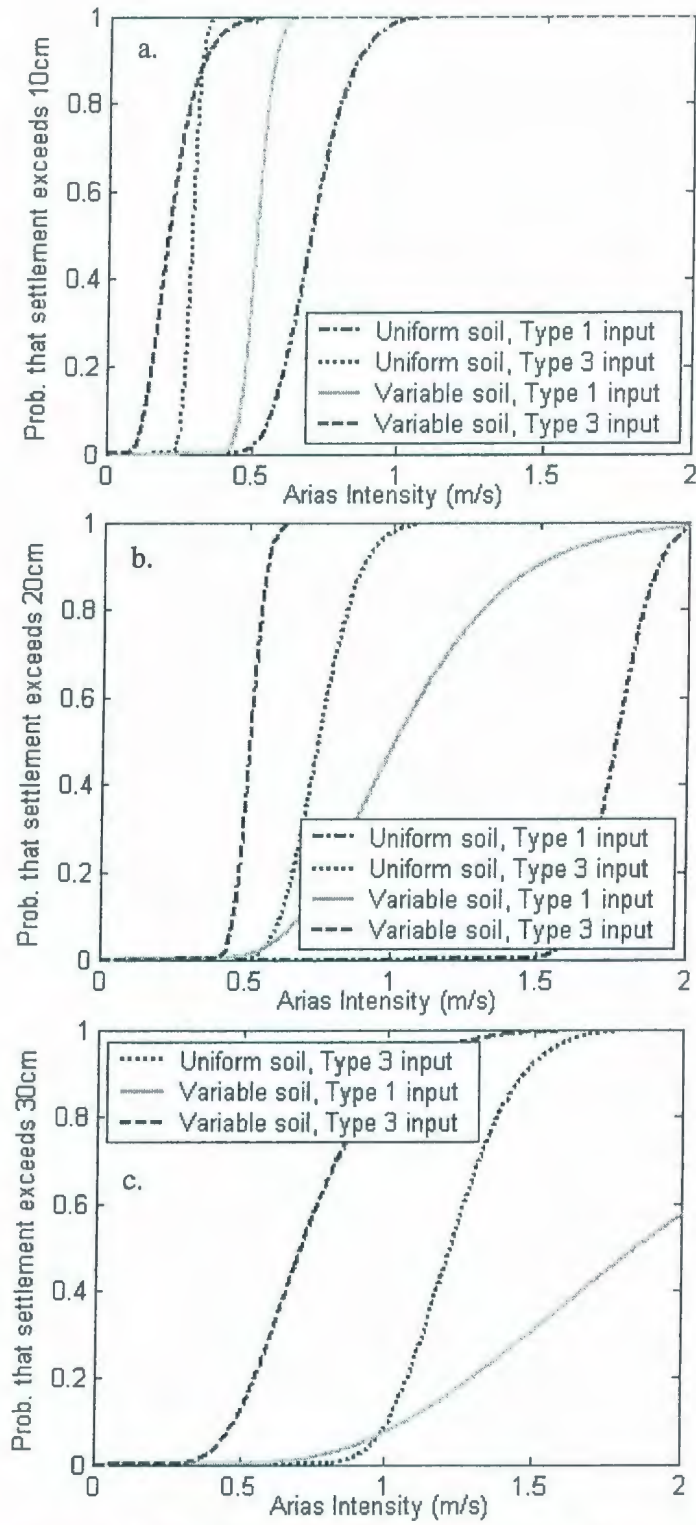


Figure A.1: Fragility curve for maximum total settlements.

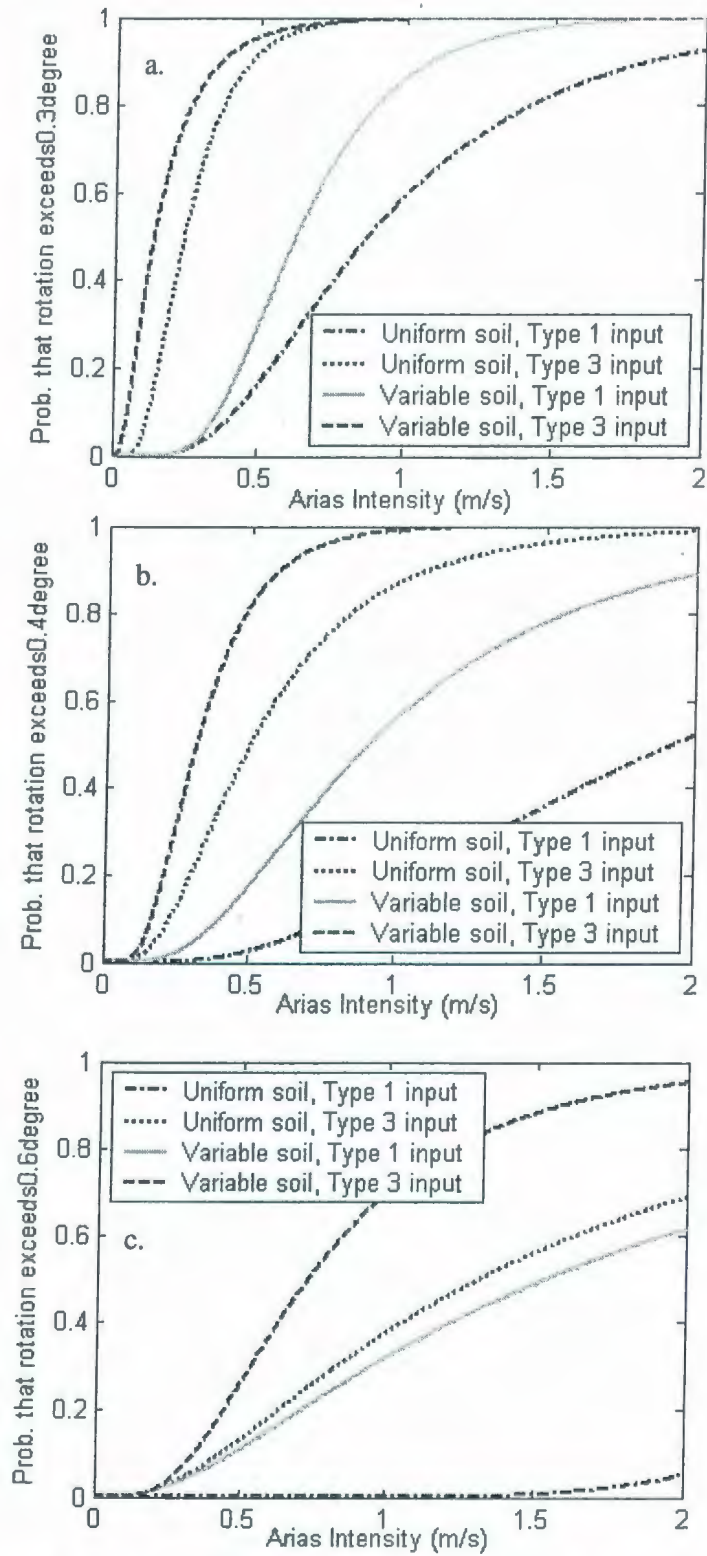


Figure A.2: Fragility curve for maximum base rotation.

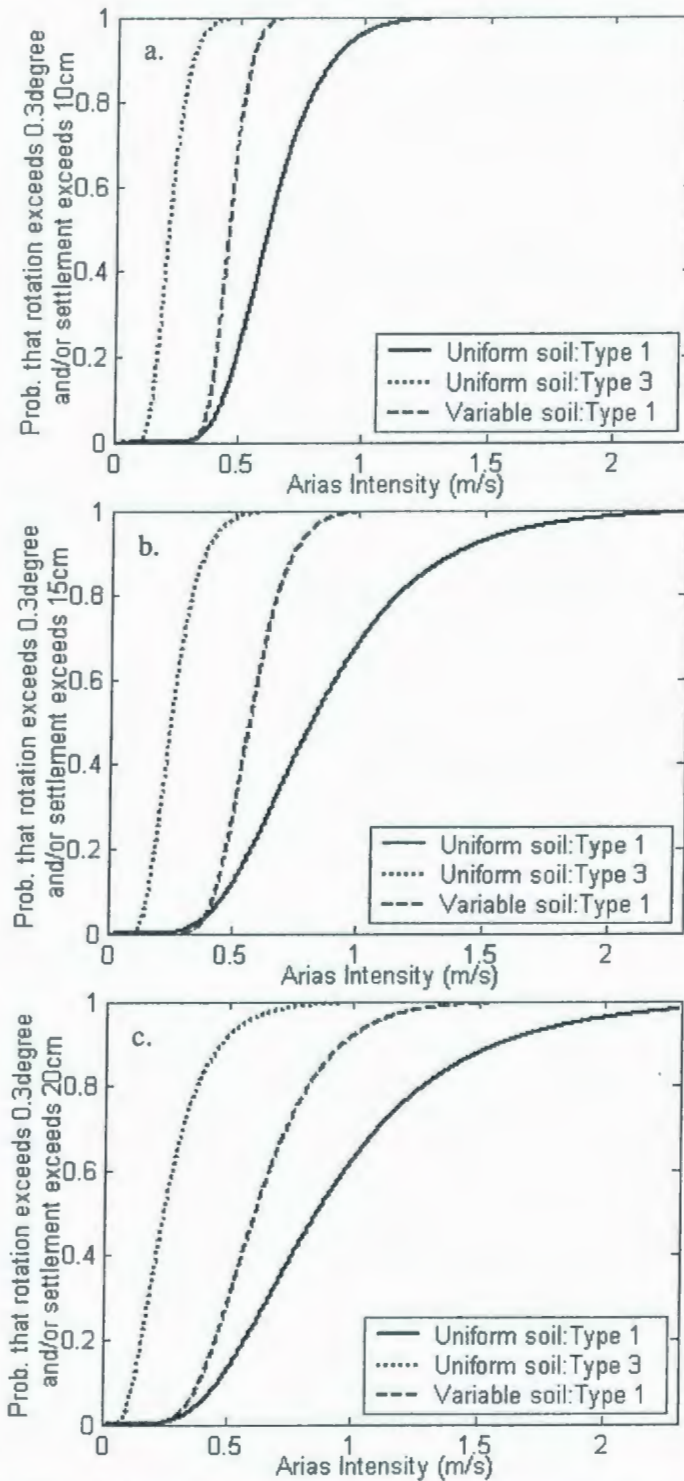


Figure A.3: Type-I damage curve: probability of damage due to exceeding a. level-1 maximum settlement and/or level-1 maximum base rotation; b. level-2 maximum settlement and/or level-1 maximum base rotation; c. level-3 maximum settlement and/or level-1 maximum base rotation.

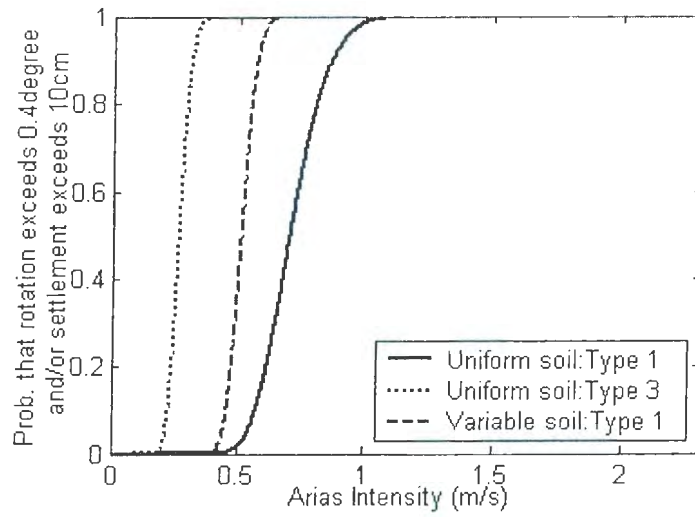


Figure A.4: Type-I damage curve: probability of damage due to exceeding a level-1 maximum settlement and/or level-2 maximum base rotation.

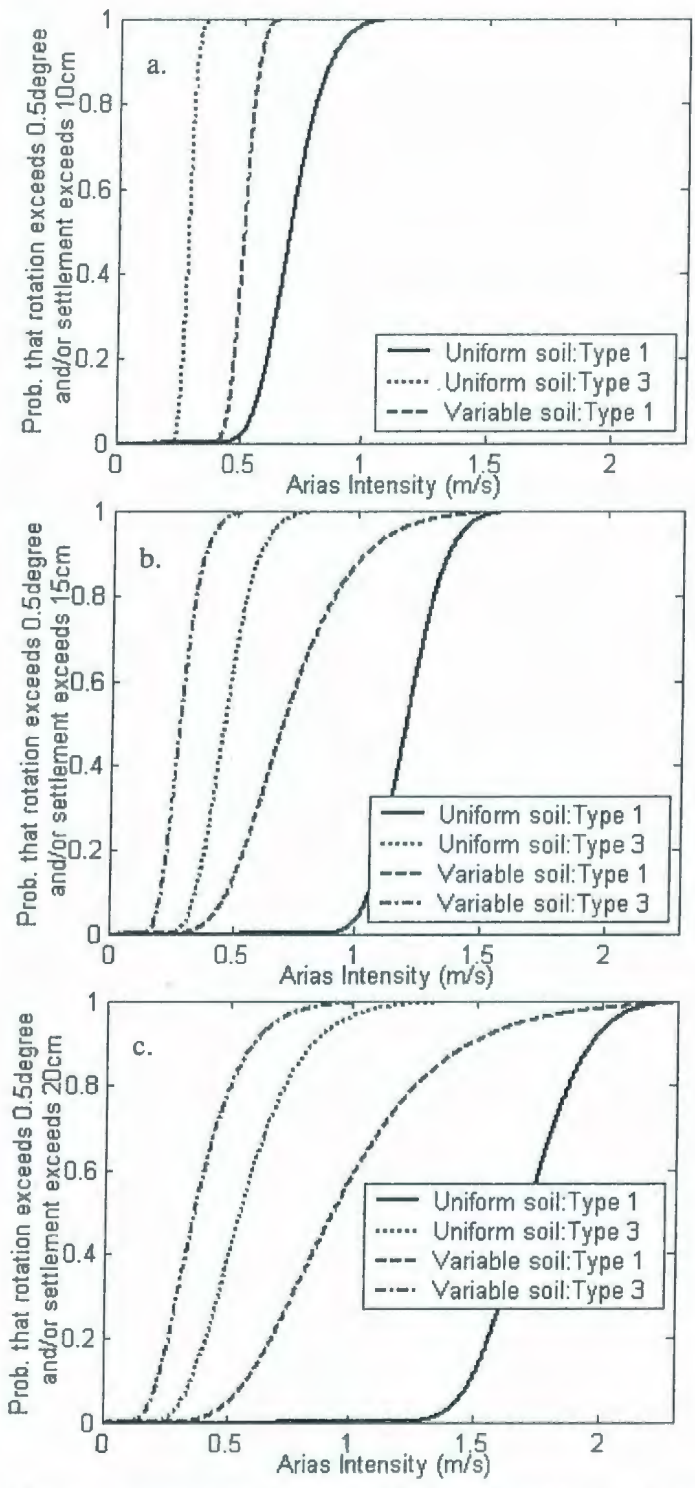


Figure A.5: Type-I damage curve: probability of damage due to exceeding a. level-1 maximum settlement and/or level-3 maximum base rotation; b. level-2 maximum settlement and/or level-3 maximum base rotation; c. level-3 maximum settlement and/or level-3 maximum base rotation.

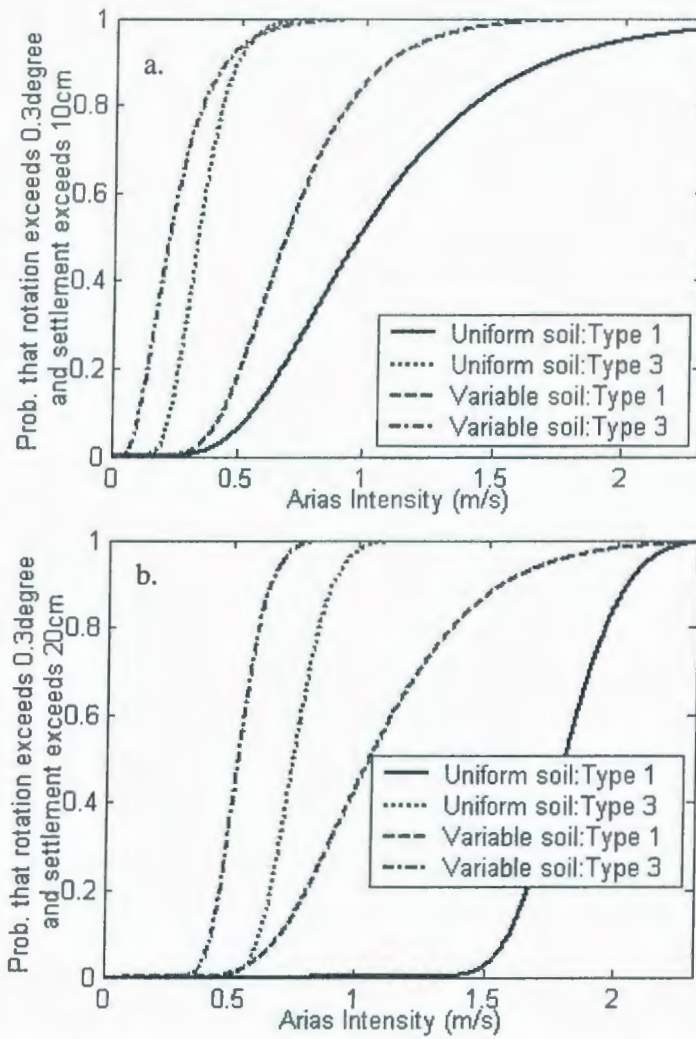


Figure A.6: Type-II damage curve: probability of damage due to exceeding a. both level-1 maximum settlement and level-1 maximum base rotation; b. both level-3 maximum settlement and level-1 maximum base rotation.

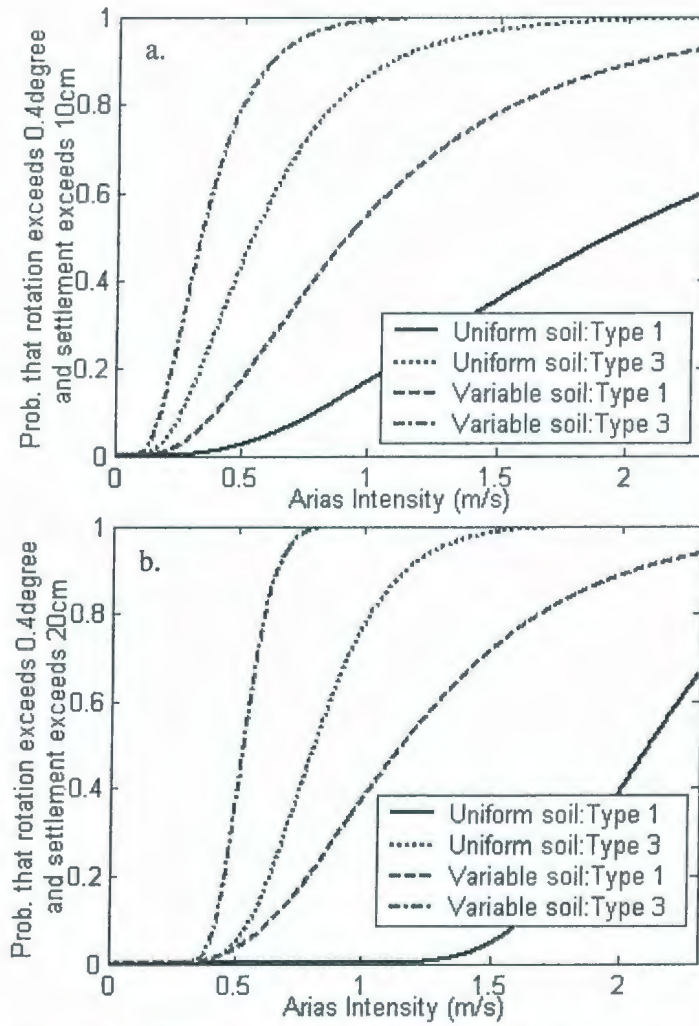


Figure A.7: Type-II damage curve: probability of damage due to exceeding a. both level-1 maximum settlement and level-2 maximum base rotation; b. both level-3 maximum settlement and level-2 maximum base rotation.

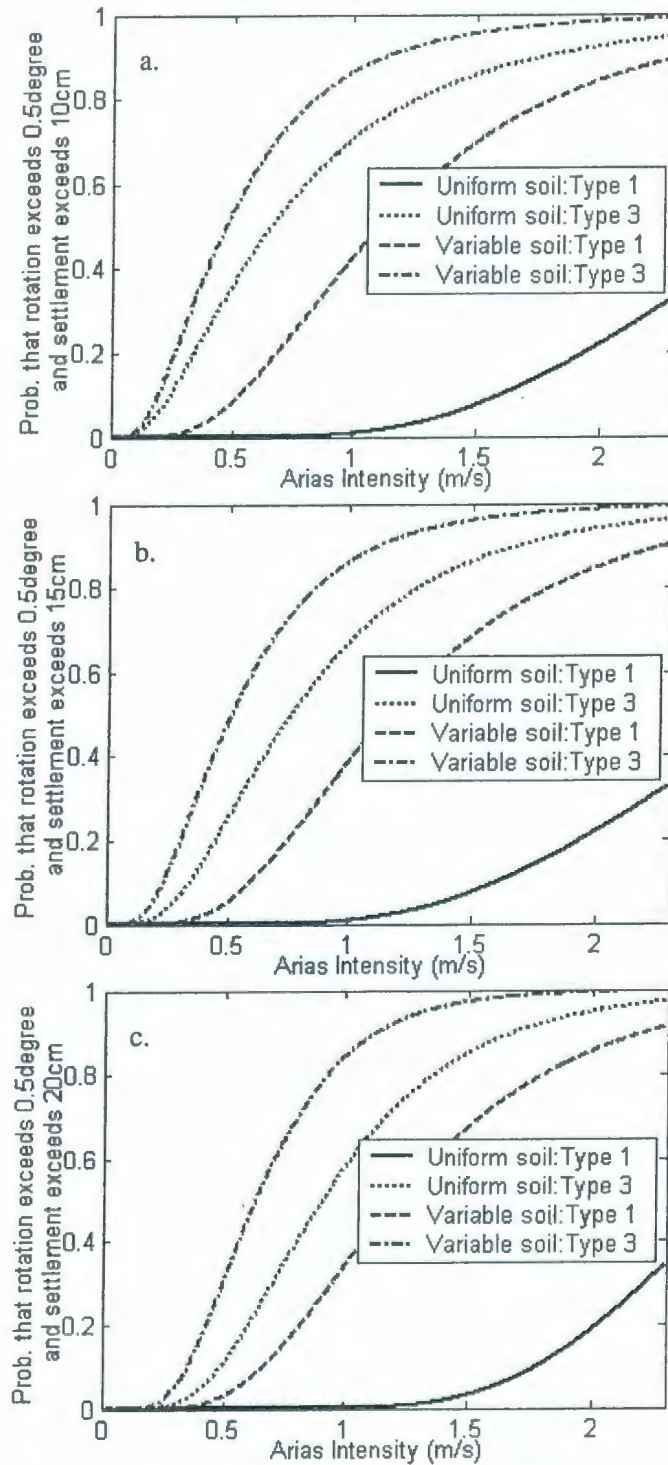


Figure A.8: Type-II damage curve: probability of damage due to exceeding a. both level-1 maximum settlement and level-3 maximum base rotation; b. both level-2 maximum settlement and level-3 maximum base rotation; c. both level-3 maximum settlement and level-3 maximum base rotation.

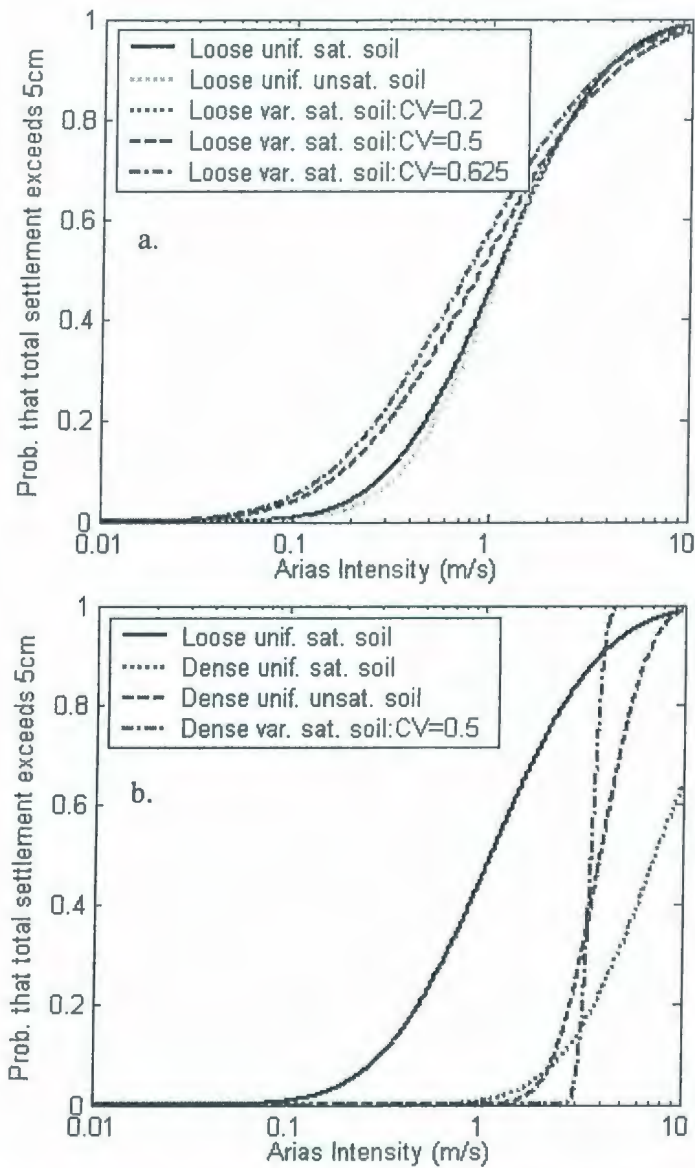


Figure A.9: Fragility curve for maximum total settlements exceeds 5cm.

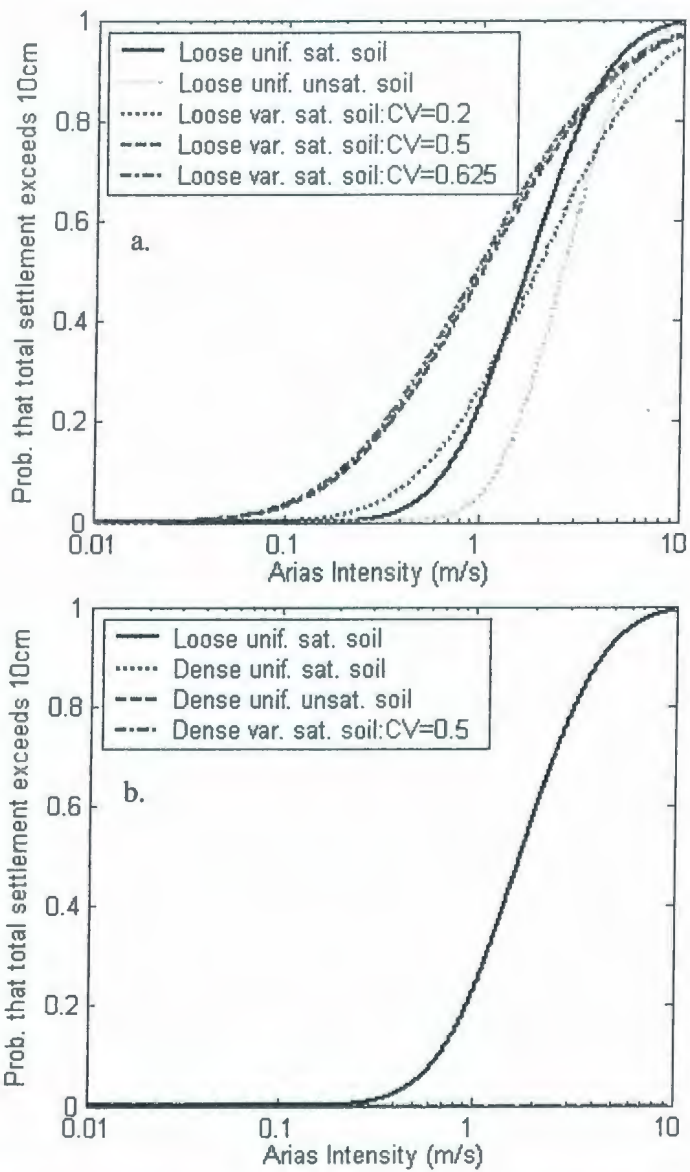


Figure A.10: Fragility curve for maximum total settlements exceeds 10cm.

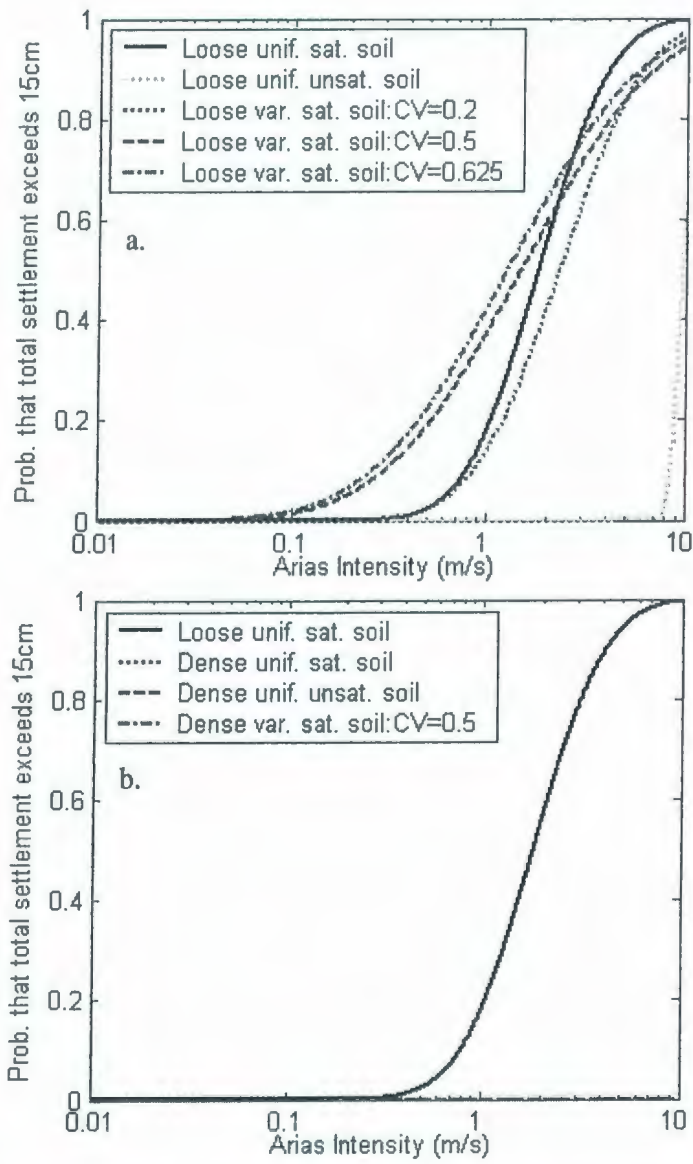


Figure A.11: Fragility curve for maximum total settlements exceeds 15cm.

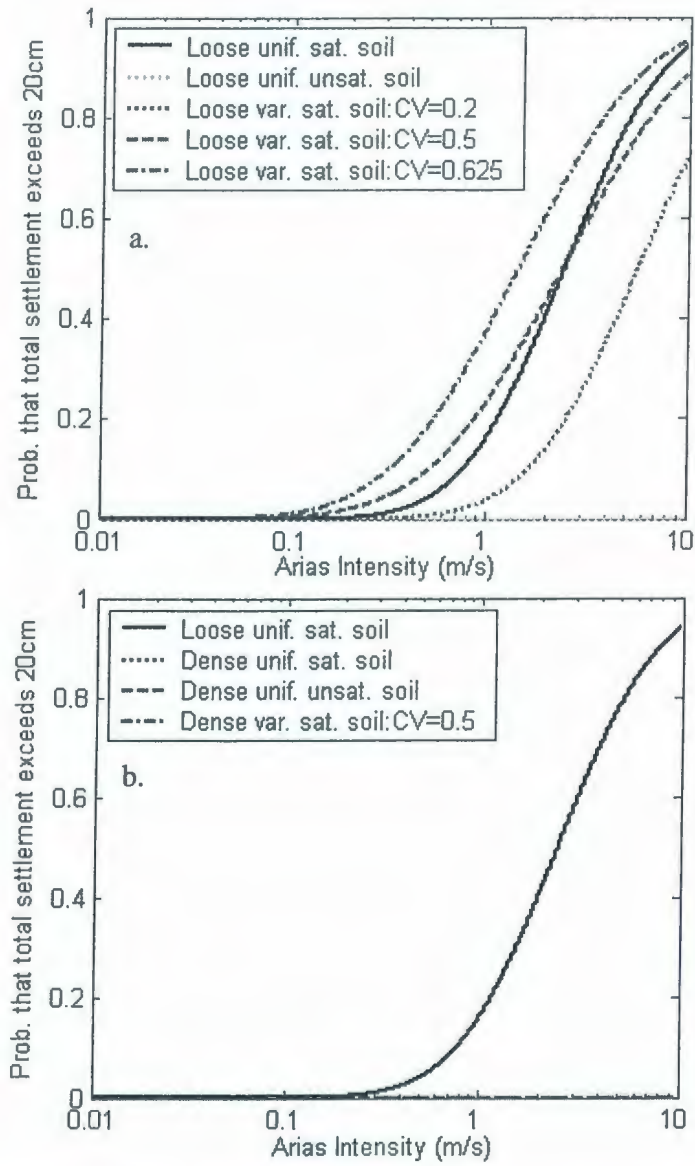


Figure A.12: Fragility curve for maximum total settlements exceeds 20cm.

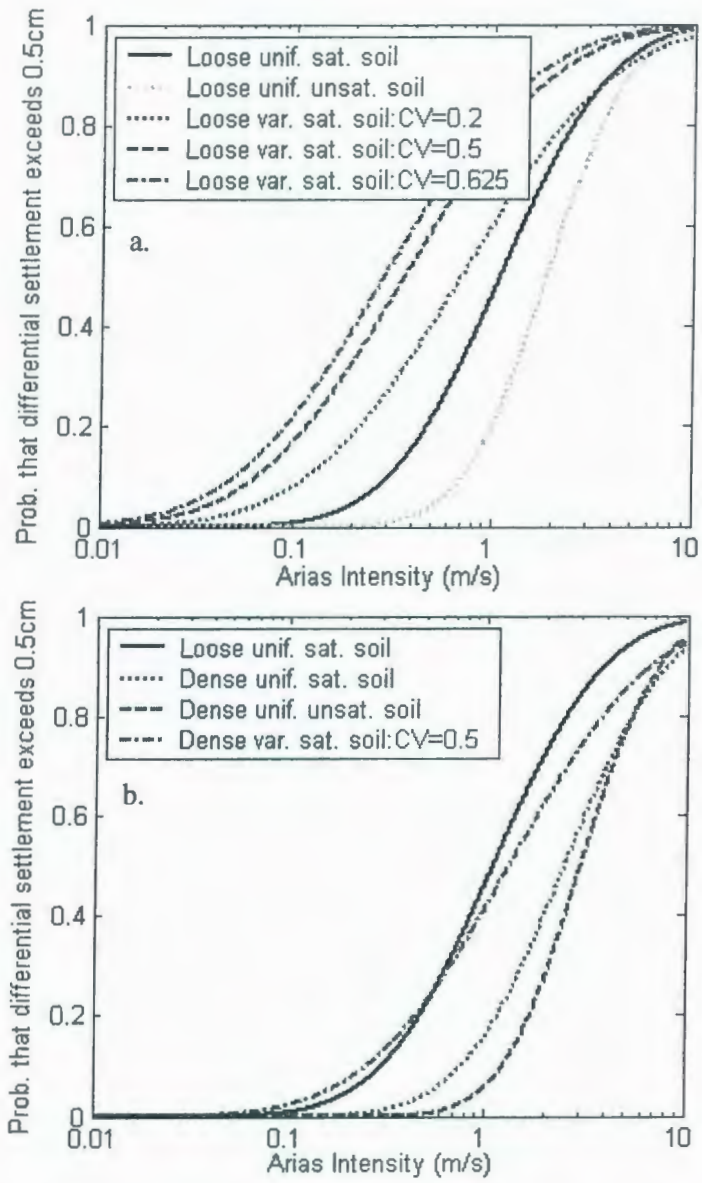


Figure A.13: Fragility curve for maximum differential settlements exceeds 0.5cm.

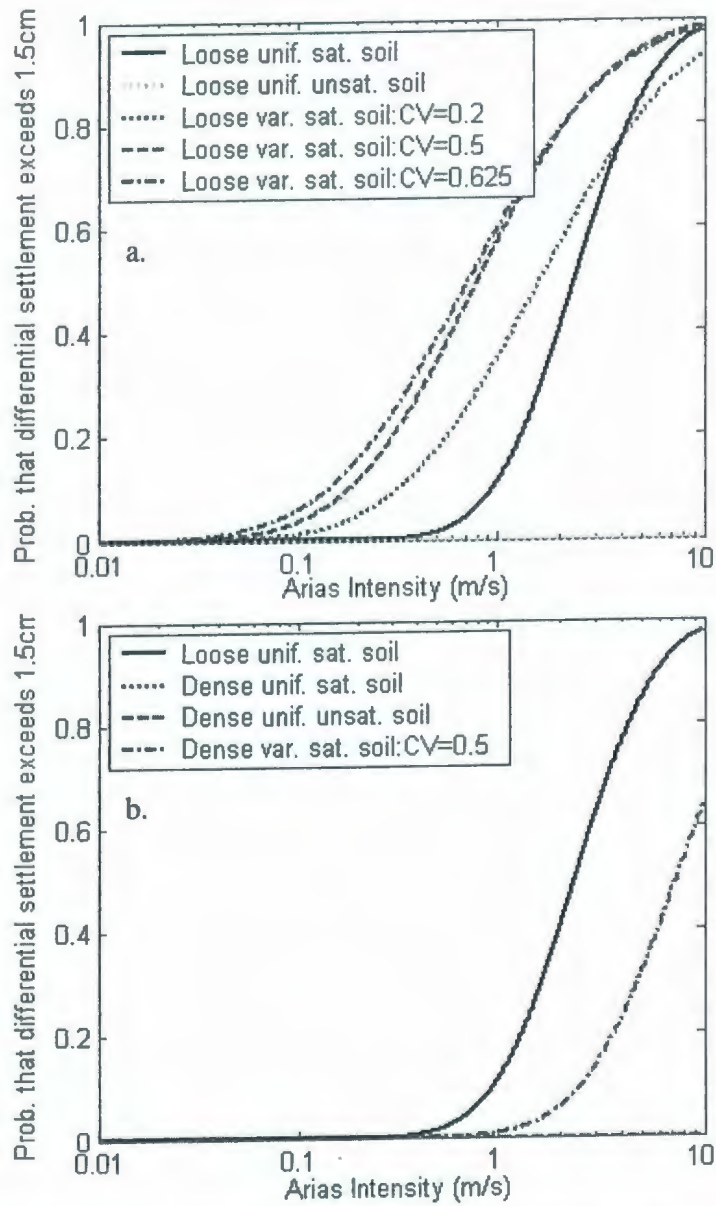


Figure A.14: Fragility curve for maximum differential settlements exceeds 1.5cm.

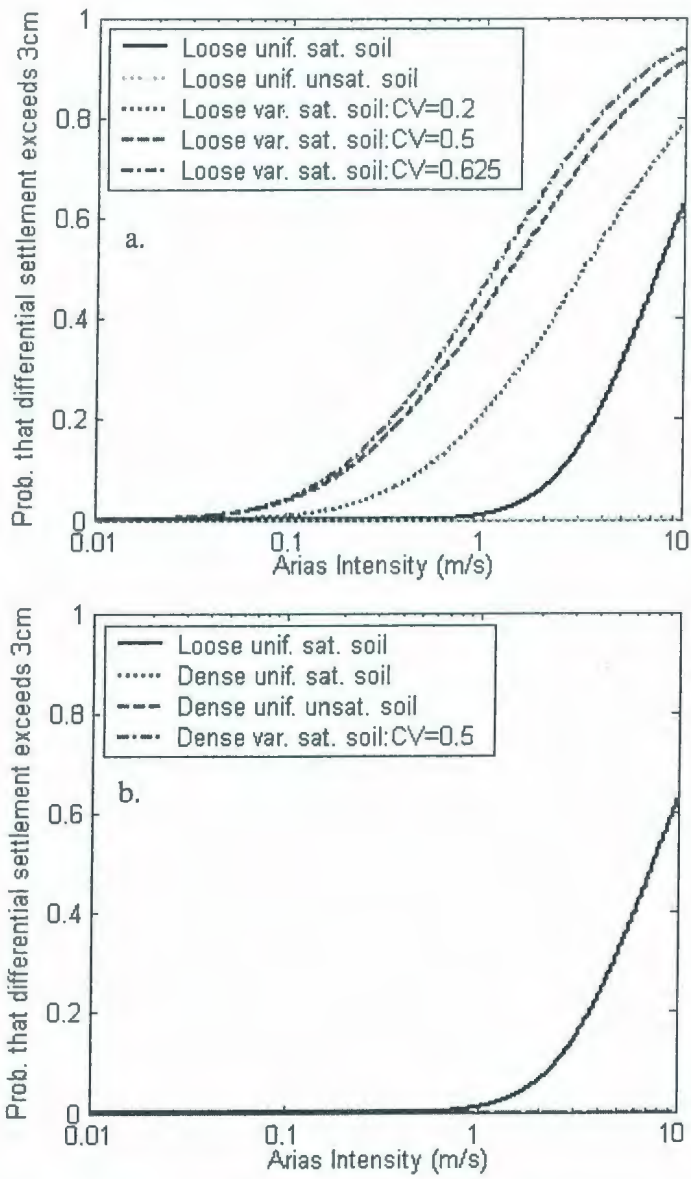


Figure A.15: Fragility curve for maximum differential settlements exceeds 3cm.

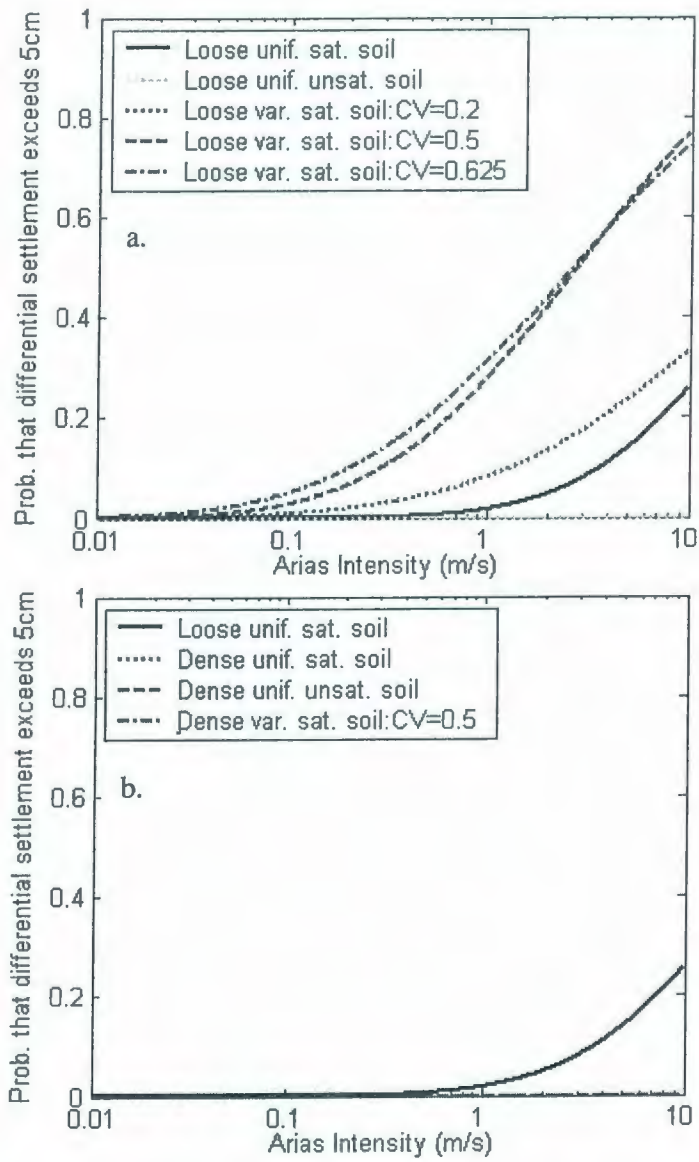


Figure A.16: Fragility curve for maximum differential settlements exceeds 5cm.

APPENDIX B

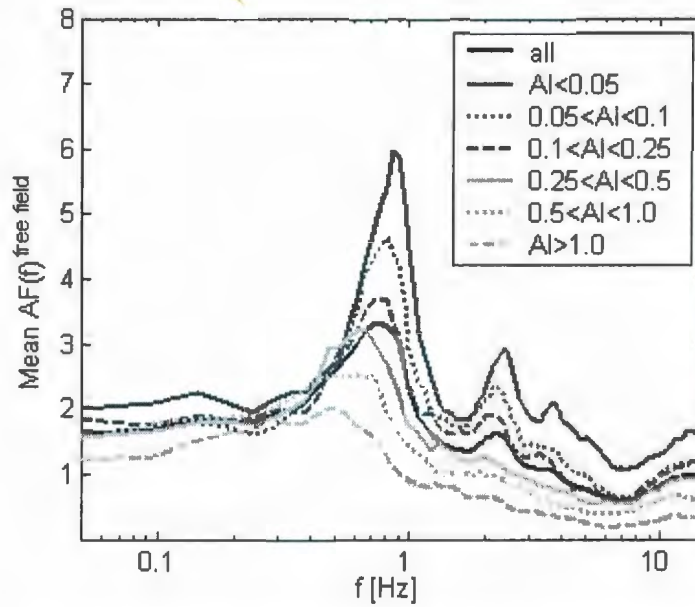


Figure B.1: Mean Amplification functions for loose saturated soil ($D_r=45\%$) site sorted by Arias intensity (m/s).

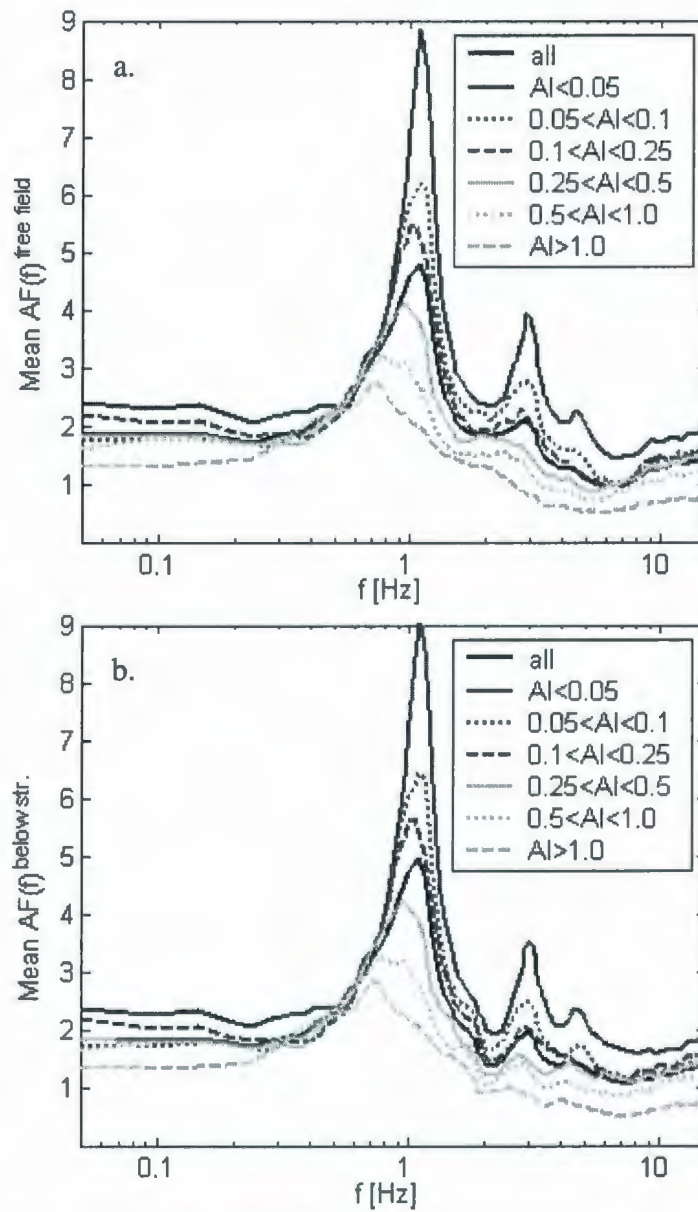


Figure B.2: Mean amplification functions for loose unsaturated soil ($D_r=45\%$) site: a. Free field- Node4; b. Below structure- Node5. Locations of nodes are shown in Figure 6.21.

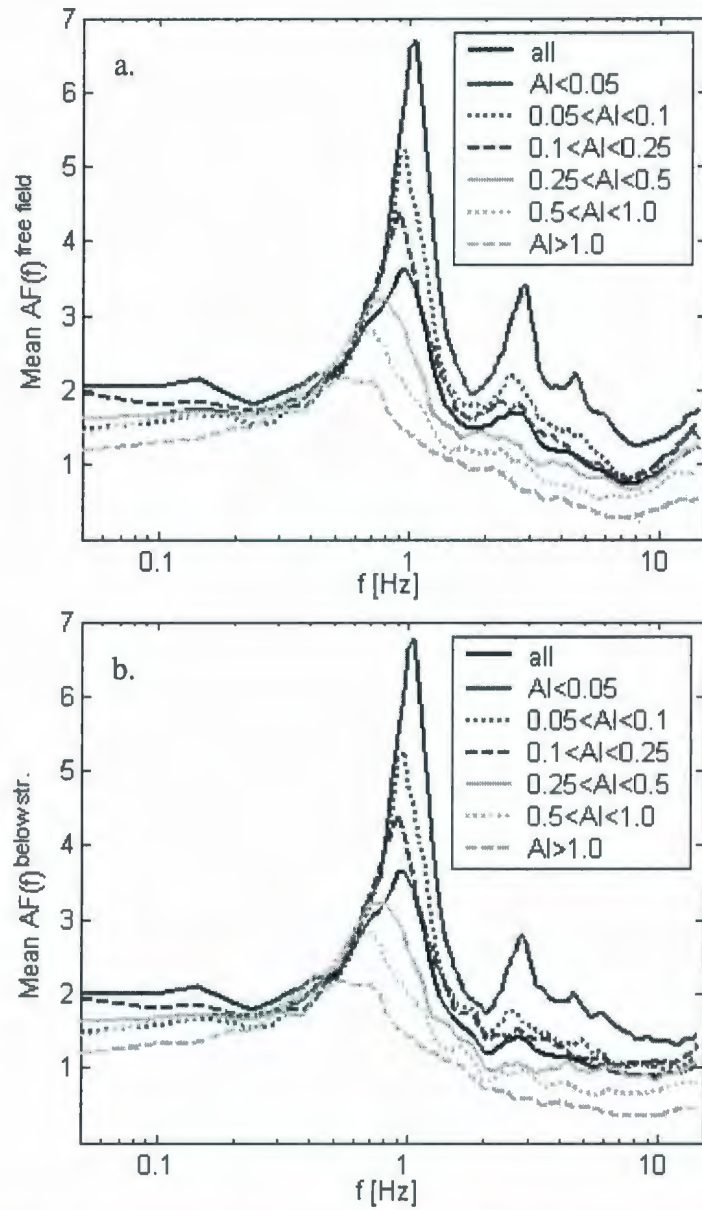


Figure B.3: Mean amplification functions for dense saturated soil ($D_r=85\%$) site: a. Free field- Node4; b. Below structure- Node5.

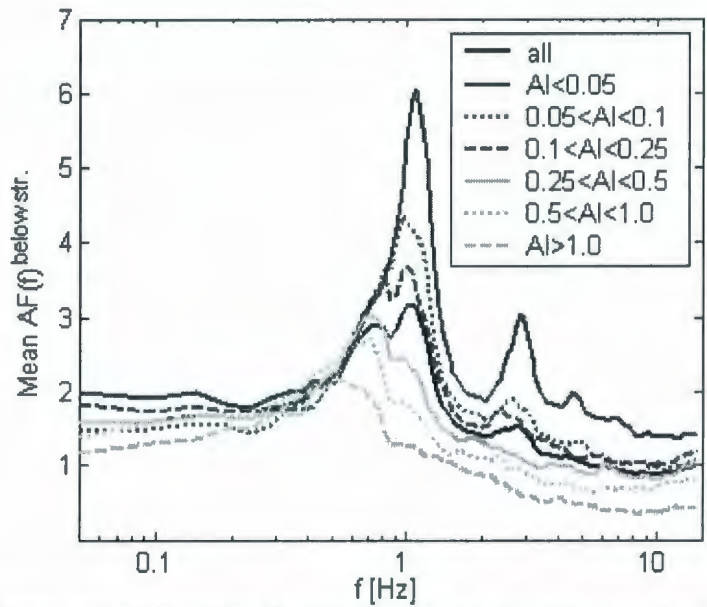


Figure B.4: Mean amplification functions for dense saturated soil ($D_r=85\%$) site for structure II: Below structure- Nodes5.

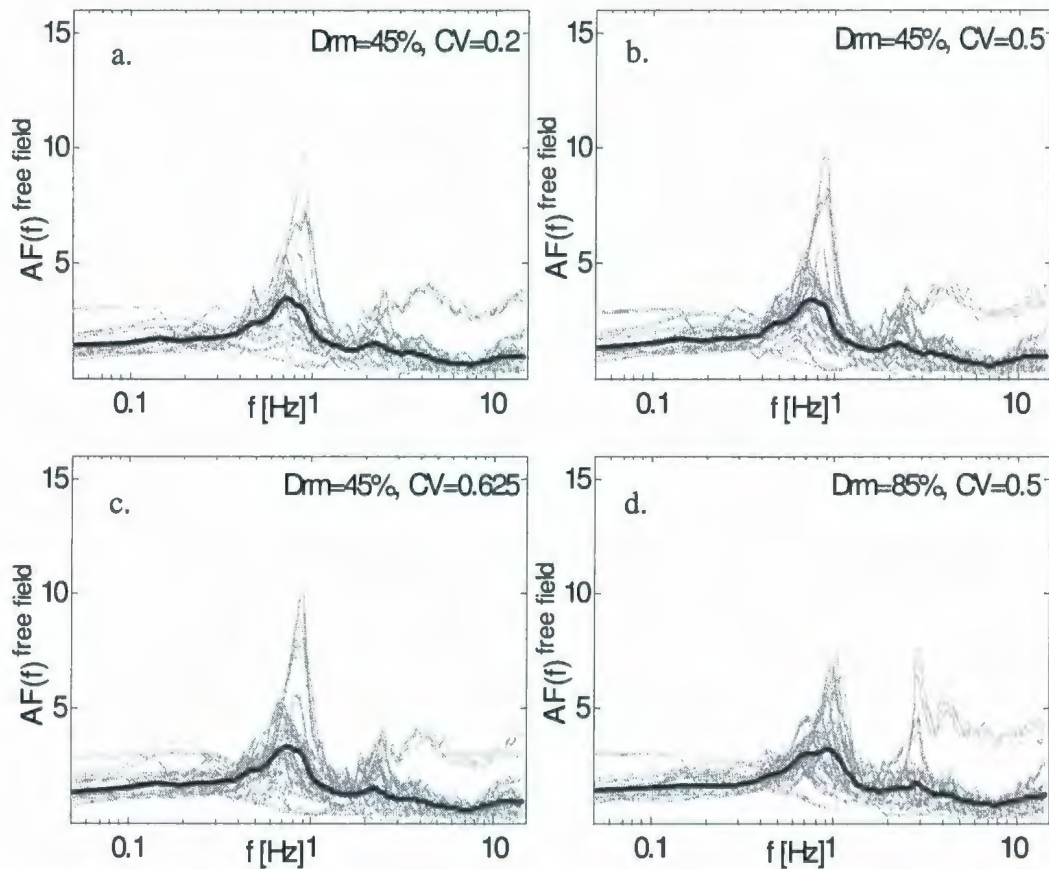


Figure B.5: Amplification function for variable soil in the free field (Node 4).



